ULB FACULTÉ DES SCIENCES
UNIVERSITÉ LIBRE DE BRUXELLES

Fluctuations, Counting Statistics, and Charge Transport in Mesoscopic Systems

Thesis presented by Jiayin GU (顾加银)
with a view to obtaining the PhD Degree in Physics
Academic year 2019-2020

Supervisor: Professor Pierre GASPARD
Center for Nonlinear Phenomena and Complex Systems

将进酒

李白

君不见黄河之水天上来，奔流到海不复回。
君不见高堂明镜悲白发，朝如青丝暮成雪。
人生得意须尽欢，莫使金樽空对月。
天生我材必有用，千金散尽还复来。
烹羊宰牛且为乐，会须一饮三百杯。
岑夫子，丹丘生，将进酒，杯莫停。
与君歌一曲，请君为我倾耳听。
钟鼓馔玉不足贵，但愿长醉不愿醒。
古来圣贤皆寂寞，惟有饮者留其名。
陈王昔时宴平乐，斗酒十千恣欢谑。
主人何为言少钱，径须沽取对君酌。
五花马、千金裘，呼儿将出换美酒，与尔同销万古愁。

Invitation to Wine

Li Bai

Do you not see the Yellow River come from the sky,
Rushing into the sea and ne'er come back?
Do you not see the mirrors bright in chambers high
Grieve o'er your snow-white hair though once it was silk-black?
When hopes are won, Oh! Drink your fill in high delight,
And never leave your wine-cup empty in moonlight!
Heaven has made us talents, we're not made in vain.
A thousand gold coins spent, more will turn up again.
Kill a cow, cook a sheep and let us merry be,
And drink three hundred cupfuls of wine in high glee!
Dear friends of mine,
Cheer up, cheer up!
I invite you to wine.
Do not put down your cup!
I will sing you a song, please hear,
O hear! Lend me a willing ear!
What difference will rare and costly dishes make?
I only want to get drunk and never to wake.
How many great men were forgotten through the ages?
But real drinkers are more famous than sober sages.
The Prince of Poets feast'd in his palace at will,
Drank wine at ten thousand a cask and laughed his fill.
A host should not complain of money he is short,
To drink with you I will sell things of any sort.
My fur coat worth a thousand coins of gold
And my flower-dappled horse may be sold
To buy good wine that we may drown the woes age-old.

Acknowledgements

First of all, I am profoundly grateful to Pierre Gaspard for being my supervisor in the writing of the thesis. I have not only benefited greatly from his large amount of knowledge, but also been deeply influenced by his devotion to science. I would also like to thank Thomas Gilbert, Gregory Kozyreff for monitoring the progress of the thesis, and Sergio Ciliberto, Bart Cleuren for being members of the thesis jury.

I thank Dong Yang, Sheng Zeng, Chunlin Wan, Duc-Thanh Tran, Yanqing Zhu, and many others. The interactions with them greatly enriched my daily life. I wish to thank the staff from Université Libre de Bruxelles and the Embassy of P. R. China in Belgium who have helped me in administrative affairs, with a particular mention to Yuan Feng for her help to facilitate the process of my Ph.D. application in the very beginning.

I acknowledge the China Scholarship Council, De Meurs-François Prize, and the Université Libre de Bruxelles (Pierre Gaspard Francqui Prize grant) for the financial support of this thesis. I would also acknowledge Shared ICT Services Centre, Université Libre de Bruxelles for the computational resources that was provided.

Finally, I want to express my gratitude to my parents, whose continuous support has been absolutely essential for the completion of the thesis.

Abstract

In this thesis, we study the transport of charged particles in mesoscopic systems where the long-range electrostatic interaction plays a key role. In particular, we focus on the statistical properties of currents which satisfy the relation known as fluctuation theorem. A stochastic approach is presented in consistency with the laws of electricity, thermodynamics, and microreversibility. In this approach, densities of charged particles are ruled by stochastic partial differential equations and the electric field generated by the charges is determined with the Poisson equation.

We start by proposing a coarse-grained model to describe the long-time behavior of particle transport in nonequilibrium systems in contact with several reservoirs. In this model, the particle exchanges between the reservoirs can be determined after a long enough time by the first and second cumulants of the probability distribution of particle transfers, thus enabling the numerical evaluation of the driving forces. It is proved that, close to equilibrium, the coarse-grained model is applicable to any system in nonequilibrium steady state. Moreover, the studies with specific examples show that the range of application of the coarse-grained model can be extended to the regime arbitrarily far from equilibrium if the detailed transition rates have linear dependence on the local particle concentration. In addition, the finite-time fluctuation theorem is established for systems with linear rates.

Then, we use our stochastic approach to study charge transport in diodes and transistors. The counting statistics of the carrier current and the measured total current including the contribution of the displacement current are performed. The fluctuation theorem is shown to hold for both currents. The convergence of the finite-time affinities towards their asymptotic values over long-time scales is tested using our proposed coarse-grained model. Accurate agreement between the numerical affinities and the theoretical predictions is found when affinities take moderate values. This brings further numerical support to the fluctuation theorem for the currents in these nonlinear electronic devices. For diodes, the current-voltage characteristics is obtained, which can be well fit by Shockley curve under the extreme condition where the concentration of majority charge carriers is overwhelmingly larger than that of minority charge carriers. For transistors, the signal amplifying effect is realized under their working conditions. Moreover, the Onsager reciprocal relations and their generalizations to nonlinear transport properties deduced from the fluctuation theorem are numerically shown to be satisfied.

Finally, we proceed to investigate the charge transport in a system of three tunneling junctions coupled together through a conductive island or quantum dot. The cumulant generating function is obtained by numerically solving the eigenvalue problem regarding the modified evolution operator including the counting parameters. The symmetry relation implied by the fluctuation theorem is verified, and the Onsager reciprocal relations together with their generalizations are again shown to be satisfied. Furthermore, under certain conditions, the current-voltage characteristics shows the staircase pattern due to the Coulomb blockade effect.

Contents

Chapter 1

Introduction

Nature has a hierarchical structure of spatial scales, ranging from the subatomic to the supergalactic scale. Accordingly, the physical theories are tailored for the system of interest at different levels of description. However, as is often the case, the resulting phenomenological descriptions may have apparent inconsistencies. The most prominent is the puzzling aspect of natural phenomena manifested as the dichotomy between reversibility and irreversibility. Going from the microscopic to macroscopic scale, the description of the evolution of systems should proceed from the Schrödinger equation to hydrodynamical ones, e.g., the diffusion equation. It became one of the central issues in physics during the past two centuries to reconcile the latter with the former. Since the 1970s, great advances have been achieved in the understanding of this fundamental question by the advent of a collection of relations called fluctuation theorem, from which irreversibility is interpreted as an emerging property from the statistical description. Thus, the opposites that are reversibility and irreversibility can be unified in statistical physics which is arguably the most unique universal theory [1].

1.1 Historical Developments

The birth of thermodynamics dates back to the period of Industrial Revolution when there was actual needs to improve the efficiency of thermal machines transforming heat to work [2]. In various attempts, scientists and engineers gradually found the equivalence between heat and work, which are unified in the concept of energy. This directly led to the establishment of the first law of thermodynamics stating that the total energy of an isolated system is conserved. Besides, it was further realized that heat cannot be completely transformed into work without any external effect, thus ruling out the possible existence of the perpetuum mobile of the second kind. Based on this observation, Carnot obtained a universal bound for the efficiency of heat-to-work conversion of thermal machines, $\eta_{\max} = 1 - T_c/T_h$, where T_c and T_h are the respective temperatures of the cold and hot thermal reservoirs between which thermal machines operate. This so-called Carnot efficiency implies no prescription on how the conversion is achieved. Inspired by Carnot's work, Clausius soon identified a new state function, the entropy S, and in 1851 declared an inequality for thermodynamic processes of a system from state A to B,

$$\int_A^B \frac{\mathrm{d}Q}{T} \leq \Delta S, \tag{1.1}$$

which bears his name nowadays. This directly implies the property that the entropy of an isolated system can never decrease over time, which is called the second law of thermodynamics. It predicts that an isolated system will eventually evolve into an equilibrium state where the entropy reaches its maximum value. There are now many applications of this celebrated second law of thermodynamics, e.g., osmotic pressure, or chemical equilibrium. A macroscopic system is

thermodynamically characterized by the way the entropy depends on its state through the fundamental relation $S = S(E, V, N, \cdots)$. The thermodynamic temperature can thus be well defined as $T \equiv \partial E/\partial S$. According to this thermodynamic definition of temperature and the second law of thermodynamics, the so-called zeroth law is postulated, which states that objects in thermal contact eventually get the same temperature.

At the same time, statistics and fluctuations were brought into thermodynamics to account for the discrete nature of constituent particles of a gas. By assuming that the motions of gas molecules follow Hamiltonian dynamics, and that the gas contains many molecules, Maxwell derived the distribution of velocities for the particles of a gas in equilibrium [3]. In 1872, Boltzmann established his equation to describe the evolution the probability function $f(\mathbf{r}, \mathbf{v}, t)$ for finding a particle of a gas in the neighborhood of $(\mathbf{r}, \mathbf{v})$, and he also introduced a quantity, $H \equiv \int f \ln f \mathrm{d}\mathbf{r}\mathrm{d}\mathbf{v}$, to quantify the state of a gas. In this way, he derived his famous H-theorem stating that a gas inevitably evolves in time until the Maxwell distribution is reached, with the H function decreasing to the minimal value. The Maxwell distribution describes a macrostate corresponding to the largest number of microstates. This gave Boltzmann an insight to link the entropy and the number of possible microstates by a novel expression, $S = k_\mathrm{B} \ln \Omega$, where k_B is called Boltzmann's constant, Ω the number of possible microstates for a macrostate. However, Boltzmann's equation was based on the molecular chaos hypothesis assuming that the velocities of colliding particles are uncorrelated, and independent of position. This drew objection from Loschmidt claiming that it should not be possible to deduce an irreversible process from the underlying time-symmetric dynamics (Loschmidt's paradox [4]). Later, Gibbs took the system of interest as a whole, and developed the ensemble theory [5]. In this theory, a configuration of the system is considered as a point in phase space, the ensemble of possible configurations is described by the probability distribution ρ. Gibbs also gave several ensemble distribution functions, of which the most useful may be the canonical ensemble, $\rho_i = \mathrm{e}^{-\beta E_i}/Z$, with partition function defined as $Z \equiv \sum_i \mathrm{e}^{-\beta E_i}$, and $\beta \equiv 1/(k_\mathrm{B}T)$ the inverse temperature. This canonical ensemble describes such a situation where a particle system is imposed with fixed number of constituent particles N, fixed volume V, and fixed temperature T by thermal contact with a heat bath. The free energy is related to the partition function by $F = -k_\mathrm{B}T \ln Z$. The entropy formula proposed by Boltzmann is generalized to $S = -k_\mathrm{B} \sum_i \rho_i \ln \rho_i$. The expression for the canonical ensemble distribution is the summit of equilibrium statistical mechanics [6]. The small fluctuations of any extensive quantity δX around its equilibrium value are described by the following formula,

$$\mathcal{P}(\delta X) \sim \exp\left(\frac{\delta^2 S}{2k_\mathrm{B}}\right), \tag{1.2}$$

where $\delta^2 S/2$ is the second-order excess entropy evaluated around the equilibrium state and corresponds to the change δX. However, Gibbs' ensemble theory only applies in the equilibrium regime. The searching for a satisfactory theory out of equilibrium was still going on.

In 1905, Einstein's seminal work on Brownian motion opened a new chapter in the development of nonequilibrium statistical mechanics [7, 8]. He explained the motion of Brownian particles as the result of the incessant random collisions by the much smaller solvent molecules, and expressed the mean-square of its one-dimensional displacement in terms of the diffusion constant: $\lambda = \sqrt{2Dt}$. Furthermore, Sutherland, Einstein, and Smoluchowski independently derived a relation, $D = \mu k_\mathrm{B}T$, linking the diffusion constant with the mobility defined as the linear response of a Brownian particle to applied force: $\langle v \rangle = \mu F$ [9, 7, 10]. Later, the theory of Brownian motion was further investigated by Ornstein, Uhlenbeck, and Wang [11, 12]. Around 1928, Johnson and Nyquist discovered a similar relation between the resistance of a circuit and the spontaneous voltage fluctuations [13, 14, 15]. These relations are the results of the fluctuation-dissipation theorem which quantifies the relation between the equilibrium fluctuations in the system that obeys detailed balance and the response of the system to the applied perturbations. Using the fluctuation-dissipation theorem as the basic formula, Onsager derived the reciprocal relations for the linear response coefficients in 1931 [16, 17], and this result was further treated by Casimir in 1945 [18]. In 1951, Callen and Welton developed the fluctuation-dissipation theorem within

a general quantum mechanics setting. They studied the time evolution of quantum-mechanical system following Hamiltonian dynamics. The system is initially in thermal equilibrium, with the state described by density matrix of canonical form. This approach was subsequently further systematized by Green [19, 20], and in particular by Kubo [21, 22, 23].

The fluctuation-dissipation theorem is only valid for systems near equilibrium. Scientists were still searching for a general statement regarding the dynamics of systems far from equilibrium. In this regard, a breakthrough appeared in 1993 when Evans and his coworkers found the relation,

$$\lim_{t\to\infty}\frac{1}{t}\ln\frac{\mathcal{P}(\bar{\Sigma}_t=A)}{\mathcal{P}(\bar{\Sigma}_t=-A)}=A, \tag{1.3}$$

in computer simulations of thermostatted shear-driven fluids in contact with a heat bath [24], where $\mathcal{P}(\bar{\Sigma}_t)$ denotes the probability distribution of the finite-time entropy production $\bar{\Sigma}_t = (1/t)\int_0^t \Sigma(s)\mathrm{d}s$ defined in terms of total irreversible entropy production $\Sigma(t) = \int_V \mathrm{d}V\sigma(\mathbf{r},t)/k_\mathrm{B}$. This relation places a constraint on the fluctuations of entropy production, and is thus called steady-state fluctuation theorem considering that it is valid in long-time limit. It implies that it is exponentially more likely to observe a positive entropy production rather than a negative one. This theorem was later mathematically proven for a large class of systems using concepts from chaotic dynamics by Gallavotti and Cohen in 1995 [25, 26], for driven Langevin dynamics by Kurchan in 1998 [27], for Markovian stochastic dynamics by Lebowitz and Spohn in 1999 [28], and it was extended to several coupled currents by Gaspard, Andrieux, and coworkers [29, 30, 31, 32]. The experimental verification of steady-state fluctuation theorem was first performed by Wang and coworkers in 2002 with the motion of a colloidal particle in water [33], and subsequently by many others with different experimental setups [34, 35, 36, 37, 38, 39].

In 1997, Jarzynski proved a remarkable relation,

$$\left\langle \mathrm{e}^{-\beta W}\right\rangle = \mathrm{e}^{-\beta\Delta F}, \tag{1.4}$$

where W is the work done on a system that is initially in thermal equilibrium and driven out of equilibrium by an external force evolving under a protocol which is parameterized by λ from the value A to B. $\Delta F = F_B - F_A$ denotes the free energy difference between the final equilibrium ensemble and the initial equilibrium ensemble, and $\langle\cdot\rangle$ stands for the average over the repetition of driving [40, 41, 42, 43, 44, 45]. In his proof, Jarzynski used the property that the volume of phase space is conserved by the Liouville theorem, as well as the time-reversal symmetry of the Hamiltonian dynamics [46]. This relation was later called Jarzynski equality, allowing to express the free energy difference between two equilibrium states by a nonlinear average over the required work to drive the system in a nonequilibrium process from one state to the other. From the Jarzynski equality, the Clausius inequality can be immediately obtained as a corollary, $\langle W\rangle \geq \Delta F$, thus in accord with the second law of thermodynamics. In 1999, Crooks obtained his fluctuation relation,

$$\frac{\mathcal{P}_\mathrm{F}(W)}{\mathcal{P}_\mathrm{R}(-W)}=\mathrm{e}^{\beta(W-\Delta F)}, \tag{1.5}$$

in the same scenario, where $\mathcal{P}_\mathrm{F}(W)$ and $\mathcal{P}_\mathrm{R}(W)$ denote the probability distributions of work done in a forward driving protocol and in its time-reversal, respectively [47]. Crooks fluctuation relation is the constraint on the fluctuations of work, and the Jarzynski equality can be immediately derived from $\int \mathcal{P}_\mathrm{R}(-W)\mathrm{d}W = 1$. Since these relations hold for driving processes in finite time intervals, they are thus called transient fluctuation theorem. These results are closely related to an earlier work by Bochkov and Kuzovlev around 1980 [48, 49, 50, 51]. The experimental verification of these relations were carried out with single-molecule manipulation experiments [52, 53, 54]. The Jarzynski equality has many applications, including (i) the development of numerical methods for estimating free energy differences in computational chemistry and physics [55], (ii) the analysis of single-molecule experiments [52, 53]. Detailed accounts of fluctuation theorems are presented in the reviews by Evans and others [56, 57, 58, 59].

The fluctuation theorems have similar structure, concerning relations between the probabilities of forward and time-reversed trajectories [60]. They are as a consequence of microreversibility, a fundamental symmetry of Nature. They can be considered as a generalization of the second law of thermodynamics. Close to equilibrium, the fluctuation theorems reduce to the well-known fluctuation-dissipation relations such as the Green-Kubo relation for the transport coefficient. Moreover, they also implies the Onsager reciprocal relations as well as the generalized nonlinear ones up to arbitrary order [29, 61].

1.2 Outline

The purpose of the present thesis is to study the charge transport in mesoscopic systems with three aims: (i) investigating the current fluctuations and their implications; (ii) elucidating the influence of long-range electrostatic interaction between charged particles on the transport behavior; (iii) with the settings of semiconductor devices, exploring their practical functionalities. The fluctuation theorem can be derived from two fundamental ingredients: the time-reversal symmetry of microscopic dynamics and the fact that thermal equilibrium is described by the Gibbs canonical ensemble. The electrostatic interaction between charged particles is evidently beyond these two fundamental ingredients, so it is reasonably hoped that new constraints on the fluctuation theorem can be found. In particular, we are also interested in the extreme case where the electrostatic interaction between charged particles can be safely neglected. Besides, the functionalities of the semiconductor devices not only depend on the charge transport obeying fluctuation theorem, but also on the detailed space- and charge-configurations. Therefore, the possible achievements with respect to the second and third aims constitute the main highlights of this thesis.

The thesis is organized as follows. In Chapter 2, the general preparatory knowledge for the remainder of the thesis is presented. Chapter 3 deals with the coarse graining of systems in nonequilibrium steady state. This endeavor is similar in spirit to the characterization of systems in equilibrium with a few parameters, such as energy, volume, temperature and the like. In this chapter, a system in contact with several particle reservoirs is coarse grained such that two constant transition rates are introduced to describe the long-time behavior of particle exchanges between any pair of reservoirs. Based on this coarse-grained model, the counting statistics is performed to establish the fluctuation theorem. Moreover, a somewhat more detailed stochastic model having a single random state variable is used to test the validity of the coarse-grained model. In this model, the transition rates have linear dependence on the state variable. In Chapter 4, we study the transport of charged particles in conductive channels with a twofold purpose. One is to present a stochastic approach for the charge transport at the mesoscopic level. This approach was first introduced in Ref. [62], and serves in this thesis as a paradigmatic example for developing more sophisticated approaches in subsequent chapters. Another is to further test the validity of the coarse-grained model in this system where the transition rates are nonlinear due to the electrostatic interaction between charged particles. Like the situation of a dilute gas, the electrostatic interaction is found to diminish as the charge density becomes lower, and in the low-density limit the linear transition rates are recovered. Chapters 5 and 6 are respectively devoted to the studies of charge transport in the p-n junction diodes and bipolar n-p-n junction transistors. In these two chapters, the preceding stochastic approach are extended to account for both the transport of electrons and holes, as well as the generation-recombination process between them. Apart from the fluctuation relation for currents and its implications, we particularly focus on the realization of the practical functionalities of these two semiconductor devices in the framework of the extended stochastic approach. Chapter 7 treats the charge transport in a system of three mesoscopic tunnel junctions coupled with a quantum dot or conductive island. This system has one random state variable and the transition rates are nonlinear. Thus, it allows the study of fluctuation theorem by numerically obtaining the cumulant generating function for charge transport as the leading eigenvalue of the modified evolution operator including the counting parameters. Moreover, the Coulomb blockade effect on the transport properties under certain conditions is also investigated. Concluding remarks are given in Chapter 8.

Chapter 2

Generalities

In this chapter, generalities are presented. They include the fluctuation theorem and its implications, the central limit theorem, the techniques that are essential for analyzing and simulating master equation systems, as well as one example of stochastic processes.

2.1 Fluctuation Theorem

Let's consider a system S in contact with n particle reservoirs R_i $(i = 0, \cdots, n-1)$, as shown in Figure 2.1. When driven out of equilibrium, the numbers of particles flowing across the system are stochastic variables. After the system has relaxed to a nonequilibrium steady state, the joint probability distribution of particle transfers Z_i $(i = 1, \cdots, n-1)$ flowing respectively from reservoir R_i $(i = 1, \cdots, n-1)$ to system during the time interval $[0,\, t]$ (taking R_0 as the reference reservoir) obeys the multivariate fluctuation relation [61], reading

$$\frac{\mathcal{P}_{\mathbf{A}}(\mathbf{Z}, t)}{\mathcal{P}_{\mathbf{A}}(-\mathbf{Z}, t)} \simeq_{t\to\infty} \exp\left(\mathbf{A}\cdot\mathbf{Z}\right), \tag{2.1}$$

where we have used the vectorial notation

$$\mathbf{Z} = \begin{pmatrix} Z_1 \\ \vdots \\ Z_{n-1} \end{pmatrix}, \qquad \mathbf{A} = \begin{pmatrix} A_1 \\ \vdots \\ A_{n-1} \end{pmatrix}. \tag{2.2}$$

Here, $\{A_i\}$ are called affinities, which are the thermodynamic forces driving the particle exchanges from the reservoirs $\{R_i\}$ to the reference reservoir R_0 [63]. If the whole system is isothermal at the temperature T, the affinities are given by

$$A_i \equiv \beta\left(\mu_i - \mu_0\right), \tag{2.3}$$

where μ_i is the chemical potential of ith reservoir, $\beta \equiv (k_{\mathrm{B}}T)^{-1}$ the inverse temperature, and k_{B} the Boltzmann's constant. When $\mathbf{A} = \mathbf{0}$, the system is in equilibrium where we recover the principle of detailed balance, according to which opposite fluctuations are equiprobable. We can define the generating function of statistical cumulants in terms of counting parameters $\boldsymbol{\lambda}$ according to

$$Q(\boldsymbol{\lambda}; \mathbf{A}) \equiv \lim_{t\to\infty} -\frac{1}{t} \ln \sum_{\mathbf{Z}} \mathcal{P}_{\mathbf{A}}(\mathbf{Z}, t)\, \mathrm{e}^{-\boldsymbol{\lambda}\cdot\mathbf{Z}}. \tag{2.4}$$

As a consequence of the multivariate fluctuation relation (2.1), we have the following symmetry relation,

$$Q(\boldsymbol{\lambda}; \mathbf{A}) = Q(\mathbf{A} - \boldsymbol{\lambda}; \mathbf{A}). \tag{2.5}$$

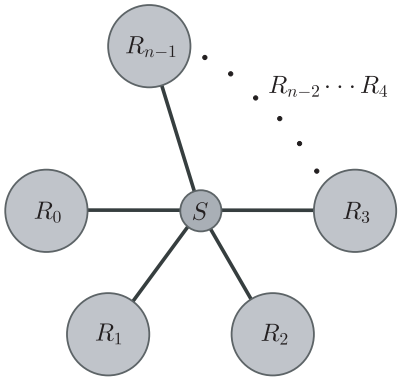

Figure 2.1: Schematic representation of a system S in contact with n particle reservoirs $R_0,\ R_1,\ R_2, \cdots, R_{n-1}$.

Such a relation can be established using the time-evolution operator that is modified to include the parameters $\boldsymbol{\lambda}$ counting particle transport [30, 31, 28, 64]. For nonequilibrium systems modeled by master equation, the affinities are determined by the transition rates through Schnakenberg's graph analysis (see Section 2.5).

The mean currents and their diffusivities can be obtained by taking the successive derivatives of the cumulant generating function (2.4) with respect to the counting parameters:

$$J_i(\mathbf{A}) \equiv \lim_{t\to\infty} \frac{1}{t} \langle Z_i(t) \rangle_{\mathbf{A}} = \left. \frac{\partial Q(\boldsymbol{\lambda}; \mathbf{A})}{\partial \lambda_i} \right|_{\boldsymbol{\lambda}=\mathbf{0}}, \tag{2.6}$$

$$D_{ij}(\mathbf{A}) \equiv \lim_{t\to\infty} \frac{1}{2t} \langle [Z_i(t) - J_i t]\, [Z_j(t) - J_j t] \rangle_{\mathbf{A}} = -\frac{1}{2} \left. \frac{\partial^2 Q(\boldsymbol{\lambda}; \mathbf{A})}{\partial \lambda_i \partial \lambda_j} \right|_{\boldsymbol{\lambda}=\mathbf{0}}, \tag{2.7}$$

where the notation $\langle \cdot \rangle$ stands for the sample average over the data from the counting statistics. By definition, the diffusivities satisfy the symmetry relation $D_{ij}(\mathbf{A}) = D_{ji}(\mathbf{A})$.

2.2 Thermodynamic Entropy Production

For nonequilibrium thermodynamics at the macroscale, the entropy production [65, 66, 67] is identified as the sum of affinities multiplied by the corresponding mean currents in units of Boltzmann's constant. In nonequilibrium steady states, the mean currents can be evaluated in the following way,

$$\mathbf{J}(\mathbf{A}) = \lim_{t\to\infty} \frac{1}{t} \sum_{\mathbf{Z}} \mathcal{P}_{\mathbf{A}}(\mathbf{Z}, t) \mathbf{Z} = \lim_{t\to\infty} \frac{\mathbf{Z}(t)}{t}, \tag{2.8}$$

where the ergodicity with respect to the probability distribution $\mathcal{P}_{\mathbf{A}}(\mathbf{Z}, t)$ is assumed in the last equality. According to the multivariate fluctuation relation (2.1), the entropy production rate is given by

$$\frac{1}{k_{\mathrm{B}}} \frac{\mathrm{d_i} S}{\mathrm{d}t} = \mathbf{A} \cdot \mathbf{J}(\mathbf{A}) = \lim_{t\to\infty} \frac{1}{t} \sum_{\mathbf{Z}} \mathcal{P}_{\mathbf{A}}(\mathbf{Z}, t) \ln \frac{\mathcal{P}_{\mathbf{A}}(\mathbf{Z}, t)}{\mathcal{P}_{\mathbf{A}}(-\mathbf{Z}, t)} \tag{2.9}$$

in terms of the Kullback-Leibler divergence between the distributions $\mathcal{P}_{\mathbf{A}}(\mathbf{Z}, t)$ and $\mathcal{P}_{\mathbf{A}}(-\mathbf{Z}, t)$. Equation (2.9) is always non-negative, which is in accord with the second law of thermodynamics. In this respect, the entropy production implied by the fluctuation relation can serve as a measure

of the breaking of the time-reversal symmetry of nonequilibrium probability distribution $\mathcal{P}_{\mathbf{A}}(\mathbf{Z},t)$. In equilibrium where $\mathbf{A}=\mathbf{0}$, detailed balance is recovered since $\mathcal{P}_{\mathbf{0}}(\mathbf{Z},t) \simeq \mathcal{P}_{\mathbf{0}}(-\mathbf{Z},t)$ by the fluctuation relation (2.1), and the entropy production rate (2.9) is vanishing together with the affinities (2.3) and the mean currents (2.8).

2.3 Symmetry Relations for the Response Properties

The fluctuation theorem provides a unified framework for deducing the Onsager reciprocal relations and their generalizations to the nonlinear transport properties [68, 29, 69, 70, 71]. For this purpose, we expand the mean currents in power series of affinities as

$$J_i = \sum_j L_{i,j} A_j + \frac{1}{2} \sum_{j,k} M_{i,jk} A_j A_k + \cdots \tag{2.10}$$

in terms of the response coefficients defined by

$$L_{i,j} \equiv \left. \frac{\partial J_i}{\partial A_j} \right|_{\mathbf{A}=\mathbf{0}} = \left. \frac{\partial^2 Q(\boldsymbol{\lambda};\mathbf{A})}{\partial \lambda_i \partial A_j} \right|_{\boldsymbol{\lambda}=\mathbf{A}=\mathbf{0}}, \tag{2.11}$$

$$M_{i,jk} \equiv \left. \frac{\partial^2 J_i}{\partial A_j \partial A_k} \right|_{\mathbf{A}=\mathbf{0}} = \left. \frac{\partial^3 Q(\boldsymbol{\lambda};\mathbf{A})}{\partial \lambda_i \partial A_j \partial A_k} \right|_{\boldsymbol{\lambda}=\mathbf{A}=\mathbf{0}}, \tag{2.12}$$

where we have made use of Eq. (2.6). $\{L_{i,j}\}$ are the so-called Onsager linear response coefficients, which characterize the linear transport properties and $\{M_{i,jk}\}$ are the nonlinear response coefficients of second order in the affinities. We note that $M_{i,jk} = M_{i,kj}$ by the definition of these coefficients. The response coefficients of higher order can also be introduced in a similar way.

If we take the derivatives of the symmetry relation (2.5) of the fluctuation theorem with respect to λ_i and A_j, we find that

$$\frac{\partial^2 Q}{\partial \lambda_i \partial A_j}(\boldsymbol{\lambda};\mathbf{A}) = -\frac{\partial^2 Q}{\partial \lambda_i \partial \lambda_j}(\mathbf{A}-\boldsymbol{\lambda};\mathbf{A}) - \frac{\partial^2 Q}{\partial \lambda_i \partial A_j}(\mathbf{A}-\boldsymbol{\lambda};\mathbf{A}), \tag{2.13}$$

which can be further reduced to

$$2\frac{\partial^2 Q}{\partial \lambda_i \partial A_j}(\mathbf{0};\mathbf{0}) = -\frac{\partial^2 Q}{\partial \lambda_i \partial \lambda_j}(\mathbf{0};\mathbf{0}) \tag{2.14}$$

by setting $\boldsymbol{\lambda}=\mathbf{A}=\mathbf{0}$. So, we obtain

$$L_{i,j} = -\frac{1}{2}\frac{\partial^2 Q}{\partial \lambda_i \partial \lambda_j}(\mathbf{0};\mathbf{0}). \tag{2.15}$$

Because of Eq. (2.7), we can get the fluctuation-dissipation relations

$$L_{i,j} = D_{ij}(\mathbf{0}), \tag{2.16}$$

and thus the Onsager reciprocal relations [16, 17, 18]

$$L_{i,j} = L_{j,i}. \tag{2.17}$$

If we take a further derivative of the identity (2.13) with respect to A_k before setting $\boldsymbol{\lambda}=\mathbf{A}=\mathbf{0}$, we find

$$M_{i,jk} = R_{ij,k} + R_{ik,j} \tag{2.18}$$

in terms of the linear response coefficients of the diffusivities around equilibrium defined by

$$R_{ij,k} \equiv \left. \frac{\partial D_{ij}}{\partial A_k} \right|_{\mathbf{A}=\mathbf{0}} = -\frac{1}{2}\frac{\partial^3 Q}{\partial \lambda_i \partial \lambda_j \partial A_k}(\mathbf{0},\mathbf{0}). \tag{2.19}$$

The Onsager reciprocal relations (2.17) as well as the relation (2.18) find their origin in the microreversibility underlying the fluctuation theorem for currents [68, 32, 57, 58, 59, 61]. The generalization of these relations to higher cumulants and higher nonlinear response coefficients can be deduced.

2.4 Central Limit Theorem

According to the central limit theorem [72], the probability distribution $\mathcal{P}_{\mathbf{A}}(\mathbf{Z},t)$ is expected to be well approximated after a long enough time by the following Gaussian distribution,

$$\mathscr{P}(\mathbf{Z},t)=\frac{1}{\sqrt{(4\pi t)^{n-1}\det\mathbf{D}}}\exp\left[-\frac{1}{4t}(\mathbf{Z}-\mathbf{J}t)\cdot\mathbf{D}^{-1}\cdot(\mathbf{Z}-\mathbf{J}t)\right], \tag{2.20}$$

where

$$\mathbf{J}=\begin{pmatrix}J_1\\J_2\\\vdots\\J_{n-1}\end{pmatrix},\qquad \mathbf{D}=\begin{pmatrix}D_{1,1}&D_{1,2}&\cdots&D_{1,n-1}\\D_{2,1}&D_{2,2}&\cdots&D_{2,n-1}\\\vdots&\vdots&\ddots&\vdots\\D_{n-1,1}&D_{n-1,2}&\cdots&D_{n-1,n-1}\end{pmatrix}, \tag{2.21}$$

are the mean currents and their diffusivities, with the elements given by Eqs. (2.6)-(2.7). Substituting $\mathscr{P}(\mathbf{Z},t)$ for $\mathcal{P}_{\mathbf{A}}(\mathbf{Z},t)$ into the multivariate fluctuation relation (2.1), we obtain that

$$\mathbf{Z}\cdot\mathbf{A}=\ln\frac{\mathscr{P}(\mathbf{Z},t)}{\mathscr{P}(-\mathbf{Z},t)}=\mathbf{Z}\cdot\mathbf{D}^{-1}\cdot\mathbf{J}, \tag{2.22}$$

in which case the affinities are given by

$$\mathbf{A}=\mathbf{D}^{-1}\cdot\mathbf{J}. \tag{2.23}$$

This evaluation of the affinities by means of the Gaussian approximation is only applicable when systems are near equilibrium where the probability distribution $\mathcal{P}_{\mathbf{A}}(\mathbf{Z},t)$ and its symmetric version $\mathcal{P}_{\mathbf{A}}(-\mathbf{Z},t)$ still share a large overlapping region in the space spanned by $\{\mathbf{Z}\}$ for large time t. Actually, Eq. (2.23) can also be derived for systems near equilibrium from Eq. (2.10) by discarding the terms of nonlinear responses and then substituting the fluctuation-dissipation relations (2.16) into it, that is

$$J_i\approx\sum_j D_{ij}(\mathbf{0})A_j, \tag{2.24}$$

which directly leads to Eq. (2.23). The reason why Eq. (2.23) is only valid in the linear regime close to equilibrium lies in the fact that the central limit theorem only captures the top of the probability distribution $\mathcal{P}_{\mathbf{A}}(\mathbf{Z},t)$ with its first and second cumulants (2.6) and (2.7), although the multivariate fluctuation relation (2.1) is a large-deviation property fully characterizing the distribution with all its cumulants. In particular, the cumulants higher than the first and second ones are essential to determine the tails of the distributions and thus the affinities. In this regard, a fundamental issue is to understand the stochastic process beyond the central limit theorem. Addressing this issue constitutes one of the themes of the thesis.

2.5 Schnakenberg's Network Theory

Inspired by Kirchhoff's method for linear electric circuits, scientists began to use network theory to analyze the behavior of master equation systems in nonequilibrium steady states [73, 74, 75, 76, 77, 78, 79]. In particular, Schnakenberg developed the network theory in order to determine

the properties of the steady state solution [78]. In his network theory of Markov jump processes, a graph G can be associated with the master equation in such a way that each state of the system corresponds to a vertex and the different allowed transitions $\omega \rightleftharpoons \omega'$ between the states are represented by edges. In the so-constructed graph, cyclic paths are sequences of edges joining a finite set of vertices and coming back to the starting vertex. Denoting by ω the vertices and e the edges of the graph, the affinity of the cyclic path $\mathcal{C}$ is defined as

$$A(\mathcal{C}) \equiv \ln \prod_{e \in \mathcal{C}} \frac{W(\omega \xrightarrow{e} \omega')}{W(\omega \xleftarrow{e} \omega')} \tag{2.25}$$

in terms of the ratio of transition rates along the path divided by the transition rates along the reversed path. This affinity characterizes the nonequilibrium constraints imposed by the boundaries on the cyclic path. Although the transition rates in Eq. (2.25) normally depend on the mesoscopic states, the so-obtained affinity only depends on the macroscopic thermodynamic force which is of physical importance. Schnakenberg's network theory has shown that many of the fundamental properties of a system in nonequilibrium steady state can be investigated and understood in terms of the graph analysis associated with the master equation. Moreover, the implication of affinities identified from the cycles of the graph leads to the establishment of the fluctuation theorem in its early form [79].

2.6 Gillespie's Algorithm

Gillespie's algorithm is an exact method for generating random trajectories in Markov stochastic processes [80]. Let's consider a master equation system whose transition rates are grouped in the set $\{k_\nu\}_{\nu=1}^{M}$. These rates are calculated according to the underlying physics. The probability density for μth transition to occur at time τ can be easily obtained and given by

$$\mathcal{P}(\tau, \mu) = k_\mu \exp\left(-\sum_{\nu=1}^{M} k_\nu \tau\right). \tag{2.26}$$

The whole procedure can be eventually divided into the following steps:

- Set the time variable $t = 0$ and calculate the transition rates according to the initial state. Specify the "stopping time" t_{stop}.
- By employing a suitable Monte-Carlo method, generate the random pair (τ, μ) according to the probability density function $\mathcal{P}(\tau, \mu)$[1].
- Use the obtained pair (τ, μ) to advance t by τ and change the system state according to the μth transition. Recalculate the transition rates according to the new state.
- If $t > t_{\text{stop}}$, terminate the whole procedure; otherwise, go back to the second step for looping.

We now introduce the application of the Monte-Carlo method in generating a number μ whose probability is determined by the weight of the transition rate k_μ in the set $\{k_\nu\}_{v=1}^{M}$. Define the cumulative distribution function

$$K(\mu) \equiv \sum_{\nu=1}^{\mu} k_\nu. \tag{2.27}$$

[1] The library GSL provides the function `gsl_ran_exponential` for returning a random time step τ according to exponential probability law $\mathrm{e}^{-t/k}$, with k as one of the arguments.

$K(\mu)$ is a monotonically increasing function with $K(0) = 0$ and $K(M) = \sum_{\nu=1}^{M} k_\nu$. Let X be a random variable whose value can be assigned by a random number generator $rand()$[2], which is tailored to produce random numbers that are uniformly distributed from 0 to $\sum_{\nu=1}^{M} k_\nu$. In one assignment, the random variable gets a value x, then the desired random number μ is determined according to the condition that

$$K(\mu - 1) < x < K(\mu). \tag{2.28}$$

2.7 A Simple Stochastic Process

Let's consider a simple Markov stochastic process that serves as an illuminating and illustrative example. In this process, there are two constant rates W_+ and W_-, corresponding to particle transitions from the left to the right reservoir, and the reverse transition, respectively. The signed cumulated particle transfers Z from the left to the right reservoir during the time interval $[0, t]$ is therefore the difference of two random numbers whose probability distributions are Poissonian with parameters $\lambda_+ = W_+ t$ and $\lambda_- = W_- t$. The probability distribution Z during the time interval $[0, t]$ obeys the master equation

$$\frac{\mathrm{d}}{\mathrm{d}t}\mathcal{P}(Z,t) = \hat{L}\mathcal{P}(Z,t) = \left[\left(\mathrm{e}^{-\partial_Z} - 1\right) W_+ + \left(\mathrm{e}^{+\partial_Z} - 1\right) W_-\right] \mathcal{P}(Z,t), \tag{2.29}$$

expressed in terms of the raising and lowering operators such that $\mathrm{e}^{\pm\partial_Z}\mathcal{P}(Z) = \mathcal{P}(Z \pm 1)$. The evolution operator $\hat{L}$ is thus expressed as $\hat{L} = \left(\mathrm{e}^{-\partial_Z} - 1\right) W_+ + \left(\mathrm{e}^{+\partial_Z} - 1\right) W_-$, with its adjoint operator given by $\hat{L}^\dagger = \left(\mathrm{e}^{+\partial_Z} - 1\right) W_+ + \left(\mathrm{e}^{-\partial_Z} - 1\right) W_-$. We can define the modified operator of $\hat{L}$ to let it depend on the counting parameter λ, reading $\hat{L}_\lambda = \mathrm{e}^{-\lambda Z}\hat{L}\mathrm{e}^{+\lambda Z}$. So we have

$$\begin{aligned}
\hat{L}_\lambda F(Z) &= \mathrm{e}^{-\lambda Z}\left[W_+\mathrm{e}^{-\partial_Z}\mathrm{e}^{\lambda Z}F(Z) + W_-\mathrm{e}^{+\partial_Z}\mathrm{e}^{\lambda Z}F(Z)\right] - \left(W_+ + W_-\right)F(Z) \\
&= \mathrm{e}^{-\lambda Z}\left[W_+\mathrm{e}^{\lambda(Z-1)}F(Z-1) + W_-\mathrm{e}^{\lambda(Z+1)}F(Z+1)\right] - \left(W_+ + W_-\right)F(Z) \\
&= \left[W_+\mathrm{e}^{-\lambda}F(Z-1) + W_-\mathrm{e}^{+\lambda}F(Z+1)\right] - \left(W_+ + W_-\right)F(Z) \\
&= \left[\left(\mathrm{e}^{-\lambda}\mathrm{e}^{-\partial_Z} - 1\right) W_+ + \left(\mathrm{e}^{+\lambda}\mathrm{e}^{+\partial_Z} - 1\right) W_-\right] F(Z),
\end{aligned} \tag{2.30}$$

from which we obtain the modified operator and its adjoint in the explicit forms:

$$\hat{L}_\lambda = \left(\mathrm{e}^{-\lambda}\mathrm{e}^{-\partial_Z} - 1\right) W_+ + \left(\mathrm{e}^{+\lambda}\mathrm{e}^{+\partial_Z} - 1\right) W_-, \tag{2.31}$$

$$\hat{L}_\lambda^\dagger = \left(\mathrm{e}^{-\lambda}\mathrm{e}^{+\partial_Z} - 1\right) W_+ + \left(\mathrm{e}^{+\lambda}\mathrm{e}^{-\partial_Z} - 1\right) W_-. \tag{2.32}$$

According to Schnakenberg's graph analysis, the affinity for this Markov jump process is given by $A = \ln\left(W_+/W_-\right)$. Thus, we find that there exists the symmetry relation

$$\hat{L}_{A-\lambda}^\dagger = \hat{L}_\lambda, \tag{2.33}$$

from which we can establish the fluctuation theorem for this Markov jump process. If $W_+ = W_-$ that gives $A = 0$, the process is in equilibrium and detailed balance is recovered.

We now define the moment generating function of signed cumulated flux,

$$G(s,t) \equiv \sum_{Z=-\infty}^{+\infty} s^Z \mathcal{P}(Z,t), \tag{2.34}$$

[2]Pseudo-random numbers are actually used in computers. Readers are referred to Ref. [81] about seminumerical algorithms for more detailed account. In the standard C/C++ library, the function `rand` returns independent identically distributed random integers from 0 to `RAND_MAX`, a constant integer. This latter may take different values on different platforms, but normally it should not be smaller than 32767. The library GSL also provides various functions for generating random numbers.

whose time derivative is as follows,

$$\begin{aligned}\partial_t G(s,t) &= W_+ \sum_{Z=-\infty}^{+\infty} s^Z \mathcal{P}(Z-1,t) + W_- \sum_{Z=-\infty}^{+\infty} s^Z \mathcal{P}(Z+1,t) - (W_+ + W_-) \sum_{Z=-\infty}^{+\infty} s^Z \mathcal{P}(Z,t) \\ &= \left(W_+ s + \frac{W_-}{s} - W_+ - W_- \right) G(s,t). \end{aligned} \tag{2.35}$$

For convenience, the initial probability distribution is taken to be $\mathcal{P}(Z,0) = \delta_{Z,0}$, so

$$G(s,0) = \sum_{Z=-\infty}^{\infty} s^Z \delta_{Z,0} = 1, \tag{2.36}$$

and

$$G(s,t) = \exp\left[\left(W_+ s + \frac{W_-}{s} - W_+ - W_- \right) t \right]. \tag{2.37}$$

Using the generating series of modified Bessel functions [82]

$$\exp\left[\frac{u}{2} \left(\theta + \frac{1}{\theta} \right) \right] = \sum_{Z=-\infty}^{+\infty} \theta^Z I_Z(u) \tag{2.38}$$

with

$$u = 2t\sqrt{W_+ W_-}, \tag{2.39}$$

$$\theta = s\sqrt{\frac{W_+}{W_-}}, \tag{2.40}$$

we finally obtain the solution

$$\mathcal{P}(Z,t) = \mathrm{e}^{-(W_+ + W_-)t} \left(\frac{W_+}{W_-} \right)^{\frac{Z}{2}} I_Z\left(2t\sqrt{W_+ W_-} \right), \tag{2.41}$$

where the modified Bessel function $I_Z(u)$ is defined as[3]

$$I_Z(u) = I_{-Z}(u) \equiv \left(\frac{u}{2} \right)^Z \sum_{k=0}^{\infty} \frac{(u^2/4)^k}{k!(k+Z)!}. \tag{2.42}$$

The fluctuation relation is thus derived,

$$\frac{\mathcal{P}(Z,t)}{\mathcal{P}(-Z,t)} = \mathrm{e}^{AZ}, \tag{2.43}$$

holding at every time. We now define cumulant generating function,

$$Q(\lambda) \equiv \lim_{t\to\infty} -\frac{1}{t} \ln G\left(\mathrm{e}^{-\lambda}, t \right) = W_+ \left(1 - \mathrm{e}^{-\lambda} \right) + W_- \left(1 - \mathrm{e}^{+\lambda} \right). \tag{2.44}$$

It can be easily check that $Q(\lambda) = Q(A-\lambda)$ which is implied by the symmetry relation (2.33).

The mean particle current and its diffusivity are calculated as follows,

$$J = \left. \frac{\partial Q}{\partial \lambda} \right|_{\lambda=0} = W_+ - W_-, \tag{2.45}$$

$$D = \left. -\frac{1}{2} \frac{\partial^2 Q}{\partial \lambda^2} \right|_{\lambda=0} = \frac{W_+ + W_-}{2}. \tag{2.46}$$

[3]The Python package Scipy provides the function `special.iv` for modified Bessel function of the first kind of real order.

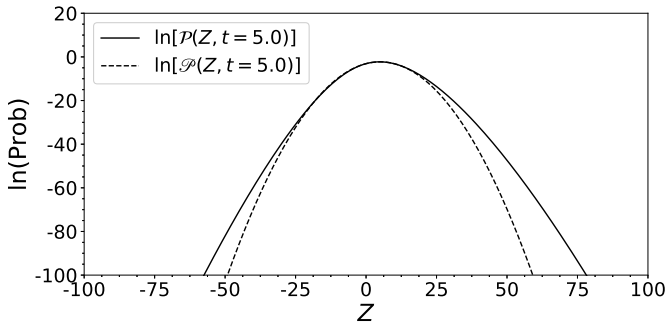

Figure 2.2: Comparison in logarithm scale between the probability distribution $\mathcal{P}(Z,t)$ and $\mathscr{P}(Z,t)$ whose explicit form are given by Eq. (2.41) and Eq. (2.47), respectively. For Eq. (2.41), the parameters take the value $W_+ = 2.0$, $W_- = 1.0$. Correspondingly, $J = W_+ - W_- = 1.0$, $D = (W_+ + W_-)/2 = 1.5$ are the parameter values for Eq. (2.47).

The Gaussian approximation of the probability distribution (2.41) is

$$\mathscr{P}(Z,t) = \frac{1}{\sqrt{4\pi D t}} \exp\left[-\frac{(Z-Jt)^2}{4Dt}\right], \tag{2.47}$$

with the J and D given by Eqs. (2.45)-(2.46). Figure 2.2 shows the comparison between the distribution (2.41) and its Gaussian approximation (2.47) in logarithm scale. In this figure, the deviation between the two distributions is very clear in the tails. This has been explained in Section 2.4 when saying that in the Gaussian approximation (2.47) there is an absence of cumulants higher than second order, which are essential to characterize the tails of probability distribution (2.41). Fortunately, according to Eqs. (2.45)-(2.46), the values of the two constant transition rates W_+ and W_- can be fully determined by the mean current J and its diffusivity D which can be numerically evaluated in counting statistics through their definitions (2.6)-(2.7). Therefore, the affinity can be calculated by

$$A = \ln\frac{W_+}{W_-} = \ln\frac{D+\frac{J}{2}}{D-\frac{J}{2}} = \frac{J}{D} + \frac{1}{12}\left(\frac{J}{D}\right)^3 + \cdots. \tag{2.48}$$

If the process is near equilibrium, J/D is very small and thus the affinity can be estimated from Eq. (2.48) by discarding the nonlinear terms due to their negligible contributions, that is

$$A \approx \frac{J}{D}, \tag{2.49}$$

which can be directly obtained by comparing the probabilities of opposite fluctuations from the Gaussian (2.47) according to the definition of the fluctuation relation (2.1).

It is here pointed out that, in order to increase the speed of numerical simulations, in following chapters, the Markov stochastic process for the time evolution of the considered system is transformed into the corresponding Langevin stochastic process (see Appendix B). In this way, only Gaussian distributions can be obtained from counting statistics in simulation, supposing that infinite number of data is available. So, one should be cautious in testing the fluctuation theorem from the data-constructed distributions according to its definition. This can be easily seen if the Markov stochastic process (2.29) is reduced to Langevin stochastic process for numerical simulation.

Further investigations about the determination of affinities from the first and second cumulants of the probability distribution is presented in the next chapter.

Chapter 3

Two Stochastic Models

We have seen in Section 2.7 that for two-reservoir systems where the process of particle exchanges is characterized by two constant transition rates, the mean particle current together with its diffusivity can be used to recover the two rates and therefore the affinity. The superiority of this method over the Gaussian approximation of the probability distribution has also been demonstrated in this case. This motivates the need to develop a generalized method for systems in contact with arbitrarily many reservoirs.

In this chapter, we study and compare two different Markov stochastic models in order to understand whether the multivariate fluctuation relations are satisfied at finite times or asymptotically at long enough times, and what are the implications of such relations. The first stochastic model is a natural extension of the process discussed in Section 2.7. In this model, the stochastic particle exchanges between reservoirs involve no internal variable and are characterized by constant transition rates. The required conditions about these transition rates are obtained in order to satisfy the multivariate fluctuation relation. Moreover, these conditions are used in evaluating the affinities from the mean currents and their diffusivities. In the second stochastic model, there are three reservoirs and a single internal random variable. The transition rates are linearly dependent on fixed particle concentrations at reservoirs or on the internal random number of particles. By comparison, we find that the long-time behavior of particle exchanges between the reservoirs can be described by the first stochastic model in a coarse-grained way. In addition, the finite-time fluctuation relation for the second stochastic model is established.

3.1 Model With Constant Rates

For a general nonequilibrium steady-state system in contact with n reservoirs (see Figure 2.1), a model at the highest non-trivial level of coarse graining can be used to approximate the full description of particle transitions through the system. In such a coarse-grained model, two equivalent transition rates are hypothesized to exist between any two different reservoirs in the long-time limit, that is

$$R_i \underset{W_{ji}}{\overset{W_{ij}}{\rightleftharpoons}} R_j \qquad i,j = 0,\cdots,n-1; i \neq j. \tag{3.1}$$

3.1.1 Counting Statistics

The counting statistics is performed for particle transfers between the $n-1$ reservoirs ($i = 1,\cdots,n-1$) and the reference reservoir ($i = 0$) during some time interval $[0, t]$, and the numbers of particle transfers are denoted in vectorial notation by $\mathbf{Z} = (Z_1,\cdots,Z_{n-1})$. The time evolution of the

probability distribution $\mathcal{P}(\mathbf{Z},t)$ is ruled by the master equation

$$\frac{\mathrm{d}}{\mathrm{d}t}\mathcal{P}(\mathbf{Z},t)=\Bigg\{\sum_{i=1}^{n-1}\left[W_{i0}\left(\mathrm{e}^{-\partial_{Z_i}}-1\right)+W_{0i}\left(\mathrm{e}^{+\partial_{Z_i}}-1\right)\right] +\sum_{i=1}^{n-1}\sum_{j=i+1}^{n-1}\left[W_{ij}\left(\mathrm{e}^{-\partial_{Z_i}}\mathrm{e}^{+\partial_{Z_j}}-1\right)+W_{ji}\left(\mathrm{e}^{-\partial_{Z_j}}\mathrm{e}^{+\partial_{Z_i}}-1\right)\right]\Bigg\}\mathcal{P}(\mathbf{Z},t). \tag{3.2}$$

The moment generating function of the signed cumulated fluxes is defined as [83]

$$G(s_1,\cdots,s_{n-1},t)\equiv\sum_{Z_1,\cdots,Z_{n-1}=-\infty}^{+\infty}s_1^{Z_1}\cdots s_{n-1}^{Z_{n-1}}\mathcal{P}(Z_1,\cdots,Z_{n-1},t), \tag{3.3}$$

whose evolution equation can be deduced from Eq. (3.2), reading

$$\partial_t G(s_1,\cdots,s_{n-1},t)=\Bigg[\sum_{i=1}^{n-1}\left(W_{i0}s_i+\frac{W_{0i}}{s_i}-W_{i0}-W_{0i}\right) +\sum_{i=1}^{n-1}\sum_{j=i+1}^{n-1}\left(W_{ij}\frac{s_i}{s_j}+W_{ji}\frac{s_j}{s_i}-W_{ij}-W_{ji}\right)\Bigg]G(s_1,\cdots,s_{n-1},t). \tag{3.4}$$

With the initial condition

$$\mathcal{P}(Z_1,\cdots,Z_{n-1},t=0)=\delta_{Z_1,0}\cdots\delta_{Z_{n-1},0}\quad\text{ and thus }\quad G(s_1,\cdots,s_{n-1},t=0)=1, \tag{3.5}$$

the solution is easily to be found, i.e.,

$$G(s_1,\cdots,s_{n-1},t)=\exp\Bigg\{\Bigg[\sum_{i=1}^{n-1}\left(W_{i0}s_i+\frac{W_{0i}}{s_i}-W_{i0}-W_{0i}\right) +\sum_{i=1}^{n-1}\sum_{j=i+1}^{n-1}\left(W_{ij}\frac{s_i}{s_j}+W_{ji}\frac{s_j}{s_i}-W_{ij}-W_{ji}\right)\Bigg]t\Bigg\}. \tag{3.6}$$

Subsequently, we can obtain the cumulant generating function

$$\begin{aligned}Q(\lambda_1,\cdots,\lambda_{n-1})&\equiv\lim_{t\to\infty}-\frac{1}{t}\ln G\left(\mathrm{e}^{-\lambda_1},\cdots,\mathrm{e}^{-\lambda_{n-1}},t\right)\\&=\sum_{i=1}^{n-1}\left[W_{i0}\left(1-\mathrm{e}^{-\lambda_i}\right)+W_{0i}\left(1-\mathrm{e}^{\lambda_i}\right)\right]\\&\quad+\sum_{i=1}^{n-1}\sum_{j=i+1}^{n-1}\left[W_{ij}\left(1-\mathrm{e}^{-\lambda_i+\lambda_j}\right)+W_{ji}\left(1-\mathrm{e}^{\lambda_i-\lambda_j}\right)\right],\end{aligned} \tag{3.7}$$

which, under the condition of our hypothesis, can be regarded as a general form of cumulant generating function for any specific system in the sense that every possible transitions are allowed between the reservoirs. From the general cumulant generating function (3.7), we have the symmetry relation

$$Q(\lambda_1,\cdots,\lambda_{n-1})=Q(A_1-\lambda_1,\cdots,A_{n-1}-\lambda_{n-1}), \tag{3.8}$$

with the definition

$$A_i\equiv\ln\frac{W_{i0}}{W_{0i}} \tag{3.9}$$

if the following conditions are satisfied,

$$A_i - A_j = \ln \frac{W_{ij}}{W_{ji}}. \tag{3.10}$$

The symmetry relation (3.8) is now seen as a result of multivariate fluctuation relation, and thus A_i is identified as the affinity between the reservoirs R_i and R_0 (this latter considered as the reference reservoir), which automatically leads to the required conditions (3.10). As such, the affinity between the reservoirs R_i and R_j can therefore be given by

$$A_{ij} = \ln \frac{W_{ij}}{W_{ji}}. \tag{3.11}$$

So, in order to obtain the affinities between any two reservoirs, we must first determine the value of the transition rates $\{W_{ij}\}$. There is a total of

$$S = n^2 - n \tag{3.12}$$

such transition rates. Our task is to find S conditions from which the values of $\{W_{ij}\}$ can be determined. As shown above, the required conditions (3.10) gives the affinity relations

$$A_{ij} + A_{jk} = A_{ik}, \tag{3.13}$$

which correspondingly lead to

$$W_{ij}W_{jk}W_{ki} - W_{ji}W_{kj}W_{ik} = 0. \tag{3.14}$$

For a n-reservoir system, we can write down

$$S_1 = \frac{1}{2}\left(n^2 - 3n + 2\right) \tag{3.15}$$

independent affinity relations such as (3.13). Additionally, from the consequences of the central limit theorem, we can establish

$$S_2 = \frac{1}{2}\left(n^2 + n - 2\right) \tag{3.16}$$

conditions for the rates $\{W_{ij}\}$. Surprisingly, it can be easily verified that

$$S_1 + S_2 = S. \tag{3.17}$$

So all the necessary independent conditions are found. Detailed accounts about these S conditions are given in following two subsections. Generally, these conditions constitute a set of nonlinear equations which can be numerically solved with the Newton-Raphson method (see Appendix E). After obtaining the numerical value of all transition rates $\{W_{ij}\}$ as roots, the affinities between any two reservoirs can be evaluated by Eq. (3.11).

When evaluating the affinities, we now compare the computational/experimental expenses between this indirect method and the direct method which is based on the fluctuation theorem, supposing that both methods are operationally feasible. Clearly, the indirect method developed here above is much cheaper since it is using a finite number of quantities, although the direct method is instead using a whole probability distribution.

3.1.2 Affinity Relations

We now introduce a convenient procedure to find all the independent affinity relations (3.13). For a n-reservoir system, we can have a polygon with n vertices by analogy, with each vertex corresponding to a reservoir. Each affinity relation (3.13) is represented by three vectors $\vec{ij}$, $\vec{jk}$,

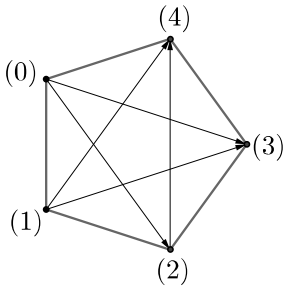

Figure 3.1: Polygon representation of a n-reservoir system which facilitates the process of finding all the independent affinity relations (3.13). Here, a pentagon ($n = 5$) is shown as an illustrative example.

and $i\vec{k}$, forming a triangle $\Delta_{(ijk)}$. Thus, the question has now been transformed into the problem of finding all the independent triangles within the associated polygon. Here, by "independent" we mean that any triangle can not be represented by other triangles through vector analysis. A pentagon corresponding to 5-reservoir system is taken as an illustrative example (see Figure 3.1). We describe the procedure in the following steps:

- Starting from vertex (0), sequentially draw vectors to vertices (2), (3), to the left-hand side of which we can find the triangles $\Delta_{(021)}$ and $\Delta_{(032)}$;
- Starting from vertex (1), sequentially draw vectors to vertices (3), (4), to the left-hand side of which we can find the triangles $\Delta_{(132)}$ and $\Delta_{(143)}$;
- Starting from vertex (2), there only exists one vector to vertex (4) to the left-side of which we can find the triangle $\Delta_{(243)}$;
- Combining the triangles found above and the pentagon itself, we can still find an extra independent triangle $\Delta_{(034)}$.

So, there exists 6 independent triangles which is equal to the number of vectors inside the pentagon plus one. The reason for the extra one is evident when the polygon itself is a triangle. Generalizing to the polygon with n vertices, there is a total of

$$S_1 = \frac{1}{2}\left(n^2 - 3n + 2\right) \tag{3.18}$$

independent triangles, from which we can write down all independent affinity relations.

3.1.3 Consequences of the Central Limit Theorem

The Markov jump process can be approximated by a Langevin stochastic process in the limit of large cumulated fluxes ($|Z_i| \gg 1$ for all indices i). In this approximation, we expand the raising and lowering operators in the master equation (3.2) up to the second order. Therefore, the Fokker-Planck equation

$$\begin{aligned}\partial_t \mathscr{P} = \sum_{i=1}^{n-1}\left[-\sum_{j=0}^{n-1}\left(W_{ij} - W_{ji}\right)\right]\partial_{Z_i}\mathscr{P} + \sum_{i=1}^{n-1}\left[\frac{1}{2}\sum_{j=0,j\neq i}^{n-1}\left(W_{ij} + W_{ji}\right)\right]\partial_{Z_i}^2\mathscr{P} \\ + \sum_{i=1}^{n-1}\sum_{j=1,j\neq i}^{n-1}\left[-\frac{1}{2}\left(W_{ij} + W_{ji}\right)\right]\partial_{Z_i}\partial_{Z_j}\mathscr{P}\end{aligned} \tag{3.19}$$

is derived for the time evolution of the probability density $\mathscr{P}(\mathbf{Z},t)$. The solution of this Fokker-Planck equation (3.19) is nothing but the Gaussian distribution (2.20) whose governing equation can be explicitly expressed as

$$\partial_t \mathscr{P} = -\boldsymbol{\nabla}\cdot(\mathbf{J}\mathscr{P}) + \boldsymbol{\nabla}\cdot(\mathbf{D}\cdot\boldsymbol{\nabla}\mathscr{P}), \tag{3.20}$$

where $\boldsymbol{\nabla}$ is the gradient operator defined as $\left(\partial_{Z_1},\cdots,\partial_{Z_{n-1}}\right)$. Comparing Eq. (3.19) and Eq. (3.20), we get

$$J_i = \sum_{j=0,j\neq i}^{n-1}(W_{ij}-W_{ji}) \qquad i=1,\cdots,n-1, \tag{3.21}$$

$$D_{ii} = \frac{1}{2}\sum_{j=0,j\neq i}^{n-1}(W_{ij}+W_{ji}) \qquad i=1,\cdots,n-1, \tag{3.22}$$

$$D_{ij} = -\frac{1}{2}(W_{ij}+W_{ji}) \qquad i,j=1,\cdots,n-1;\ i\neq j, \tag{3.23}$$

with the values of the mean currents $\{J_i\}$ and their diffusivities $\{D_{ij}\}$ being numerically evaluated in counting statistics by Eqs. (2.6)-(2.7). These relations constitute

$$S_2 = \frac{1}{2}\left(n^2+n-2\right) \tag{3.24}$$

independent conditions. Using Eqs. (2.6)-(2.7), the relations (3.21)-(3.23) can also be directly deduced from the cumulant generating function (3.7) without invoking the central limit theorem.

3.1.4 Fluctuation Relation

If we denote by X_{ij} the particle numbers transferred during the time interval $[0,t]$ from the reservoir R_i and R_j, the number of signed cumulated particle transfers from the reservoir R_i to the remaining part of the system can be expressed as

$$Z_i(\mathbf{X}) = \sum_{j=0,j\neq i}^{n-1}(X_{ij}-X_{ji}) \qquad i=1,\cdots,n-1, \tag{3.25}$$

where $\mathbf{X}=\{X_{ij}\}$. The mean value of the number X_{ij} is given by $\langle X_{ij}\rangle_t = W_{ij}t$ in terms of the corresponding rate W_{ij}. These numbers X_{ij} can be supposed to have Poisson distributions

$$\mathcal{P}(X_{ij},t) = \mathrm{e}^{-\langle X_{ij}\rangle_t}\frac{\langle X_{ij}\rangle_t^{X_{ij}}}{X_{ij}!}. \tag{3.26}$$

Now, the probability distribution ruled by the master equation (3.2) can be written as

$$\mathcal{P}(Z_1,\cdots,Z_{n-1},t) = \sum_{\mathbf{X}}\prod_i \delta_{Z_i,Z_i(\mathbf{X})}\prod_{i\neq j}\mathcal{P}(X_{ij},t). \tag{3.27}$$

In this case, the moment generating function (3.3) is indeed given by the solution (3.6) of Eq. (3.4), as can be verified by direct calculation. Therefore, the stochastic process is here a superposition of several Poisson processes.

The fluctuation theorem can be directly proved starting from the expression (3.27) and using the change of summation variable $X_{ij}=X'_{ji}$. As a consequence, we have that Eq. (3.25) is equivalent to $Z_i = -Z_i(\mathbf{X}') = \sum_{j(\neq i)}\left(X'_{ji}-X'_{ij}\right)$. Therefore, using Eq. (3.26) and (3.10), Eq. (3.27) becomes

$$\mathcal{P}(\mathbf{Z},t) = \sum_{\mathbf{X}'}\prod_i \delta_{-Z_i,Z_i(\mathbf{X}')}\mathrm{e}^{-\sum_{i\neq j}W_{ij}t}\prod_{i\neq j}\frac{(W_{ji}t)^{X'_{ji}}}{X'_{ji}!}\mathrm{e}^{\sum_{i\neq j}(A_i-A_j)X'_{ji}}. \tag{3.28}$$

Now, we have that

$$\sum_{i\neq j}(A_i - A_j)X'_{ji} = \sum_i A_i \sum_{j(\neq i)} \left(X'_{ji} - X'_{ij}\right) = \sum_i A_i Z_i = \mathbf{A}\cdot\mathbf{Z}, \tag{3.29}$$

hence the fluctuation relation

$$\frac{\mathcal{P}(\mathbf{Z},t)}{\mathcal{P}(-\mathbf{Z},t)} = \mathrm{e}^{\mathbf{A}\cdot\mathbf{Z}} \tag{3.30}$$

which holds exactly at every time. However, the coarse-grained model with constant rates is meant to describe the behavior of particle exchanges through the system in the long-time limit, the asymptotic form of multivariate fluctuation relation (2.1) for the probability distribution of currents flowing across the system can be naturally established from Eq. (3.30).

3.1.5 Proof of Consistency for Systems Near Equilibrium

We now prove that the method developed with the above coarse-grained model (3.1) is exactly valid for any system near equilibrium in terms of evaluating affinities. Let's consider a system which is in equilibrium, then the affinities between any two reservoirs are equal to zero, and the currents vanish. We now apply a small perturbation to this system through minor changes in the values of the affinities, then the currents can be expressed as linear responses of affinities, i.e.,

$$\delta J_i = \sum_{j=1}^{n-1} L_{i,j}\delta A_j^{(\mathrm{t})}. \tag{3.31}$$

where $\{L_{i,j}\}$ are the Onsager linear response coefficients and $\{A_j^{(\mathrm{t})}\}$ denotes the theoretical affinities that are actual ones. Here, we have reasonably omitted the nonlinear terms due to their very insignificant contribution. Considering the fluctuation-dissipation relations (2.16), we can further write Eq. (3.31) as

$$\delta J_i = \sum_{j=1}^{n-1} D_{ij}\delta A_j^{(\mathrm{t})}, \tag{3.32}$$

where $\{D_{ij}\}$ are the diffusivities of currents for the system in equilibrium. Let's now turn to the coarse-grained formalism (3.1). The equilibrium condition implies that

$$D_{ii} = \sum_{j=0,j\neq i}^{n-1} W_{ij}, \qquad D_{ij} = -W_{ij} = -W_{ji}. \tag{3.33}$$

so the variation of the numerical affinities $A_{ij}^{(\mathrm{n})} \equiv \ln(W_{ij}/W_{ji})$ around equilibrium is as follows,

$$\delta A_{ij}^{(\mathrm{n})} = \delta\left(\ln\frac{W_{ij}}{W_{ji}}\right) = \frac{\delta W_{ij}}{W_{ij}} - \frac{\delta W_{ji}}{W_{ji}} = \frac{1}{W_{ij}}\left(\delta W_{ij} - \delta W_{ji}\right). \tag{3.34}$$

With Eqs. (3.33)-(3.34), δJ_i can also be expressed as

$$\delta J_i = \sum_{j=0,j\neq i}^{n-1}\left(\delta W_{ij} - \delta W_{ji}\right) = \sum_{j=0,j\neq i}^{n-1} W_{ij}\frac{\left(\delta W_{ij} - \delta W_{ji}\right)}{W_{ij}} = \sum_{j=0,j\neq i}^{n-1} W_{ij}\delta A_{ij}^{(\mathrm{n})}. \tag{3.35}$$

Because of $\delta A_{ij}^{(\mathrm{n})} = \delta A_i^{(\mathrm{n})} - \delta A_j^{(\mathrm{n})}$, δJ_i can be further expressed as

$$\delta J_i = \sum_{j=0,j\neq i}^{n-1} W_{ij}\left(\delta A_i^{(\mathrm{n})} - \delta A_j^{(\mathrm{n})}\right) = \sum_{j=0,j\neq i}^{n-1} W_{ij}\delta A_i^{(\mathrm{n})} - \sum_{j=0,j\neq i}^{n-1} W_{ij}\delta A_j^{(\mathrm{n})}. \tag{3.36}$$

Due to Eq. (3.33), we reach the final desired form of δJ_i, i.e.,

$$\delta J_i = D_{ii}\delta A_i^{(\mathrm{n})} + \sum_{j=1, j\neq i}^{n-1} D_{ij}\delta A_j^{(\mathrm{n})} = \sum_{j=1}^{n-1} D_{ij}\delta A_j^{(\mathrm{n})}. \tag{3.37}$$

Comparing Eq. (3.37) with Eq. (3.32), we immediately conclude that

$$\delta A_i^{(\mathrm{n})} = \delta A_i^{(\mathrm{t})}, \tag{3.38}$$

which means that the numerical affinities $A_i^{(\mathrm{n})}$ evaluated as $\ln(W_{i0}/W_{0i})$ can be identified as the actual ones for systems near equilibrium.

3.1.6 Response Properties

The time-reversal symmetry relations in Section 2.3 can be obtained for the linear and nonlinear response coefficients of the stochastic model with constant rates. The mean currents (3.21) can be expressed in terms of the affinities given by Eqs. (3.9) and (3.10) according to

$$J_i = W_{0i}\left(\mathrm{e}^{A_i} - 1\right) + \sum_{k>i} W_{ki}\left(\mathrm{e}^{A_i - A_k} - 1\right) - \sum_{k<i} W_{ik}\left(\mathrm{e}^{A_k - A_i} - 1\right). \tag{3.39}$$

The diffusivities (3.22) and (3.23) are similarly given by

$$D_{ii} = \frac{1}{2}W_{0i}\left(\mathrm{e}^{A_i} + 1\right) + \frac{1}{2}\sum_{k>i} W_{ki}\left(\mathrm{e}^{A_i - A_k} + 1\right) + \frac{1}{2}\sum_{k<i} W_{ik}\left(\mathrm{e}^{A_k - A_i} + 1\right), \tag{3.40}$$

$$D_{ij} = -\frac{1}{2}W_{ji}\left(\mathrm{e}^{A_i - A_j} + 1\right) \qquad \text{for} \qquad i < j. \tag{3.41}$$

The linear response coefficients (2.11) are thus taking the following values,

$$L_{i,i} = W_{0i} + \sum_{k>i} W_{ki} + \sum_{k<i} W_{ik}, \tag{3.42}$$

$$L_{i,j} = L_{j,i} = -W_{ji} \qquad \text{for} \qquad i < j, \tag{3.43}$$

so that the fluctuation-dissipation relations (2.16) and Onsager reciprocal relations (2.17) are satisfied in the linear regime close to equilibrium. Beyond, the nonlinear response coefficients (2.12) have the following expressions,

$$M_{i,ii} = W_{0i} + \sum_{k>i} W_{ki} - \sum_{k<i} W_{ik}, \tag{3.44}$$

$$M_{i,ij} = M_{j,ii} = -M_{i,jj} = -M_{j,ji} = -W_{ji} \qquad \text{for} \qquad i < j, \tag{3.45}$$

$$M_{i,jk} = 0 \qquad \text{for} \qquad i \neq j \neq k, \tag{3.46}$$

while the first responses (2.19) of the diffusivities are here given by

$$R_{ii,i} = \frac{1}{2}W_{0i} + \frac{1}{2}\sum_{k>i} W_{ki} - \frac{1}{2}\sum_{k<i} W_{ik}, \tag{3.47}$$

$$R_{ii,j} = R_{ij,i} = -R_{ij,j} = -R_{jj,i} = -\frac{1}{2}W_{ji} \qquad \text{for} \qquad i < j, \tag{3.48}$$

$$R_{ij,k} = 0 \qquad \text{for} \qquad i \neq j \neq k, \tag{3.49}$$

so that the symmetry relations (2.18) are also satisfied, since $M_{i,ii} = 2R_{ii,i}$ for $i = j = k$, $M_{i,jj} = 2R_{ij,j}$ for $j = k$, $M_{i,ij} = R_{ii,j} + R_{ij,i}$ for $k = i$, and $0 = 0$ for $i \neq j \neq k$. These results confirm for the model with constant rates that the nonlinear response coefficients of the mean currents can be expressed in terms of the first responses of the diffusivities, as a consequence of the multivariate fluctuation relation (2.1). These results will be used in the next section devoted to a more complicated model.

3.2 Model With Linear Rates

In this section, we consider a Markov stochastic model where the transition rates depend linearly on an internal random variable N, representing the occupancy of the system by particles. This model is used as an example to show how we evaluate affinities. The system is in contact with three particle reservoirs R_0, R_1 and R_2, which are here seen as spatial regions with fixed volume and particle density. Correspondingly, the particle numbers inside the reservoirs are constant in time, and denoted by the same notations R_0, R_1 and R_2 for convenience.

3.2.1 Master Equation

The process of particle transitions in the whole system is schematically depicted by the kinetic network

$$R_1 \underset{k_{-1}}{\overset{k_{+1}}{\rightleftharpoons}} N \underset{k_{+0}}{\overset{k_{-0}}{\rightleftharpoons}} R_0 \qquad N \underset{k_{-2}}{\overset{k_{+2}}{\rightleftharpoons}} R_2 \tag{3.50}$$

with the transition rates given by

$$W_0^{(+)}(N) = k_{+0}R_0, \qquad W_0^{(-)}(N) = k_{-0}N, \tag{3.51}$$

$$W_1^{(+)}(N) = k_{+1}R_1, \qquad W_1^{(-)}(N) = k_{-1}N, \tag{3.52}$$

$$W_2^{(+)}(N) = k_{+2}R_2, \qquad W_2^{(-)}(N) = k_{-2}N. \tag{3.53}$$

The injecting rates $\{W_i^{(+)}\}$ are independent of the internal state N of the system because they are all determined by the particle concentration of the corresponding reservoir. In contrast, the releasing rates $\{W_i^{(-)}\}$ do depend linearly on the system state N. The probability distribution of the internal state N of the system is ruled by the master equation

$$\frac{\mathrm{d}}{\mathrm{d}t}\mathcal{P}(N,t) = \sum_{i=0}^{2}\left[\left(\mathrm{e}^{-\partial_N}-1\right)W_i^{(+)}(N) + \left(\mathrm{e}^{+\partial_N}-1\right)W_i^{(-)}(N)\right]\mathcal{P}(N,t). \tag{3.54}$$

The evolution equation for the mean value $\langle N\rangle$ can be deduced from the master equation (3.54), reading

$$\frac{\mathrm{d}}{\mathrm{d}t}\langle N\rangle = (k_{+0}R_0 + k_{+1}R_1 + k_{+2}R_2) - (k_{-0}+k_{-1}+k_{-2})\langle N\rangle. \tag{3.55}$$

Consequently, the mean value in the steady state is given by

$$\langle N\rangle_{\mathrm{st}} = \frac{k_{+0}R_0 + k_{+1}R_1 + k_{+2}R_2}{k_{-0}+k_{-1}+k_{-2}}. \tag{3.56}$$

Since the rates $\{W_i^{(-)}\}$ are linear functions of the system state variable N, the kinetic equation (3.55) is linear. The stationary solution of the master equation (3.54) is thus given by the following Poisson distribution,

$$\mathcal{P}_{\mathrm{st}}(N) = \mathrm{e}^{-\langle N\rangle_{\mathrm{st}}}\frac{\langle N\rangle_{\mathrm{st}}^N}{N!}. \tag{3.57}$$

3.2.2 Graph Analysis and Affinities

The graph associated with the kinetic network (3.50) is depicted in Figure 3.2. Taking the event of a particle transfer from the reservoir R_1 to the reservoir R_0 as an example, the cyclic path and

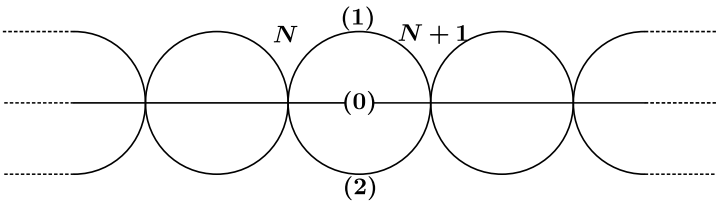

Figure 3.2: Graph associated with the kinetic network (3.50).

its reversed path are

$$\mathcal{C} : (N) \xrightarrow{W_1^{(+)}} (N+1) \xrightarrow{W_0^{(-)}} (N), \tag{3.58}$$

$$\mathcal{C}^{\mathrm{r}} : (N) \xrightarrow{W_0^{(+)}} (N+1) \xrightarrow{W_1^{(-)}} (N). \tag{3.59}$$

Then, according to Schnakenberg's graph analysis, the affinity between the reservoirs R_1 and R_0 is given by

$$A_1 \equiv A_{10} = \ln \frac{W_1^{(+)}(N) W_0^{(-)}(N+1)}{W_0^{(+)}(N) W_1^{(-)}(N+1)} = \ln \frac{k_{+1} R_1 k_{-0}}{k_{+0} R_0 k_{-1}}. \tag{3.60}$$

Similarly, we have

$$A_2 \equiv A_{20} = \ln \frac{k_{+2} R_2 k_{-0}}{k_{+0} R_0 k_{-2}}, \tag{3.61}$$

which is the affinity between the reservoirs R_2 and R_0.

3.2.3 Counting Statistics

For the Markov stochastic process (3.50), let us introduce the probability distribution $\mathcal{P}(N, Z_1, Z_2, t)$ to have N particles at time t and signed cumulated fluxes Z_1 and Z_2, respectively from reservoirs R_1 and R_2 towards the system. This probability distribution evolves in time according to the following extended master equation,

$$\begin{aligned} \frac{\mathrm{d}}{\mathrm{d}t}\mathcal{P}(N, Z_1, Z_2, t) = \Big[& \left(\mathrm{e}^{-\partial_N} - 1\right) k_{+0} R_0 + \left(\mathrm{e}^{+\partial_N} - 1\right) k_{-0} N \\ & + \left(\mathrm{e}^{-\partial_N} \mathrm{e}^{-\partial_{Z_1}} - 1\right) k_{+1} R_1 + \left(\mathrm{e}^{+\partial_N} \mathrm{e}^{+\partial_{Z_1}} - 1\right) k_{-1} N \\ & + \left(\mathrm{e}^{-\partial_N} \mathrm{e}^{-\partial_{Z_2}} - 1\right) k_{+2} R_2 + \left(\mathrm{e}^{+\partial_N} \mathrm{e}^{+\partial_{Z_2}} - 1\right) k_{-2} N \Big] \mathcal{P}(N, Z_1, Z_2, t). \end{aligned} \tag{3.62}$$

Let us define the moment generating function of the signed cumulated fluxes [83], reading

$$G(s, s_1, s_2, t) \equiv \sum_{N=0}^{\infty} \sum_{Z_1, Z_2 = -\infty}^{+\infty} s^N s_1^{Z_1} s_2^{Z_2} \mathcal{P}(N, Z_1, Z_2, t), \tag{3.63}$$

and set the initial condition according to the steady state distribution, i.e.,

$$\mathcal{P}(N, Z_1, Z_2, t = 0) = \mathrm{e}^{-\langle N \rangle_{\mathrm{st}}} \frac{\langle N \rangle_{\mathrm{st}}^N}{N!} \delta_{Z_1, 0} \, \delta_{Z_2, 0}, \tag{3.64}$$

so that

$$G(s, s_1, s_2, t = 0) = \mathrm{e}^{\langle N \rangle_{\mathrm{st}} (s-1)}. \tag{3.65}$$

Then, from the master equation (3.62), we get the evolution equation for the moment generating function

$$\begin{aligned}\partial_t G(s,s_1,s_2,t) =& \left[k_{+0}R_0(s-1)+k_{+1}R_1(ss_1-1)+k_{+2}R_2(ss_2-1)\right]G(s,s_1,s_2,t)\\ &+\left[k_{-0}(1-s)+k_{-1}\left(\frac{1}{s_1}-s\right)+k_{-2}\left(\frac{1}{s_2}-s\right)\right]\partial_s G(s,s_1,s_2,t),\end{aligned} \tag{3.66}$$

which can be written in the following form,

$$\partial_t G = (As-B)G + (C-Ds)\partial_s G \tag{3.67}$$

with

$$A = k_{+0}R_0 + k_{+1}R_1 s_1 + k_{+2}R_2 s_2, \tag{3.68}$$
$$B = k_{+0}R_0 + k_{+1}R_1 + k_{+2}R_2, \tag{3.69}$$
$$C = k_{-0} + \frac{k_{-1}}{s_1} + \frac{k_{-2}}{s_2}, \tag{3.70}$$
$$D = k_{-0} + k_{-1} + k_{-2}. \tag{3.71}$$

Obviously, we note that $B = A(s_1 = s_2 = 1)$ and $D = C(s_1 = s_2 = 1)$. This first-order partial differential equation with given initial condition can be solved using the method of characteristics [83]. Accordingly, Eq. (3.67) is reduced to two ordinary differential equations:

$$\frac{\mathrm{d}G}{\mathrm{d}t} = (As-B)G, \tag{3.72}$$
$$\frac{\mathrm{d}s}{\mathrm{d}t} = -C + Ds, \tag{3.73}$$

from the initial condition G_0 and s_0 that are coupled together by Eq. (3.65), which reads $G_0 = \exp\left[\langle N\rangle_{\mathrm{st}}(s_0-1)\right]$ with $\langle N\rangle_{\mathrm{st}} = B/D$. Integrating these ordinary differential equations and eliminating G_0 and s_0, we obtain the solution

$$\begin{aligned}G(s,s_1,s_2,t) =& \exp\left[t\frac{AC-BD}{D} - \frac{B}{D} - \frac{(A-B)C}{D^2}\left(1-\mathrm{e}^{-Dt}\right)\right]\\ &\times\exp\left\{\left[\frac{B}{D}\mathrm{e}^{-Dt} + \frac{A}{D}\left(1-\mathrm{e}^{-Dt}\right)\right]s\right\}.\end{aligned} \tag{3.74}$$

The cumulant generating function

$$Q(\lambda_1,\lambda_2) = \lim_{t\to\infty} -\frac{1}{t}\ln G\left(1,\mathrm{e}^{-\lambda_1},\mathrm{e}^{-\lambda_2},t\right) = \frac{BD-AC}{D} \tag{3.75}$$

is therefore obtained with

$$A = k_{+0}R_0 + k_{+1}R_1\mathrm{e}^{-\lambda_1} + k_{+2}R_2\mathrm{e}^{-\lambda_2}, \tag{3.76}$$
$$B = k_{+0}R_0 + k_{+1}R_1 + k_{+2}R_2, \tag{3.77}$$
$$C = k_{-0} + k_{-1}\mathrm{e}^{\lambda_1} + k_{-2}\mathrm{e}^{\lambda_2}, \tag{3.78}$$
$$D = k_{-0} + k_{-1} + k_{-2}. \tag{3.79}$$

In Eq. (3.75), we have put $s = 1$ and this, according to the definition (3.63), amounts to summing over the probability distribution of N. If we make the following identification

$$W_{10} \equiv \frac{k_{+1}R_1k_{-0}}{k_{-0}+k_{-1}+k_{-2}}, \qquad W_{01} \equiv \frac{k_{+0}R_0k_{-1}}{k_{-0}+k_{-1}+k_{-2}}, \tag{3.80}$$
$$W_{20} \equiv \frac{k_{+2}R_2k_{-0}}{k_{-0}+k_{-1}+k_{-2}}, \qquad W_{02} \equiv \frac{k_{+0}R_0k_{-2}}{k_{-0}+k_{-1}+k_{-2}}, \tag{3.81}$$
$$W_{12} \equiv \frac{k_{+1}R_1k_{-2}}{k_{-0}+k_{-1}+k_{-2}}, \qquad W_{21} \equiv \frac{k_{+2}R_2k_{-1}}{k_{-0}+k_{-1}+k_{-2}}, \tag{3.82}$$

then the cumulant generating function (3.75) becomes

$$\begin{aligned} Q(\lambda_1,\lambda_2) =& W_{10}\left(1-\mathrm{e}^{-\lambda_1}\right)+W_{20}\left(1-\mathrm{e}^{-\lambda_2}\right)+W_{12}\left(1-\mathrm{e}^{-\lambda_1+\lambda_2}\right) \\ &+W_{01}\left(1-\mathrm{e}^{+\lambda_1}\right)+W_{02}\left(1-\mathrm{e}^{+\lambda_2}\right)+W_{21}\left(1-\mathrm{e}^{+\lambda_1-\lambda_2}\right), \end{aligned} \tag{3.83}$$

which has the same form as Eq. (3.7) with $n=3$. So, the quantities given by Eqs. (3.80)-(3.82) are the corresponding global transition rates between different reservoirs. Consequently, a symmetry relation such as (3.8) is here also satisfied, reading

$$Q(\lambda_1,\lambda_2)=Q(A_1-\lambda_1,A_2-\lambda_2), \tag{3.84}$$

with the affinities

$$A_1\equiv A_{10}=\ln\frac{W_{10}}{W_{01}}=\ln\frac{k_{+1}R_1k_{-0}}{k_{+0}R_0k_{-1}}, \tag{3.85}$$

$$A_2\equiv A_{20}=\ln\frac{W_{20}}{W_{02}}=\ln\frac{k_{+2}R_2k_{-0}}{k_{+0}R_0k_{-2}}, \tag{3.86}$$

which are equivalent with those of Eqs. (3.60)-(3.61) given by Schnakenberg's graph analysis. This, to some extent, supports the hypothesis made at the beginning of Section 3.1.

3.2.4 Finite-Time Fluctuation Relation

We observe that the moment generating function (3.74) with $s=1$ has the same structure as the function (3.6). This observation suggests that the stochastic process is here also a superposition of Poisson processes of type (3.26). Indeed, since $Z_1=X_{10}-X_{01}+X_{12}-X_{21}$ and $Z_2=X_{20}-X_{02}+X_{21}-X_{12}$, we may write

$$G(s=1,s_1,s_2,t)=\sum_{\{X_{ij}\}}s_1^{X_{10}-X_{01}+X_{12}-X_{21}}s_2^{X_{20}-X_{02}+X_{21}-X_{12}}\prod_{i\neq j}\mathrm{e}^{-\nu_{ij}}\frac{\nu_{ij}^{X_{ij}}}{X_{ij}!} \tag{3.87}$$

to obtain

$$\begin{aligned} G(s=1,s_1,s_2,t)=\exp\Bigg[&\nu_{10}\left(s_1-1\right)+\nu_{01}\left(\frac{1}{s_1}-1\right)+\nu_{20}\left(s_2-1\right) \\ &+\nu_{02}\left(\frac{1}{s_2}-1\right)+\nu_{12}\left(\frac{s_1}{s_2}-1\right)+\nu_{21}\left(\frac{s_2}{s_1}-1\right)\Bigg]. \end{aligned} \tag{3.88}$$

Comparing to expression (3.74) with $s=1$ and the coefficients (3.68)-(3.71), we can identify the parameters $\{\nu_{ij}\}$ of the Poisson distributions as

$$\nu_{10}\equiv\langle X_{10}\rangle_t=W_{10}t+\left(W_{11}+W_{12}\right)\frac{f(t)}{D}, \tag{3.89}$$

$$\nu_{01}\equiv\langle X_{01}\rangle_t=W_{01}t+\left(W_{11}+W_{21}\right)\frac{f(t)}{D}, \tag{3.90}$$

$$\nu_{20}\equiv\langle X_{20}\rangle_t=W_{20}t+\left(W_{22}+W_{21}\right)\frac{f(t)}{D}, \tag{3.91}$$

$$\nu_{02}\equiv\langle X_{02}\rangle_t=W_{02}t+\left(W_{22}+W_{12}\right)\frac{f(t)}{D}, \tag{3.92}$$

$$\nu_{12}\equiv\langle X_{12}\rangle_t=W_{12}\left[t-\frac{f(t)}{D}\right], \tag{3.93}$$

$$\nu_{21}\equiv\langle X_{21}\rangle_t=W_{21}\left[t-\frac{f(t)}{D}\right], \tag{3.94}$$

in terms of the rates (3.80)-(3.82), the further quantities

$$W_{ii} \equiv \frac{k_{+i} R_i k_{-i}}{k_{-0} + k_{-1} + k_{-2}} \qquad \text{for} \qquad i = 1, 2, \tag{3.95}$$

and the function

$$f(t) = 1 - \exp\left(-Dt\right). \tag{3.96}$$

We note that the relation

$$\nu_{01}(t)\nu_{12}(t)\nu_{20}(t) = \nu_{02}(t)\nu_{21}(t)\nu_{10}(t) \tag{3.97}$$

is implied by the time-dependent parameters (3.89)-(3.94) of the Poisson distributions. If we introduce the time-dependent affinities as

$$\tilde{A}_{10}(t) \equiv \ln \frac{\nu_{10}(t)}{\nu_{01}(t)}, \tag{3.98}$$

$$\tilde{A}_{20}(t) \equiv \ln \frac{\nu_{20}(t)}{\nu_{02}(t)}, \tag{3.99}$$

$$\tilde{A}_{12}(t) \equiv \ln \frac{\nu_{12}(t)}{\nu_{21}(t)}, \tag{3.100}$$

in terms of the parameters (3.89)-(3.94), we thus have the property that

$$\Delta\tilde{A}(t) \equiv \tilde{A}_{12}(t) - \tilde{A}_{10}(t) + \tilde{A}_{20}(t) = 0. \tag{3.101}$$

The signed cumulated particle transfers between the three reservoirs are defined as

$$\Delta X_{10} \equiv X_{10} - X_{01}, \tag{3.102}$$

$$\Delta X_{20} \equiv X_{20} - X_{02}, \tag{3.103}$$

$$\Delta X_{12} \equiv X_{12} - X_{21}, \tag{3.104}$$

whose joint probability distribution is given by

$$\mathcal{P}(\Delta X_{10}, \Delta X_{20}, \Delta X_{12}, t) = \sum_{\{X_{ij}\}} \delta_{\Delta X_{10}, X_{10} - X_{01}} \delta_{\Delta X_{20}, X_{20} - X_{02}} \delta_{\Delta X_{12}, X_{12} - X_{21}} \prod_{i \neq j} \mathrm{e}^{-\nu_{ij}} \frac{\nu_{ij}^{X_{ij}}}{X_{ij}!}. \tag{3.105}$$

Comparing with the probability distribution for the opposite fluctuations of the signed cumulated particle transfers, we deduce the following finite-time trivariate symmetry relation,

$$\frac{\mathcal{P}(\Delta X_{10}, \Delta X_{20}, \Delta X_{12}, t)}{\mathcal{P}(-\Delta X_{10}, -\Delta X_{20}, -\Delta X_{12}, t)} = \exp\left[\tilde{A}_{10}(t)\Delta X_{10} + \tilde{A}_{20}(t)\Delta X_{20} + \tilde{A}_{12}(t)\Delta X_{12}\right], \tag{3.106}$$

which holds at every time in terms of the time-dependent affinities (3.98)-(3.100). Since the numbers of particle transfers from the reservoirs $i = 1, 2$ to the remaining part of the system are given by $Z_1 = \Delta X_{10} + \Delta X_{12}$ and $Z_2 = \Delta X_{20} - \Delta X_{12}$, the finite-time trivariate fluctuation relation (3.106) can be written equivalently in the following form,

$$\frac{\mathcal{P}(Z_1, Z_2, \Delta X_{12}, t)}{\mathcal{P}(-Z_1, -Z_2, -\Delta X_{12}, t)} = \exp\left[\tilde{A}_{10}(t)Z_1 + \tilde{A}_{20}(t)Z_2 + \Delta\tilde{A}(t)\Delta X_{12}\right], \tag{3.107}$$

in terms of the quantity (3.101) that vanishes. Consequently, the right-hand side of Eq. (3.107) no longer depends on ΔX_{12}. Therefore, multiplying Eq. (3.107) by $\mathcal{P}(-Z_1, -Z_2, \Delta X_{12}, t)$ and summing over ΔX_{12} to form the marginal probability distribution

$$\mathcal{P}(Z_1, Z_2, t) \equiv \sum_{\Delta X_{12} = -\infty}^{+\infty} \mathcal{P}(Z_1, Z_2, \Delta X_{12}, t), \tag{3.108}$$

we obtain the bivariate fluctuation relation

$$\frac{\mathcal{P}(Z_1,Z_2,t)}{\mathcal{P}(-Z_1,-Z_2,t)} = \exp\left[\tilde{A}_{10}(t)Z_1 + \tilde{A}_{20}(t)Z_2\right], \tag{3.109}$$

here also holding at every time with the finite-time affinities defined by Eqs. (3.98)-(3.99). In the long-time limit, these affinities behave as $\tilde{A}_{i0} = A_i + O\left[(Dt)^{-1}\right]$, where A_i are the affinities (3.60)-(3.61) (for $i = 1, 2$). Therefore, the asymptotic fluctuation theorem

$$\frac{\mathcal{P}(Z_1,Z_2,t)}{\mathcal{P}(-Z_1,-Z_2,t)} \simeq_{t\to\infty} \exp\left(A_{10}Z_1 + A_{20}Z_2\right) \tag{3.110}$$

is recovered in the long-time limit, which is consistent with the validity of the symmetry relation (3.84) satisfied by the cumulant generating function. The analysis shows that the asymptotic symmetry (3.110) is slowly approached in time with correction going as t^{-1}, and becoming negligible over time scales $t \gg D^{-1} = (k_{-0} + k_{-1} + k_{-2})^{-1}$.

The fact that the affinities can be expressed in terms of the rates defined by Eqs. (3.80)-(3.82) as for the coarse-grained model with constant rates suggests that the affinities can be determined from the knowledge of the mean currents and their diffusivities. We now numerically test this using the present stochastic model with linear rates.

The Markov stochastic process described by Eq. (3.54) can be exactly simulated using the Gillespie's algorithm presented in Section 2.6. However, it is computationally expensive since the particles transit one by one in the corresponding simulation. To increase the simulation speed, the master equation (3.54) is approximated by corresponding Fokker-Planck equation under the condition that the particle number N is very large. In this way, the stochastic process of Langevin type can be invoked and easily implemented with standard routines. The details of this procedure are presented in Appendix B.

In the simulation, we perform the counting statistics of signed cumulated particle transfers Z_1 and Z_2 respectively from the reservoirs R_1 and R_2 to the system during a large time interval $[0, t]$. The joint probability distribution of Z_1 and Z_2 is well approximated by the Gaussian distribution (2.20), from which we obtain the numerical values of J_1, J_2, D_{11}, D_{22}, and D_{12} according to Eqs. (2.6)-(2.7). Gathering all the independent conditions, we have the nonlinear equations:

$$W_{10} - W_{01} + W_{12} - W_{21} = J_1, \tag{3.111}$$
$$W_{20} - W_{02} + W_{21} - W_{12} = J_2, \tag{3.112}$$
$$W_{10} + W_{01} + W_{12} + W_{21} = 2D_{11}, \tag{3.113}$$
$$W_{20} + W_{02} + W_{21} + W_{12} = 2D_{22}, \tag{3.114}$$
$$W_{12} + W_{21} = -2D_{12}, \tag{3.115}$$
$$W_{01}W_{12}W_{20} = W_{02}W_{21}W_{10}, \tag{3.116}$$

which can be numerically solved using the Newton-Raphson method (see Appendix E). Here, Eq. (3.116) can also be naturally recovered from the long-time limit of the time-dependent relation (3.97). After finding roots of these nonlinear equations, we can readily obtain numerical affinities through

$$A_1 \equiv A_{10} = \ln\frac{W_{10}}{W_{01}}, \tag{3.117}$$
$$A_2 \equiv A_{20} = \ln\frac{W_{20}}{W_{02}}. \tag{3.118}$$

In Table 3.1, we present the comparison for several pairs of numerical affinities (3.117)-(3.118) and theoretical affinities (3.60)-(3.61). The agreement of each pair of affinities confirms the control of the counting statistics by the first and second cumulants for the stochastic model with linear rates.

Table 3.1: Model (3.50) with linear rates: Comparison between numerical affinities $A_1^{(\mathrm{n})}$, $A_2^{(\mathrm{n})}$ given by Eqs. (3.117)-(3.118) and their theoretical predictions $A_1^{(\mathrm{t})}$, $A_2^{(\mathrm{t})}$ given by Eqs. (3.60)-(3.61). We set $k_{\pm 0} = k_{\pm 1} = k_{\pm 2} = 1$ in the transition rates (3.51)-(3.53) for numerical simulation. The numerical affinities are computed from the statistics carried out over time interval $[0,\, t = 100]$ with 2×10^5 data. Here, the parameter values satisfy $t \gg (k_{-0} + k_{-1} + k_{-2})^{-1}$, so that the computed affinities are well representing their asymptotic values. The numerical method for estimating the error can be found in Appendix E.

Case	R_0	R_1	R_2	$A_1^{(\mathrm{t})}$	$A_2^{(\mathrm{t})}$	$A_1^{(\mathrm{n})}$	$A_2^{(\mathrm{n})}$
(1)	1000	3000	2000	1.0986	0.6931	1.0890 ± 0.0076	0.6841 ± 0.0072
(2)	3000	1000	2000	-1.0986	-0.4054	-1.0957 ± 0.0049	-0.4033 ± 0.0029
(3)	2000	10000	1000	1.6094	-0.6931	1.5949 ± 0.0118	-0.7063 ± 0.0106
(4)	1000	10000	1000	2.3025	0.0000	2.2698 ± 0.0234	-0.0294 ± 0.0202
(5)	10000	2000	1000	-1.6094	-2.3025	-1.6076 ± 0.0089	-2.3036 ± 0.0137
(6)	15000	2000	1000	-2.0149	-2.7080	-2.0150 ± 0.0126	-2.7126 ± 0.0193
(7)	3000	20000	1000	1.8971	-1.0986	1.8758 ± 0.0169	-1.1195 ± 0.0184
(8)	1000	1000	15000	0.0000	2.7080	-0.0406 ± 0.0306	2.6512 ± 0.0349
(9)	10000	1000	20000	-2.3025	0.6931	-2.3007 ± 0.0237	0.6891 ± 0.0053

3.2.5 Response Properties

As shown in Section 2.3, the symmetry relation (3.84) implies the fluctuation-dissipation relations (2.16) and the Onsager reciprocal relations (2.17) in the linear regime close to equilibrium, as well as their generalizations such as Eq. (2.18) in the nonlinear regimes farther away from equilibrium.

Since the cumulant generating function (3.83) is here precisely of the same form as Eq. (3.7) with $n = 3$ for the model with constant rates, the response coefficients of the present stochastic model have the same expressions as those obtained in Subsection 3.1.6 for the previous stochastic model. We thus have that the linear response coefficients and the diffusivities satisfy Eqs. (2.16) and (2.17) because

$$L_{1,1} = W_{01} + W_{21} = D_{11}(0,0), \tag{3.119}$$
$$L_{1,2} = L_{2,1} = -W_{21} = D_{12}(0,0) = D_{21}(0,0), \tag{3.120}$$
$$L_{2,2} = W_{02} + W_{21} = D_{22}(0,0). \tag{3.121}$$

Moreover, the nonlinear response coefficients (2.12) are indeed related to the first responses (2.19) of the diffusivities since

$$M_{1,11} = W_{01} + W_{21} = 2R_{11,1}, \qquad M_{2,11} = -W_{21} = 2R_{21,1}, \tag{3.122}$$
$$M_{1,12} = -W_{21} = R_{11,2} + R_{12,1}, \quad M_{2,12} = W_{21} = R_{21,2} + R_{22,1}, \tag{3.123}$$
$$M_{1,21} = -W_{21} = R_{12,1} + R_{11,2}, \quad M_{2,21} = W_{21} = R_{22,1} + R_{21,2}, \tag{3.124}$$
$$M_{1,22} = W_{21} = 2R_{12,2}, \qquad M_{2,22} = W_{02} - W_{21} = 2R_{22,2}, \tag{3.125}$$

as predicted by Eq. (2.18).

Chapter 4

Charge Transport in Conductive Channels

The general coarse-grained model for nonequilibrium systems describing the long-time behavior of the particle exchanges between reservoirs has been given in Section 3.1. The validity of this coarse-grained model is justified if the particle transition rates for the system of interest are linearly dependent on local particle concentrations. Moreover, it has been proved in Subsection 3.1.5 that this coarse-grained model is exactly valid for any system near equilibrium in terms of evaluating affinities. It leaves open whether this coarse-grained model still works when it comes to the far-from-equilibrium system with nonlinear transition rates.

In this chapter, we study transport of charged particles in conductive channels at the mesoscopic level. The relevant stochastic approach has already been developed in Ref. [62], and is presented here again for the purpose of inspiring the studies in subsequent two chapters for charge transport in semiconductor devices. In this approach, the electric field is not only generated by external means, but also self-consistently incorporates the contributions of the local deviations from electroneutrality. In addition, the approach also assumes that the electric field propagates instantaneously, the quasi-static limit of the Maxwell's equations, which greatly simplifies the calculation of the fluctuating electric field from the charge distribution that is constantly changing. The channel is spatially discretized into cells, so that a master equation can be introduced to describe the Markov jump process of charged particles. In the master equation, the transition rates are chosen such that the laws of thermodynamics and microreversibility are guaranteed. In the case of equilibrium, the detailed balance is recovered.

Due to the long-range electrostatic interaction, the transition rates in the master equation are typically nonlinear. Numerical evidences show that the numerically obtained affinity based on the coarse-grained model is generally larger than expected, especially when the system is far from equilibrium. This seems to give an interesting inequality between affinity, mean current, and its diffusivity. However, we find that when the charge density is very low the fluctuating electric field can be approximated as a static background field. In the limiting case, the transition rates become linear and thus the coarse-grained model is proved to be applicable in the regime arbitrarily far from equilibrium. Furthermore, the finite-time fluctuation theorem is established in this case of low-density limit.

4.1 Conductive Channels

The conductive channel we consider here is modeled as a three-dimensional rod of length l with its coordinate x extending from $-l/2$ to $l/2$ and of section area Σ in the transverse y- and z-directions. The position is denoted by $\mathbf{r} = (x, y, z)$. Two kinds of charged particles are supposed to be distributed in this channel: mobile positive-charged particles with density $n(\mathbf{r})$, and anchored

negative-charged ions with uniform density $n_-(\mathbf{r}) = n_-$. The charge density is given by

$$\rho(\mathbf{r}) = e\,[n(\mathbf{r}) - n_-] \tag{4.1}$$

in terms of the elementary electric charge $e = |e|$, and the densities of two kinds of charged particles. The charge density determines the electric potential $\Phi(\mathbf{r})$ by Gauss's law and Poisson equation [84, 85]. In equilibrium, the density of mobile charged particles would be, moreover, related to the electric potential by

$$n_{\mathrm{eq}}(\mathbf{r}) \sim \mathrm{e}^{-\beta e\Phi(\mathbf{r})}. \tag{4.2}$$

Both ends of the conductive channel are in contact with reservoirs with fixed potentials and densities for positive-charged mobile particles:

$$\Phi(x = -l/2) = \Phi_{\mathrm{L}}, \qquad \Phi(x = l/2) = \Phi_{\mathrm{R}}, \tag{4.3}$$

$$n(x = -l/2) = n_{\mathrm{L}}, \qquad n(x = l/2) = n_{\mathrm{R}}. \tag{4.4}$$

If the conductive channel is in equilibrium, then Eq. (4.2) holds and the potential difference is related to the densities at the reservoirs according to the Nernst potential

$$(\Phi_{\mathrm{L}} - \Phi_{\mathrm{R}})_{\mathrm{eq}} = \frac{1}{\beta e} \ln \frac{n_{\mathrm{R}}}{n_{\mathrm{L}}}. \tag{4.5}$$

If the conductive channel is out of equilibrium, the applied voltage with respect to Nernst potential can be defined as

$$V = \Phi_{\mathrm{L}} - \Phi_{\mathrm{R}} + \frac{1}{\beta e} \ln \frac{n_{\mathrm{L}}}{n_{\mathrm{R}}}, \tag{4.6}$$

which induces current flowing in the conductive channel. The equilibrium state is recovered if the applied voltage is vanishing, $V = 0$.

4.1.1 Stochastic Diffusion Equations

Because of thermal fluctuations, the mobile charged particles inside the conductive channel undergo ceaseless erratic movements. Their mobility μ is related to their diffusion coefficient D according to Einstein's relation $\mu = \beta D$. It should be noted that the diffusion coefficient here needs to be distinguished from the diffusivity appearing elsewhere. Since particle transport is fluctuating, the density obeys a stochastic partial differential equation. Due to the conservation of the number of mobile charged particles, the continuity equation for their density is satisfied, reading

$$\partial_t n + \boldsymbol{\nabla} \cdot \mathbf{j} = 0, \tag{4.7}$$

with the current density

$$\mathbf{j} = \mu n e \boldsymbol{\mathcal{E}} - D\boldsymbol{\nabla} n + \delta\mathbf{j}. \tag{4.8}$$

Therein, the electric field is expressed as

$$\boldsymbol{\mathcal{E}} = -\boldsymbol{\nabla}\Phi \tag{4.9}$$

in terms of the electric potential satisfying the Poisson equation

$$\nabla^2\Phi = -\frac{\rho}{\epsilon}, \tag{4.10}$$

where ϵ is the permittivity and the electric charge density is given by Eq. (4.1).

The contribution of the fluctuations, $\delta\mathbf{j}$, to the current density (4.8) is given by Gaussian white noise fields characterized by

$$\langle \delta\mathbf{j}(\mathbf{r},t)\rangle = 0, \tag{4.11}$$

$$\langle \delta\mathbf{j}(\mathbf{r},t)\otimes\delta\mathbf{j}(\mathbf{r}',t')\rangle = \Gamma(\mathbf{r},t)\delta^3(\mathbf{r}-\mathbf{r}')\delta(t-t')\mathbf{I}, \tag{4.12}$$

where $\mathbf{I}$ is the 3×3 identity matrix and

$$\Gamma(\mathbf{r},t) \equiv 2Dn(\mathbf{r},t) \tag{4.13}$$

is the spectral density of the noise associated with diffusion. We note that the current density can be equivalently written as

$$\mathbf{j} = -D\mathrm{e}^{-\beta e\Phi}\boldsymbol{\nabla}\left(\mathrm{e}^{\beta e\Phi}n\right) + \delta\mathbf{j}. \tag{4.14}$$

4.1.2 Mean-Field Equations Under Stationary Conditions

By averaging the continuity equation (4.7) and the expression (4.8) over the noise using Eq. (4.11), we can obtain the mean-field equations for the stationary mean profiles of density and the current density of charged particles in the x direction. Together with Gauss's law and the Poisson equation for the electric field and potential, these mean-field equations are given by the following coupled ordinary differential equations (ODEs):

$$\frac{\mathrm{d}n(x)}{\mathrm{d}x} = -\frac{j(x)}{D} + \beta e n(x)\mathcal{E}(x), \tag{4.15}$$

$$\frac{\mathrm{d}j(x)}{\mathrm{d}x} = 0, \tag{4.16}$$

$$\frac{\mathrm{d}\mathcal{E}(x)}{\mathrm{d}x} = \frac{e}{\epsilon}\left[n(x)-n_-\right], \tag{4.17}$$

$$\frac{\mathrm{d}\Phi(x)}{\mathrm{d}x} = -\mathcal{E}(x), \tag{4.18}$$

with the boundary conditions given by Eqs. (4.3)-(4.4). The above ODE system constitutes a typical two-point boundary value problem that is not analytically solvable because of its nonlinearity, but it can be solved numerically[1].

4.2 Numerical Simulation Method

At the mesoscopic level, the evolution of distributions of mobile charged particles in the conductive channel can be described as a Markov jump process, which is formulated in terms of a master equation. The fluctuations down to the mesoscopic scale can be fully characterized by such a process. For this purpose, the conductive channel is spatially discretized into cells, each containing some numbers of mobile charge carriers. These numbers are supposed to change in time because of random transitions. The stochastic approach introduced here incorporates the self-consistent electric field which is generated by the fluctuating distribution of charged particles.

4.2.1 Discretizing the Conductive Channel in Space

The channel is discretized into cells, each with the same volume Ω and same length Δx. Thus, the cross section is given by $\Sigma = \Omega/\Delta x$, and there is total of $L = l/\Delta x$ cells indexed from 1 to L. The number of negative-charged ions in each cell is $N_{-i} = n_-\Omega$. Similarly, there are $N_i = n(x_i)\Omega$ positive-charged particles in the ith cell, with $x_i = (i-0.5)\Delta x - l/2$ $(i = 1, 2, \cdots, L)$. The reservoirs

[1] The Python package Scipy provides the function `integrate.solve_bvp` for solving a first-order system of ODEs subject to two-point boundary conditions.

are modeled as cells respectively indexed as 0 for the left reservoir and $L+1$ for the right reservoir. The numbers of mobile particles in both reservoirs are maintained constant in time, and given by $N_0 \equiv \bar{N}_{\mathrm{L}} = n_{\mathrm{L}}\Omega$ and $N_{L+1} \equiv \bar{N}_{\mathrm{R}} = n_{\mathrm{R}}\Omega$. The particle numbers in the cells change every time a particle jumps between two neighboring cells, or between a reservoir and the neighboring cell. The discretized version of Poisson equation is given by

$$\frac{\Phi_{i+1} - 2\Phi_i + \Phi_{i-1}}{\Delta x^2} = -\frac{e}{\epsilon\Omega}(N_i - N_-) \tag{4.19}$$

with the boundary conditions $\Phi_0 = \Phi_{\mathrm{L}}$ and $\Phi_{L+1} = \Phi_{\mathrm{R}}$. This linear system should be solved each time a particle transition occurs.

4.2.2 Master Equation

The system state is specified by the numbers $\mathbf{N} = \{N_i\}_{i=1}^{L}$ of charge carriers in the cells and they evolve in time according to the network

$$\bar{N}_{\mathrm{L}} \underset{W_0^{(-)}}{\overset{W_0^{(+)}}{\rightleftharpoons}} N_1 \underset{W_1^{(-)}}{\overset{W_1^{(+)}}{\rightleftharpoons}} N_2 \underset{W_2^{(-)}}{\overset{W_2^{(+)}}{\rightleftharpoons}} \cdots \underset{W_{L-2}^{(-)}}{\overset{W_{L-2}^{(+)}}{\rightleftharpoons}} N_{L-1} \underset{W_{L-1}^{(-)}}{\overset{W_{L-1}^{(+)}}{\rightleftharpoons}} N_L \underset{W_L^{(-)}}{\overset{W_L^{(+)}}{\rightleftharpoons}} \bar{N}_{\mathrm{R}}.$$

The probability $\mathcal{P}(\mathbf{N}, t)$ that the cells contain the particle numbers $\mathbf{N}$ for time t obeys the master equation

$$\frac{\mathrm{d}\mathcal{P}}{\mathrm{d}t} = \sum_{i=0}^{L}\left[\left(\mathrm{e}^{+\partial_{N_i}}\mathrm{e}^{-\partial_{N_{i+1}}} - 1\right)W_i^{(+)} + \left(\mathrm{e}^{-\partial_{N_i}}\mathrm{e}^{+\partial_{N_{i+1}}} - 1\right)W_i^{(-)}\right]\mathcal{P}, \tag{4.20}$$

with the transition rates[2]

$$W_i^{(+)} = \frac{D}{\Delta x^2}\psi(\Delta U_{i,i+1})N_i, \tag{4.21}$$

$$W_i^{(-)} = \frac{D}{\Delta x^2}\psi(\Delta U_{i+1,i})N_{i+1}. \tag{4.22}$$

$\Delta U_{i,i+1}$ is the intrinsic energy change in the whole conductive channel associated with the one particle jump from the ith to $(i+1)$th cell, and is given by

$$\Delta U_{i,i+1} = e(\Phi_{i+1} - \Phi_i) + \frac{e^2 L\Delta x^2}{2(L+1)\epsilon\Omega}. \tag{4.23}$$

For details about U and ΔU, see the Appendix A. The function $\psi(\Delta U)$ is defined as

$$\psi(\Delta U) = \frac{\beta\Delta U}{\exp(\beta\Delta U) - 1}, \tag{4.24}$$

which guarantees the detailed balance condition in equilibrium,

$$\psi(\Delta U) = \psi(-\Delta U)\exp(-\beta\Delta U). \tag{4.25}$$

At the ends of the chain, we have that $\exp(\pm\partial_X) = 1$ for $X = N_0$ and N_{L+1} in the master equation (4.20). Indeed, the quantities $N_0 = \bar{N}_{\mathrm{L}}$ and $N_{L+1} = \bar{N}_{\mathrm{R}}$ are associated with the reservoirs

[2] In the expression for the local transition rates (4.21)-(4.22), $D/\Delta x^2$ is due to the pure diffusion, and $\psi(\Delta U)$ is the contribution of drift driven by external electric force. In the case of pure diffusion, the mean current is expressed as

$$J = -k(N_{i+1} - N_i) = -k\Omega\Delta x\frac{\partial n}{\partial x} = j\Sigma = -D\frac{\Omega}{\Delta x}\frac{\partial n}{\partial x},$$

from which $k = D/\Delta x^2$ is obtained.

and they thus take constant values. The boundary conditions are imposed at the left and right reservoirs by setting $N_0 = \bar{N}_{\rm L}$, $\Phi_0 = \Phi_{\rm L}$, $N_{L+1} = \bar{N}_{\rm R}$, and $\Phi_{L+1} = \Phi_{\rm R}$ in the transition rates.

For the numerical simulation of transport of charge carriers in the conductive channel, the Markov stochastic process ruled by Eq. (4.20) is transformed into the corresponding Langevin stochastic process (see Appendix B for the detailed procedure).

In equilibrium or nonequilibrium stationary states, the statistical average numbers of charge carriers in the cells can be evaluated in numerical simulations by the time average,

$$\langle N_i \rangle = \lim_{T\to\infty} \frac{1}{T} \int_0^T N_i(t) {\rm d}t, \tag{4.26}$$

which is equivalent by ergodicity to the ensemble average $\langle N_i \rangle = \sum_{\mathbf{N}} N_i \mathcal{P}_{\rm st}(\mathbf{N})$ over the stationary probability distribution $\mathcal{P}_{\rm st}$. In the continuum limit, the volume of the cells is supposed to vanish together with the particle numbers, so that the densities obeying Eqs. (4.7)-(4.13) are recovered through $n(x_i, t) = N_i(t)/\Omega$. We can also recover the stochastic partial differential equation (4.7) with the current densities (4.8) from the Langevin stochastic equations (B.7)-(B.8) (see Appendix C). This method is similar to the one used in Refs. [62, 86].

4.3 Graph Analysis and Affinity

The affinity for this transport system can be identified from Schnakenberg's graph analysis [78]. For example, we take a cyclic path such that a particle is transferred from the left to the right reservoir:

$$\mathcal{C} : \mathbf{N} \xrightarrow{W_0^{(+)}} \mathbf{N} + \mathbf{n}_1 \xrightarrow{W_1^{(+)}} \mathbf{N} + \mathbf{n}_2 \longrightarrow \cdots \longrightarrow \mathbf{N} + \mathbf{n}_{L-1} \xrightarrow{W_{L-1}^{(+)}} \mathbf{N} + \mathbf{n}_L \xrightarrow{W_L^{(+)}} \mathbf{N}, \tag{4.27}$$

written in terms of the system state $\mathbf{N}$ and the notation $(\mathbf{n}_i)_j = +\delta_{i,j}$. The corresponding nonequilibrium constraint is determined by the applied voltage that we should recover by calculating the affinity. Indeed, the transition rates $W_i^{(+)}$ defined by Eq. (4.21) involve the energy differences

$$\Delta U_{i,i+1} = U(\mathbf{N} + \mathbf{n}_{i+1}) - U(\mathbf{N} + \mathbf{n}_i) = e(\Phi_{i+1} - \Phi_i) + \frac{e^2(L-2i)\Delta x^2}{2(L+1)\epsilon\Omega} = -\Delta U_{i+1,i} \tag{4.28}$$

for $i = 0, \cdots, L$ with $\Phi_0 = \Phi_{\rm L}$ and $\Phi_{L+1} = \Phi_{\rm R}$. It should be noted that the discretized distribution of electric potential $\{\Phi_i\}$ here corresponds to the system state $\mathbf{N}$. Equation (4.28) can be obtained from calculations similar as those in Appendix A. Substituting Eqs. (4.21) and (4.22) in the definition (2.25) and using the detailed balance relation (4.25), we find that

$$A(\mathcal{C}) = \ln \left[\frac{n_{\rm L}}{n_{\rm R}} {\rm e}^{\beta e(\Phi_{\rm L} - \Phi_{\rm R})} \right] = \beta e V \tag{4.29}$$

according to Eq. (4.6), which shows the consistency of the scheme for this cyclic path. Similar results can be obtained for other cyclic paths.

4.4 The Current and Counting Statistics

Here, we consider the fluctuating electric current flowing across the middle of the conductive channel at the location $x = 0$. The instantaneous electric current can be written as

$$\mathcal{I}(t) = \sum_{n=-\infty}^{+\infty} q_n \delta(t - t_n) \tag{4.30}$$

with $q_n = \pm e$ depending on whether the charged particle moves towards $x > 0$ or $x < 0$. The corresponding random number of signed cumulated particle transfers over the time interval $[0, t]$ is defined as

$$Z(t) = \frac{1}{e}\int_0^t \mathcal{I}(t')\mathrm{d}t'. \tag{4.31}$$

Through numerous repeated measurements in simulation, we get the counting statistics of $Z(t)$, and thus $\mathcal{P}(Z, t)$ can be numerically constructed. Moreover, according to Eqs. (2.6)-(2.7), the mean current J and its diffusivity D can be evaluated.

4.5 Fluctuation Theorem for the Current

In order to evaluate the affinity from counting statistics, we can use the coarse-grained model

$$\textit{Left Reservoir} \underset{W_-}{\overset{W_+}{\rightleftharpoons}} \textit{Right Reservoir} \tag{4.32}$$

to describe the long-time behavior of transport in terms of two transition rates W_+ and W_- characterizing the stochastic exchange of particles between the two reservoirs. We have seen in Section 2.7 that the stochastic process described by this model can be analytically solved, with the affinity be given by

$$A = \ln\frac{W_+}{W_-} = \ln\frac{2D + J}{2D - J}, \tag{4.33}$$

which serves here as the numerical estimate of the value of the affinity (4.29).

We now simulate the process of particle transport according to the method in Section 4.2. In simulation, the counting statistics is performed and the values of mean current J and its diffusivity D are thus obtained. The numerical results from simulation are presented in Figure 4.1, where the of mean currents J as a function of affinity A is shown in panel (a), and comparison between the numerically obtained affinity (4.33) according to the coarse-grained model (4.32) and the theoretical affinities (4.29) obtained from graph analysis is drawn in panel (b). In both panels of Figure 4.1, the results for different densities are presented also for comparison. From observation, we have several findings which are summarized as follows:

- The mean current J is a linear function of the theoretical affinity (4.29) with the slope being proportional to the particle density.
- The numerical affinity (4.33) is indeed a good approximation of the theoretical affinity (4.29) for this transport system close to equilibrium.
- The numerical affinity (4.33) is generally larger than the theoretical affinity (4.29), especially when this transport system is far from equilibrium.
- The lower the densities inside the conductive channel, the wider the range of numerical affinity (4.33) being able to approximate the theoretical affinity (4.29).

In the following, we try explain what we observe in Figure 4.1. The transport system behaves like a resistor where Ohm's law can be established, and it is very natural that the current J is proportional to the particle density under the same affinity (4.29). We consider that it is nonlinearity of the transition rates (4.21)-(4.22) arising from long-range electrostatic interaction between the charged particles that make the coarse-grained model limited in application. The repulsive force between the electric charges induce correlations in motion between them which directly leads to a smaller diffusivity D than expected. So, the numerical affinity (4.33) is larger than the theoretical affinity (4.29), especially when the transport system is far from equilibrium. In

the low-density limit where the cell volume Ω can be seen as very large, Eq. (4.23) is approximated as

$$\Delta U_{i,i+1} \approx e(\Phi_{i+1} - \Phi_i). \tag{4.34}$$

Besides, Eq. (4.23) can also be expressed as

$$\Delta U_{i,i+1} = \frac{e}{2}\left(\Phi_{i+1} - \Phi_i + \Phi'_{i+1} - \Phi'_i\right), \tag{4.35}$$

in terms of the electric potential difference across the ith and $(i+1)$th cells before and after a transition event. So, we find that in the low-density limit we have

$$\Phi_{i+1} - \Phi_i \approx \Phi'_{i+1} - \Phi'_i, \tag{4.36}$$

which means that the electric field tends to form a static background. The electric field in such case can be approximated by the mean electric field determined by the two potentials of particle reservoirs from the Poisson equation with no charge source. The electrostatic interaction between the charges are thus diluted by the large volume, and the transition rates (4.21)-(4.22) tend to have linear dependence on the local particle concentration.

According to the findings from Figure 4.1, it seems that an interesting inequality

$$D \leq J\left(\frac{1}{\mathrm{e}^A - 1} + \frac{1}{2}\right) \tag{4.37}$$

can be established between the (theoretical/exact) affinity, the mean current, and its diffusivity. This inequality gives the upper bound for the diffusivity when the values of the mean current and affinity are known. This inequality may be supposed to hold in general. The equality sign holds if and only if there is no interaction between the constituent particles of the system under consideration, or asymptotically holds when the system tends to equilibrium.

From the observation of Figure 4.1, we can write down the following relations for the low-density limit,

$$J = W_+ - W_- = \kappa A, \tag{4.38}$$

$$\ln \frac{W_+}{W_-} = A, \tag{4.39}$$

where κ is a constant. From the above relations, we get the rate function

$$W(A) = \frac{\kappa A}{1 - \mathrm{e}^{-A}}, \tag{4.40}$$

with W_+ associated with the rate W for positive A, and W_- the rate W for negative A. In Figure 4.2, we plot the rates determined as a function of the affinity A for the low-density case in Figure 4.1, and fit them with Eq. (4.40) to get the value of constant κ. According to $J = W_+ - W_- = D(0)A$, κ is physically interpreted as the diffusivity of particle current when the transport system is in equilibrium.

4.6 Finite-Time Fluctuation Relation in the Low-Density Limit

In the low-density limit, the fluctuating electric field is approximated as a static background field. In this case, the energy difference associated with particle transitions between discretized cells are given by

$$\Delta U_{i,i+1} = e(\Phi_{i+1} - \Phi_i) = -\frac{e(\Phi_{\mathrm{L}} - \Phi_{\mathrm{R}})}{L+1}, \tag{4.41}$$

$$\Delta U_{i+1,i} = e(\Phi_i - \Phi_{i+1}) = +\frac{e(\Phi_{\mathrm{L}} - \Phi_{\mathrm{R}})}{L+1}, \tag{4.42}$$

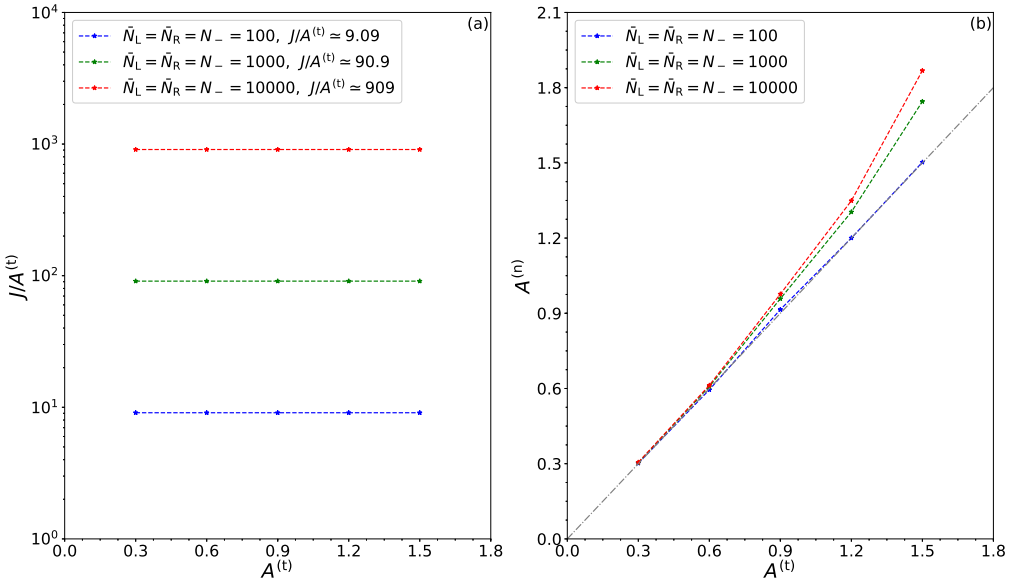

Figure 4.1: Panel (a): The behaviors of mean current versus the theoretical affinity. Panel (b): The comparison between numerical affinities (4.33) and theoretical affinities (4.29). It is set that $\bar{N}_L = \bar{N}_R = N_-$, and takes different values N in three cases, as shown in legends. The asterisks are numerical points with dashed lines joining them. The dot dash line indicates the equality between both kinds of affinities. The parameter values used in simulation are $\beta = e = 1.0$, $D = \epsilon = 0.01$, $\Omega = 10000$, $\Delta x = 0.1$, $L = 10$. The affinities are computed over time interval [0, 5000] with 20000 data.

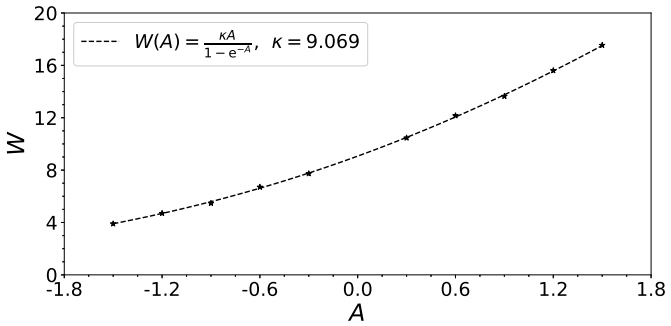

Figure 4.2: The transition rate W computed as a function of affinity A. The asterisks are numerical points that are fit with the dashed line. The analytic expression and corresponding constant are shown in the legend. The parameter values used in simulation are $\beta = e = 1.0$, $D = \epsilon = 0.01$, $\Omega = 10000$, $\Delta x = 0.1$, $L = 10$, $\bar{N}_L = \bar{N}_R = N_- = 100$, which are the same as the case of lowest density in Figure 4.1. The affinities are computed over time interval [0, 5000] with 20000 data.

which can be uniformly expressed as

$$\Delta U^{(\pm)} = \mp \frac{e(\Phi_{\rm L} - \Phi_{\rm R})}{L+1}. \tag{4.43}$$

Correspondingly, $\psi(\Delta U)$ is denoted as

$$\psi^{(\pm)} = \psi(\Delta U^{(\pm)}) = \frac{\beta \Delta U^{(\pm)}}{\exp\left(\beta \Delta U^{(\pm)}\right) - 1}. \tag{4.44}$$

The transition rates are thus expressed as

$$W_i^{(+)} = \frac{D}{\Delta x^2} \psi^{(+)} N_i = k_+ N_i, \tag{4.45}$$

$$W_i^{(-)} = \frac{D}{\Delta x^2} \psi^{(-)} N_{i+1} = k_- N_{i+1}, \tag{4.46}$$

with the rate constants k_+ and k_- defined as obvious. The rates corresponding to the transitions from the reservoirs to the system are

$$W_0^{(+)} = k_+ \bar{N}_{\rm L}, \qquad W_L^{(-)} = k_- \bar{N}_{\rm R}. \tag{4.47}$$

Clearly, all these transition rates are determined locally, and as such the transport system in the low-density limit is linear.

We consider the time evolution of the probability

$$\mathcal{P}(Z, N_1, \cdots, N_L, t) \tag{4.48}$$

that the cells contain given particle numbers and that the signed cumulated number Z of particles is transferred from the Ith to the $(I+1)$th cells during time interval $[0, t]$. This probability is ruled by the following master equation,

$$\begin{aligned}
\frac{{\rm d}\mathcal{P}}{{\rm d}t} =& k_+ \bar{N}_{\rm L} \left({\rm e}^{-\partial_{N_1}} - 1\right) \mathcal{P} + k_- \left({\rm e}^{+\partial_{N_1}} - 1\right) N_1 \mathcal{P} + k_+ \left({\rm e}^{+\partial_{N_1}} {\rm e}^{-\partial_{N_2}} - 1\right) N_1 \mathcal{P} \\
&+ \sum_{i=2}^{I-1} \left[k_- \left({\rm e}^{+\partial_{N_i}} {\rm e}^{-\partial_{N_{i-1}}} - 1\right) N_i \mathcal{P} + k_+ \left({\rm e}^{+\partial_{N_i}} {\rm e}^{-\partial_{N_{i+1}}} - 1\right) N_i \mathcal{P} \right] \\
&+ k_- \left({\rm e}^{+\partial_{N_I}} {\rm e}^{-\partial_{N_{I-1}}} - 1\right) N_I \mathcal{P} + k_+ \left({\rm e}^{+\partial_{N_I}} {\rm e}^{-\partial_{N_{I+1}}} {\rm e}^{-\partial_Z} - 1\right) N_I \mathcal{P} \\
&+ k_- \left({\rm e}^{+\partial_{N_{I+1}}} {\rm e}^{-\partial_{N_I}} {\rm e}^{+\partial_Z} - 1\right) N_{I+1} \mathcal{P} + k_+ \left({\rm e}^{+\partial_{N_{I+1}}} {\rm e}^{-\partial_{N_{I+2}}} - 1\right) N_{I+1} \mathcal{P} \\
&+ \sum_{i=I+2}^{L-1} \left[k_- \left({\rm e}^{+\partial_{N_i}} {\rm e}^{-\partial_{N_{i-1}}} - 1\right) N_i \mathcal{P} + k_+ \left({\rm e}^{+\partial_{N_i}} {\rm e}^{-\partial_{N_{i+1}}} - 1\right) N_i \mathcal{P} \right] \\
&+ k_- \bar{N}_{\rm R} \left({\rm e}^{-\partial_{N_L}} - 1\right) \mathcal{P} + k_- \left({\rm e}^{+\partial_{N_L}} {\rm e}^{-\partial_{N_{L-1}}} - 1\right) N_L \mathcal{P} + k_+ \left({\rm e}^{+\partial_{N_L}} - 1\right) N_L \mathcal{P}.
\end{aligned} \tag{4.49}$$

Using the method of Ref. [87], this master equation is solved by introducing the moment generating function

$$G(\eta, s_1, \cdots, s_L, t) = \sum_{Z, N_1, \cdots, N_L} \eta^Z \prod_i s_i^{N_i} \mathcal{P}(Z, N_1, \cdots, N_L, t). \tag{4.50}$$

where

$$\eta = {\rm e}^{-\lambda}, \tag{4.51}$$

and λ is the counting parameter for the particle transfers Z. This moment generating function is ruled by the following first-order partial differential equation,

$$\begin{aligned}
&\partial_t G + \left[k_-(s_1 - 1) + k_+(s_1 - s_2)\right]\partial_{s_1} G \\
&\quad + \sum_{i=2}^{I-1}\left[k_-(s_i - s_{i-1}) + k_+(s_i - s_{i+1})\right]\partial_{s_i} G \\
&\quad + \left[k_-(s_I - s_{I-1}) + k_+(s_I - \eta s_{I+1})\right]\partial_{s_I} G \\
&\quad + \left[k_-(s_{I+1} - \eta^{-1} s_I) + k_+(s_{I+1} - s_{I+2})\right]\partial_{s_{I+1}} G \\
&\quad + \sum_{i=I+1}^{L-1}\left[k_-(s_i - s_{i-1}) + k_+(s_i - s_{i+1})\right]\partial_{s_i} G \\
&\quad + \left[k_-(s_L - s_{L-1}) + k_+(s_L - 1)\right]\partial_{s_L} G \\
&\quad = \left[k_+\bar{N}_{\mathrm{L}}(s_1 - 1) + k_-\bar{N}_{\mathrm{R}}(s_L - 1)\right] G,
\end{aligned} \tag{4.52}$$

which, in vectoral notations, can be written in the following form,

$$\partial_t G + (\mathbf{L}\cdot\mathbf{s} + \mathbf{f})\cdot\partial_{\mathbf{s}} G = (\mathbf{g}\cdot\mathbf{s} + h)G \tag{4.53}$$

where

$$\mathbf{L} \equiv \begin{pmatrix}
k_- + k_+ & -k_+ & & & & & & & \\
-k_- & k_- + k_+ & -k_+ & & & & & & \\
& \ddots & \ddots & \ddots & & & & & \\
& & -k_- & k_- + k_+ & -\eta k_+ & & & & \\
& & & -\eta^{-1}k_- & k_- + k_+ & -k_+ & & & \\
& & & & \ddots & \ddots & \ddots & & \\
& & & & & -k_- & k_- + k_+ & -k_+ & \\
& & & & & & -k_- & k_- + k_+
\end{pmatrix}, \tag{4.54}$$

$$\mathbf{s} \equiv \begin{pmatrix} s_1 \\ s_2 \\ \vdots \\ s_{L-1} \\ s_L \end{pmatrix}, \qquad \mathbf{f} \equiv -\begin{pmatrix} k_- \\ 0 \\ \vdots \\ 0 \\ k_+ \end{pmatrix}, \qquad \mathbf{g} \equiv \begin{pmatrix} k_+\bar{N}_{\mathrm{L}} \\ 0 \\ \vdots \\ 0 \\ k_-\bar{N}_{\mathrm{R}} \end{pmatrix}, \tag{4.55}$$

and

$$h \equiv -k_+\bar{N}_{\mathrm{L}} - k_-\bar{N}_{\mathrm{R}}. \tag{4.56}$$

The parameter η in matrix $\mathbf{L}$ appears in the Ith and the $(I+1)$th rows. From the matrix $\mathbf{L}$, we can define $\mathbf{L}_0$ by setting $\eta = 1$ and thus $\lambda = 0$. So, we have the relations

$$\mathbf{f} = -\mathbf{L}_0\cdot\mathbf{1}, \tag{4.57}$$

$$h = -\mathbf{g}\cdot\mathbf{1}, \tag{4.58}$$

where $\mathbf{1}$ denotes the vector with all entries equal to one. Besides, the stationary values of particle numbers are given by

$$\mathbf{\Gamma}_0 = \mathbf{L}_0^{-1\mathrm{T}}\cdot\mathbf{g}. \tag{4.59}$$

The first-order partial differential equation (4.53) can be solved by the method of characteristics. The equations for the characteristics are given by

$$\frac{\mathrm{d}\mathbf{s}}{\mathrm{d}t} = \mathbf{L}\cdot\mathbf{s} + \mathbf{f}, \tag{4.60}$$

$$\frac{\mathrm{d}G}{\mathrm{d}t} = (\mathbf{g}\cdot\mathbf{s} + h)G. \tag{4.61}$$

The solution of Eq. (4.60) gives the characteristics

$$\mathbf{s} = \mathrm{e}^{\mathbf{L}t}\cdot\left[\mathbf{s}_0 + \mathbf{L}^{-1}\cdot\left(\mathbf{I} - \mathrm{e}^{-\mathbf{L}t}\right)\cdot\mathbf{f}\right]. \tag{4.62}$$

Replacing in Eq. (4.61), we obtain after integration that

$$G = G_0 \exp\left[\mathbf{g}\cdot\mathbf{L}^{-1}\cdot\left(\mathbf{I} - \mathrm{e}^{-\mathbf{L}t}\right)\cdot\left(\mathbf{s} + \mathbf{L}^{-1}\cdot\mathbf{f}\right) + \left(h - \mathbf{g}\cdot\mathbf{L}^{-1}\cdot\mathbf{f}\right)t\right], \tag{4.63}$$

where $\mathbf{I}$ denotes the identity matrix. The initial condition being the Poisson distribution describing the steady state and the counter reset to zero $Z = 0$, we have that

$$G_0(\eta, \mathbf{s}_0) = \mathrm{e}^{\mathbf{\Gamma}_0\cdot(\mathbf{s}_0 - \mathbf{1})}, \tag{4.64}$$

which can be directly written down by generalizing Eq. (3.65). The solution of Eq. (4.53) is thus given by

$$\begin{aligned} G(\eta, \mathbf{s}, t) = &\exp\left[\mathbf{g}\cdot\mathbf{L}^{-1}\cdot\left(\mathbf{I} - \mathrm{e}^{-\mathbf{L}t}\right)\cdot\left(\mathbf{s} + \mathbf{L}^{-1}\cdot\mathbf{f}\right) + \left(h - \mathbf{g}\cdot\mathbf{L}^{-1}\cdot\mathbf{f}\right)t\right] \\ &\times \exp\left\{\mathbf{\Gamma}_0\cdot\left[\mathrm{e}^{-\mathbf{L}t}\cdot\mathbf{s} - \mathbf{L}^{-1}\cdot\left(\mathbf{I} - \mathrm{e}^{-\mathbf{L}t}\right)\cdot\mathbf{f} - 1\right]\right\}. \end{aligned} \tag{4.65}$$

The finite-time cumulant generating function of the signed cumulated transfers of particles from the Ith to the $(I+1)$th cell is defined as

$$Q(\lambda, t) \equiv -\frac{1}{t}\ln\left[G(\eta = \mathrm{e}^{-\lambda}, \mathbf{1}, t)\right], \tag{4.66}$$

so that we derive

$$Q(\lambda, t) = Q(\lambda, \infty) - \frac{1}{t}\Xi(\lambda, t), \tag{4.67}$$

where

$$Q(\lambda, \infty) = \mathbf{g}\cdot\left(\mathbf{1} + \mathbf{L}^{-1}\cdot\mathbf{f}\right) \tag{4.68}$$

and

$$\Xi(\lambda, t) = \mathbf{g}\cdot\left(\mathbf{L}^{-1} - \mathbf{L}_0^{-1}\right)\cdot\left(\mathbf{I} - \mathrm{e}^{-\mathbf{L}t}\right)\cdot\left(\mathbf{1} + \mathbf{L}^{-1}\cdot\mathbf{f}\right). \tag{4.69}$$

We observe that

$$\mathbf{L} = \mathbf{M}\cdot\mathbf{L}_0\cdot\mathbf{M}^{-1}, \tag{4.70}$$

where

$$\mathbf{M} = \eta\mathbf{P}_\mathrm{L} + \mathbf{P}_\mathrm{R} \tag{4.71}$$

with the projection matrices

$$\mathbf{P}_\mathrm{L} = \begin{pmatrix} 1 & \cdots & 0 & 0 & \cdots & 0 \\ \vdots & \ddots & \vdots & \vdots & \ddots & \vdots \\ 0 & \cdots & 1 & 0 & \cdots & 0 \\ 0 & \cdots & 0 & 0 & \cdots & 0 \\ \vdots & \ddots & \vdots & \vdots & \ddots & \vdots \\ 0 & \cdots & 0 & 0 & \cdots & 0 \end{pmatrix} \quad \text{and} \quad \mathbf{P}_\mathrm{R} = \begin{pmatrix} 0 & \cdots & 0 & 0 & \cdots & 0 \\ \vdots & \ddots & \vdots & \vdots & \ddots & \vdots \\ 0 & \cdots & 0 & 0 & \cdots & 0 \\ 0 & \cdots & 0 & 1 & \cdots & 0 \\ \vdots & \ddots & \vdots & \vdots & \ddots & \vdots \\ 0 & \cdots & 0 & 0 & \cdots & 1 \end{pmatrix}. \tag{4.72}$$

The identity matrix in $\mathbf{P}_{\rm L}$ is of dimension $I\times I$, while the identity matrix in $\mathbf{P}_{\rm R}$ is $(L-I)\times(L-I)$. Since the projection matrices satisfy the condition $\mathbf{P}_{\rm L}+\mathbf{P}_{\rm R}=\mathbf{I}$, we thus have

$$\mathbf{M}=\mathbf{I}+(\eta-1)\mathbf{P}_{\rm L}, \tag{4.73}$$

$$\mathbf{M}^{-1}=\mathbf{I}+(\eta^{-1}-1)\mathbf{P}_{\rm L}. \tag{4.74}$$

From the above related expressions, the finite-time cumulant generating function (4.68) can be written in the following form,

$$Q(\lambda,t)=\mathbf{g}\cdot\Big[\mathbf{I}-\mathbf{M}\cdot\mathbf{L}_0^{-1}\cdot\mathbf{M}^{-1}\cdot\mathbf{L}_0 - \frac{1}{t}\left(\mathbf{M}\cdot\mathbf{L}_0^{-1}-\mathbf{L}_0^{-1}\cdot\mathbf{M}\right)\cdot\left(\mathbf{I}-\mathrm{e}^{-\mathbf{L}_0 t}\right)\cdot\left(\mathbf{M}^{-1}-\mathbf{L}_0^{-1}\cdot\mathbf{M}^{-1}\cdot\mathbf{L}_0\right)\Big]\cdot\mathbf{1}. \tag{4.75}$$

Because of Eqs. (4.73)-(4.74), we find that

$$Q(\lambda,t)=\mathbf{g}\cdot\Big[(1-\eta)\mathbf{P}_{\rm L}+(1-\eta^{-1})\mathbf{L}_0^{-1}\cdot\mathbf{P}_{\rm L}\cdot\mathbf{L}_0-(2-\eta-\eta^{-1})\mathbf{P}_{\rm L}\cdot\mathbf{L}_0^{-1}\cdot\mathbf{P}_{\rm L}\cdot\mathbf{L}_0 + \frac{1}{t}\left(2-\eta-\eta^{-1}\right)\left(\mathbf{L}_0^{-1}\cdot\mathbf{P}_{\rm L}-\mathbf{P}_{\rm L}\cdot\mathbf{L}_0^{-1}\right)\cdot\left(\mathbf{I}-\mathrm{e}^{-\mathbf{L}_0 t}\right)\cdot\left(\mathbf{P}_{\rm L}-\mathbf{L}_0^{-1}\cdot\mathbf{P}_{\rm L}\cdot\mathbf{L}_0\right)\Big]\cdot\mathbf{1}. \tag{4.76}$$

Using Eq. (4.59) and $\mathbf{P}_{\rm R}=\mathbf{I}-\mathbf{P}_{\rm L}$, the finite-time cumulant generating function becomes

$$Q(\lambda,t)=\tilde{W}_+(t)\left(1-\mathrm{e}^{-\lambda}\right)+\tilde{W}_-(t)\left(1-\mathrm{e}^{+\lambda}\right), \tag{4.77}$$

with the time-dependent transition rates given by

$$\tilde{W}_+(t)=\mathbf{\Gamma}_0\cdot\mathbf{L}_0\cdot\mathbf{P}_{\rm L}\cdot\mathbf{L}_0^{-1}\cdot\mathbf{P}_{\rm R}\cdot\mathbf{L}_0\cdot\mathbf{1}+\frac{1}{t}\Psi(t), \tag{4.78}$$

$$\tilde{W}_-(t)=\mathbf{\Gamma}_0\cdot\mathbf{L}_0\cdot\mathbf{P}_{\rm R}\cdot\mathbf{L}_0^{-1}\cdot\mathbf{P}_{\rm L}\cdot\mathbf{L}_0\cdot\mathbf{1}+\frac{1}{t}\Psi(t), \tag{4.79}$$

with

$$\Psi(t)\equiv\mathbf{\Gamma}_0\cdot\left(\mathbf{P}_{\rm L}-\mathbf{L}_0\cdot\mathbf{P}_{\rm L}\cdot\mathbf{L}_0^{-1}\right)\cdot\left(\mathbf{I}-\mathrm{e}^{-\mathbf{L}_0 t}\right)\cdot\left(\mathbf{P}_{\rm L}-\mathbf{L}_0^{-1}\cdot\mathbf{P}_{\rm L}\cdot\mathbf{L}_0\right)\cdot\mathbf{1}. \tag{4.80}$$

Invoking Eq. (4.66), we obtain the finite-time moment generating function as

$$G\left(\eta,\mathbf{1},t\right)=\sum_{Z=-\infty}^{+\infty}\eta^Z\mathcal{P}(Z,t)=\exp\left[t(\eta-1)\tilde{W}_+(t)+t(\eta^{-1}-1)\tilde{W}_-(t)\right], \tag{4.81}$$

with the probability distribution

$$\mathcal{P}(Z,t)\equiv\sum_{N_1,\cdots,N_L}\mathcal{P}(Z,N_1,\cdots,N_L,t). \tag{4.82}$$

Using Eqs. (2.38)-(2.40), we get

$$\mathcal{P}(Z,t)=\mathrm{e}^{-\left[\tilde{W}_+(t)+\tilde{W}_-(t)\right]t}\left[\frac{\tilde{W}_+(t)}{\tilde{W}_-(t)}\right]^{\frac{Z}{2}}I_Z\left(2t\sqrt{\tilde{W}_+(t)\tilde{W}_-(t)}\right), \tag{4.83}$$

where $I_Z(u)$ is the modified Bessel function defined by Eq. (2.42). Since $I_Z(u)=I_{-Z}(u)$, the probability distribution (4.83) obeys the finite-time fluctuation relation

$$\frac{\mathcal{P}(Z,t)}{\mathcal{P}(-Z,t)}=\mathrm{e}^{\tilde{A}(t)Z}, \tag{4.84}$$

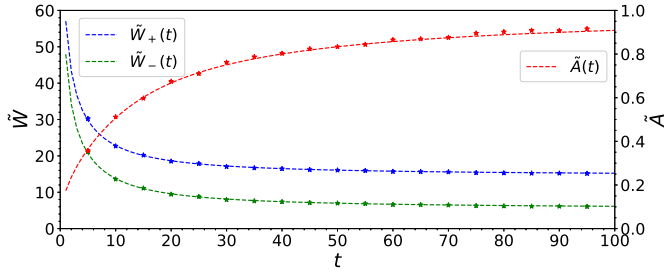

Figure 4.3: Time-dependent transition rates $\tilde{W}_+(t)$, $\tilde{W}_-(t)$ and $\tilde{A}(t) \equiv \ln\left[\tilde{W}_+(t)/\tilde{W}_-(t)\right]$ versus time t. The blue and green dashed lines are for the two time-dependent transition rates according to Eqs. (4.78)-(4.79), while the red dashed one is for the corresponding time-dependent affinity. The asterisks are obtained from simulation according to $\tilde{W}_+(t) = \tilde{D}(t) + J/2$ and $\tilde{W}_-(t) = \tilde{D}(t) - J/2$, where $\tilde{D}(t)$ is the time-dependent diffusivity. The parameter values used in simulation are $\beta = e = 1.0$, $D = \epsilon = 0.01$, $\Omega = 10000$, $\Delta x = 0.1$, $L = 10$, $\bar{N}_{\rm L} = \bar{N}_{\rm R} = N_- = 100$ and $V = \Phi_{\rm L} - \Phi_{\rm R} = 1.0$. The time-dependent rates and affinity from simulation are computed with 20000 data. The counting statistics is performed in the middle of the transport channel.

which holds at every time. $\tilde{A}(t)$ is the finite-time affinity defined as

$$\tilde{A}(t) \equiv \ln \frac{\tilde{W}_+(t)}{\tilde{W}_-(t)}. \tag{4.85}$$

Figure 4.3 shows how the time-dependent transition rates (4.78)-(4.79) and the corresponding time-dependent affinity (4.85) change in time and converge to their asymptotic values. In this figure, the results from numerical simulation are shown in comparison with the calculation from Eqs. (4.78)-(4.79) and (4.85) in which the matrix exponential can be computed using Padé approximation (see Appendix E)[3], and we see striking quantitative agreement between them. In simulation, the time-dependent transition rates are given by $\tilde{W}_+(t) = \tilde{D}(t)+J/2$ and $\tilde{W}_-(t) = \tilde{D}(t)-J/2$, where $\tilde{D}(t)$ is the diffusivity of current calculated from the statistics carried out over the finite-time interval $[0,\, t]$. In the long-time limit, $\mathcal{P}(Z,t)$ goes to Eq. (2.41), which is the solution corresponding to the coarse-grained model (4.32), and, considering the positivity of $\mathbf{L}_0$,

$$W_+ = \lim_{t\to\infty} \tilde{W}_+(t) = \mathbf{\Gamma}_0 \cdot \mathbf{L}_0 \cdot \mathbf{P}_{\rm L} \cdot \mathbf{L}_0^{-1} \cdot \mathbf{P}_{\rm R} \cdot \mathbf{L}_0 \cdot \mathbf{1}, \tag{4.86}$$

$$W_- = \lim_{t\to\infty} \tilde{W}_-(t) = \mathbf{\Gamma}_0 \cdot \mathbf{L}_0 \cdot \mathbf{P}_{\rm R} \cdot \mathbf{L}_0^{-1} \cdot \mathbf{P}_{\rm L} \cdot \mathbf{L}_0 \cdot \mathbf{1}, \tag{4.87}$$

are interpreted as the global transition rates between the two particle reservoirs. The asymptotic fluctuation relation

$$\frac{\mathcal{P}(Z,t)}{\mathcal{P}(-Z,t)} \simeq_{t\to\infty} \exp\left(AZ\right) \tag{4.88}$$

is recovered in the long-time limit, with the affinity given by

$$A = \lim_{t\to\infty} \tilde{A}(t) = \ln \frac{W_+}{W_-}. \tag{4.89}$$

According to Eqs. (4.78)-(4.80), the asymptotic fluctuation relation (4.88) is slowly approached in time with corrections going as t^{-1}. The above analysis shows that the coarse-grained model with constant rates (3.1) is exactly valid in describing the long-time behavior of the transport in the low-density limit. The global transition rates (4.86)-(4.87) can be developed as

$$W_+ = k_+^2 \bar{N}_{\rm L} \left(\mathbf{L}_0^{-1}\right)_{1L} \qquad \text{and} \qquad W_- = k_-^2 \bar{N}_{\rm R} \left(\mathbf{L}_0^{-1}\right)_{L1}. \tag{4.90}$$

[3]The Python package Scipy provides the function `linalg.inv` for computing the inverse of a matrix.

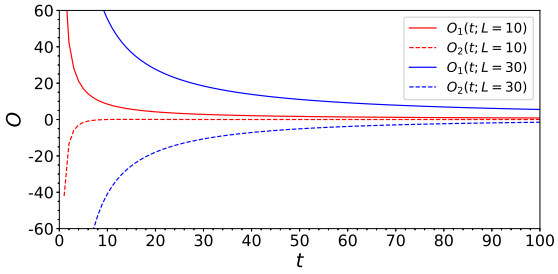

Figure 4.4: The time-dependent components $O_1(t)$ and $O_2(t)$ given by Eqs. (4.95)-(4.96) versus time t. We set $\bar{N}_{\rm L} = \bar{N}_{\rm R} = N_- = 100$, and $k_\pm$ are calculated with the parameter values $\beta = e = 1.0$, $D = \epsilon = 0.01$, $\Delta x = 0.1$, $V = \Phi_{\rm L} - \Phi_{\rm R} = 1.0$. Red lines are for the case of short channel with $L = 10$ cells, while the blue ones are for the case of long channel with $L = 30$ cells. The counting is performed in the middle of the transport channel.

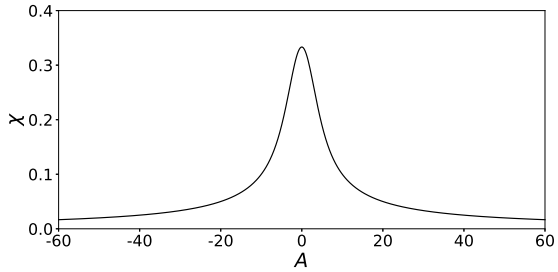

Figure 4.5: The quantity χ given in Eq. (4.105) as a function of affinity $A = \beta e(\Phi_{\rm L} - \Phi_{\rm R})$.

Inverting the matrix $\mathbf{L}_0$, we get

$$\left(\mathbf{L}_0^{-1}\right)_{ij} = \begin{cases} \frac{k_+^{j-i}\left(k_+^i - k_-^i\right)\left(k_+^{L+1-j} - k_-^{L+1-j}\right)}{(k_+ - k_-)\left(k_+^{L+1} - k_-^{L+1}\right)} & \text{if} \quad i \le j, \\ \frac{k_-^{i-j}\left(k_+^j - k_-^j\right)\left(k_+^{L+1-i} - k_-^{L+1-i}\right)}{(k_+ - k_-)\left(k_+^{L+1} - k_-^{L+1}\right)} & \text{if} \quad i > j. \end{cases} \tag{4.91}$$

So, the two global transition rates are calculated as

$$W_+ = \bar{N}_{\rm L}\frac{k_+^{L+1}(k_+ - k_-)}{k_+^{L+1} - k_-^{L+1}} = \frac{D\bar{N}_{\rm L}}{\Delta x^2(L+1)}\frac{\beta e(\Phi_{\rm L} - \Phi_{\rm R})}{1 - \exp\left[-\beta e(\Phi_{\rm L} - \Phi_{\rm R})\right]}, \tag{4.92}$$

$$W_- = \bar{N}_{\rm R}\frac{k_-^{L+1}(k_+ - k_-)}{k_+^{L+1} - k_-^{L+1}} = \frac{D\bar{N}_{\rm R}}{\Delta x^2(L+1)}\frac{\beta e(\Phi_{\rm R} - \Phi_{\rm L})}{1 - \exp\left[-\beta e(\Phi_{\rm R} - \Phi_{\rm L})\right]}, \tag{4.93}$$

which are in accord with the rate function (4.40) when $\bar{N}_{\rm L} = \bar{N}_{\rm R}$, and thus the constant κ in Eq. (4.40) has the expression

$$\kappa = \frac{D\bar{N}_{\rm L}}{\Delta x^2(L+1)} = \frac{D\bar{N}_{\rm R}}{\Delta x^2(L+1)}. \tag{4.94}$$

With the parameter values used in Figure 4.2, a simple calculation gives $\kappa \approx 9.091$, roughly equal to that obtained through fitting the data from simulation.

We now turn to study the convergence rate of time-dependent transition rates. For this purpose, we split the time-dependent part $\Psi(t)/t$ of the transition rates (4.78) and (4.79) into two

components

$$O_1(t) = \frac{1}{t}\left[\mathbf{\Gamma}_0 \cdot \left(\mathbf{P}_\mathrm{L} - \mathbf{L}_0 \cdot \mathbf{P}_\mathrm{L} \cdot \mathbf{L}_0^{-1}\right) \cdot \left(\mathbf{P}_\mathrm{L} - \mathbf{L}_0^{-1} \cdot \mathbf{P}_\mathrm{L} \cdot \mathbf{L}_0\right) \cdot \mathbf{1}\right], \tag{4.95}$$

$$O_2(t) = -\frac{1}{t}\left[\mathbf{\Gamma}_0 \cdot \left(\mathbf{P}_\mathrm{L} - \mathbf{L}_0 \cdot \mathbf{P}_\mathrm{L} \cdot \mathbf{L}_0^{-1}\right) \cdot \mathrm{e}^{-\mathbf{L}_0 t} \cdot \left(\mathbf{P}_\mathrm{L} - \mathbf{L}_0^{-1} \cdot \mathbf{P}_\mathrm{L} \cdot \mathbf{L}_0\right) \cdot \mathbf{1}\right]. \tag{4.96}$$

Because $O_2(t)$ is damped by the additional exponential factor, it is quite reasonable to expect that $O_1(t)$ is the dominant one in $\Psi(t)/t$. In Figure 4.4, we show $O_1(t)$ and $O_2(t)$ from numerical calculation, and find that $O_2(t)$ indeed decays faster. We also show the situations with different lengths of transport channel in Figure 4.4. The comparison clearly tells us that the longer the channel is, the slower the convergence of the time-dependent rates, as expected. We now write $O_1(t)$ with four explicit terms,

$$\begin{aligned} O_1(t) = \frac{1}{t}\Big[&\mathbf{\Gamma}_0 \cdot \mathbf{P}_\mathrm{L} \cdot \mathbf{1} - \mathbf{\Gamma}_0 \cdot \mathbf{P}_\mathrm{L} \cdot \mathbf{L}_0^{-1} \cdot \mathbf{P}_\mathrm{L} \cdot \mathbf{L}_0 \cdot \mathbf{1} \\ &- \mathbf{\Gamma}_0 \cdot \mathbf{L}_0 \cdot \mathbf{P}_\mathrm{L} \cdot \mathbf{L}_0^{-1} \cdot \mathbf{P}_\mathrm{L} \cdot \mathbf{1} + \mathbf{\Gamma}_0 \cdot \mathbf{L}_0 \cdot \mathbf{P}_\mathrm{L} \cdot \mathbf{L}_0^{-1} \cdot \mathbf{L}_0^{-1} \cdot \mathbf{P}_\mathrm{L} \cdot \mathbf{L}_0 \cdot \mathbf{1}\Big]. \end{aligned} \tag{4.97}$$

In order to simplify the calculation, we take the projection matrix $\mathbf{P}_\mathrm{L}$ as

$$\mathbf{P}_\mathrm{L} = \begin{pmatrix} 1 & 0 & \cdots & 0 \\ 0 & 0 & \cdots & 0 \\ \vdots & \vdots & \ddots & \vdots \\ 0 & 0 & \cdots & 0 \end{pmatrix}, \tag{4.98}$$

with $I = 1$, which indicates that we perform counting statistics in between the first and second cells of discretized channel. So, $O_1(t)$ is developed as

$$\begin{aligned} O_1(t) &= \frac{\bar{N}}{t}\left\{1 - (k_- + k_+)\left(\mathbf{L}_0^{-1}\right)_{11} + k_- k_+ \left(\mathbf{L}_0^{-1} \cdot \mathbf{L}_0^{-1}\right)_{11}\right\} \\ &= \frac{\bar{N}}{t}\left\{1 - \frac{(k_+ + k_-)(k_+^L - k_-^L)}{k_+^{L+1} - k_-^{L+1}} + \frac{k_- k_+}{\left(k_+^{L+1} - k_-^{L+1}\right)^2} \sum_{i=1}^{L}\left[k_+^{i-1} k_-^{i-1}\left(k_+^{L+1-i} - k_-^{L+1-i}\right)^2\right]\right\}. \end{aligned} \tag{4.99}$$

Setting

$$x = \frac{k_+}{k_-}, \tag{4.100}$$

we have

$$\begin{aligned} O_1(t) &= \frac{\bar{N}}{t}\left\{1 - \frac{(x+1)(x^L - 1)}{x^{L+1} - 1} + \frac{1}{(x^{L+1} - 1)^2}\left[-2Lx^{L+1} + x^{2L+2}\sum_{i=1}^{L} x^{-i} + \sum_{i=1}^{L} x^i\right]\right\} \\ &= \frac{n_- \Sigma l}{Lt}\left\{1 - \frac{(x+1)(x^L - 1)}{x^{L+1} - 1} + \frac{1}{(x^{L+1} - 1)^2}\left[-2Lx^{L+1} + \frac{(x^{L+2} + x)(x^L - 1)}{x - 1}\right]\right\}, \end{aligned} \tag{4.101}$$

where we have made use of

$$\bar{N} = n_- \Sigma \Delta x = \frac{n_- \Sigma l}{L}. \tag{4.102}$$

The variable x defined by Eq. (4.100) is explicitly calculated as

$$x = \exp\left[\frac{\beta e\left(\Phi_{\mathrm{L}} - \Phi_{\mathrm{R}}\right)}{L+1}\right]. \tag{4.103}$$

In the continuum limit where $L \to \infty$ with the total length of l fixed, we have

$$O_1(t) = \frac{n_- \Sigma l}{t}\chi(A), \tag{4.104}$$

where $\chi(A)$ is a function of affinity $A = \beta e\left(\Phi_{\mathrm{L}} - \Phi_{\mathrm{R}}\right)$, and given by

$$\chi(A) = \frac{\mathrm{e}^A + 1}{A\left(\mathrm{e}^A - 1\right)} - \frac{2\mathrm{e}^A}{\left(\mathrm{e}^A - 1\right)^2}. \tag{4.105}$$

It is noted that $\chi(A)$ has the symmetry property,

$$\chi(A) = \chi(-A), \tag{4.106}$$

with the limit towards the origin given by

$$\lim_{A\to 0}\chi(A) = \frac{1}{3}. \tag{4.107}$$

The symmetry of Eq. (4.104) with respect to A is expected from the homogeneous configuration of the transport channel in space. Figure 4.5 plots the χ as a function of A, and the symmetry (4.106) is clearly seen. In addition, Eq. (4.104) gives time scales, $t_{\mathrm{s}} \equiv n_- \Sigma l$, for the asymptotic symmetry (4.88) to be approached in time with the correction going as t^{-1}. It indicates that the smaller the transport channel is, the faster the asymptotic symmetry (4.88) is reached.

The analysis in this section fully demonstrated that a Markov jump process with linear rates can be invoked to describe the transport of charged particles driven by external field in the low-density limit. Moreover, the finite-time fluctuation theorem can be established in this case with the defined time-dependent affinities converging in time to their asymptotic values with corrections going as $1/t$.

Chapter 5

Charge Transport in p-n Junction Diodes

Diodes are the basic semiconductor devices consisting of a single p-n junction[1]. In modern electronic applications, p-n junctions play a fundamental role and, therefore, receive considerable attention. As shown by Shockley, the electric potential barrier generated at the junction induces the highly nonlinear and asymmetric current-voltage characteristics that are used in rectifiers and switching circuits[2][88, 89, 90, 91, 92, 93, 94, 95, 96].

In electric systems, fluctuation theorems for nonequilibrium work and heat have been theoretically and experimentally investigated in linear RC circuits [97, 98, 99], leaving open the study of current fluctuations in nonlinear electronic devices. This is motivating the need to develop a stochastic approach and to establish the fluctuation theorem for charge transport in diodes, consistently with the laws of electricity, thermodynamics, and microreversibility. Stochastic models have already been proposed for the random number of charges crossing a diode [100, 101].

In this chapter, a spatially extended stochastic description of the p-n junction diode is developed. Since there exists two mobile charge carriers inside diodes: negative-charged electrons and positive-charged holes, while electron-hole pairs are randomly generated and recombined, this approach is an extension of the stochastic approach presented in Chapter 4 to additionally account for two species and the reaction between them. As such, this approach is based on diffusion-reaction stochastic partial differential equations for electrons and holes, including their Coulomb interaction described by the Poisson equation. In this framework, the fluctuation theorem is numerically shown to hold for both the charge carrier current and the measured total current including the contribution of the displacement current [102, 62]. Moreover, the functionality of diodes under ideal conditions is numerically realized.

5.1 p-n Junction Diodes

A p-n junction is formed when a p-type semiconductor and an n-type semiconductor are in contact, as shown in Figure 5.1. Inside p-type semiconductors, the doped impurities accept electrons, leaving the so-called negative-charged acceptors, and as such the majority charge carriers are holes and the minority charge carriers are electrons. Inside n-type semiconductors, the doped impurities are called donors which are positive-charged due to their donation of electrons, and therefore there are more electrons than holes. We can consider the p-n junction as a three-dimensional rod of length l with its coordinate x extending from $-l/2$ to $+l/2$, and of section area Σ in the transverse y- and z-directions. The position is denoted by $\mathbf{r} = (x, y, z)$. For simplicity, the acceptor density $a(\mathbf{r})$ and the donor density $d(\mathbf{r})$ are taken to be uniform respectively in the p- and n-sides and there is an abrupt change at the junction. They can thus be expressed as

$$a(\mathbf{r}) = a\,\theta(-x), \qquad d(\mathbf{r}) = d\,\theta(x), \tag{5.1}$$

[1] If the p- and n-type regions are made out of the same semiconductor material, the junction is a homojunction.
[2] Some diodes can emit light (light-emitting diodes), and others can emit laser light (laser diodes).

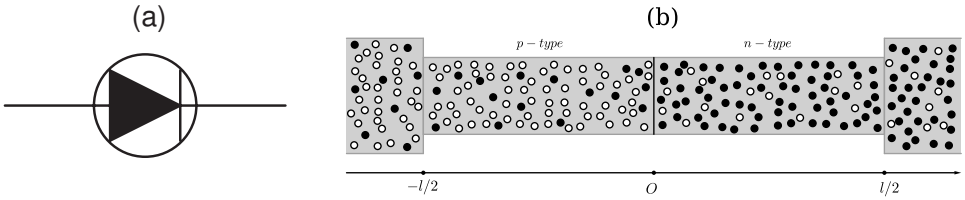

Figure 5.1: Schematic representation of diode (left) and p-n junction (right). In the p-n junction, the black dots represent electrons and the white ones represent holes.

where $\theta(x)$ is Heaviside's step function, which is defined such that $\theta(x) = 0$ if $x < 0$ and $\theta(x) = 1$ if $x > 0$. For simplicity, we set $a = d$. The charge density is given by

$$\rho(\mathbf{r}) = e\,[p(\mathbf{r}) - n(\mathbf{r}) + d(\mathbf{r}) - a(\mathbf{r})] \tag{5.2}$$

in terms of the elementary electric charge $e = |e|$, the hole density $p(\mathbf{r})$, the electron density $n(\mathbf{r})$, the donor density $d(\mathbf{r})$, and the acceptor density $a(\mathbf{r})$. Here, we have assumed that every donor gives one electron and every acceptor one hole. The charge density determines the electric potential Φ by Gauss's law and the Poisson equation [85, 84]. According to electroneutrality, the inhomogeneity (5.1) of the acceptor and donor densities is thus responsible for the global asymmetric distribution of mobile electrons and holes across the junction, leading to current rectification by the diode. In p-n junctions, electrons and holes undergo the diffusion process due to the their inhomogeneous distribution and drift process under the electric field. Moreover, electrons and holes are generated and recombined by the reaction

$$\emptyset \underset{k_-}{\overset{k_+}{\rightleftharpoons}} e^- + h^-, \tag{5.3}$$

where k_+ and k_- are respectively the electron-hole pair generation and recombination rate constants.

If the semiconductor is in equilibrium, then the electron and hole densities obey the condition

$$n_{\mathrm{eq}} p_{\mathrm{eq}} = \nu^2, \qquad \text{where} \qquad \nu = \sqrt{\frac{k_+}{k_-}} \tag{5.4}$$

is the intrinsic carrier density. In equilibrium, the electron and hole densities are, moreover, related to the electric potential by

$$n_{\mathrm{eq}}(\mathbf{r}) \sim \mathrm{e}^{+\beta e \Phi_{\mathrm{eq}}(\mathbf{r})} \qquad \text{and} \qquad p_{\mathrm{eq}}(\mathbf{r}) \sim \mathrm{e}^{-\beta e \Phi_{\mathrm{eq}}(\mathbf{r})}. \tag{5.5}$$

The diode is in contact on its left- and right-hand sides with reservoirs at different potentials and densities for electrons and holes:

$$\Phi(x = -l/2) = \Phi_{\mathrm{L}}, \quad n(x = -l/2) = n_{\mathrm{L}}, \quad p(x = -l/2) = p_{\mathrm{L}}, \tag{5.6}$$

$$\Phi(x = +l/2) = \Phi_{\mathrm{R}}, \quad n(x = +l/2) = n_{\mathrm{R}}, \quad p(x = +l/2) = p_{\mathrm{R}}. \tag{5.7}$$

For simplicity, we set $n_{\mathrm{L}} = p_{\mathrm{R}}$ and $p_{\mathrm{L}} = n_{\mathrm{R}}$. Furthermore, we consider the boundary conditions

$$p_{\mathrm{L}} = n_{\mathrm{L}} + a, \qquad n_{\mathrm{R}} = p_{\mathrm{R}} + d, \tag{5.8}$$

so that the whole p-n junction is symmetric under inversion and permutation between electrons and holes, as depicted in Figure 5.1(b). The p-n junction diode is thus characterized by the ratio of majority to minority carrier concentrations,

$$\frac{c_{\mathrm{major}}}{c_{\mathrm{minor}}} \equiv \frac{p_{\mathrm{L}}}{n_{\mathrm{L}}} = \frac{n_{\mathrm{R}}}{p_{\mathrm{R}}}. \tag{5.9}$$

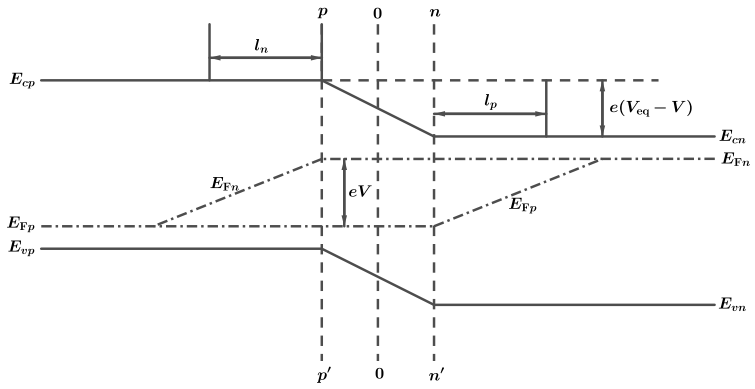

Figure 5.2: Energy-band diagram of p-n junction that is forward biased. Between pp' and nn' is the space charge region that is also referred to as the depletion region. The electric field is concentrated in this region in which all electrons and holes are swept out. E_c, E_v are the edges of conduction band and valence band, respectively. $E_{\mathrm{F}n}$, $E_{\mathrm{F}p}$ are the quasi-Fermi levels for elections respectively in the two regions. If we assume that no voltage is applied across the p-n junction, then the junction is in equilibrium, and the Fermi energy level is constant throughout the entire system, $E_{\mathrm{F}p} = E_{\mathrm{F}n} = E_{\mathrm{F}}$.

If the diode is in equilibrium, Eq. (5.5) holds and the potential difference is related to the densities at the reservoirs according to the Nernst potential

$$(\Phi_{\mathrm{L}} - \Phi_{\mathrm{R}})_{\mathrm{eq}} = \frac{1}{\beta e} \ln \frac{n_{\mathrm{L}}}{n_{\mathrm{R}}} = \frac{1}{\beta e} \ln \frac{p_{\mathrm{R}}}{p_{\mathrm{L}}}. \tag{5.10}$$

The diode is driven out of equilibrium if the applied voltage with respect to the Nernst potential,

$$V = \Phi_{\mathrm{L}} - \Phi_{\mathrm{R}} - \frac{1}{\beta e} \ln \frac{n_{\mathrm{L}}}{n_{\mathrm{R}}} = \Phi_{\mathrm{L}} - \Phi_{\mathrm{R}} + \frac{1}{\beta e} \ln \frac{p_{\mathrm{L}}}{p_{\mathrm{R}}}, \tag{5.11}$$

is non vanishing. As a consequence, there is an electric current flowing in the diode. The equilibrium state is recovered if the applied voltage is zero, $V = 0$. In this case, the diffusion force and electric force exactly balance each other. If $V > 0$ the junction is said to be forward biased, and if $V < 0$ it is reverse biased. Figure 5.2 shows the energy-band diagram of the forward biased p-n junction. According to energy band theory, the applied voltage makes the Fermi level of electrons unbalanced across the p-n junction, and as a consequence the current is induced.

5.1.1 Stochastic Diffusion-Reaction Equations

The thermal agitation inside the p-n junction generates incessant erratic movements for electrons and holes, in turn causing local fluctuations in the currents and reaction rates. These fluctuations can be described within the stochastic approach by introducing Gaussian white noise fields in the diffusion-reaction equations for the electron and hole densities. The advantage of this approach is that the usual phenomenological parameters suffice for the stochastic description. The mobilities of electrons and holes are related to their diffusion coefficients through Einstein's relations:

$$\mu_n = \beta D_n \qquad \text{and} \qquad \mu_p = \beta D_p. \tag{5.12}$$

In general, the parameters D_n, D_p, and $k_\pm$ are spatially dependent in an inhomogeneous medium. However, for simplicity, we assume that they are uniform across the whole p-n junction.

The balance equations for electrons and holes of respective densities n and p can be expressed as

$$\partial_t n + \boldsymbol{\nabla} \cdot \mathbf{j}_n = \sigma_n, \tag{5.13}$$
$$\partial_t p + \boldsymbol{\nabla} \cdot \mathbf{j}_p = \sigma_p, \tag{5.14}$$

with the current densities

$$\mathbf{j}_n = -\mu_n n e \boldsymbol{\mathcal{E}} - D_n \boldsymbol{\nabla} n + \delta \mathbf{j}_n, \tag{5.15}$$
$$\mathbf{j}_p = +\mu_p p e \boldsymbol{\mathcal{E}} - D_p \boldsymbol{\nabla} p + \delta \mathbf{j}_p, \tag{5.16}$$

and equal reaction rate densities

$$\sigma_n = \sigma_p = k_+ - k_- np + \delta\sigma \tag{5.17}$$

since the same reactive events determine both of them. The electric field is expressed as

$$\boldsymbol{\mathcal{E}} = -\boldsymbol{\nabla}\Phi \tag{5.18}$$

in terms of the electric potential satisfying the Poisson equation

$$\nabla^2 \Phi = -\frac{\rho}{\epsilon}, \tag{5.19}$$

where ϵ is the permittivity and the electric charge density is given by Eq. (5.2).

The Gaussian white noises $\delta\mathbf{j}_n$, $\delta\mathbf{j}_p$, and $\delta\sigma$ are characterized by

$$\langle \delta\mathbf{j}_n(\mathbf{r},t)\rangle = \langle \delta\mathbf{j}_p(\mathbf{r},t)\rangle = 0, \tag{5.20}$$
$$\langle \delta\mathbf{j}_n(\mathbf{r},t) \otimes \delta\mathbf{j}_n(\mathbf{r}',t')\rangle = \Gamma_{nn}(\mathbf{r},t)\delta^3(\mathbf{r}-\mathbf{r}')\delta(t-t')\mathbf{I}, \tag{5.21}$$
$$\langle \delta\mathbf{j}_p(\mathbf{r},t) \otimes \delta\mathbf{j}_p(\mathbf{r}',t')\rangle = \Gamma_{pp}(\mathbf{r},t)\delta^3(\mathbf{r}-\mathbf{r}')\delta(t-t')\mathbf{I}, \tag{5.22}$$
$$\langle \delta\mathbf{j}_n(\mathbf{r},t) \otimes \delta\mathbf{j}_p(\mathbf{r}',t')\rangle = 0, \tag{5.23}$$
$$\langle \delta\sigma(\mathbf{r},t)\rangle = 0, \tag{5.24}$$
$$\langle \delta\sigma(\mathbf{r},t)\,\delta\sigma(\mathbf{r}',t')\rangle = \Gamma_{\sigma\sigma}(\mathbf{r},t)\delta^3(\mathbf{r}-\mathbf{r}')\delta(t-t'), \tag{5.25}$$
$$\langle \delta\sigma(\mathbf{r},t)\delta\mathbf{j}_n(\mathbf{r}',t')\rangle = \langle \delta\sigma(\mathbf{r},t)\delta\mathbf{j}_p(\mathbf{r}',t')\rangle = 0, \tag{5.26}$$

where $\mathbf{I}$ is the 3×3 identity matrix and

$$\Gamma_{nn}(\mathbf{r},t) \equiv 2D_n n(\mathbf{r},t), \tag{5.27}$$
$$\Gamma_{pp}(\mathbf{r},t) \equiv 2D_p p(\mathbf{r},t), \tag{5.28}$$
$$\Gamma_{\sigma\sigma}(\mathbf{r},t) \equiv k_+ + k_- n(\mathbf{r},t)p(\mathbf{r},t), \tag{5.29}$$

are the spectral densities of the noises respectively associated with the electron diffusion, hole diffusion, and reaction.

We notice that the current densities can be equivalently written as

$$\mathbf{j}_n = -D_n \mathrm{e}^{\beta e\Phi}\boldsymbol{\nabla}\left(\mathrm{e}^{-\beta e\Phi} n\right) + \delta\mathbf{j}_n, \tag{5.30}$$
$$\mathbf{j}_p = -D_p \mathrm{e}^{-\beta e\Phi}\boldsymbol{\nabla}\left(\mathrm{e}^{\beta e\Phi} p\right) + \delta\mathbf{j}_p. \tag{5.31}$$

5.1.2 Mean-Field Equations Under Stationary Conditions

By averaging the balance equations (5.13)-(5.14) and the expressions (5.15)-(5.16) over the noises using Eqs. (5.20) and (5.24), we can obtain mean-field equations for the stationary mean profiles of the densities and current densities in the x-direction. Together with Gauss's law and the Poisson

equation for the electric field and potential, these mean-field equations are given by the following coupled ordinary differential equations (ODEs):

$$\frac{\mathrm{d}n(x)}{\mathrm{d}x} = -\frac{j_n(x)}{D_n} - \beta e n(x)\mathcal{E}(x), \tag{5.32}$$

$$\frac{\mathrm{d}p(x)}{\mathrm{d}x} = -\frac{j_p(x)}{D_p} + \beta e p(x)\mathcal{E}(x), \tag{5.33}$$

$$\frac{\mathrm{d}j_n(x)}{\mathrm{d}x} = k_+ - k_- n(x)p(x), \tag{5.34}$$

$$\frac{\mathrm{d}j_p(x)}{\mathrm{d}x} = k_+ - k_- n(x)p(x), \tag{5.35}$$

$$\frac{\mathrm{d}\mathcal{E}(x)}{\mathrm{d}x} = \frac{e}{\epsilon}\left[p(x) - n(x) + d(x) - a(x)\right], \tag{5.36}$$

$$\frac{\mathrm{d}\Phi(x)}{\mathrm{d}x} = -\mathcal{E}(x), \tag{5.37}$$

with the aforementioned boundary conditions (5.6)-(5.7). The discontinuity of $a(x)$ and $d(x)$ at the junction makes it hard for numerical integration, so we use the following continuous alternatives as approximations,

$$a(x) = \frac{a}{1+\exp(x/\delta)}, \qquad d(x) = \frac{d}{1+\exp(-x/\delta)}, \tag{5.38}$$

with the width δ being sufficiently small, say, $\delta = 0.01$ that is actually adopted. The electric field remains uniform in contact with the reservoirs according to Eq. (5.36) with the conditions (5.8). In addition, the current densities also remain uniform at the reservoirs by Eqs. (5.34)-(5.35). So, only the potential difference between the ends of the diode is responsible for inducing particle currents. We notice that the first four ODEs are nonlinear. In this set of ODEs, the net current density

$$j = j_p(x) - j_n(x) \tag{5.39}$$

is a constant of integration, as a consequence of electric charge conservation. Moreover, the electric potential does not appear before the last equation, which is thus decoupled from the other ones. Accordingly, the set can be reduced to four ODEs for $n(x)$, $p(x)$, $j_n(x)$, and $\mathcal{E}(x)$.

5.2 Numerical Simulation Method

For the numerical simulation of the p-n junction diode, the system is spatially discretized into cells, each containing some numbers of electrons and holes, respectively, and a Markov jump process in a accord with the stochastic partial differential equations (5.13)-(5.19) is associated to fully describe the stochastic evolution of electron and hole distributions.

5.2.1 Discretizing the p-n Junction Diode in Space

The p-n junction is spatially discretized into L cells of length $\Delta x = l/L$, section area Σ, and volume $\Omega = \Sigma\Delta x$. These cells are labelled with index $i = 1, 2, \cdots, L$. The indices $i = 0$ and $i = L+1$ are respectively used to refer to the left and right reservoirs, which impose certain boundary conditions on the p-n junction. The numbers of electrons and holes in each cell are respectively given by $N_i = n(x_i)\Omega$, $P_i = p(x_i)\Omega$, with $x_i = (i-0.5)\Delta x - l/2$ $(i = 1, 2, \cdots, L)$. The numbers of electrons and holes in the reservoirs are maintained constant in time, and given by $N_0 \equiv \bar{N}_\mathrm{L} = n_\mathrm{L}\Omega$, $N_{L+1} \equiv \bar{N}_\mathrm{R} = n_\mathrm{R}\Omega$, $P_0 \equiv \bar{P}_\mathrm{L} = p_\mathrm{L}\Omega$, and $P_{L+1} \equiv \bar{P}_\mathrm{R} = p_\mathrm{R}\Omega$. According to the boundary conditions (5.8), the number of acceptors in each cell of the p-type semiconductor is given by $A = a\Omega = \bar{P}_\mathrm{L} - \bar{N}_\mathrm{L}$, and the number of donors in each cell of n-type semiconductor by $D = d\Omega = \bar{N}_\mathrm{R} - \bar{P}_\mathrm{R}$. The electron and hole numbers in the cells change every time a particle

Table 5.1: The values of quantities for the physics of semiconductors.

permittivity	$\epsilon = 0.01$
inverse temperature	$\beta = 1.0$
elementary charge	$e = \lvert e \rvert = 1.0$
diffusion coefficient for electrons	$D_n = 0.01$
diffusion coefficient for holes	$D_p = 0.01$
electron-hole pairs generation rate constant	$k_+ = 0.01$
electron-hole pairs recombination rate constant	$k_- = 0.01$

Table 5.2: The values of parameters for specifying the discretized p-n junction diode.

Meaning	Set I	Set II
number of cells in left region	20	20
number of cells in right region	20	20
width of each cell Δx	0.1	0.1
volume of each cell Ω	800	8×10^5
section area $\Sigma = \Omega/\Delta x$	8000	8×10^6
number of electrons in left-reservoir cell	400	400
number of holes in left-reservoir cell	1600	1.6×10^9
number of electrons in right-reservoir cell	1600	1.6×10^9
number of holes in right-reservoir cell	400	400

jumps between two neighboring cells, between a reservoir and the neighboring cell, or if a reactive event occurs generating or recombining an electron-hole pair. The Poisson equation is replaced by its discretized version

$$\frac{\Phi_{i+1} - 2\Phi_i + \Phi_{i-1}}{\Delta x^2} = -\frac{e}{\epsilon\Omega}(P_i - N_i + D_i - A_i) \tag{5.40}$$

with the boundary conditions $\Phi_0 = \Phi_{\mathrm{L}}$ and $\Phi_{L+1} = \Phi_{\mathrm{R}}$. This linear system should be solved every time a particle transition occurs. Table 5.1 lists the values of physical quantities adopted in numerical simulation. In Table 5.2, two sets of parameter values for specifying the discretized p-n junction diode are listed for different purposes discussed here below. These parameter variables can be rescaled into dimensionless ones with the procedure presented in Appendix D.

5.2.2 Master Equation

The system state is specified by the electron numbers $\mathbf{N} = \{N_i\}_{i=1}^L$ and the hole numbers $\mathbf{P} = \{P_i\}_{i=1}^L$ in the cells and they evolve in time according to the network

$$\begin{array}{ccccccccccccccc}
\bar{N}_{\mathrm{L}} & \underset{W_0^{(-N)}}{\overset{W_0^{(+N)}}{\rightleftharpoons}} & N_1 & \underset{W_1^{(-N)}}{\overset{W_1^{(+N)}}{\rightleftharpoons}} & N_2 & \underset{W_2^{(-N)}}{\overset{W_2^{(+N)}}{\rightleftharpoons}} & \cdots & \underset{W_{L-2}^{(-N)}}{\overset{W_{L-2}^{(+N)}}{\rightleftharpoons}} & N_{L-1} & \underset{W_{L-1}^{(-N)}}{\overset{W_{L-1}^{(+N)}}{\rightleftharpoons}} & N_L & \underset{W_L^{(-N)}}{\overset{W_L^{(+N)}}{\rightleftharpoons}} & \bar{N}_{\mathrm{R}} \\
 & & W_1^{(+)} \updownarrow W_1^{(-)} & & W_2^{(+)} \updownarrow W_2^{(-)} & & \cdots & & W_{L-1}^{(+)} \updownarrow W_{L-1}^{(-)} & & W_L^{(+)} \updownarrow W_L^{(-)} & & \\
\bar{P}_{\mathrm{L}} & \underset{W_0^{(-P)}}{\overset{W_0^{(+P)}}{\rightleftharpoons}} & P_1 & \underset{W_1^{(-P)}}{\overset{W_1^{(+P)}}{\rightleftharpoons}} & P_2 & \underset{W_2^{(-P)}}{\overset{W_2^{(+P)}}{\rightleftharpoons}} & \cdots & \underset{W_{L-2}^{(-P)}}{\overset{W_{L-2}^{(+P)}}{\rightleftharpoons}} & P_{L-1} & \underset{W_{L-1}^{(-P)}}{\overset{W_{L-1}^{(+P)}}{\rightleftharpoons}} & P_L & \underset{W_L^{(-P)}}{\overset{W_L^{(+P)}}{\rightleftharpoons}} & \bar{P}_{\mathrm{R}}
\end{array} .$$

The probability $\mathcal{P}(\mathbf{N},\mathbf{P},t)$ that the cells contain the particle numbers $\mathbf{N}=\{N_i\}_{i=1}^{L}$ and $\mathbf{P}=\{P_i\}_{i=1}^{L}$ for time t is ruled by the master equation

$$\begin{aligned}\frac{d\mathcal{P}}{dt}=&\sum_{i=0}^{L}\Big[\left(\mathrm{e}^{+\partial_{N_i}}\mathrm{e}^{-\partial_{N_{i+1}}}-1\right)W_i^{(+N)}\mathcal{P}+\left(\mathrm{e}^{-\partial_{N_i}}\mathrm{e}^{+\partial_{N_{i+1}}}-1\right)W_i^{(-N)}\mathcal{P}\\&+\left(\mathrm{e}^{+\partial_{P_i}}\mathrm{e}^{-\partial_{P_{i+1}}}-1\right)W_i^{(+P)}\mathcal{P}+\left(\mathrm{e}^{-\partial_{P_i}}\mathrm{e}^{+\partial_{P_{i+1}}}-1\right)W_i^{(-P)}\mathcal{P}\Big]\\&+\sum_{i=1}^{L}\Big[\left(\mathrm{e}^{-\partial_{N_i}}\mathrm{e}^{-\partial_{P_i}}-1\right)W_i^{(+)}\mathcal{P}+\left(\mathrm{e}^{+\partial_{N_i}}\mathrm{e}^{+\partial_{P_i}}-1\right)W_i^{(-)}\mathcal{P}\Big].\end{aligned}\tag{5.41}$$

with the transition rates

$$W_i^{(+N)}=\frac{D_n}{\Delta x^2}\psi(\Delta U_{i,i+1}^{(N)})N_i,\tag{5.42}$$

$$W_i^{(-N)}=\frac{D_n}{\Delta x^2}\psi(\Delta U_{i+1,i}^{(N)})N_{i+1},\tag{5.43}$$

$$W_i^{(+P)}=\frac{D_p}{\Delta x^2}\psi(\Delta U_{i,i+1}^{(P)})P_i,\tag{5.44}$$

$$W_i^{(-P)}=\frac{D_p}{\Delta x^2}\psi(\Delta U_{i+1,i}^{(P)})P_{i+1},\tag{5.45}$$

$$W_i^{(+)}=\Omega k_+,\tag{5.46}$$

$$W_i^{(-)}=\Omega k_-\frac{N_i}{\Omega}\frac{P_i}{\Omega},\tag{5.47}$$

where $\Delta U_{i,i+1}$ is the intrinsic energy change in the whole p-n junction diode associated with the transition of one particle from the ith to $(i+1)$th cell. According to the calculation in Appendix A, we find that

$$\Delta U_{i,i+1}^{(N)}=-e(\Phi_{i+1}-\Phi_i)+\frac{e^2L\Delta x^2}{2(L+1)\epsilon\Omega},\tag{5.48}$$

$$\Delta U_{i,i+1}^{(P)}=+e(\Phi_{i+1}-\Phi_i)+\frac{e^2L\Delta x^2}{2(L+1)\epsilon\Omega}.\tag{5.49}$$

We notice that, for transitions at the boundaries, these expressions hold by taking the values of the potentials in the reservoirs, $\Phi_0=\Phi_{\mathrm{L}}$ and $\Phi_{L+1}=\Phi_{\mathrm{R}}$. The function $\psi(\Delta U)$ is defined by Eq. (4.24). At the ends of the chain, we have that $\exp(\pm\partial_X)=1$ for $X=N_0$, P_0, N_{L+1}, and P_{L+1} in the master equation (5.41).

For numerical purpose, the Markovian stochastic process ruled by Eq. (5.41) is approximated by its corresponding Langevin stochastic process (see Appendix B for the detailed procedure). After the system has relaxed to its stationary state in simulation, every mean quantity in some cell can be estimated by the time average

$$\langle X\rangle=\lim_{T\to\infty}\frac{1}{T}\int_0^T X(t)\mathrm{d}t,\tag{5.50}$$

with $X=N_i$, P_i, Φ_i, or the fluxes $F_i^{(P)}$, $F_i^{(N)}$. By ergodicity, this is equivalent to the ensemble average $\langle X\rangle=\sum_{\mathbf{N},\mathbf{P}}X(t)\mathcal{P}_{\mathrm{st}}(\mathbf{N},\mathbf{P})$ over the stationary probability distribution $\mathcal{P}_{\mathrm{st}}$. Due to the electron-hole pair generation and recombination, the mean fluxes $\langle F_i^{(P)}\rangle$ and $\langle F_i^{(N)}\rangle$ vary with the position x_i. However, by charge conservation, their difference $\langle F_i^{(P)}\rangle-\langle F_i^{(N)}\rangle$ is independent of the position in the junction, which defines the mean net current in the diode. In the continuum limit where $\Delta x\to 0$ and $\Delta t\to 0$, the densities of electrons and holes obeying Eqs. (5.13)-(5.29) are recovered through $n(x_i,t)=N_i(t)/\Omega$ and $p(x_i,t)=P_i(t)/\Omega$. We can also recover the stochastic partial differential equations (5.13)-(5.14) with the current and rate densities (5.15)-(5.17) from the Langevin stochastic equations (B.12)-(B.16) (see Appendix C).

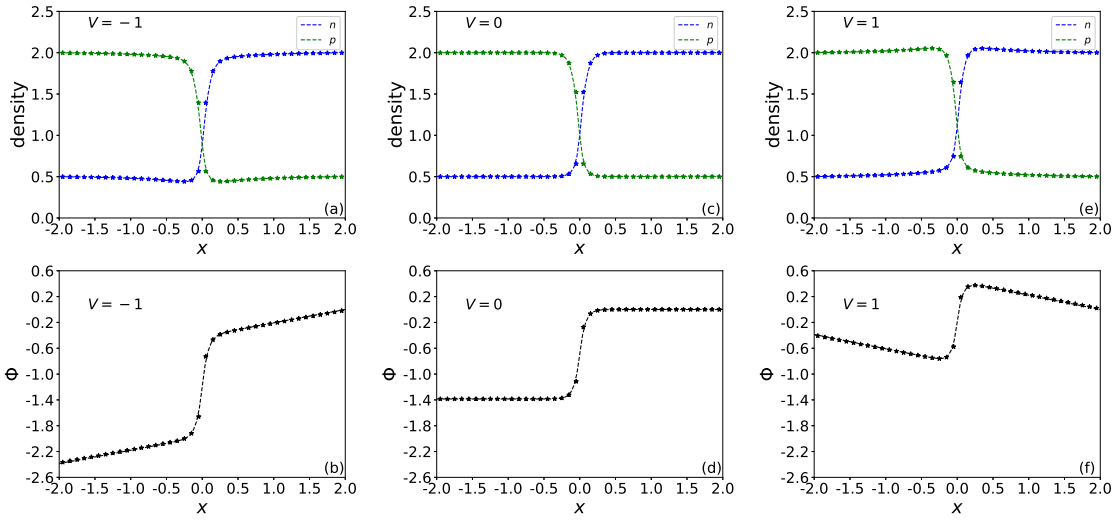

Figure 5.3: The junction for different values of the applied voltage V. Top panels (a), (c), (e): the profiles of the electron density n (blue dashed lines) and hole density p (green dashed lines). Bottom panels (b), (d), (f): the corresponding profiles of the mean electric potential. The lines depict the profiles obtained by solving the ODEs and the asterisks by simulating the stochastic process. The values of physical quantities and parameters listed in Table 5.1 and the Set I in Table 5.2 are used. The statistics in simulation is carried out over 4×10^5 iterates.

5.3 Density Profiles of Charge Carriers and Potential

Here, we study the effect of the different boundary conditions on the densities and electric potential across the p-n junction, in order to explore the properties of the junction. In the following, the results of the numerical simulations are compared with the solutions of the ODEs (5.32)-(5.37) giving the mean fields.

Figure 5.3 shows the profiles for different values of the applied voltage V. Now, the profiles are deformed by the nonequilibrium constraint of the applied voltage V. The slope of the electric potential gives the electric field by Eq. (5.37), which is nonvanishing under the nonequilibrium voltages $V = \pm 1$. In the panels (a) and (e) of Figure 5.3, the density profiles are also deformed in their approach towards uniform profiles away from the junction. As expected [90, 91], there is an excess of holes on the p-type side of the junction under a positive voltage with respect to the situation in equilibrium. Again, there is a good agreement between the results of the simulation and the mean-field profiles, which brings a strong support to the validity of the stochastic approach.

5.4 The Current and Counting Statistics

Here, we consider the fluctuations of the electric current in the middle of the junction at the location $x = 0$. This current is composed of electrons and holes moving in either directions and crossing the section area Σ at $x = 0$ for random times t_n. Accordingly, this instantaneous current can be defined as

$$\mathcal{I}(t) = \sum_{n=-\infty}^{+\infty} q_n \delta(t - t_n) \tag{5.51}$$

with $q_n = \pm e$ depending on whether the carrier is positive- or negative-charged and moves towards $x > 0$ or $x < 0$. We also define the instantaneous total electric current including the contribution

of displacement current as

$$\mathcal{I}'(t) = \mathcal{I}(t) - \epsilon \partial_t \partial_x \Phi \Sigma, \tag{5.52}$$

which are the experimentally measured electric currents [62, 102, 103, 104].

In the framework of the Langevin stochastic process (see Appendix B), the net charge current at the location $x = 0$ is approximately given by

$$\mathcal{I}(t) = e \int \mathrm{d}\boldsymbol{\Sigma} \cdot (\mathbf{j}_p - \mathbf{j}_n) \approx e \left(F_{L/2}^{(P)} - F_{L/2}^{(N)} \right), \tag{5.53}$$

in terms of the fluxes (B.14)-(B.15). The current that is experimentally measured is the total current, which includes the contribution from the displacement current. After spatial discretization and surface integration over the section area $\Sigma = \Omega/\Delta x$, this contribution becomes

$$\Sigma \epsilon \partial_t \mathcal{E}_{x,i} \approx -\frac{e\epsilon\Sigma}{\Delta x} \sum_{j=0}^{L} \left[\left(\mathbf{C}^{-1}\right)_{i+1,j+1} - \left(\mathbf{C}^{-1}\right)_{i+1,j} - \left(\mathbf{C}^{-1}\right)_{i,j+1} + \left(\mathbf{C}^{-1}\right)_{i,j} \right] \left(F_j^{(P)} - F_j^{(N)} \right), \tag{5.54}$$

where the matrix $\mathbf{C}$ is related to the discretized Poisson equation (5.40) with the explicit form given by Eq. (A.2), and

$$\left(\mathbf{C}^{-1}\right)_{i+1,j+1} - \left(\mathbf{C}^{-1}\right)_{i+1,j} - \left(\mathbf{C}^{-1}\right)_{i,j+1} + \left(\mathbf{C}^{-1}\right)_{i,j} = \frac{L\Delta x^2}{(L+1)\epsilon\Omega}\delta_{ij} - \frac{\Delta x^2}{(L+1)\epsilon\Omega}(1-\delta_{ij}). \tag{5.55}$$

Therefore, the discretized form of the total charge current is given by

$$\mathcal{I}'(t) = \int \mathrm{d}\boldsymbol{\Sigma} \cdot \left[e\left(\mathbf{j}_p - \mathbf{j}_n\right) + \epsilon \partial_t \boldsymbol{\mathcal{E}} \right] \approx \frac{e}{L+1} \sum_{j=0}^{L} \left(F_j^{(P)} - F_j^{(N)} \right), \tag{5.56}$$

which is independent of the location.

The corresponding random numbers of charges accumulated over the time interval $[0, t]$ are defined as

$$Z(t) = \frac{1}{e} \int_0^t \mathcal{I}(t')\mathrm{d}t', \tag{5.57}$$

$$Z'(t) = \frac{1}{e} \int_0^t \mathcal{I}'(t')\mathrm{d}t'. \tag{5.58}$$

Through numerous repeated measurements in simulation, we get the counting statistics of $Z(t)$, and thus $\mathcal{P}(Z, t)$ can be numerically constructed. Similarly, $\mathcal{P}(Z', t)$ can be numerically constructed from the counting statistics of $Z'(t)$. The mean charge current J is given by

$$J \equiv \lim_{t\to\infty} \frac{1}{t} \langle Z(t) \rangle = \lim_{t\to\infty} \frac{1}{t} \langle Z'(t) \rangle, \tag{5.59}$$

and the corresponding mean electric current by $I = |e|J$. The equality between the mean values without and with the displacement current comes from the fact that the displacement current are given by a time derivative. The time-dependent diffusivities are given as

$$\tilde{D}(t) \equiv \frac{1}{2t} \langle [Z(t) - Jt] [Z(t) - Jt] \rangle, \tag{5.60}$$

$$\tilde{D}'(t) \equiv \frac{1}{2t} \langle [Z'(t) - Jt] [Z'(t) - Jt] \rangle. \tag{5.61}$$

In the long-time limit, we obtain the asymptotic diffusivity,

$$D = \lim_{t\to\infty} \tilde{D}(t) = \lim_{t\to\infty} \tilde{D}'(t), \tag{5.62}$$

which also take the same value whether the displacement current is included or not.

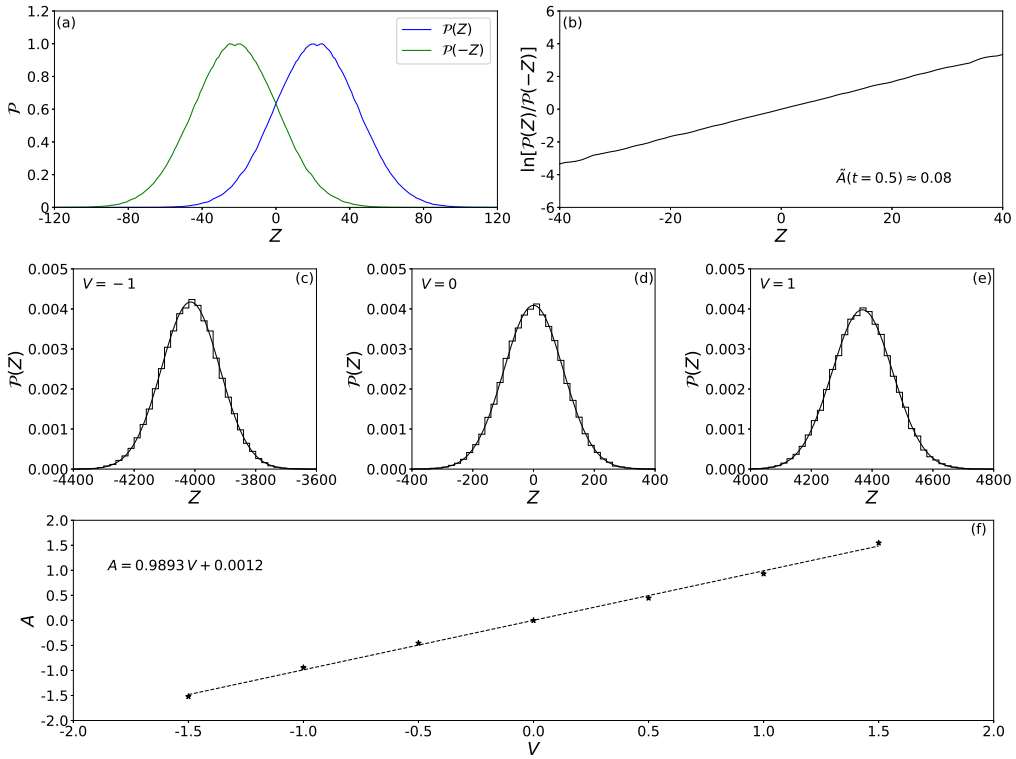

Figure 5.4: Full-counting statistics of the carrier electric current through the section area at the middle of the junction: (a) The probability distributions $\mathcal{P}(\pm Z)$ for time $t = 0.5$ versus the charge number Z with peak value normalized to one. The statistics is carried out over 10^6 random trajectories. (b) $\ln[\mathcal{P}(Z)/\mathcal{P}(-Z)]$ versus Z showing the linearity with the slope $\tilde{A}(t = 0.5) \approx 0.08$ for time $t = 0.5$. (c)-(d)-(e) Histograms $\mathcal{P}(Z)$ of the carrier charge distributions for relatively long time $t = 100$ and different values of the applied voltage (c) $V = -1$, (d) $V = 0$, and (e) $V = 1$. The histograms are obtained with 5×10^4 data and they are fitted to Gaussian distributions (2.47). (f) The affinities computed with these fitted Gaussian distributions according to Eq. (5.67) versus the applied voltage V, checking the linear dependence $A \simeq V$ with a unit slope up to numerical accuracy (dashed line) for relatively long time $t = 100$. The values of physical quantities and parameters listed in Table 5.1 and the Set I in Table 5.2 are used.

5.5 Fluctuation Theorem for the Current

By extending the method of Section 2.7, the current of such a Markov jump process obey a fluctuation theorem. For the current (5.51), the fluctuation theorem can be expressed as

$$\frac{\mathcal{P}(Z,t)}{\mathcal{P}(-Z,t)} \simeq_{t\to\infty} \exp(AZ), \tag{5.63}$$

in terms of the probability $\mathcal{P}(Z,t)$ that the number (5.57) of charges crossing the section area Σ during the time interval $[0, t]$. With the same analysis as in Section 4.3, the macroscopic affinity is given by

$$A = \ln\left[\frac{p_{\rm L}}{p_{\rm R}} e^{\beta e(\Phi_{\rm L}-\Phi_{\rm R})}\right] = \beta eV \tag{5.64}$$

in terms of the applied voltage, as expected. In equilibrium, $A = 0$, we recover the detailed balance condition, according to which the probabilities of opposite fluctuations are equal. If the logarithm

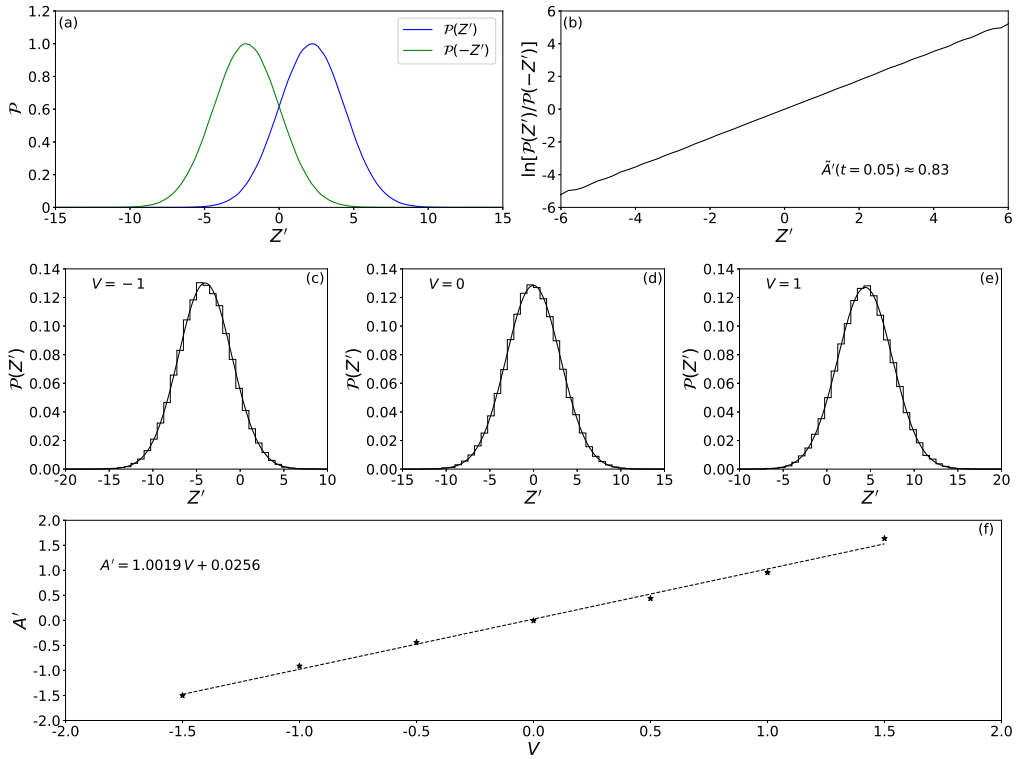

Figure 5.5: Full-counting statistics of the total electric current including the contribution of the displacement current: (a) The probability distributions $\mathcal{P}(\pm Z')$ for time $t = 0.05$ versus the charge number Z' with peak value normalized to one. The statistics is carried out over 10^6 random trajectories. (b) $\ln[\mathcal{P}(Z')/\mathcal{P}(-Z')]$ versus Z' showing the linearity with the slope $\tilde{A}'(t = 0.05) \approx 0.83$. (c)-(d)-(e) Histograms $\mathcal{P}(Z')$ of the total charge distributions for relatively long time $t = 0.1$ and different values of the applied voltage (c) $V = -1$, (d) $V = 0$, and (e) $V = 1$. The histograms are obtained with 5×10^4 data and they are fitted to Gaussian distributions (2.47). (f) The affinities computed with these fitted Gaussian distributions according to Eq. (5.67) versus the applied voltage V, checking the linear dependence $A' \simeq V$ with a unit slope up to numerical accuracy (dashed line) for relatively long time $t = 0.1$. The values of physical quantities and parameters listed in Table 5.1 and the Set I in Table 5.2 are used.

of the ratio of the probabilities $\mathcal{P}(\pm Z, t)$ is linear in the random variable Z, we may consider the time-dependent affinity

$$\tilde{A}(t) \equiv \frac{1}{Z} \ln \frac{\mathcal{P}(Z,t)}{\mathcal{P}(-Z,t)} \tag{5.65}$$

for the given time t. The prediction of the fluctuation theorem is that its asymptotic value should be equal to the macroscopic affinity given by the applied voltage,

$$\lim_{t\to\infty} \tilde{A}(t) = A = \beta e V. \tag{5.66}$$

In order to test numerically the prediction of the fluctuation theorem, we consider the full counting statistics of the random variable (5.57) as simulated by the Langevin stochastic differential equations (B.12)-(B.19). These quantities are shown in Figure 5.4(a)(b) for the short time $t = 0.5$. In this case, the probability distributions $\mathcal{P}(\pm Z, t)$ have a strong overlap so that the time-dependent

affinity (5.65) can be directly evaluated to be $\tilde{A}(t=0.5) \approx 0.08$, which is much smaller than the asymptotic value giving the macroscopic affinity $A = \tilde{A}(\infty) = \beta e V = 1$.

In order to reach the macroscopic affinity, the time interval is increased. However, the overlap between the probability distributions $\mathcal{P}(\pm Z, t)$ soon becomes very narrow as time increases if $V \neq 0$. Indeed, $\mathcal{P}(\pm Z, t)$ are distributed around their mean value $\pm\langle Z\rangle$, which increases linearly with time at a rate equal to the mean current. As seen in Figure 5.4(c) for time $t = 100$ and voltage $V = -1$, the distribution $\mathcal{P}(Z, t = 100)$ is centered around $\langle Z\rangle \approx -4017$ so that its overlap is tiny with the opposite distribution $\mathcal{P}(-Z, t = 100)$, which is centered around $\langle Z\rangle \approx +4017$. A similar feature holds for the distribution of Figure 5.4(e) at time $t = 100$ and voltage $V = 1$, which has the mean value $\langle Z\rangle \approx +4366$. Therefore, the method based on coarse-grained model is used here to evaluate the affinity in such circumstances. In the same way as in Section 4.5, the global transition rate W_+ is introduced for charge transfers from the left reservoir to the right reservoir in the long-time limit, and W_- for the reverse process. On the other hand, in Figure 5.4(c)(d)(e), we observe that the histograms $\mathcal{P}(Z, t = 100)$ for three different values of the applied voltage are very close to Gaussian distributions, from which we get the mean charge current J and the asymptotic diffusivity D according to Eqs (5.59) and (5.62). In Figure 5.4, the histograms $\mathcal{P}(Z, t = 100)$ are fitted to Gaussian distributions (2.47). The relations between the mean current J, diffusivity D, transition rates W_+ and W_- are given by using Eqs. (2.45)-(2.46) and the affinity is thus evaluated with

$$A = \ln \frac{W_+}{W_-} = \ln \frac{2D + J}{2D - J}, \tag{5.67}$$

for relatively long time $t = 100$ and different values of the applied voltage. The values of the numerically calculated affinity are plotted in Figure 5.4(f) as a function of the applied voltage V, showing agreement with the prediction (5.64) of the fluctuation theorem ($\beta = e = 1$ in the figure, see Table 5.1). Therefore, the time-dependent affinity converges to the macroscopic value (5.66), as predicted by the fluctuation theorem (5.63) for the carrier electric current.

The fluctuation theorem with the macroscopic affinity (5.64) also applies to the fluctuations of the random variable (5.58),

$$\frac{\mathcal{P}(Z', t)}{\mathcal{P}(-Z', t)} \simeq_{t\to\infty} \exp(AZ'), \tag{5.68}$$

by extension of the previously considered theorem [62, 31]. Figure 5.5(a)(b) shows the probability distributions $\mathcal{P}(\pm Z', t)$ for time $t = 0.05$, as well as the associated time-dependent affinity $\tilde{A}'(t)$ given in a similar way as Eq. (5.65). Remarkably, for this short time, this affinity is already close to the asymptotic value given by the macroscopic value (5.64). In Figure 5.5(c)(d)(e), the histograms are fitted to Gaussian distribution to compute the time-dependent affinity A' for relatively long time $t = 0.1$ and different values of the applied voltage. In Figure 5.5(f), the affinity is plotted versus the applied voltage, showing that they are equal up to numerical accuracy. Therefore, the fluctuation theorem (5.68) is confirmed by these results. Furthermore, the convergence to the macroscopic affinity is observed to be much faster for the measured total current fluctuations than for the carrier current fluctuations.

An implication of the fluctuation theorem is that the thermodynamic entropy production is always non-negative. Indeed, the entropy production rate can be expressed as [61]

$$\frac{1}{k_B}\frac{\mathrm{d_i}S}{\mathrm{d}t} = \lim_{t\to\infty} \frac{1}{2t} \int \mathrm{d}Z' \left[\mathcal{P}(Z', t) - \mathcal{P}(-Z', t)\right] \ln \frac{\mathcal{P}(Z', t)}{\mathcal{P}(-Z', t)} \geq 0 \tag{5.69}$$

in terms of the probability density $\mathcal{P}(Z', t)$ and this expression is always non-negative because $(p-q)\ln(p/q) \geq 0$ for any non-vanishing real numbers p and q. Using the fluctuation theorem (5.68), the expression (5.69) gives the dissipated power divided by the thermal energy,

$$\frac{1}{k_B}\frac{\mathrm{d_i}S}{\mathrm{d}t} = \lim_{t\to\infty} \frac{1}{t} A\langle Z'(t)\rangle = \frac{VI(V)}{k_B T} \geq 0, \tag{5.70}$$

as expected. Hence, the entropy production is non-negative in accord with the second law of thermodynamics.

Here, it is necessary to mention that the coarse-grained model would fail to evaluate the asymptotic affinity if the p-n junction diode is farther from equilibrium. That is, the fitted dashed lines in Figure 5.4(f) and Figure 5.5(f) would severely deviate from being with the expected slope if the the applied voltages V are too large. As we have already discussed in Chapter 4, the reason lies in the nonlinearity of the local transition rates (5.42)-(5.47) as well as those at the boundaries. In contrast with the situation for the conductive channels, the nonlinearity here not only arises from the long-range electrostatic interaction, but also from the stochastic process of electron-hole pair generation and recombination.

5.6 Current-Voltage Characteristics

In this section, we study the nonlinear response of the electric current to the applied voltage with the stochastic approach. The heterogeneous distributions of charge carriers induce the effect of current rectification in diodes. This rectifying effect is characterized by the nonlinear dependence of the mean electric current on the voltage. The basic theory of current-voltage characteristics of p-n junctions was established by Shockley [88, 89]. Based on the following four assumptions:

- The built-in potential and applied voltage are completely loaded in the small depletion layer[3], and outside this region the semiconductor is assumed to be neutral.
- The densities of charge carriers are scaled by Boltzmann factor[4].
- The injected minority carrier densities are small compared with the majority carrier densities.
- No generation-recombination current exists inside the depletion layer, and the electron and hole currents are constant throughout the depletion layer.

the ideal current-voltage characteristics can be described by so-called Shockley equation

$$I(V) = I_s \left[\exp\left(\frac{eV}{k_{\mathrm{B}}T} \right) - 1 \right]. \tag{5.71}$$

Here, the reverse-bias current I_s is called the saturation current, which is independent of the applied voltage. It is, however, quite dependent on temperature. The second assumption has already been assumed by Eq. (5.5).

We see in Figure 5.6(a) the current-voltage characteristics of the junction under the same conditions as in Figure 5.3. Under this condition, the ratio of majority to minority carrier concentration is $c_{\mathrm{major}}{:}c_{\mathrm{minor}} = 4$. As expected, the mean electric current increases more rapidly for a positive than a negative voltage. However, the rectification effect is moderate and the I-V curve differs from the Shockley equation (5.71) because the barrier of the electric potential at the junction is not sharp enough with respect to the voltage drop across the diode, as seen in the inset of Figure 5.6(a). If the current-voltage characteristics (5.71) was realized, the rectification ratio $\mathscr{R} = |I(V)/I(-V)|$ would be equal to $\mathscr{R}_{\mathrm{S}} = \exp(V)$. However, this ratio takes the value $\mathscr{R} \approx 1.5$ at $V = 4$, much lower than the expected value $\mathscr{R}_{\mathrm{S}} = 54.6$, which confirms that the Shockley model does not apply in the conditions of Figure 5.6(a).

In order to reach the Shockley regime, the concentration ratio of majority to minority carriers is increased up to the very large value $c_{\mathrm{major}}{:}c_{\mathrm{minor}} = 4 \times 10^6$, so that the potential step takes

[3] It is a small region around the junction, where there is a abrupt potential change and the mobile charge carriers are swept out in equilibrium. See Figure 5.2 for the region between pp' and nn'.

[4] The Fermi-Dirac distribution is approximated as an exponential function, that is

$$f(E) = \frac{1}{1 + \exp\left[\beta\left(E - E_{\mathrm{F}}\right)\right]} \approx \exp\left[\beta\left(E_{\mathrm{F}} - E\right)\right]$$

when E is larger than E_{F} by several orders of magnitude with respect to $1/\beta \equiv k_{\mathrm{B}}T$.

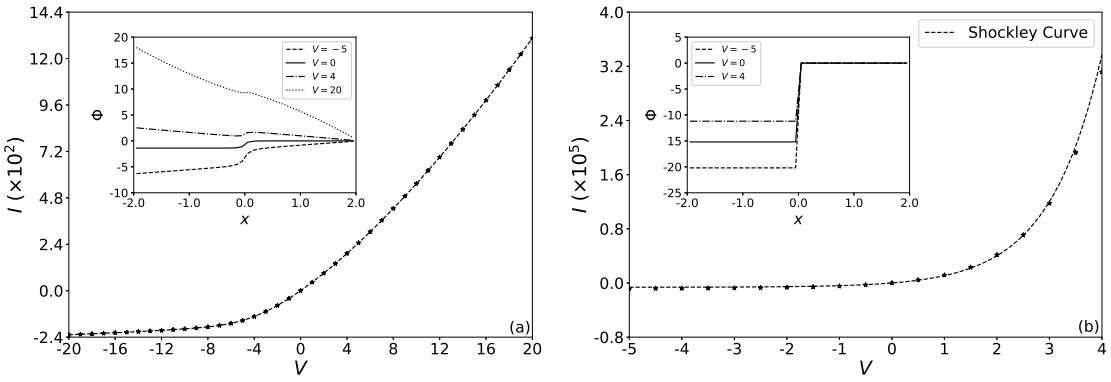

Figure 5.6: The current-voltage characteristic curves of the p-n junction. I denotes the mean electric current and V the applied voltage. The inset in each panel shows the electric potential profiles under several values of the applied voltage. The asterisks show the results of the stochastic simulation. In panel (a), the line is joining the data points. In panel (b), the line is the Shockley curve fitted to simulation data. The values of physical quantities listed in Table 5.1 are used for both panels. The two sets of parameter values listed in Table 5.2 are also used, with Set I for (a) and Set II for (b). The statistics is carried out over 4×10^5 iterates.

the value $(\Delta\Phi)_{\rm eq} = \ln(4 \times 10^6) \approx 15.2$ in equilibrium. The low-injection assumption is reasonably satisfied under this condition. Figure 5.6(b) shows that the I-V curve indeed follows the Shockley equation (5.71) in this case with the relatively small value $I_{\rm s} \approx 0.063\,(\times 10^5)$ of the saturation current at negative voltage. The step-like shape of potential profile along the p-n junction confirms the first assumption. The generation-recombination currents can be safely neglected in the depletion region with such a small width, as we see from the potential profile in Figure 5.6(b). The last assumption is thus also valid. The small number of charge carriers across the depletion region undergoes pure diffusion and recombine with the majority charge carriers.

The stochastic process of charge transfers between the two sides of the junction can be approximately described by the coarse-grained model, in which there are two associated global transition rates W_+ and W_-. In general, both of these rates have a complicated dependence on the applied voltage V. In the case there is a sharp potential barrier at the junction, and if the transition rate W_- to descend the barrier becomes independent of the voltage while the transition rate to climb the barrier can be expressed as $W_+ = W_- \exp(\beta e V)$ in terms of the Boltzmann factor $\exp(\beta e V)$, then the mean electric current is given by

$$I = e\,(W_+ - W_-) = eW_-\,[\exp(\beta e V) - 1]\,, \tag{5.72}$$

which is exactly the Shockley equation (5.71). Considering that the limitation of the coarse-grained model far from equilibrium has already been discussed, it seems that these two rates can not be understood in a stochastic way. However, the staircase potential profile in Figure 5.6(b) indicates that the p-n junction in the Shockley regime can be seen as two regions respectively in equilibrium. The coarse-grained model is supposed to work very well in this Shockley regime. However, the issue remains open whether W_+ and W_- behave as stated above under ideal p-n junction conditions. Actually it is difficult to extract the accurate values of these two rates from the counting statistics in numerical simulations, since the W_- is relatively too small compared with W_+. Nevertheless, the agreement between simulations and the predictions of the Shockley equation supports the validity of these assumptions if the concentration ratio of majority to minority carriers is large enough.

Chapter 6

Charge Transport in Bipolar n-p-n Junction Transistors

The proper combination of two p-n junctions produces a bipolar transistor, the main compounds of electronic devices[1]. Therefore, bipolar transistors have an unprecedented impact on the electronic industry in general and on solid-state research in particular. Inside a bipolar transistor, there are three types of semiconductors separated by two junctions. The middle semiconductor is doped with charged impurities different from those in the two other semiconductors. Unlike diodes, there are three terminals in a bipolar transistor and electric currents flow between pairs of them. The resistance between two terminals can thus be controlled by the third. This enables transistors to amplify electric signals [105, 106, 90, 107, 94, 93, 92, 95, 96].

The fundamental issue is that the coupling between the electric currents is ruled by microreversibility, as in any type of device or process. In linear regimes close to thermodynamic equilibrium, microreversibility implies the Onsager reciprocal relations. However, bipolar transistors are functioning in highly nonlinear regimes beyond the domain of application of the Onsager reciprocal relations. Remarkably, the generalizations of these relations beyond the linear regime are known (see Section 2.3). Moreover, the novel aspect is that two coupled currents are flowing in bipolar transistors, instead of only one in diodes that are studied in Chapter 5. This motivates us to numerically test all these relations with the electric currents in bipolar transistors.

In this chapter, the stochastic approach developed in Chapter 5 for the diodes is extended to the studies of charge transport in bipolar transistors. In this way, the fluctuation theorem is numerically shown to hold for the joint probability distribution of two electric currents. Similar results are obtained including the displacement currents. The Onsager reciprocal relations as well as their generalizations to nonlinear transport properties are numerically shown to be satisfied. In addition, signal-amplifying capability is numerically demonstrated for bipolar transistors under their working conditions.

6.1 Bipolar n-p-n Junction Transistors

Depending on the configuration, there are two types of bipolar junction transistors (BJT): the n-p-n transistors, in which a p-type semiconductor is sandwiched between two n-type semiconductors, and the p-n-p transistors, where an n-type semiconductor is confined between two p-type semiconductors. They are complementary devices. In the following, we only consider the case of bipolar n-p-n junction transistors that are widely used devices (see Figure 6.1). The electrons e^- and holes h^+ are the two mobile charge carriers across the bipolar n-p-n junction, with electrons being

[1]The first bipolar transistor was invented in 1947 by Brattain, Bardeen and Shockley at Bell Laboratories. The three of them received the Nobel prize in 1956 for their invention. Apart from bipolar transistors, there also exists two other basic types, namely, the metal-oxide-semiconductor field-effect transistors (MOSFET), and the junction field-effect transistors (JFET).

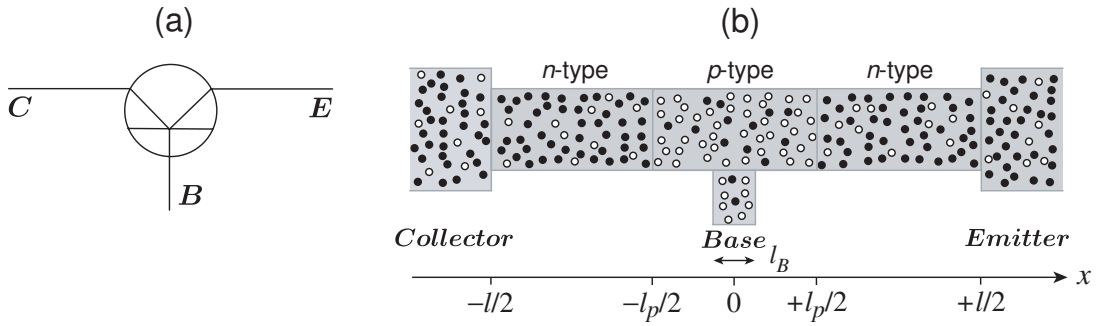

Figure 6.1: Schematic representation of (a) the transistor and (b) the bipolar n-p-n junction. In panel (b), the black (respectively, white) dots represent electrons (respectively, holes). The three reservoirs, called *Collector*, *Base*, and *Emitter*, fix the values of the electron density, the hole density, and the electric potentials at their contact with the transistor.

the majority ones in n-type semiconductor, and holes the majority ones in p-type semiconductor. The positive-charged donors and negative-charged acceptors are the impurities respectively doped in n-type and p-type semiconductors. Each doped region has a terminal and the three terminals are in contact with some charge carrier reservoir. They are respectively called *Collector*, *Base*, and *Emitter* (see Figure 6.1). To model the transistor, a Cartesian coordinate system is associated with the system. As shown in Figure 6.1(b), the semiconducting material extends from $x = -l/2$ to $x = +l/2$ and is divided in three parts. The part from $x = -l/2$ to $x = -l_p/2$ is of n-type, the one from $x = -l_p/2$ to $x = +l_p/2$ of p-type, and the one from $x = +l_p/2$ to $x = +l/2$ of n-type. The three parts are respectively of lengths $l_n = (l - l_p)/2$, l_p, and $l_n = (l - l_p)/2$. The *Collector* is in contact at $x = -l/2$, the *Emitter* at $x = +l/2$, and the *Base* along a length l_B symmetrically located around the origin $x = 0$. The length of the contact with the *Base* is smaller than the one of the p-type part: $l_B < l_p$. The geometry is chosen to be symmetric with respect to $x = 0$ for simplicity. In addition, the bipolar n-p-n junction has the section area Σ_x in the transverse y- and z-directions. The section areas of the contacts with the *Collector* and *Emitter* are assumed to be equal, $\Sigma_C = \Sigma_E = \Sigma_x$. Accordingly, the semiconducting material extends over a domain of volume $V = l\Sigma_x$. Moreover, we denote by $\Sigma_B = \Sigma_y$ the section area of the contact with the *Base*. The donor density $d(\mathbf{r})$ and acceptor density $a(\mathbf{r})$ are supposed to be uniform in the different types of semiconductor. Therefore, they can be expressed as

$$d(\mathbf{r}) = d\,\theta\,(-x - l_p/2) + d\,\theta\,(x - l_p/2)\,, \tag{6.1}$$

$$a(\mathbf{r}) = a\,\theta\,(x + l_p/2)\,\theta\,(-x + l_p/2)\,, \tag{6.2}$$

in terms of two constant values a and d, combined with Heaviside's step function $\theta(x)$ defined such that $\theta(x) = 1$ if $x > 0$ and $\theta(x) = 0$ otherwise. The charge density $\rho(\mathbf{r})$ is thus expressed as Eq. (5.2). Because of the electrostatic interaction between the charges, these densities are coupled to the electric potential $\Phi(\mathbf{r})$. Electrons and holes are generated and recombined by the reaction (5.3) with the electron-hole pair generation and recombination rate constants k_+ and k_-.

The electron and hole densities as well as the electric potential have fixed boundary values at the contacts with the three reservoirs. They are respectively given by n_C, p_C, Φ_C at the *Collector*; n_B, p_B, Φ_B at the *Base*; and n_E, p_E, Φ_E at the *Emitter*. The three parts of the transistor are supposed to be doped from a semiconducting material of uniform intrinsic density ν, so that the boundary values of the electron and hole densities should satisfy the conditions

$$n_C p_C = n_B p_B = n_E p_E = \nu^2. \tag{6.3}$$

For simplicity, we set $n_C = n_E$ and $p_C = p_E$ to have a system that is symmetric with respect to

$x = 0$, as depicted in Figure 6.1(b). Furthermore, we consider the boundary conditions

$$n_C = p_C + d, \qquad p_B = n_B + a, \qquad n_E = p_E + d. \tag{6.4}$$

If the transistor is in equilibrium without flow of charge carriers, detailed balance between the generation and recombination of electron-hole pairs requires that $n_{\rm eq} p_{\rm eq} = \nu^2$, where $\nu = \sqrt{k_+/k_-}$ is the so-called the intrinsic carrier density. Moreover, the Eq. (5.5) holds for the electron and hole densities in equilibrium. Thus, if the BJT is in equilibrium, the inhomogeneous distributions of the charge carriers produce the Nernst potentials

$$(\Phi_C - \Phi_E)_{\rm eq} = \frac{1}{\beta e} \ln \frac{n_C}{n_E} = \frac{1}{\beta e} \ln \frac{p_E}{p_C} \tag{6.5}$$

and

$$(\Phi_B - \Phi_E)_{\rm eq} = \frac{1}{\beta e} \ln \frac{n_B}{n_E} = \frac{1}{\beta e} \ln \frac{p_E}{p_B}. \tag{6.6}$$

The transistor is driven out of equilibrium by applying voltages with respect to the Nernst potentials

$$V_C = \Phi_C - \Phi_E - \frac{1}{\beta e} \ln \frac{n_C}{n_E}, \tag{6.7}$$

$$V_B = \Phi_B - \Phi_E - \frac{1}{\beta e} \ln \frac{n_B}{n_E}, \tag{6.8}$$

which induce currents across the BJT. When $V_B > 0$, the *Emitter-Base* junction is said to be forward biased, and when $V_B < 0$ it is reverse biased. Similarly, the *Collector-Base* junction is forward biased when $V_C - V_B < 0$, and reverse biased when $V_C - V_B > 0$. If no bias is applied to the terminals, i.e., $V_C = V_B = 0$, both junctions are in equilibrium and there is no electric current flow. A BJT with a forward biased *Emitter-Base* junction and a reverse biased *Collector-Base* junction is said to operate in the forward active mode[2].

Considering the electrostatic interaction, the diffusion, and the generation-recombination reaction, we have the following stochastic partial differential equations obeyed by carrier densities, current densities, and electric potential:

$$\mathbf{j}_n = -\mu_n e n \boldsymbol{\mathcal{E}} - D_n \boldsymbol{\nabla} n + \delta \mathbf{j}_n, \tag{6.9}$$

$$\mathbf{j}_p = +\mu_p e p \boldsymbol{\mathcal{E}} - D_p \boldsymbol{\nabla} p + \delta \mathbf{j}_p, \tag{6.10}$$

$$\partial_t n + \boldsymbol{\nabla} \cdot \mathbf{j}_n = k_+ - k_- np + \delta\sigma, \tag{6.11}$$

$$\partial_t p + \boldsymbol{\nabla} \cdot \mathbf{j}_p = k_+ - k_- np + \delta\sigma, \tag{6.12}$$

$$\nabla \cdot \boldsymbol{\mathcal{E}} = \frac{\rho}{\epsilon}, \tag{6.13}$$

$$\boldsymbol{\mathcal{E}} = -\boldsymbol{\nabla} \Phi, \tag{6.14}$$

where the mobilities μ_n and μ_p are related to the diffusion coefficients through Einstein's relations (5.12), while $\delta \mathbf{j}_n$, $\delta \mathbf{j}_p$, and $\delta\sigma$ are the Gaussian white noises characterized by Eqs. (5.20)-(5.29).

6.2 Numerical Simulation Method

For the numerical simulation of the BJT, the system is spatially discretized into cells, each containing some numbers of electrons and holes, respectively, and a Markov jump process in a accord with the stochastic partial differential equations (6.9)-(6.14) is associated to fully describe the stochastic evolution of electron and hole distributions.

[2]Several combinations of forward- and reverse-biased junctions are possible, leading to different operating modes. The transistors are therefore referred to as active devices whereas the diodes are passive.

Table 6.1: The values of parameters for specifying the discretized BJT.

Meaning	Set I	Set II
number of cells in each side region	10	10
number of cells in middle region	3	3
width of each cell Δx	0.1	0.1
height of each cell Δy	0.2	0.2
volume of each cell Ω	1000	10^9
section area $\Sigma_x = \Omega/\Delta x$	10000	10^{10}
section area $\Sigma_y = \Omega/\Delta y$	5000	5×10^9
number of electrons in *Collector* cell	10000	10^{13}
number of holes in *Collector* cell	100	10^5
number of electrons in *Base* cell	100	10^8
number of holes in *Base* cell	10000	10^{10}
number of electrons in *Emitter* cell	10000	10^{13}
number of holes in *Emitter* cell	100	10^5

6.2.1 Discretizing the Bipolar n-p-n Junction Transistor in Space

The BJT is spatially discretized into L cells of length $\Delta x = l/L$, section area Σ_x, and volume $\Omega = \Sigma_x \Delta x$, located at the coordinates $x_i = (i - 0.5)\Delta x - l/2$ $(i = 1, 2, \cdots, L)$. The indices $i = 0$ and $i = L + 1$ are respectively used to refer to the *Collector* and *Emitter* cells. Consistently with Figure 6.1(b), there are $L_n = l_n/\Delta x$ cells in both parts of n-type, $L_p = l_p/\Delta x$ cells for the part of p-type, and $L_B = l_B/\Delta x$ cells in contact with the *Base*. The numbers of electrons and holes in each cell of the BJT are related to the corresponding densities respectively by $N_i = n(x_i)\Omega$ and $P_i = p(x_i)\Omega$. At the contacts with the three reservoirs, the boundary conditions on the charge carrier densities determine the boundary values for the corresponding particle numbers:

$$\bar{N}_C = n_C\Omega, \qquad \bar{P}_C = p_C\Omega, \tag{6.15}$$

$$\bar{N}_B = n_B\Omega, \qquad \bar{P}_B = p_B\Omega, \tag{6.16}$$

$$\bar{N}_E = n_E\Omega, \qquad \bar{P}_E = p_E\Omega. \tag{6.17}$$

According to boundary conditions (6.4), the number of donors in each cell of the p-type semiconductor is given by $D = d\Omega = \bar{N}_C - \bar{P}_C = \bar{N}_E - \bar{P}_E$, and the number of acceptors in each cell of n-type semiconductor by $A = a\Omega = \bar{P}_B - \bar{N}_B$. The electron and hole numbers in the cells change every time a particle jumps between two neighboring cells, between a reservoir and the neighboring cell, or if a reactive event occurs generating or recombining an electron-hole pair. Moreover, the Poisson equation is also discretized along the chain of L cells forming the system, taking into account the electric potentials of the *Collector*, the *Base*, and the *Emitter*. The discretized Poisson equation reads

$$\frac{\Phi_{i+1} - 2\Phi_i + \Phi_{i-1}}{\Delta x^2} + \frac{\Phi_B - 2\Phi_i + \Phi_B}{\Delta y^2}\chi_{iB} = -\frac{e}{\epsilon\Omega}\left(P_i - N_i + D_i - A_i\right) \tag{6.18}$$

with the boundary conditions $\Phi_0 = \Phi_C$ and $\Phi_{L+1} = \Phi_E$ at the two ends of BJT, and the symbol $\chi_{iB} = 1$ if the ith cell is in contact with the *Base* and $\chi_{iB} = 0$ otherwise. This linear system should be solved after every electron or hole transition between cells. We suppose that the electric

potential Φ_B of the *Base* is set on both sides of the chain in the transverse y-direction, in order to get a symmetric geometry. In numerical simulations, same values of physical quantities as for p-n junction diodes in Chapter 5 are adopted here, and listed in Table 5.1. Two sets of parameter values for specifying the discretized BJT are listed in Table 6.1 for different purposes explained here below. Additionally, for convenience, we set the middle cell with index m to be the only one in contact with the *Base*, in which case the sum $\sum_{iB}$ in the subsequent master equation (6.19) has the sole term $i = m$. These parameter variables can be rescaled into dimensionless ones with the procedure presented in Appendix D.

6.2.2 Master Equation

The state of the discretized BJT is fully characterized by the electron numbers $\mathbf{N} = \{N_i\}_{i=1}^{L}$ and the hole numbers $\mathbf{P} = \{P_i\}_{i=1}^{L}$ in the cells and they evolve in time according to the network

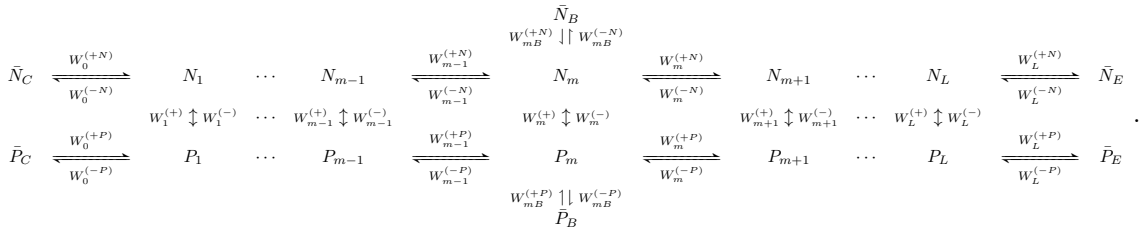

The probability $\mathcal{P}(\mathbf{N}, \mathbf{P}, t)$ to find the system in a certain state for the time t is governed by the master equation

$$\begin{aligned}
\frac{\mathrm{d}\mathcal{P}}{\mathrm{d}t} = &\sum_{i=0}^{L} \Big[\left(\mathrm{e}^{+\partial_{N_i}} \mathrm{e}^{-\partial_{N_{i+1}}} - 1\right) W_i^{(+N)} \mathcal{P} + \left(\mathrm{e}^{-\partial_{N_i}} \mathrm{e}^{+\partial_{N_{i+1}}} - 1\right) W_i^{(-N)} \mathcal{P} \\
&\quad + \left(\mathrm{e}^{+\partial_{P_i}} \mathrm{e}^{-\partial_{P_{i+1}}} - 1\right) W_i^{(+P)} \mathcal{P} + \left(\mathrm{e}^{-\partial_{P_i}} \mathrm{e}^{+\partial_{P_{i+1}}} - 1\right) W_i^{(-P)} \mathcal{P} \Big] \\
&+ \sum_{iB} \Big[\left(\mathrm{e}^{-\partial_{N_i}} - 1\right) W_{iB}^{(+N)} \mathcal{P} + \left(\mathrm{e}^{+\partial_{N_i}} - 1\right) W_{iB}^{(-N)} \mathcal{P} \\
&\quad + \left(\mathrm{e}^{-\partial_{P_i}} - 1\right) W_{iB}^{(+P)} \mathcal{P} + \left(\mathrm{e}^{+\partial_{P_i}} - 1\right) W_{iB}^{(-P)} \mathcal{P} \Big] \\
&+ \sum_{i=1}^{L} \Big[\left(\mathrm{e}^{-\partial_{N_i}} \mathrm{e}^{-\partial_{P_i}} - 1\right) W_i^{(+)} \mathcal{P} + \left(\mathrm{e}^{+\partial_{N_i}} \mathrm{e}^{+\partial_{P_i}} - 1\right) W_i^{(-)} \mathcal{P} \Big]
\end{aligned} \tag{6.19}$$

with the transition rates given by

$$W_i^{(+N)} = \frac{D_n}{\Delta x^2} \psi(\Delta U_{i,i+1}^{(N)}) N_i, \tag{6.20}$$

$$W_i^{(-N)} = \frac{D_n}{\Delta x^2} \psi(\Delta U_{i+1,i}^{(N)}) N_{i+1}, \tag{6.21}$$

$$W_i^{(+P)} = \frac{D_p}{\Delta x^2} \psi(\Delta U_{i,i+1}^{(P)}) P_i, \tag{6.22}$$

$$W_i^{(-P)} = \frac{D_p}{\Delta x^2} \psi(\Delta U_{i+1,i}^{(P)}) P_{i+1}, \tag{6.23}$$

$$W_i^{(+)} = \Omega k_+, \tag{6.24}$$

$$W_i^{(-)} = \Omega k_- \frac{N_i}{\Omega} \frac{P_i}{\Omega}. \tag{6.25}$$

The transition rates at the boundaries are given by

$$W_0^{(+N)} = \frac{D_n}{\Delta x^2}\psi(\Delta U_{0,1}^{(N)})\bar{N}_C, \tag{6.26}$$

$$W_0^{(-N)} = \frac{D_n}{\Delta x^2}\psi(\Delta U_{1,0}^{(N)})N_1, \tag{6.27}$$

$$W_L^{(+N)} = \frac{D_n}{\Delta x^2}\psi(\Delta U_{L,L+1}^{(N)})N_L, \tag{6.28}$$

$$W_L^{(-N)} = \frac{D_n}{\Delta x^2}\psi(\Delta U_{L+1,L}^{(N)})\bar{N}_E, \tag{6.29}$$

$$W_{iB}^{(+N)} = \frac{D_n}{\Delta y^2}\psi(\Delta U_{B,i}^{(N)})\bar{N}_B, \tag{6.30}$$

$$W_{iB}^{(-N)} = \frac{D_n}{\Delta y^2}\psi(\Delta U_{i,B}^{(N)})N_i, \tag{6.31}$$

for electrons, and similar expressions for holes. $\Delta U_{i,i+1}$ denotes the intrinsic energy change in the whole BJT associated with the transition of one particle from the ith cell to the $(i+1)$th cell, and $\Delta U_{B,i}$, $\Delta U_{i,B}$ the intrinsic energy changes in the whole BJT for the particle transitions between the ith cell and the *Base* cell. The detailed calculation is presented in Appendix A. The function $\psi(\Delta U)$ is defined by Eq. (4.24). At the ends of the chain, we have that $\exp(\pm\partial_X) = 1$ for $X = N_0$, P_0, N_{L+1}, and P_{L+1} in the master equation (6.19).

For numerical purpose, the approximated Langevin stochastic process is simulated instead of the Markovian stochastic process ruled by Eq. (6.19) (see Appendix B for the detailed procedure). In the continuum limit, the Markovian stochastic process leads to the stochastic reaction-diffusion equations (6.9)-(6.14), as shown in Appendix C for the p-n junction diodes.

6.3 The Currents and Counting Statistics

We consider the fluctuating electric currents flowing respectively across the contact with the *Collector* and the contact with the *Base*. These electric currents are due to the random motion of electrons and holes crossing the contact sections between the transistor and the corresponding reservoirs. The instantaneous electric currents are thus defined as

$$\mathcal{I}_C(t) = \sum_{n=-\infty}^{+\infty} q_n^{(C)}\delta\left(t - t_n^{(C)}\right), \tag{6.32}$$

$$\mathcal{I}_B(t) = \sum_{n=-\infty}^{+\infty} q_n^{(B)}\delta\left(t - t_n^{(B)}\right), \tag{6.33}$$

where $t_n^{(C)}$ (respectively $t_n^{(B)}$) are the random times of the crossing events and $q_n^{(C)}$ (respectively $q_n^{(B)}$) are the transferred charges equal to $\pm e$ depending on whether the carrier is an electron or a hole and if its motion is inward or outward the transistor. We also define the instantaneous total electric currents including the contribution of displacement currents as

$$\mathcal{I}'_C(t) = \mathcal{I}_C(t) - \epsilon\partial_t\partial_x\Phi\Sigma_C, \tag{6.34}$$

$$\mathcal{I}'_B(t) = \mathcal{I}_B(t) - \epsilon\partial_t\partial_y\Phi\Sigma_B. \tag{6.35}$$

In the framework of the Langevin stochastic process (see Appendix B), the net charge current at the contacts with the *Collector* and the *Base* are approximately given by

$$\mathcal{I}_C(t) = e\int \mathrm{d}\mathbf{\Sigma}_x\cdot(\mathbf{j}_p - \mathbf{j}_n) \approx e\left(F_0^{(P)} - F_0^{(N)}\right), \tag{6.36}$$

$$\mathcal{I}_B(t) = e\int \mathrm{d}\mathbf{\Sigma}_y\cdot(\mathbf{j}_p - \mathbf{j}_n) \approx e\sum_{iB}\left(F_{iB}^{(P)} - F_{iB}^{(N)}\right), \tag{6.37}$$

in terms of the fluxes (B.23)-(B.24) and (B.26)-(B.27). After spatial discretization and surface integration over the section areas, the contribution of the displacement currents can be added to get the total charge currents $\mathcal{I}'_C(t)$ and $\mathcal{I}'_B(t)$.

The corresponding random numbers of charges accumulated over the time interval $[0, t]$ are defined as

$$Z_C(t) = \frac{1}{e}\int_0^t \mathcal{I}_C(t')\mathrm{d}t', \tag{6.38}$$

$$Z_B(t) = \frac{1}{e}\int_0^t \mathcal{I}_B(t')\mathrm{d}t'. \tag{6.39}$$

For the total electric currents, the accumulated charge numbers $Z'_C(t)$ and $Z'_B(t)$ can also be defined similarly. Through numerous repeated measurements in simulation, we get the counting statistics of $Z_C(t)$, $Z_B(t)$, and thus $\mathcal{P}(Z_C, Z_B, t)$ can be numerically constructed. Similarly, $\mathcal{P}(Z'_C, Z'_B, t)$ can be numerically constructed from the counting statistics of $Z'_C(t)$ and $Z'_B(t)$. The mean charge currents are given by

$$J_C \equiv \lim_{t\to\infty}\frac{1}{t}\langle Z_C(t)\rangle = \lim_{t\to\infty}\frac{1}{t}\langle Z'_C(t)\rangle, \tag{6.40}$$

$$J_B \equiv \lim_{t\to\infty}\frac{1}{t}\langle Z_B(t)\rangle = \lim_{t\to\infty}\frac{1}{t}\langle Z'_B(t)\rangle, \tag{6.41}$$

and the corresponding mean electric currents by $I_C = |e|J_C$ and $I_B = |e|J_B$. The diffusivities of the currents are defined as

$$D_{CC} \equiv \lim_{t\to\infty}\frac{1}{2t}\mathrm{var}_{Z_C Z_C}(t) = \lim_{t\to\infty}\frac{1}{2t}\mathrm{var}_{Z'_C Z'_C}(t), \tag{6.42}$$

$$D_{BB} \equiv \lim_{t\to\infty}\frac{1}{2t}\mathrm{var}_{Z_B Z_B}(t) = \lim_{t\to\infty}\frac{1}{2t}\mathrm{var}_{Z'_B Z'_B}(t), \tag{6.43}$$

$$D_{CB} \equiv \lim_{t\to\infty}\frac{1}{2t}\mathrm{cov}_{Z_C Z_B}(t) = \lim_{t\to\infty}\frac{1}{2t}\mathrm{cov}_{Z'_C Z'_B}(t) \tag{6.44}$$

in terms of the variances and the covariances between the accumulated random charge numbers

$$\mathrm{var}_{Z_C Z_C}(t) \equiv \langle Z_C(t)Z_C(t)\rangle - \langle Z_C(t)\rangle^2, \tag{6.45}$$

$$\mathrm{var}_{Z_B Z_B}(t) \equiv \langle Z_B(t)Z_B(t)\rangle - \langle Z_B(t)\rangle^2, \tag{6.46}$$

$$\mathrm{cov}_{Z_C Z_B}(t) \equiv \langle Z_C(t)Z_B(t)\rangle - \langle Z_C(t)\rangle\langle Z_B(t)\rangle = \mathrm{cov}_{Z_B Z_C}(t). \tag{6.47}$$

6.4 Fluctuation Theorem for Currents

We suppose that the voltages (6.7) and (6.8) are applied at the boundaries of the transistor. Consequently, the transistor is driven out of equilibrium and the stochastic process of charge transfers between the reservoirs eventually reaches a nonequilibrium steady state. This latter is expected to depend on the applied voltages, or equivalently on the affinities,

$$A_C = \ln\left[\frac{\bar{P}_C}{\bar{P}_E}\mathrm{e}^{\beta e(\Phi_C-\Phi_E)}\right] = \ln\left[\frac{\bar{N}_E}{\bar{N}_C}\mathrm{e}^{\beta e(\Phi_C-\Phi_E)}\right] = \beta e V_C, \tag{6.48}$$

$$A_B = \ln\left[\frac{\bar{P}_B}{\bar{P}_E}\mathrm{e}^{\beta e(\Phi_B-\Phi_E)}\right] = \ln\left[\frac{\bar{N}_E}{\bar{N}_B}\mathrm{e}^{\beta e(\Phi_B-\Phi_E)}\right] = \beta e V_B, \tag{6.49}$$

which are determined by the differences of electrochemical potentials between the corresponding reservoirs. Here, the *Emitter* is taken as the reference reservoir. The dependences of the mean values of the currents on the affinities define the characteristic functions of the transistor: $J_C(A_C, A_B)$ and $J_B(A_C, A_B)$. In equilibrium, the affinities are vanishing together with the applied voltages

and the mean values of the currents, so that $J_C(0,0) = J_B(0,0) = 0$. However, the diffusivities do not necessarily vanish in equilibrium.

Beyond the mean values of the currents and the diffusivities, the process can be characterized by higher cumulants or the full probability distribution $\mathcal{P}(Z_C, Z_B, t)$ that $Z_C(t)$ and $Z_B(t)$ charges are crossing the *Collector* and the *Base* during the time interval $[0, t]$, while the transistor is in a nonequilibrium steady state of affinities A_C and A_B. This steady state is given by the stationary solution of the master equation of the Markov jump process. Using the network representation of this Markov jump process and its decomposition into cyclic paths [78] combined with the method of Section 2.7, the process can be shown to obey a fluctuation theorem for all the currents as a consequence of local detailed balance [31, 62]. This theorem states that the joint probability distribution of random variables Z_C and Z_B at time t satisfies the following fluctuation relation,

$$\frac{\mathcal{P}(Z_C, Z_B, t)}{\mathcal{P}(-Z_C, -Z_B, t)} \simeq_{t\to\infty} \exp\left(A_C Z_C + A_B Z_B\right). \tag{6.50}$$

A similar fluctuation relation holds if the displacement currents are included in the accumulated charge numbers [62].

As a consequence of the fluctuation theorem, the thermodynamic entropy production is always non-negative in accord with the second law of thermodynamics. The entropy production can indeed be expressed as the Kullback-Leibler divergence between the probability distributions of opposite fluctuations of the currents [61], giving the dissipated power divided by the thermal energy,

$$\frac{1}{k_{\rm B}} \frac{{\rm d}_{\rm i} S}{{\rm d}t} = A_C J_C + A_B J_B = \beta \left(V_C I_C + V_B I_B\right) \geq 0, \tag{6.51}$$

as expected.

We notice that the fluctuation relation (6.50) holds in the long-time limit. The time-dependent affinities converge towards their asymptotic values (6.48) and (6.49). While the time-dependent affinities $\tilde{A}_C(t)$ and $\tilde{A}_B(t)$ can be defined such that

$$\frac{\mathcal{P}(Z_C, Z_B, t)}{\mathcal{P}(-Z_C, -Z_B, t)} = \exp\left[\tilde{A}_C(t) Z_C + \tilde{A}_B(t) Z_B\right]. \tag{6.52}$$

Similarly, the time-dependent affinities $\tilde{A}'_C(t)$ and $\tilde{A}'_B(t)$ can also be defined when the accumulated charge numbers $Z'_C(t)$ and $Z'_B(t)$ are used instead. The convergence time is determined by diffusion [108] and it can be estimated to range between the time of diffusion across the middle part, $t_{\rm diff} \sim l_p^2/D \sim 9$, and the one before recombination, $t_{\rm diff} \sim \ell^2/D \sim 100$.

The direct test of the fluctuation relation (6.50) requires the availability of an overlap between the probability distributions $\mathcal{P}(Z_C, Z_B, t)$ and $\mathcal{P}(-Z_C, -Z_B, t)$. Since the maxima of these distributions move apart under nonequilibrium conditions, the overlap rapidly decreases as time increases. Therefore, the direct test of the fluctuation relation is restricted to short times. Nevertheless, the test is possible as shown in Figure 6.2 for the joint probability distributions of the accumulated charge numbers without and with the displacement currents. For the bare charge numbers, Figure 6.2(a) depicts the joint distribution itself at time $t = 20$, which is roughly Gaussian and shifted with respect to the origin because of the elapsed time. There is a significant overlap with the opposite distribution $\mathcal{P}(-Z_C, -Z_B, t)$ and Figure 6.2(b) shows several contours of the two-dimensional function $\ln\left[\mathcal{P}(Z_C, Z_B, t)/\mathcal{P}(-Z_C, -Z_B, t)\right]$ in the plane of the variables Z_C and Z_B. These contours appear straight given the presence of statistical errors, in agreement with the prediction of the fluctuation theorem that the function should be linear. The function $\ln\left[\mathcal{P}(Z_C, Z_B, t)/\mathcal{P}(-Z_C, -Z_B, t)\right]$ can thus be fitted to a linear function $\tilde{A}_C(t) Z_C + \tilde{A}_B(t) Z_B$, defining the finite-time affinities $\tilde{A}_C(t)$ and $\tilde{A}_B(t)$. However, their values remain smaller than the applied affinities $A_C = A_B = 0.1$ because convergence is expected for $t \gg t_{\rm diff}$ and has not yet been reached in Figure 6.2.

As shown in Figure 6.2(c)(d), we have similar results for the joint probability distribution $\mathcal{P}(Z'_C, Z'_B, t)$ of the charge numbers with the displacement currents. As seen in Figure 6.2(c),

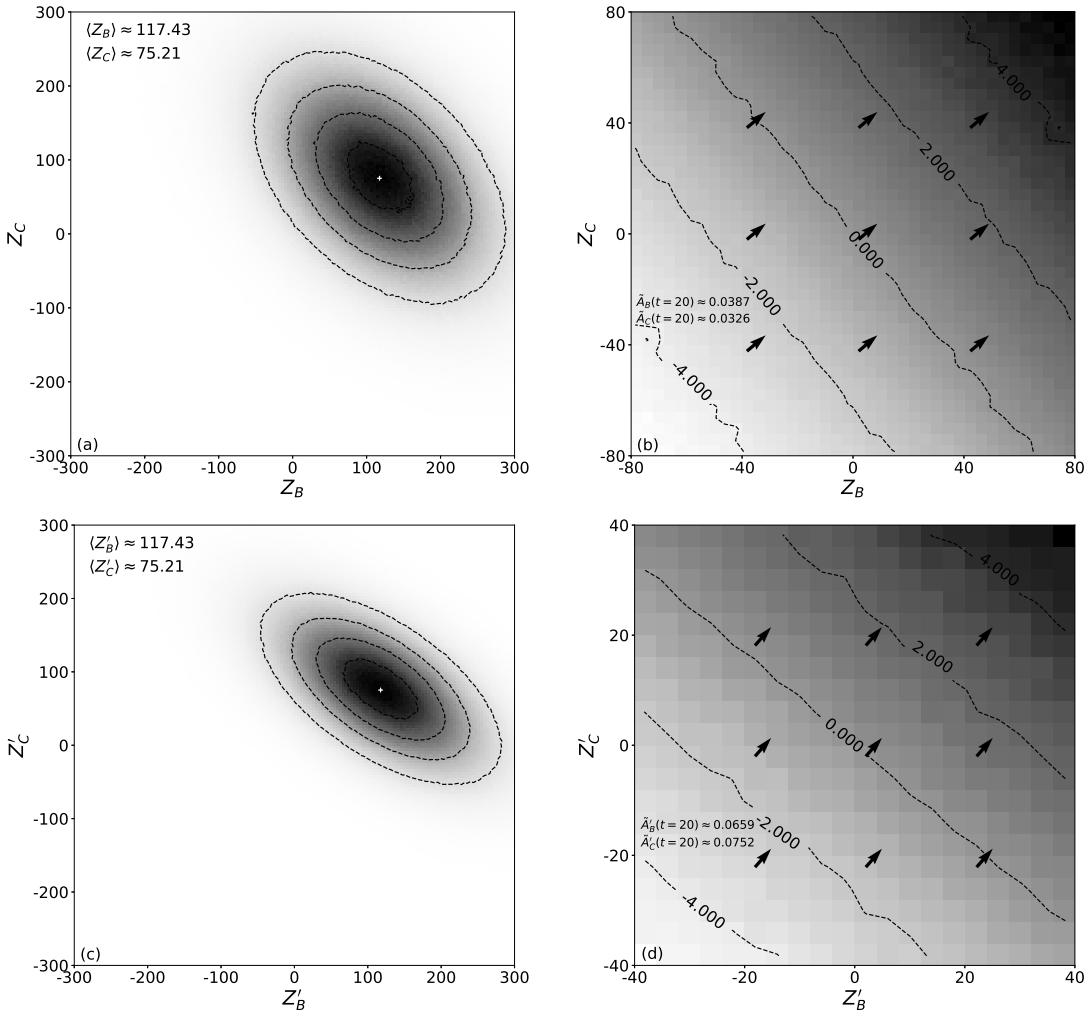

Figure 6.2: (a) Joint probability distribution $\mathcal{P}(Z_C, Z_B, t)$ of the transferred charges Z_C and Z_B at time $t = 20$. The center of this distribution marked with the symbol "+" corresponds to the mean values $\langle Z_B \rangle \approx 117.43$ and $\langle Z_C \rangle \approx 75.21$. Several contours of the distribution are also plotted. (b) The function $\ln[\mathcal{P}(Z_C, Z_B, t)/\mathcal{P}(-Z_C, -Z_B, t)]$ versus Z_C and Z_B at the same time $t = 20$. Several contours are shown. The arrows indicate the gradient of the distribution. The time-dependent affinities take the values $\tilde{A}_B(t = 20) \approx 0.0387$ and $\tilde{A}_C(t = 20) \approx 0.0326$. (c) Joint probability distribution $\mathcal{P}(Z'_C, Z'_B, t)$ of the transferred total charges Z'_C and Z'_B including the displacement currents, at the same time $t = 20$. This distribution is centered on the same mean values $\langle Z'_B \rangle \approx 117.43$ and $\langle Z'_C \rangle \approx 75.21$. (d) The corresponding function $\ln[\mathcal{P}(Z'_C, Z'_B, t)/\mathcal{P}(-Z'_C, -Z'_B, t)]$ versus Z'_C and Z'_B at the same time $t = 20$, giving the time-dependent affinities $\tilde{A}'_B(t = 20) \approx 0.0659$ and $\tilde{A}'_C(t = 20) \approx 0.0752$. For both cases, the affinities are set in the simulation to the value $A_C = A_B = 0.1$. The simulation is carried out with the time step $\mathrm{d}t = 0.1$ and the statistics over 3×10^7 trajectories. The pixels in the four panels are all of size 4×4. The values of physical quantities and parameters listed in Table 5.1 and the Set I in Table 6.1 are used.

the displacement currents have for effect that the distribution $\mathcal{P}(Z'_C, Z'_B, t)$ is narrower than $\mathcal{P}(Z_C, Z_B, t)$ depicted in Figure 6.2(a). Consequently, the time-dependent affinities $\tilde{A}'_C(t)$ and $\tilde{A}'_B(t)$ are larger than $\tilde{A}_C(t)$ and $\tilde{A}_B(t)$ and the convergence in time towards the asymptotic values of the affinities should be faster for the statistics of the transferred total charges Z'_C and Z'_B including the displacement currents, than for the statistics of the transferred charges Z_C and Z_B.

In order to test the convergence of the time-dependent affinities towards their asymptotic values over longer time scales, the method developed in Section 3.1 is used here. In this method, we have the coarse-grained model

$$Collector \underset{W_{EC}}{\overset{W_{CE}}{\rightleftharpoons}} Emitter, \tag{6.53}$$

$$Base \underset{W_{EB}}{\overset{W_{BE}}{\rightleftharpoons}} Emitter, \tag{6.54}$$

$$Collector \underset{W_{BC}}{\overset{W_{CB}}{\rightleftharpoons}} Base, \tag{6.55}$$

where the charges are supposed to be transferred directly between the three reservoirs in the long-time limit with the global transition rates $\{W_{kl}\}_{k,l=C,B,E}$. Similar to Eqs. (3.111)-(3.116), we have the following set of six nonlinear equations for the global transition rates:

$$W_{CE} - W_{EC} + W_{CB} - W_{BC} = J_C, \tag{6.56}$$

$$W_{BE} - W_{EB} + W_{BC} - W_{CB} = J_B, \tag{6.57}$$

$$W_{CE} + W_{EC} + W_{CB} + W_{BC} = 2D_{CC}, \tag{6.58}$$

$$W_{BE} + W_{EB} + W_{BC} + W_{CB} = 2D_{BB}, \tag{6.59}$$

$$W_{CB} + W_{BC} = -2D_{CB}, \tag{6.60}$$

$$W_{CB}W_{BE}W_{EC} = W_{BC}W_{EB}W_{CE}, \tag{6.61}$$

where J_C, J_B, D_{CC}, D_{BB}, and D_{CB} are the mean currents and diffusivities whose values can be evaluated from counting statistics according to Eqs. (6.40)-(6.44). The values of the rates $\{W_{kl}\}_{k,l=C,B,E}$ are determined from solving the nonlinear equations (6.56)-(6.61) with the Newton-Raphson method (see Appendix E). Thereafter, the affinities are readily evaluated by

$$A_C \equiv A_{CE} = \ln \frac{W_{CE}}{W_{EC}}, \tag{6.62}$$

$$A_B \equiv A_{BE} = \ln \frac{W_{BE}}{W_{EB}}. \tag{6.63}$$

Figure 6.3 shows the comparison between the numerical affinities given by Eqs. (6.62)-(6.63) and the theoretical predictions given by Eqs. (6.48)-(6.49) for several cases. Accurate agreement is found if the affinities remain moderate, confirming the convergence of the time-dependent affinities $\tilde{A}_C(t)$ and $\tilde{A}_B(t)$ towards their expected asymptotic values within the domain of validity of the model (6.53)-(6.55). Subsection 3.1.5 gives an exact proof of the agreement between numerical affinities and the theoretical predictions if the system is near equilibrium. It is also notable in Figure 6.3 that for case (8) there exists obvious deviation beyond errors between the numerical affinities and the theoretical expectations. The reason lies in the nonlinearity of the rates (6.20)-(6.25) as well as those at the boundaries.

Despite the limited scope of application of this method, the agreement between the numerical and theoretical values of the affinities brings further numerical support to the fluctuation relation for the currents.

6.5 Response Properties

In this section, we focus on the numerical test of the fluctuation-dissipation relations (2.16), the Onsager reciprocal relations (2.17) as well as their generalizations (2.18). The methods given in

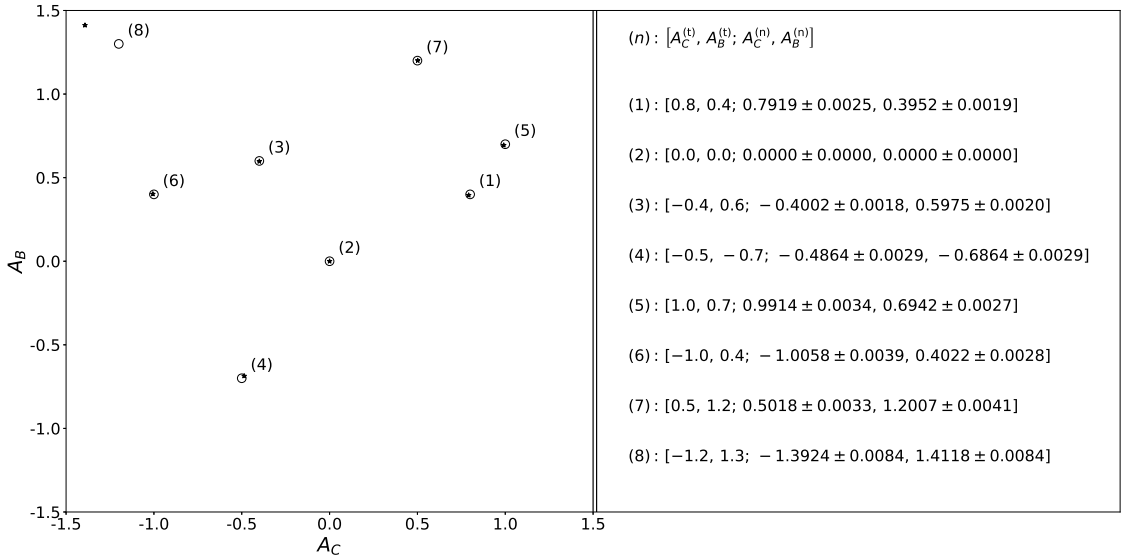

Figure 6.3: The comparison between the numerical affinities $A_C^{(\mathrm{n})}$, $A_B^{(\mathrm{n})}$ given by Eqs (6.62)-(6.63) (marked with asterisks) and the theoretical expectations $A_C^{(\mathrm{t})}$, $A_B^{(\mathrm{t})}$ given by Eqs. (6.48)-(6.49) (marked with circles). The values of both kinds of affinities as well as their errors are listed on the right part of the figure. The statistic data used to evaluate numerical affinities are obtained by simulation with the time step $\mathrm{d}t = 0.05$, the total time $t = 2.5 \times 10^3$, and 5×10^5 iterates for every case. The values of physical quantities and parameters listed in Table 5.1 and the Set I in Table 6.1 are used. The numerical method for estimating the error can be found in Appendix E.

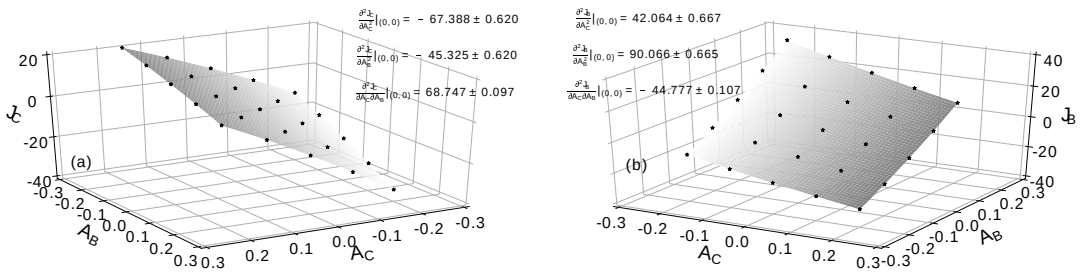

Figure 6.4: The mean charge currents as a function of the affinities A_B and A_C: (a) The current J_C from the *Collector* to BJT; (b) The current J_B from the *Base* to BJT. The asterisks are the numerical data points from the simulation. The surfaces are obtained from Lagrange interpolation using the data points. Furthermore, the data points are used to get the second derivatives $\partial^2 J_i/\partial A_j \partial A_k|_{(0,0)}$ around the equilibrium point $(A_C = 0, A_B = 0)$, as explained in Appendix E. The numerical values of these second derivatives are labeled and also listed in Table 6.3. The simulations are carried out with the time step $\mathrm{d}t = 0.05$ and 10^9 iterates for every data point. The values of physical quantities and parameters listed in Table 5.1 and the Set I in Table 6.1 are used. The numerical method for estimating the error can be found in Appendix E.

Appendix E for the numerical evaluation of derivatives and their error analysis are used.

The evaluation of the linear response coefficients relies on the determination of the mean charge currents as a function of the affinities. To achieve this evaluation, we have computed the mean charge currents for several values of the affinities, as shown in Figure 6.4. We have used the Lagrange interpolation method (see Appendix E) to obtain one-variable polynomials approximating $J_C(A_C, A_B = 0)$, $J_C(A_C = 0, A_B)$, $J_B(A_C, A_B = 0)$, and $J_B(A_C = 0, A_B)$ based on the numerical data plotted in Figure 6.5(a)(c)(e). Subsequently, the linear response coefficients can be computed by taking the first partial derivatives of the Lagrange polynomials at the equilibrium point ($A_C = 0, A_B = 0$). Their numerical values are listed in the first column of Table 6.2. The observation that the two dashed lines in Figure 6.5(e) are tangent with each other at the equilibrium point ($A_C = A_B = 0$) already confirms the Onsager reciprocal relations (2.17), which can be also checked from the values of $L_{C,B}$ and $L_{B,C}$ within the numerical accuracy.

Furthermore, the equilibrium values of the diffusivities are computed from the linear regression of several points of the quantities $0.5 \times \mathrm{var}_{Z_C Z_C}(t)$, $0.5 \times \mathrm{var}_{Z_B Z_B}(t)$, and $0.5 \times \mathrm{cov}_{Z_C Z_B}(t)$ versus t, as shown in Figure 6.5(b)(d)(f)[3]. The values of diffusivities are identified as the slopes of the resulting lines, and given in the second column of Table 6.2. The differences between the linear response coefficients and the diffusivities are reported in the third column of Table 6.2, showing that the fluctuation-dissipation relations (2.16) are also satisfied within the numerical accuracy.

Next, the numerical values of the charge currents J_C and J_B are computed for different values of the affinities A_C and A_B in order to construct the two-variable functions $J_C(A_C, A_B)$ and $J_B(A_C, A_B)$ using two-dimensional Lagrange interpolations, as shown in Figure 6.4. The values of second derivatives at the equilibrium point ($A_C = A_B = 0$),

$$M_{i,jk} \equiv \left.\frac{\partial^2 J_i}{\partial A_j \partial A_k}\right|_{(0,0)} \qquad \text{for} \qquad i,j,k = C,B, \tag{6.64}$$

are thus numerically evaluated using the numerical method explained in Appendix E. On the other hand, the diffusivities D_{ij} are again computed with the same method as illustrated in Figure 6.5(b)(d)(f), but for the transistor driven away from equilibrium. They are plotted in Figure 6.6 as functions of the affinities. Therefore, the derivatives of the diffusivities with respect to the affinities

$$R_{ij,k} \equiv \left.\frac{\partial D_{ij}}{\partial A_k}\right|_{(0,0)} \qquad \text{for} \qquad i,j,k = C,B \tag{6.65}$$

can also be evaluated numerically at the equilibrium point ($A_C = A_B = 0$). The results for the quantities $M_{i,jk}$ and $R_{ij,k}$ are given in Table 6.3 where we calculate the differences, $M_{i,jk} - R_{ij,k} - R_{ik,j}$, testing the validity of the prediction (2.18) of the fluctuation theorem beyond the linear transport properties. We see that these differences are smaller than the numerical errors in agreement with the predictions.

6.6 Current-Voltage Characteristics

The purpose of this section is to show that the properties characterizing the functionality of transistors can be described within the stochastic approach. In electronic technology, transistors are primarily used to amplify signals in electric circuits. This amplification results from the coupling between the two electric currents, I_C and I_B. By this coupling, one current can serve as input and the other as output. The basic transistor action is the control of electric current at one terminal by voltage applied across two other terminals. This is called the transistor effect. The amplification factor is defined as the electric current at the *Collector* divided by that at the *Base*, I_C/I_B, which is simply called the electric current gain. We may also introduce the differential amplification factor

[3] The reason that the values of diffusivities are computed from linear regression instead of directly from Eqs. (6.42)-(6.44) is to increase the accuracy.

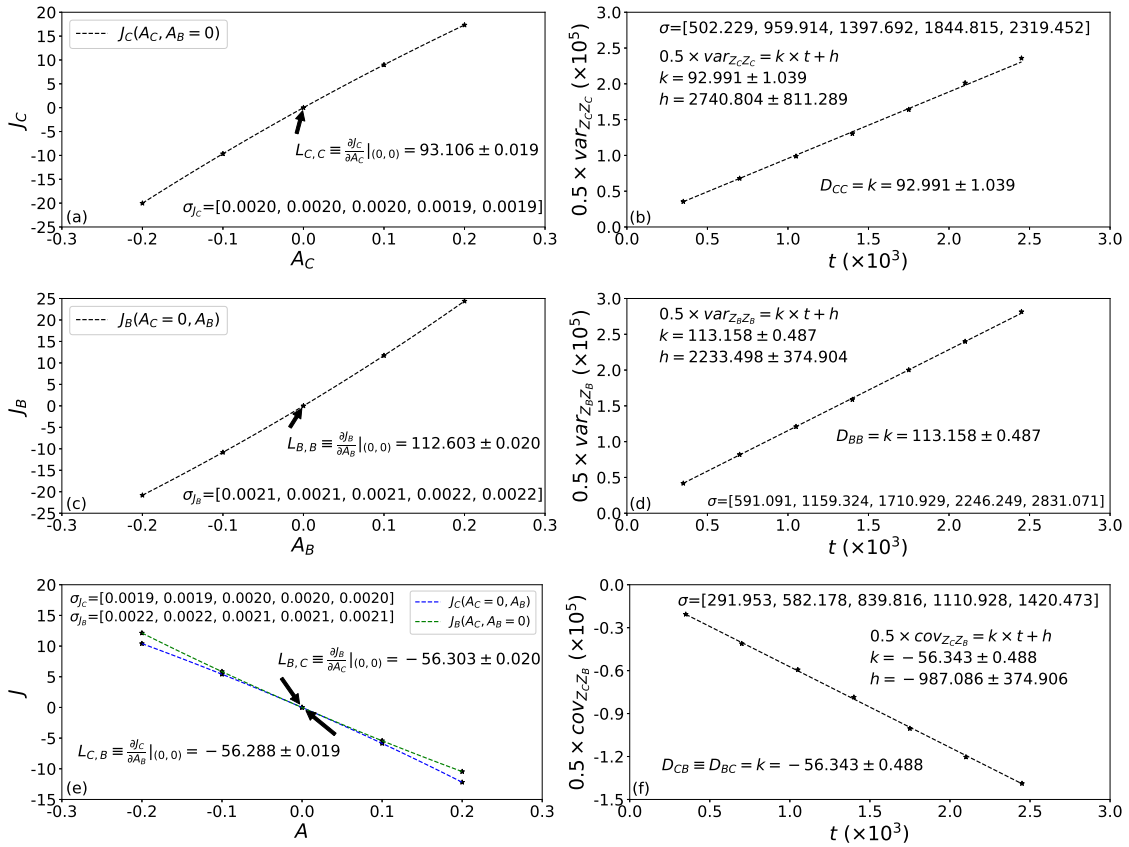

Figure 6.5: Panels (a)(c)(e): the mean charge current as a function of one affinity with another affinity being zero. The asterisks are numerical points from the simulation. The dashed lines show the Lagrange polynomials interpolating numerical points. The first partial derivatives around equilibrium point ($A_C = A_B = 0$) can be estimated from the Lagrange polynomials, with the approximate values labeled. Panels (b)(d)(f): the quantities $0.5 \times var_{Z_C Z_C}$, $0.5 \times var_{Z_B Z_B}$, $0.5 \times cov_{Z_C Z_B}$ respectively as a function of the time t used to compute them. Here, $var_{Z_C Z_C}$, $var_{Z_B Z_B}$, $cov_{Z_C Z_B}$ are respectively defined by Eqs. (6.45)-(6.47). The asterisks are the numerical points, from which dashed lines are obtained by linear regression. The resulting linear functions as well as the values and errors of coefficients are labeled. The values of diffusivities are identified as the slopes. The values of σ in all panels denote the errors of numerical points. The values of physical quantities and parameters listed in Table 5.1 and the Set I in Table 6.1 are used. The numerical method for estimating the error can be found in Appendix E.

Table 6.2: The numerical values of the quantities used for testing the fluctuation-dissipation relations (2.16) and the Onsager reciprocal relations (2.17).

(i,j)	$L_{i,j}$	$D_{ij}(\mathbf{A}=\mathbf{0})$	$L_{i,j} - D_{ij}(\mathbf{A}=\mathbf{0})$
(C,C)	93.106 ± 0.019	92.991 ± 1.039	0.115
(C,B)	-56.288 ± 0.019	-56.343 ± 0.488	0.055
(B,C)	-56.303 ± 0.020	-56.343 ± 0.488	0.040
(B,B)	112.603 ± 0.020	113.158 ± 0.487	-0.555

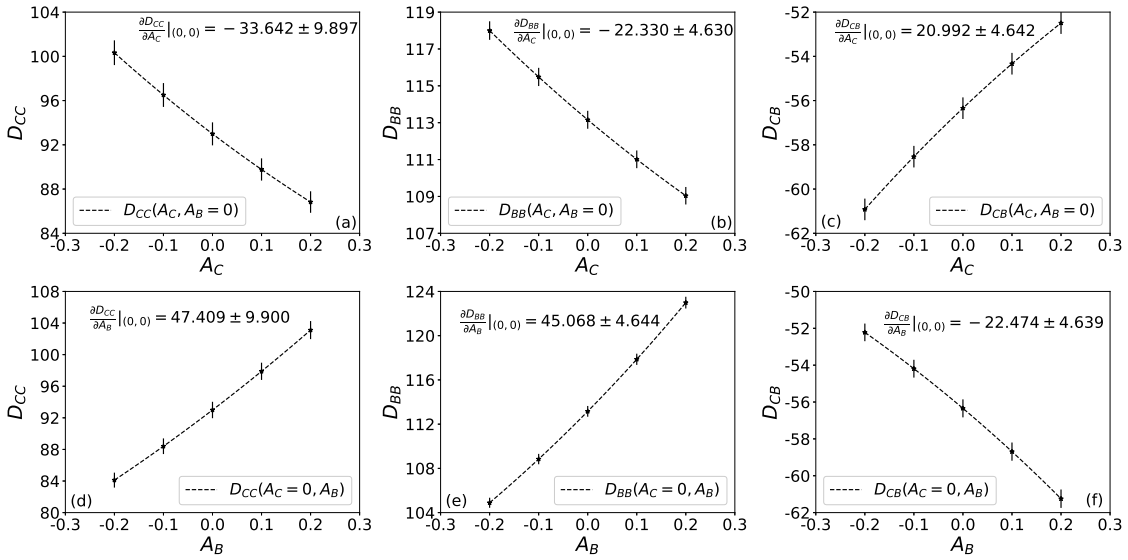

Figure 6.6: The diffusivities D_{ij} versus one affinity A_k, the other affinity being zero. The numerical data points are plotted together with the error bars and the dashed lines give the Lagrange polynomial interpolations of the data points. These interpolations provide the first derivatives $\partial D_{ij}/\partial A_k|_{(0,0)}$ at the equilibrium point ($A_C = A_B = 0$). Their numerical values as well as the errors are labeled and also listed in Table 6.3. The simulations are carried out with the time step $\mathrm{d}t = 0.05$, the total time $t = 2500$, and the statistics of 5×10^4 trajectories for every data point. The values of physical quantities and parameters listed in Table 5.1 and the Set I in Table 6.1 are used. The numerical method for estimating the error can be found in Appendix E.

Table 6.3: The numerical values of the quantities used for testing the nonlinear transport relations (2.18).

(i,j,k)	$M_{i,ij}$	$R_{ij,k}$	$R_{ik,j}$	$M_{i,jk} - R_{ij,k} - R_{ij,k}$
(C,C,C)	-67.388 ± 0.620	-33.642 ± 9.897	-33.642 ± 9.897	-0.104
(C,B,B)	-45.325 ± 0.620	-22.474 ± 4.639	-22.474 ± 4.639	-0.377
(C,C,B)	68.747 ± 0.097	47.409 ± 9.900	20.992 ± 4.642	0.346
(B,C,C)	42.064 ± 0.667	20.992 ± 4.642	20.992 ± 4.642	0.080
(B,B,B)	90.066 ± 0.665	45.068 ± 4.644	45.068 ± 4.644	-0.070
(B,C,B)	-44.777 ± 0.107	-22.474 ± 4.639	-22.330 ± 4.630	0.027

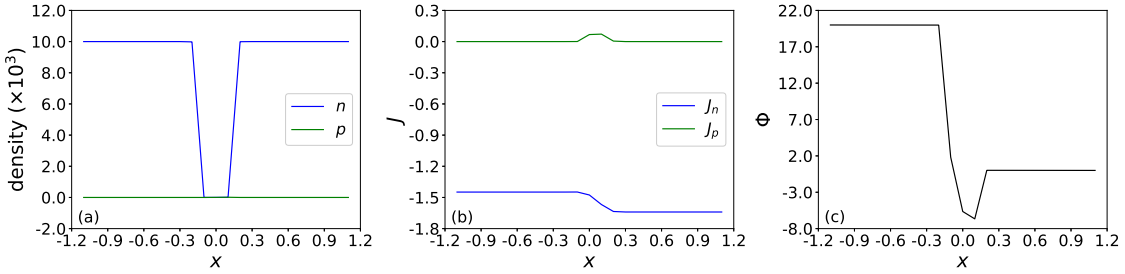

Figure 6.7: The profiles of (a) the charge carrier densities, (b) the current densities, and (c) the electric potential across the BJT which is used as signal amplifier under the working conditions $V_C = 20$ and $V_B = 6$. The simulations were carried out with the time step $\mathrm{d}t = 0.00015$ and 10^6 iterates. The values of physical quantities and parameters listed in Table 5.1 and the Set II in Table 6.1 are used.

as follows. When the voltage V_C is fixed, the variation of the other voltage V_B leads to variations of I_C and I_B. The amplification factor is defined as the ratio between these two variations (regarded here as signals),

$$\alpha = \left(\frac{\partial I_C}{\partial I_B}\right)_{V_C}, \tag{6.66}$$

under specific working conditions. Since this definition does not involve the electric current at the *Emitter* which often is grounded, the configuration is said to be "common-*Emitter*". To achieve the functionality of signal amplification, the transistors should satisfy the following requirements:

- The concentration of the majority charge carriers in the *Collector* region should be overwhelmingly larger than the concentration of minority charge carriers in the *Base* region.
- The concentration of the majority charge carriers in the *Emitter* region should be overwhelmingly larger than the concentration of minority charge carriers in the *Base* region.
- The *Collector*-*Base* junction should be reverse biased.
- The *Emitter*-*Base* junction should be forward biased.
- The *Base* region should be very thin so that the majority charge carriers in the *Emitter* region can easily get swept to the *Collector* region.
- The contacting section areas Σ_C and Σ_E should be larger than Σ_B.

The third and fourth conditions just require the bipolar *n*-*p*-*n* junction transistor to work in the forward active mode. The Set II in Table 6.1 gives a set of parameter values approaching these requirements in order to show that the present stochastic model can describe transistors in such regimes. The first two conditions are satisfied since $\bar{N}_C = \bar{N}_E \gg \bar{N}_B$, and the last one because $\Sigma = \Sigma_C = \Sigma_E > \Sigma_B$. If the transistor was in equilibrium without applied voltage ($A_C = A_B = 0$), the Nernst potentials (6.5) and (6.6) would take the values $(\Phi_C - \Phi_E)_{\mathrm{eq}} = 0$ and $(\Phi_B - \Phi_E)_{\mathrm{eq}} = -11.5$ with the parameter Set II in Table 6.1. In equilibrium, the electric field would have a symmetric profile around $x = 0$ with $(\Phi_C - \Phi_B)_{\mathrm{eq}} = (\Phi_E - \Phi_B)_{\mathrm{eq}} = 11.5$.

Figure 6.7 shows the profiles of charge carrier densities and current densities together with the electric potential under nonequilibrium conditions with applied voltages corresponding to $V_C = 20$ and $V_B = 6$. In Figure 6.7(a), we see that the *Base* region is thin in the model, so that the fifth condition is satisfied. As observed in Figure 6.7(b), the current densities are non-vanishing because the transistor is out of equilibrium. According to Eqs. (6.7)-(6.8), we here have that $\Phi_C - \Phi_E = 20$

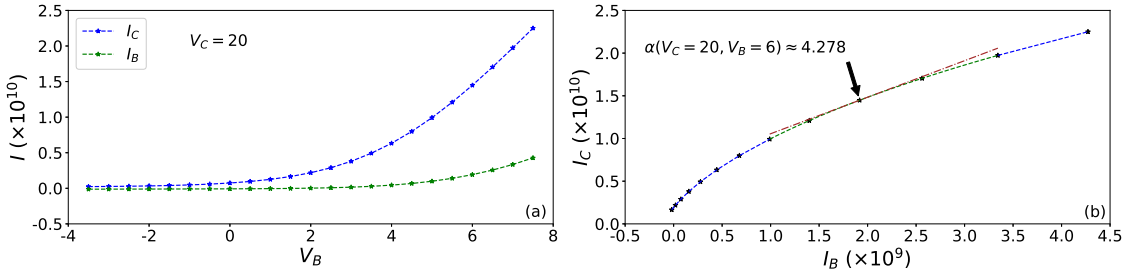

Figure 6.8: (a) The mean electric currents I_C and I_B versus the voltage V_B, with the other voltage fixed to the value $V_C = 20$. The lines join the numerical points depicted by the asterisks. (b) The electric current I_C versus the other electric current I_B. The line also joins the asterisks. The dashed line in the middle region is determined from Lagrange interpolation using the five asterisks of this domain. The derivative of I_C with respect to I_B at the point $(V_C = 20, V_B = 6)$ is evaluated giving the amplification factor (6.67). The simulations were carried out with the time step $\mathrm{d}t = 0.00015$ and 10^6 iterates for every data point. The values of physical quantities and parameters listed in Table 5.1 and the Set II in Table 6.1 are used.

and $\Phi_B - \Phi_E = -5.5$, so that $\Phi_C - \Phi_B = 25.5$ and $\Phi_E - \Phi_B = 5.5$, in agreement with the electric field plotted in Figure 6.7(c). Since $\Phi_C - \Phi_B = 25.5$ is larger than $(\Phi_C - \Phi_B)_{\mathrm{eq}} = 11.5$, the *Collector-Base* junction is reverse biased, as it should by the third condition. Moreover, $\Phi_E - \Phi_B = 5.5$ is smaller than $(\Phi_E - \Phi_B)_{\mathrm{eq}} = 11.5$, so that the *Emitter-Base* junction is forward biased and the fourth condition is also satisfied. Under these working conditions, the transistor can indeed achieve signal amplification, as demonstrated in Figure 6.8. The electric currents I_C and I_B are shown in Figure 6.8(a) as functions of V_B, with V_C fixed. Since the current I_C is greater than I_B, the amplification factor I_C/I_B is larger than unity, as expected[4]. Furthermore, Figure 6.8(b) depicts how the current I_C increases with the other current I_B and the associated voltage V_B. For $V_B = 6$, the differential amplification factor (6.66) is evaluated to be

$$\alpha(V_C = 20, V_B = 6) \approx 4.278, \tag{6.67}$$

which is also larger than unity, as required. It should be noticed that the amplification factors can take different values for different working conditions of the transistor.

These results show that the stochastic approach is relevant to study transistors in their regimes of signal amplification. Under the working conditions, a large number of electrons are injected from the *Emitter* to the *Base*. Some of these electrons recombine with holes in the *Base*, giving rise to the electric current I_B. The majority of electrons, however, go through the middle n-type region without recombining and give rise to the electric current I_C. The electric current I_C is directly proportional to the electron current injected by the *Emitter* in the *Base*, and the electric current I_B is proportional to the hole current injected by the *Base* into the *Emitter*. It is worth noting that the magnitude of electric current flowing in the *Collector* does not depend on the magnitude of the *Collector* voltage. The *Collector-Base* junction simply needs to be reverse biased. Rather, the electric current I_C is fixed by the bias applied to the *Emitter-Base* junction.

[4]The typical value of electric current gain, I_C/I_B, ranges between 50 and 300. Since the one-dimensional modeling of the transistor in the study, the electric current gain takes relatively low values. It is expected that, if the transistor was modeled in three spatial dimensions, much higher values of electric current gain would be achieved.

Chapter 7

Charge Transport in Tunnel Junctions

We have investigated in previous three chapters the properties of charge transport in mesoscopic systems. The common point of these systems is that they are all spatially extended and, therefore, multiple random variables are needed to characterize their discretized state. In this case, it becomes impossible to obtain the explicit matrix form of evolution operator from the master equation ruling the Markov jump process of the system under consideration. However, such an awkward situation can be naturally circumvented if the system of interest is compact and has a single internal random variable.

In this chapter, we study the charge transport across three mesoscopic tunnel junctions connected to a common conductive island or quantum dot [109, 30]. Particularly, such a system describes single-electron transistors [110, 111]. The number of excess electrons occupied in the central region, N, constitutes the only single internal random variable that characterizes the state of this system. In contrast with the stochastic model in Section 3.2, the rates for electron tunneling have nonlinear dependence on the state variable. This leaves us only the numerical way to compute the cumulant generating function for the currents as the leading eigenvalue of the modified evolution operator including the counting parameters. Starting from the numerically obtained cumulant generating function, the fluctuation relation is shown to hold, and the Onsager reciprocal relations together with their generalizations to nonlinear transport properties are also shown to be satisfied. Moreover, the staircase pattern of current-voltage characteristics due to the Coulomb blockade effect is realized under certain conditions.

7.1 Tunnel Junctions

We consider three mesoscopic tunnel junctions coupled to a common conductive island or quantum dot, as shown in Figure 7.1 [109, 30]. Electron tunneling events across the junctions frequently happen when the energy $E_c = e^2/2C$ is larger than the thermal energy $k_{\mathrm{B}}T$, with $C = C_0+C_1+C_2$. The voltage of electrode 0 is fixed to the value $V_0 = 0$ and taken as the reference. According to classical electrodynamics (see Appendix A for detailed calculation), during the time interval between two tunneling events, the voltage of the central region is found to be

$$V_{\mathrm{M}} = \frac{V_0C_0 + V_1C_1 + V_2C_2}{C_0 + C_1 + C_2} - \frac{Ne}{C_0 + C_1 + C_2} + V_p, \tag{7.1}$$

where N is the number of excess electrons concentrated in the central region characterizing the state of the system in the semiclassical description, and V_p is included to account for any possible misalignment of the Fermi level in the central region with respect to the three electrodes when the junction system is in equilibrium, i.e., $V_1 = V_2 = V_0 = 0$. This parameter can also be interpreted in terms of the background charge $q_0 = -(C_0 + C_1 + C_2)V_p$ in the central region, or as a gate voltage tuned by a capacitively coupled electrode. From Eq. (7.1), we note that the shift of N in

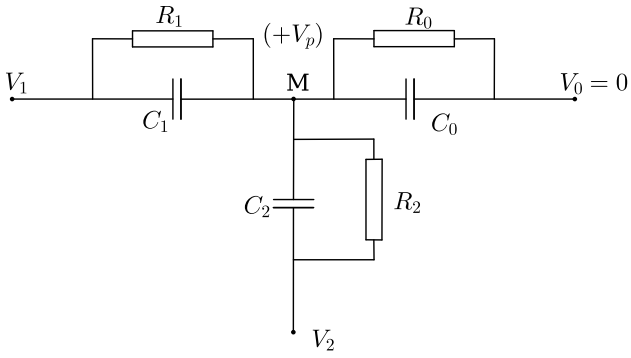

Figure 7.1: Schematic representation of the three junctions which are characterized by their respective resistances $\{R_0,\ R_1,\ R_2\}$ and capacitances $\{C_0,\ C_1,\ C_2\}$. Two electrodes are set with voltages V_1, V_2 and the other is fixed to $V_0 = 0$ as the reference. V_p is included to account for any possible misalignment of the Fermi level of the central region with respect to those of the three electrodes when $V_1 = V_2 = V_0 = 0$.

discrete way can offset the influence of V_p on the junction system. So, only the remainder of V_p divided by $e/(C_0 + C_1 + C_2)$,

$$V_p \bmod \frac{e}{C_0 + C_1 + C_2}, \tag{7.2}$$

serves as an indicator of influence (except the number of excess electrons in the central region) of V_p on the junction system. We will see in Figure 7.7 that the currents flowing across the junction indeed show periodic pattern as a function of V_p.

7.2 Master Equation

We now denote by $\mathcal{P}(N,t)$ the probability of the system at time t having N excess electrons in the central region. Then, $\mathcal{P}(N,t)$ obeys the master equation

$$\frac{\mathrm{d}}{\mathrm{d}t}\mathcal{P}(N,t) = \sum_{i=0,1,2}\sum_{\pm}\Big[W_i^{(\pm)}(N \mp 1)\mathcal{P}(N \mp 1,t) - W_i^{(\pm)}(N)\mathcal{P}(N,t)\Big], \tag{7.3}$$

with the transition rates computed using Fermi's golden rule and thus given by

$$W_i^{(\pm)}(N) = \frac{1}{e^2 R_i}\frac{\Delta U_i^{(\pm)}(N)}{\exp\left[\beta \Delta U_i^{(\pm)}(N)\right] - 1}. \tag{7.4}$$

Here, $\Delta U_i^{(\pm)}(N)$ denotes the intrinsic energy change of the whole junction system associated with the tunneling of an electron. They can be expressed by

$$\Delta U_i^{(\pm)}(N) = \mp e\left[V_{\mathrm{M}}(N) - V_i\right] + E_c. \tag{7.5}$$

Appendix A provides detailed derivation of $\Delta U_i^{(\pm)}(N)$. The long-range electrostatic interaction is embodied in all transition rates (7.4) being nonlinear functions of excess number of electrons in the central region.

7.3 Counting Statistics

The graph 3.2 can be associated with the process of electron tunneling across the junctions. According to Schnakenberg's graph analysis [78], two affinities $\mathbf{A} = (A_1, A_2)$ are calculated as

$$A_1 = \ln \frac{W_1^{(+)}(N) W_0^{(-)}(N+1)}{W_0^{(+)}(N) W_1^{(-)}(N+1)} = -\beta e V_1, \tag{7.6}$$

$$A_2 = \ln \frac{W_2^{(+)}(N) W_0^{(-)}(N+1)}{W_0^{(+)}(N) W_2^{(-)}(N+1)} = -\beta e V_2. \tag{7.7}$$

We now perform counting statistics by modifying Eq. (7.3) to include the counts of electrons $\mathbf{Z} = (Z_1, Z_2)$ tunneling respectively from electrodes 1 and 2 to the central region, yielding the extended master equation

$$\begin{aligned}\frac{\mathrm{d}}{\mathrm{d}t}\mathcal{P}(N, Z_1, Z_2, t) = \Big[&\left(\mathrm{e}^{-\partial_N} - 1\right) W_0^{(+)}(N) + \left(\mathrm{e}^{+\partial_N} - 1\right) W_0^{(-)}(N) \\ &+ \left(\mathrm{e}^{-\partial_N}\mathrm{e}^{-\partial_{Z_1}} - 1\right) W_1^{(+)}(N) + \left(\mathrm{e}^{+\partial_N}\mathrm{e}^{+\partial_{Z_1}} - 1\right) W_1^{(-)}(N) \\ &+ \left(\mathrm{e}^{-\partial_N}\mathrm{e}^{-\partial_{Z_2}} - 1\right) W_2^{(+)}(N) + \left(\mathrm{e}^{+\partial_N}\mathrm{e}^{+\partial_{Z_2}} - 1\right) W_2^{(-)}(N)\Big] \mathcal{P}(N, Z_1, Z_2, t).\end{aligned} \tag{7.8}$$

The cumulant generating function can thus be defined as

$$Q(\lambda_1, \lambda_2) \equiv \lim_{t\to\infty} -\frac{1}{t} \ln \sum_{N, Z_1, Z_2} \mathcal{P}(N, Z_1, Z_2, t)\, \mathrm{e}^{-\lambda_1 Z_1 - \lambda_2 Z_2}, \tag{7.9}$$

where $\boldsymbol{\lambda} = (\lambda_1, \lambda_2)$ are the counting parameters. The cumulant generating function $Q(\boldsymbol{\lambda})$ can be obtained by solving the eigenvalue problem

$$\hat{L}_{\boldsymbol{\lambda}} \Psi_{\boldsymbol{\lambda}}(N) = -Q(\boldsymbol{\lambda}) \Psi_{\boldsymbol{\lambda}}(N), \qquad \hat{L}_{\boldsymbol{\lambda}}^{\dagger} \tilde{\Psi}_{\boldsymbol{\lambda}}(N) = -Q(\boldsymbol{\lambda}) \tilde{\Psi}_{\boldsymbol{\lambda}}(N), \tag{7.10}$$

with the operator $\hat{L}_{\boldsymbol{\lambda}}$ defined through the equation

$$\begin{aligned}\frac{\mathrm{d}}{\mathrm{d}t}F(N,t) = \hat{L}_{\boldsymbol{\lambda}} F(N,t) = \Big[&\left(\mathrm{e}^{-\partial_N} - 1\right) W_0^{(+)}(N) + \left(\mathrm{e}^{+\partial_N} - 1\right) W_0^{(-)}(N) \\ &+ \left(\mathrm{e}^{-\partial_N}\mathrm{e}^{-\lambda_1} - 1\right) W_1^{(+)}(N) + \left(\mathrm{e}^{+\partial_N}\mathrm{e}^{+\lambda_1} - 1\right) W_1^{(-)}(N) \\ &+ \left(\mathrm{e}^{-\partial_N}\mathrm{e}^{-\lambda_2} - 1\right) W_2^{(+)}(N) + \left(\mathrm{e}^{+\partial_N}\mathrm{e}^{+\lambda_2} - 1\right) W_2^{(-)}(N)\Big] F(N,t),\end{aligned} \tag{7.11}$$

and $\hat{L}_{\boldsymbol{\lambda}}^{\dagger}$ denotes its adjoint. In Eq. (7.10), $-Q(\boldsymbol{\lambda})$ is the leading eigenvalue, $\Psi_{\boldsymbol{\lambda}}(N)$ the corresponding right-eigenfunction, and $\tilde{\Psi}_{\boldsymbol{\lambda}}(N)$ the left-eigenfunction. The elements of the operator $\hat{L}_{\boldsymbol{\lambda}}$ are given by

$$\hat{L}_{\boldsymbol{\lambda}}(N, N') \equiv \Gamma_{\boldsymbol{\lambda}}^{(+)}(N')\delta_{N-1,N'} + \Gamma_{\boldsymbol{\lambda}}^{(-)}(N')\delta_{N+1,N'} - \left[\Gamma_{\mathbf{0}}^{(+)}(N') + \Gamma_{\mathbf{0}}^{(-)}(N')\right] \delta_{N,N'}, \tag{7.12}$$

where

$$\Gamma_{\boldsymbol{\lambda}}^{(\pm)}(N) = W_0^{(\pm)}(N) + W_1^{(\pm)}(N)\mathrm{e}^{\mp\lambda_1} + W_2^{(\pm)}(N)\mathrm{e}^{\mp\lambda_2}. \tag{7.13}$$

For numerical purpose, the operator with the elements $\hat{L}_{\boldsymbol{\lambda}}(N, N')$ is truncated as a square matrix with boundaries $N_{\min} = N'_{\min}$ and $N_{\max} = N'_{\max}$. The solution of Eq. (7.11) has the general form

$$F(N,t) = \mathrm{e}^{\hat{L}_{\boldsymbol{\lambda}} t} F(N,0). \tag{7.14}$$

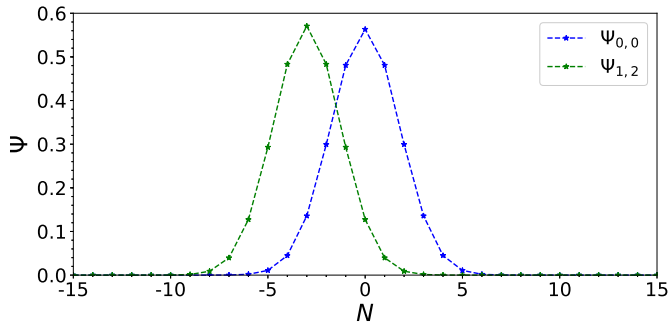

Figure 7.2: The normalized distribution $\Psi_{\lambda_1,\lambda_2}(N)$ for $\lambda_1 = \lambda_2 = 0$ and for $\lambda_2 = 2\lambda_1 = 2$. Asterisks are from numerical results with dash lines joining them. The parameter values are $C_0 = C_1 = C_2 = 1$, $R_0 = R_1 = R_2 = 1$, $\beta = e = 1$, $V_p = 0$, $V_1 = -1$, $V_2 = -2$. The corresponding affinities are $A_1 = 1$ and $A_2 = 2$.

where the initial condition $F(N, 0)$ can be randomly chosen to assume that it has the component of $\Psi_{\boldsymbol{\lambda}}(N)$[1]. The matrix exponential $e^{\hat{L}_{\boldsymbol{\lambda}} t}$ can be computed using Padé approximation (see Appendix E). Since $e^{\hat{L}_{\boldsymbol{\lambda}}} > 0$, the Perron-Frobenius theorem applies and the leading eigenvalue $-Q(\boldsymbol{\lambda})$ of $\hat{L}_{\boldsymbol{\lambda}}$ corresponds to the the real maximum eigenvalue $e^{-Q(\boldsymbol{\lambda})}$ of $e^{\hat{L}_{\boldsymbol{\lambda}}}$ in magnitude (for some value $t > 0$). So, $\Psi_{\boldsymbol{\lambda}}(N)$ can be asymptotically evaluated as

$$\Psi_{\boldsymbol{\lambda}}(N) \sim_{t\to\infty} e^{\hat{L}_{\boldsymbol{\lambda}} t} F(N, 0), \tag{7.15}$$

which is then normalized[2]

$$\Psi_{\boldsymbol{\lambda}}(N) \leftarrow \frac{\Psi_{\boldsymbol{\lambda}}(N)}{\sqrt{\sum_{N'} \Psi_{\boldsymbol{\lambda}}(N')\Psi_{\boldsymbol{\lambda}}(N')}}. \tag{7.16}$$

The cumulant generating function $Q(\boldsymbol{\lambda})$ is calculated as[3][4]

$$Q(\boldsymbol{\lambda}) = -\sum_{N,N'} \Psi_{\boldsymbol{\lambda}}(N)\hat{L}_{\boldsymbol{\lambda}}(N, N')\Psi_{\boldsymbol{\lambda}}(N'). \tag{7.17}$$

The stationary distribution is given by $\mathcal{P}_{\rm st}(N) = \Psi_{\mathbf{0}}(N)$ (see Figure 7.2). Because of the nonlinearity of the transition rates (7.4), $\mathcal{P}_{\rm st}(N)$ is no longer Poissonian in contrast with that of the model with linear rates, e.g., the one in Section 3.2.

7.4 Fluctuation Theorem for the Current

According to the fluctuation theorem, we should have the symmetry relation

$$Q(\lambda_1, \lambda_2) = Q(A_1 - \lambda_1, A_2 - \lambda_2), \tag{7.18}$$

which is the consequence of the symmetry [64, 112]

$$\hat{M}^{-1}\hat{L}_{\boldsymbol{\lambda}}\hat{M} = \hat{L}^{\dagger}_{\mathbf{A}-\boldsymbol{\lambda}}, \tag{7.19}$$

[1] Because of the inevitable roundoff error in numerical computation, this assumption is always reasonable.

[2] The computation in Eq. (7.15) with large time t makes $\Psi_{\boldsymbol{\lambda}}(N)$ too small, thus leading to numerical instability. The solution to this issue is that we can repeat the following operations many times: (i) do the computation in Eq. (7.15) with moderate time t; (ii) then normalize the obtained result with Eq. (7.16).

[3] $Q(\boldsymbol{\lambda})$ can also be directly obtained by diagonalizing the matrix $\hat{L}_{\boldsymbol{\lambda}}(N, N')$ and then finding the largest eigenvalue.

[4] In Eq. (7.17) the function to the left-hand side of $\hat{L}_{\boldsymbol{\lambda}}(N, N')$ can be replaced by any other function, only if it has the inner product unity with $\Psi_{\boldsymbol{\lambda}}(N)$. Here, $\Psi_{\boldsymbol{\lambda}}(N)$ itself is used for numerical convenience.

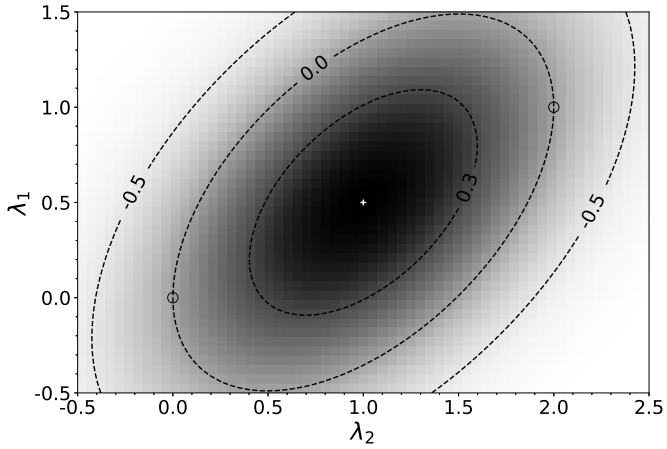

Figure 7.3: The gray scale map of the cumulant generating function $Q(\lambda_1, \lambda_2)$. Three contours are shown. The symbol "+" marks the center located at $(\lambda_1 = 0.5, \lambda_2 = 1.0)$. The two circles indicate the coordinates $(\lambda_1 = 0.0, \lambda_2 = 0.0)$ and $(\lambda_1 = 1.0, \lambda_2 = 2.0)$, which are respectively joined by the contour for $Q(\lambda_1, \lambda_2) = 0.0$. The parameter values are $C_0 = C_1 = C_2 = 1$, $R_0 = R_1 = R_2 = 1$, $\beta = e = 1$, $V_p = 0$, $V_1 = -1$, $V_2 = -2$. The corresponding affinities are $A_1 = 1$ and $A_2 = 2$.

where the operator $\hat{M}$ is defined as the diagonal matrix $\hat{M}(N, N') = M(N)\delta_{N,N'}$ with the diagonal elements obeying the recurrence

$$M(N) = \mathrm{e}^{\beta \Delta U_0^{(-)}(N)} M(N-1). \tag{7.20}$$

The symmetry (7.19) can be established by first noting that we should have $\Gamma^{(-)}_{\boldsymbol{\lambda}}(N)M(N) = \Gamma^{(+)}_{\mathbf{A}-\boldsymbol{\lambda}}(N-1)M(N-1)$. Next, the relations (7.6) and (7.7) for the affinities lead to the simplification $W_0^{(-)}(N)M(N) = W_0^{(+)}(N-1)M(N-1)$. Finally, we have that $\Delta U_0^{(-)}(N) = -\Delta U_0^{(+)}(N-1)$ because of Eq. (7.5), so that the expression (7.4) for the rates implies that $W_0^{(+)}(N-1)/W_0^{(-)}(N) = \exp\left[\beta \Delta U_0^{(-)}(N)\right]$, hence the result (7.20).

Using the method developed above, the symmetry relation (7.18) is confirmed by the numerical calculation of the cumulant generating function $Q(\lambda_1, \lambda_2)$. Figure 7.3 shows the gray scale map of $Q(\lambda_1, \lambda_2)$ with several contours in the plane of the counting parameters λ_1 and λ_2 for the affinities $A_1 = 1$ and $A_2 = 2$. In this figure, the symmetry (7.18) is apparent with respect to the inversion transformation $(\lambda_1, \lambda_2) \to (A_1 - \lambda_1, A_2 - \lambda_2)$. We observe that the cumulant generating function is not symmetric under the reflections $(\lambda_1, \lambda_2) \to (A_1 - \lambda_1, \lambda_2)$ and $(\lambda_1, \lambda_2) \to (\lambda_2, A_2 - \lambda_2)$, showing the evidence of correlation between the fluctuations of the two currents. Moreover, the cumulant generating function in Figure 7.3 is partially displayed along the line $\lambda_2 = 1.0$ in Figure 7.4(a) and the line $\lambda_1 = 0.5$ in Figure 7.4(b). These functions are compared with their transformation by the symmetry (7.18). Their coincidence again confirms the validity of the fluctuation relation.

With the method presented in Chapter 3, the counting statistics of electron tunneling is performed in simulation to numerically compute the affinities of this tunnel junction system. Gillespie's algorithm is implemented here in simulation according to the master equation (7.3). The values of the mean currents and their diffusivities are evaluated in simulation. In the same way for the model with linear rates in Section 3.2, six global transition rates $\{W_{ij}\}_{i,j=0,1,2}$ between electrodes are supposed to exist, and their values are calculated by solving the nonlinear equations (3.111)-(3.116).

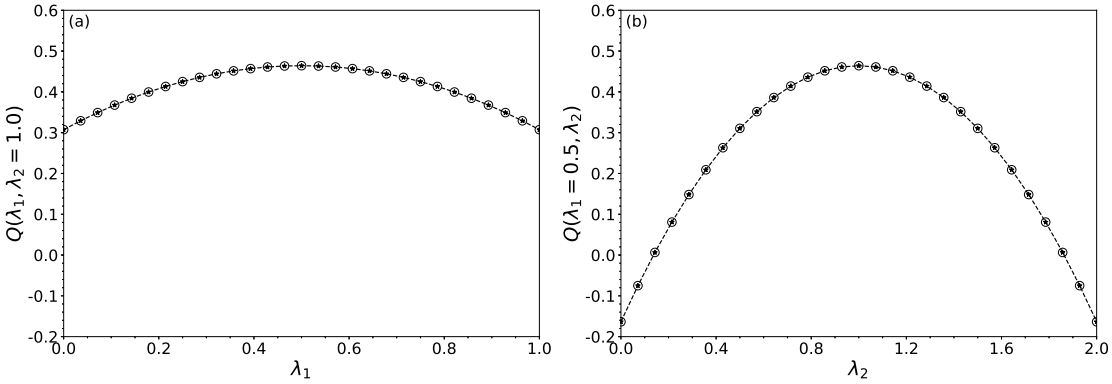

Figure 7.4: The slices of the cumulant generating function $Q(\lambda_1, \lambda_2)$, i.e., the function of λ_1 for $\lambda_2 = 1.0$ in the panel (a) and the function of λ_2 for $\lambda_1 = 0.5$ in panel (b). In both panels, the asterisks are numerical results and the dash lines join them. The circles are plotted from the function $Q(1.0-\lambda_1, \lambda_2 = 1.0)$ in panel (a) and $Q(\lambda_1 = 0.5, 2.0-\lambda_2)$ in panel (b). Clearly, each circle surrounds an asterisk. The difference between each asterisk and the center of its corresponding circle is smaller than 1.0×10^{-14}, so that the numerical error on cumulant generating function is negligible. The parameter values are $C_0 = C_1 = C_2 = 1$, $R_0 = R_1 = R_2 = 1$, $\beta = e = 1$, $V_p = 0$, $V_1 = -1$, $V_2 = -2$. The corresponding affinities are $A_1 = 1$ and $A_2 = 2$.

If the process was Poissonian, the affinities would be given by

$$A_1 \equiv A_{10} = \ln \frac{W_{10}}{W_{01}}, \tag{7.21}$$

$$A_2 \equiv A_{20} = \ln \frac{W_{20}}{W_{02}}. \tag{7.22}$$

Figure 7.5 presents the comparison between so-obtained numerical affinities and their theoretical predictions. In this figure, the agreement is found between the two sets of affinities, especially in the vicinity of equilibrium ($A_1 = A_2 = 0$). However, discrepancies beyond numerical error are also clearly seen for large affinities. As such, the process can no longer be regarded as Poissonian if the system is far from equilibrium. The reason lies in the nonlinearity of the rates (7.4) whose effect on counting statistics has already been discussed in Chapter 4.

7.5 Response Properties

The mean current J_1 of electron tunneling is depicted in Figure 7.6 as a function of the affinity A_1 for different values of A_2. According to Eq. (2.6), the value of J_1 in Figure 7.6 is obtained from two different methods, by numerical simulations (asterisks) and by numerically differentiating the cumulant generating function $Q(\lambda_1, \lambda_2)$ with respect to the counting parameter λ_1 (circles). An excellent agreement is found between both methods. The results show the nonlinear dependence of the mean current on the affinity, so that the expansion around equilibrium should involve not only linear, but also nonlinear response coefficients. The formulae for numerical differentiations can be found in Appendix E.

As shown in Figure 7.6, the mean current J_1 clearly manifests itself as the nonlinear response of affinities A_1 and A_2. So, the consequences of the fluctuation relation at the level of the linear and nonlinear response coefficients (2.11)-(2.12) can be investigated. In contrast with the way we study the response properties in Section 6.5 for bipolar n-p-n junction transistors, we here start from the cumulant generating function to evaluate the mean currents and their diffusivities using

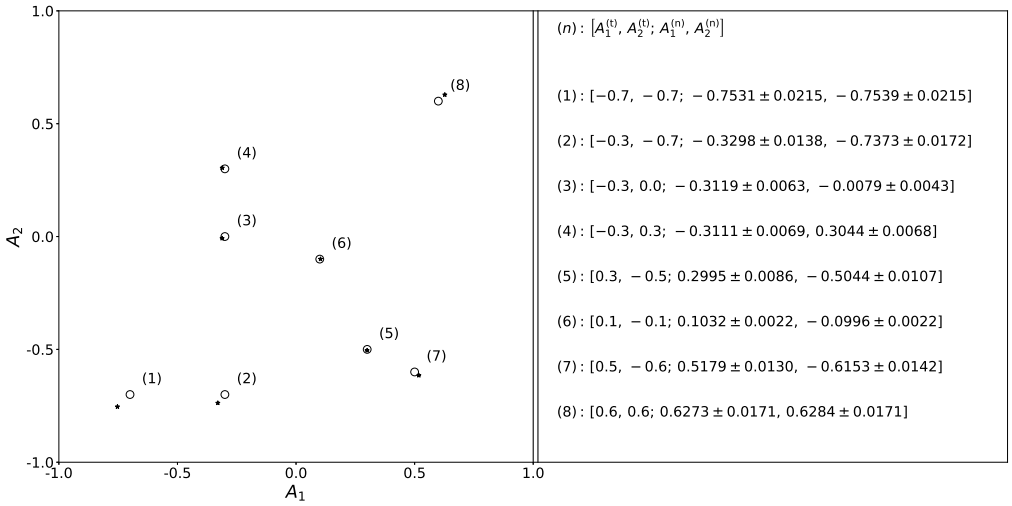

Figure 7.5: The comparison between numerical affinities (marked with asterisks) and their theoretical expectations (marked with circles). The values with corresponding errors are listed. The parameter values are $C_0 = C_1 = C_2 = 1$, $R_0 = R_1 = R_2 = 1$, $\beta = e = 1$, $V_p = 0$. The numerical affinities are evaluated from the statistics obtained in simulation over the time interval $[0, 10000]$ and 1×10^4 iterates for every case. The numerical method for estimating the error can be found in Appendix E.

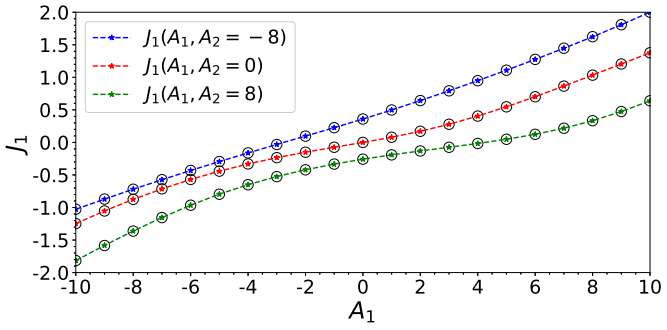

Figure 7.6: The mean current J_1 of electron tunneling as a function of A_1, with A_2 fixed. The asterisks are the results from numerical simulation, and the circles are obtained from $J_1 = \partial Q/\partial \lambda_1$ with numerical differentiations. The dash lines join the asterisks. The parameter values are $\beta = e = 1$, $C_0 = 0.02$, $C_1 = 0.03$, $C_2 = 0.05$, $R_0 = 1$, $R_1 = 3$, $R_2 = 2$, $V_p = 3.0$.

Table 7.1: The numerical values used for testing the fluctuation-dissipation relations (2.16) and the Onsager reciprocal relations (2.17). Three significant digits are obtained. The derivatives are approximated by numerical differentiations, which are accurate up to $O(10^{-4})$ with the methods implemented here. The parameter values are the same as those used for Figure 7.6.

(i,j)	$L_{i,j}$	$D_{ij}(\mathbf{A}=\mathbf{0})$	$L_{i,j}-D_{ij}(\mathbf{A}=\mathbf{0})$
$(1,1)$	7.59×10^{-2}	7.58×10^{-2}	1.15×10^{-4}
$(1,2)$	-2.53×10^{-2}	-2.53×10^{-2}	2.75×10^{-5}
$(2,1)$	-2.53×10^{-2}	-2.53×10^{-2}	3.03×10^{-5}
$(2,2)$	1.01×10^{-1}	1.01×10^{-1}	1.43×10^{-4}

Table 7.2: The numerical values of the quantities used for testing the nonlinear response relations (2.18). Three significant digits are obtained. The derivatives are approximated by numerical differentiations, which are accurate up to $O(10^{-6})$ with the methods implemented here. The parameter values are the same as those used for Figure 7.6.

(i,j,k)	$M_{i,jk}$	$R_{ij,k}$	$R_{ik,j}$	$M_{i,jk}-R_{ij,k}-R_{ik,j}$
$(1,1,1)$	5.27×10^{-3}	2.63×10^{-3}	2.63×10^{-3}	3.60×10^{-6}
$(1,2,2)$	2.54×10^{-3}	1.27×10^{-3}	1.27×10^{-3}	-1.51×10^{-6}
$(1,1,2)$	-1.24×10^{-2}	-1.15×10^{-2}	-8.81×10^{-4}	-7.48×10^{-6}
$(2,1,1)$	-1.76×10^{-3}	-8.81×10^{-4}	-8.81×10^{-4}	3.26×10^{-6}
$(2,2,2)$	-1.01×10^{-2}	-5.07×10^{-3}	-5.07×10^{-3}	-2.13×10^{-6}
$(2,1,2)$	-6.75×10^{-3}	1.27×10^{-3}	-8.01×10^{-3}	-6.33×10^{-6}

numerical differentiations (see Appendix E) according to Eqs. (2.6)-(2.7), and then proceed with the evaluation of the response coefficients also with numerical differentiations.

Table 7.1 presents the values of all the linear response coefficients and diffusivities in the same conditions as in Figure. 7.6. The fluctuation-dissipation relations (2.16) and the Onsager reciprocal relations (2.17) are verified up to numerical accuracy. Beyond, Table 7.2 gives the values of the nonlinear response coefficients (2.12) and the first responses (2.19) of the diffusivities, again in the same conditions as in Figure 7.6. Table 7.2 shows that the relations (2.18) are also satisfied up to numerical accuracy. Therefore, the implications of microreversibility beyond the linear regime are verified in this nonlinear model.

It should be mentioned that the response coefficients of even orders are all vanishing if V_p is an integer multiple of $e/(C_0+C_1+C_2)$, because the transport properties have the symmetries $J_i(\mathbf{A})+J_i(-\mathbf{A})=0$ and $D_{ij}(\mathbf{A})=D_{ij}(-\mathbf{A})$ in this case. So, the non-zero response coefficients of even orders can find their origin in the effect that excess electrons can not completely compensate the voltage V_p due to the their discrete nature.

7.6 Current-Voltage Characteristics

The nonlinear dependence becomes stronger at lower temperature, as seen in Figure 7.7 where the electric current $I_1=-|e|J_1$ is shown as a function of voltages V_1 and V_p for $C_1\gg C_0=C_2$, $R_1\gg R_0=R_2$, and the temperature a hundred times lower than in Figure 7.6. We observe in Fig-

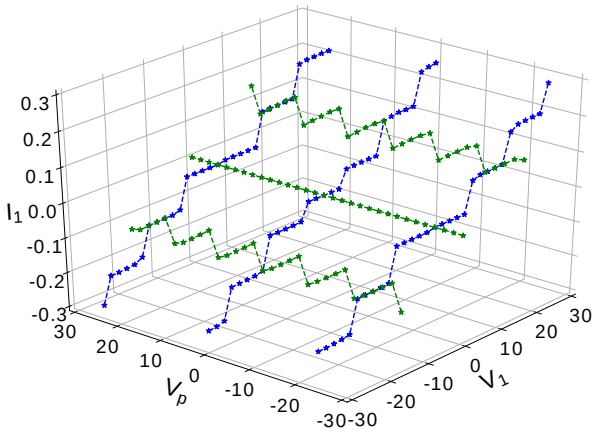

Figure 7.7: Current-voltage characteristics for the tunnel junction system when the parameters are chosen such that a pattern of Coulomb staircases is produced. The electric current defined as $I_i = -|e|J_i$ is shown versus the voltages V_1 and V_p. The asterisks are numerical results from simulation and dash lines join them. I_1-V_1 curves for $V_p = -24, 0, 24$ and I_1-V_p curves for $V_1 = -16, 0, 16$ are depicted. The parameter values are $\beta = 100$, $e = 1$, $C_1 = 0.1$, $C_0 = C_2 = 0.001$, $R_1 = 100$, $R_0 = R_2 = 1$ and $V_2 = 0$. This set of parameters is such that the tunnel junctions 0 and 2 play identical roles, so an equivalent circuit would be given by replacing both junctions in parallel with a single one having a capacitance twice larger and a resistance half smaller.

ure 7.7 that, under such conditions, Coulomb staircases manifest themselves in the current-voltage characteristics, as for single-electron transistors. For the parameter values taken in Figure 7.7 where $C_0 = C_2$, $R_0 = R_2$, and $V_0 = V_2 = 0$, an equivalent single tunnel junction can be considered to replace the tunnel junctions 0 and 2 connected in parallel, a capacitance twice larger, and a resistance half smaller. Therefore, in the analogy with a single-electron transistor, the roles of the source, the gate, and the drain would be respectively played by the electrode 1, electrode with V_p, and the electrodes 0 and 2. The Coulomb staircases appear on the lines given by

$$V_1 = \frac{C_0 + C_1 + C_2}{C_1} V_p + \frac{e}{C_1}\left(N \mp \frac{1}{2}\right) \qquad \text{with} \qquad N \in \mathbb{Z} \tag{7.23}$$

in the plane (V_p, V_1), as indeed observed in Figure 7.7. If V_1 is fixed, the staircases are separated by $\Delta V_p = e/(C_0 + C_1 + C_2)$, corresponding to the period of current-voltage characteristics as a function of V_p. In the following, we call tunnel junction 1 the source channel, and the tunnel junctions 0 and 2 collectively the drain channel.

The mean current I_1 as a function of the voltage V_1 forms plateaus separated by steep jumps. Accordingly, the effective conductance $G = \mathrm{d}I_1/\mathrm{d}V_1$ forms sharp peaks, which is the manifestation of the Coulomb blockade effect, as in single-electron transistors [111]. If $\beta|\Delta U_i^{(\pm)}| \gg 1$, the rates (7.4) are given by $W_i^{(\pm)} \approx 0$ for $\Delta U_i^{(\pm)} > 0$ and $W_i^{(\pm)} \approx |\Delta U_i^{(\pm)}|/(e^2 R_i)$ for $\Delta U_i^{(\pm)} < 0$. Because $C_1 \gg C_0 = C_2$, the voltage of the central region (7.1) can be approximately written as $V_\mathrm{M} \approx V_1 - Ne/C_1$, where we have omitted the contribution of V_p for convenience. Since the resistance R_1 is significantly larger than $R_0 = R_2$, the rates $W_1^{(\pm)}$ play negligible roles with respect to $W_0^{(\pm)}$ and $W_2^{(\pm)}$. In such conditions, V_M is closer to the drain voltage $V_0 = V_2 = 0$ than to the source voltage V_1, in such a way that the currents in both source and drain channels can be balanced. Figure 7.8 shows the fixed voltage levels of the source, drain, and possible levels of the central region. In this figure, the voltage level of source is lower than that of drain. According to the Coulomb blockade effect, it can be inferred that the system switches between two states, with V_M

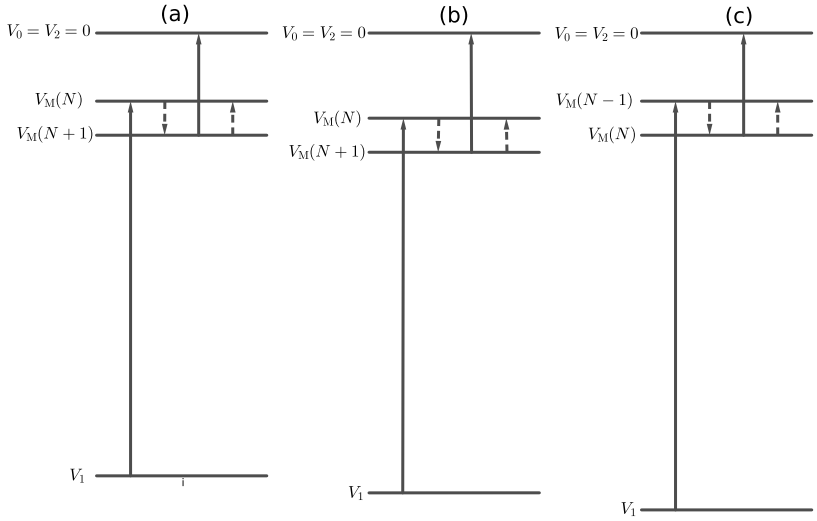

Figure 7.8: The voltage levels the source (electrode 1), drain (electrodes 0 and 2), and central region corresponding to the Coulomb staircase pattern in Figure 7.7. The drain voltage is fixed $V_0 = V_2 = 0$. The whole junction system switches between two states, during which electrons are constantly transducted from the source to the drain. The subfigures (a) to (b) to (c) shows the evolution of the voltage levels as the source voltage V_1 being manipulated.

changing frequently. During the switches, $\Delta U_i^{(-)}$ for $i = 0, 2$ change signs accordingly, and $\Delta U_i^{(+)}$ for $i = 0, 2$ always stay positive. So, when V_M is in its higher level, the drain channel is closed, whereas when V_M is in its lower level, the drain channel is open. The source channel is always open due to the large gap between V_M and the source voltage V_1. When the central region receives an electron from the source, its voltage V_M drops from the higher level to the lower level and at the same time the drain channel becomes open. After that, an electron is quickly transducted from the central region to the drain, V_M goes back to its higher level, and the drain channel closes again. The electric current I_1 depends on the gap between V_M and V_1, which determines the frequency of the switches of the system. If the source voltage V_1 slowly decreases, the two possible voltage levels of the central region also decrease as a whole, keeping the gap between V_M and V_1 unchanged and thus I_1 being constant (see Figure 7.8b). This explains the presence of plateaus in the current-voltage characteristics in Figure 7.7. However, when the two voltage levels of the central region as a whole gradually mismatch the location where they initially are, the drain channel suddenly becomes always open, and subsequently an extra electron is transducted from the central region to the drain. After that, the two voltage levels of the central region suddenly jump to where they initially are, and continues to switch, but with a higher frequency as $V_M - V_1$ becomes larger (see Figure 7.8c). This is the underlying mechanism why plateaus jump steeply.

Chapter 8

Conclusion and Perspectives

The present thesis has been devoted to the study of charge transport in mesoscopic systems, with the focus on the fluctuation theorem and its implications. Moreover, the influence of long-range electrostatic interaction between the constituent charged particles on transport properties has been investigated and qualitatively clarified.

In Chapter 3, we studied the transport properties of particles in two Markov stochastic models. In the first model, the system is composed of several reservoirs between which the particles are exchanged with constant transition rates. This indicates that the particle transport is a superposition of several Poisson processes, and as a consequence the multivariate fluctuation relation was shown to be satisfied at every instant of time. The remarkable point of this model is that the constant rates can be fully determined from the mean values of the currents and their diffusivities, thus enabling us to numerically evaluate the affinities as natural logarithm of two rates between every pair of reservoirs. This normally requires to numerically solve the nonlinear equations where the input parameters of the mean values of the currents and their diffusivities are obtained from the counting statistics of signed cumulated fluxes. Moreover, this property suggests that this model could be used to describe in a coarse-grained way the long-time behavior of particle transport in other nonequilibrium steady state systems in contact with arbitrarily many reservoirs. In this regard, it was proved that this coarse-grained model is exactly valid to estimate the values of affinities in near-equilibrium regimes. In the proof, we used the fluctuation-dissipation relations linking the linear response coefficients of currents and their diffusivities in equilibrium. In the second model studied in Chapter 3, there are three reservoirs and the state of the system is fully characterized by a single random variable, giving the concentration of particles inside the system. The transition rates have linear dependence on the system state of particle concentration. We calculated the finite-time moment generating function of signed cumulated fluxes, and from this we established the finite-time fluctuation theorem. The time-dependent affinities were defined, converging in time as $1/t$ to their asymptotic values. The global transition rates associated with the particle exchanges over long enough time intervals between reservoirs were identified from the cumulant generating function. The so-obtained affinities are equivalent with those evaluated from Schnakenberg's graph analysis. On the other hand, the numerically computed affinities are in good agreement with their theoretical predictions. The successful description of the long-time behavior of particle transport in the second model in terms of the first model brought a strong evidence that the first stochastic model can serve as a coarse-grained description of those systems having linear transition rates in regimes far from equilibrium. Moreover, the quantities defined by Eqs. (3.89)-(3.94) preserve the structure of the nonlinear equations (3.111)-(3.116) with the diffusivities replaced by the time-dependent ones. This indicates that the coarse-grained model is also suitable for the description of particle transport over finite time intervals. The so-obtained affinities are thus time dependent and, inferred from the analysis in Subsection 3.2.4, they are supposed to converge in time to their asymptotic values with corrections going as $1/t$. Numerical support can be found in Section 4.6 for a Markov jump process with linear rates between two particle reservoirs.

To test whether the coarse-grained model is applicable to the nonequilibrium systems with nonlinear transition rates, we proceeded in Chapter 4 to study the charge transport in a conductive channel maintained between two reservoirs. The stochastic approach developed in Ref. [62] was adopted. The description is based on stochastic partial differential equations for the charge densities. These balance equations are coupled to the Poisson equation for the electric potential generated by the charges. This description is consistent with the laws of electricity, thermodynamics, and microreversibility. In the noiseless limit, the macroscopic description is recovered. For the purpose of numerically simulating the stochastic process, the channel was spatially discretized into small cells, and a Markov jump process is introduced, which is ruled by a master equation for the time evolution of the probability that the cells contain given numbers of particles. If these numbers are large enough, the Markov jump process can be replaced by a Langevin stochastic process involving Gaussian white noises, as shown in Appendix B. The numerical simulation of the Langevin stochastic process is significantly more efficient than the one of the Markov jump process, although giving results of comparable accuracy for large numbers of particles in the cells. The key point for the stochastic evolution is to determine the intrinsic energy changes associated with the particle jumps between cells (see Appendix A). Then, the transition rates are weighted by the function (4.24), which satisfies the detailed balance condition (4.25) under equilibrium. However, due to the long-range electrostatic interaction, the transition rates no longer depend linearly on the local particle concentrations. We performed the counting statistics of signed cumulated particle transfers over a long enough time interval, and then calculated the values of the mean current and its diffusivity, which further led to the numerical evaluation of the affinity according to the coarse-grained model. It turned out that the numerically obtained affinity is generally larger than its theoretical prediction, especially when the system is far from equilibrium. This is a strong evidence that the range of application of the coarse-grained model is restricted to near-equilibrium regimes for the system with nonlinear rates.

An explanation was given as to why the use of the coarse-grained model is limited. This reason lies in the nonlinearity of the transition rates, which arises from the long-range electrostatic interaction. Physically, the correlations between the charged particles induced by the long-range electrostatic interaction make the diffusivity of the current smaller than expected, and therefore the affinity numerically obtained is larger. This numerical observation seems to imply an inequality between the mean current, the diffusivity, and the actual affinity. If the values of mean current and affinity are known, we can determine the upper bound of the value of diffusivity. The equivalent relation of the inequality remains to be found for nonequilibrium systems in contact with more than two reservoirs.

We also noticed an interesting feature about charge transport in the conductive channel. The charge density in the channel modulate the intensity of influence of the long-range electrostatic interaction on the charged particles. When the density becomes very low, the fluctuating electric field in the channel tends to be approximated as a static background field. In the low-density limit, the transition rates are linear due to the static nature of the electric field in this case. In such limiting case, we proved that the coarse-grained model can be applied in regimes arbitrarily far from equilibrium. Moreover, the finite-time fluctuation theorem can be established, with the time-dependent affinity converging to its asymptotic value in time as $1/t$. This finding shows that the density of charged particle flowing across the nonequilibrium system should be as low as possible for those properties to hold.

In Chapter 5, the preceding stochastic approach was extended to describe charge transport in p-n junction diodes, taking into account the random motion of electrons and holes as well as the process of generation and recombination of electron-hole pairs. The spatially extended description allows us to define the measured electric current by including the contribution of the displacement current, which is essential for the study of current fluctuations [102, 62]. The profiles of charge carrier densities and electric potential obtained with this stochastic approach agree with those calculated with the macroscopic mean-field equations under equilibrium and nonequilibrium stationary conditions. Since the stochastic description satisfies local detailed balance in consistency with microreversibility, the fluctuation theorem holds for the carrier current and the measured total

current. Using the coarse-grained model, the macroscopic affinity given by the applied voltage is reached asymptotically in time as predicted by the fluctuation theorem. The convergence to the macroscopic affinity is remarkably faster for the total current than the carrier current. The reason is that the inclusion of the displacement current in the total current expresses the effects of the long-range electrostatic interaction on the measurement of the current fluctuations. Therefore, the random jumps of the charge carriers anywhere inside the diode have an instantaneous effect on the measured total current in the quasi-static limit of Maxwell's equations. The current-voltage characteristics were computed for different concentration ratios of majority to minority carriers. The Shockley model for the I-V characteristics of the p-n junction diode was shown to be valid under the extreme condition where the concentration is overwhelmingly larger for the majority carriers than for the minority carriers.

In Chapter 6, we continued our study of charge transport in other semiconductor devices, bipolar n-p-n junction transistors, with the same stochastic approach. We have shown that a fluctuation theorem holds for the two electric currents that are coupled together in the bipolar n-p-n junction transistor. Using the coarse-grained model, the asymptotic values of affinities were recovered from the first and second cumulants numerically obtained in counting statistics. However, according to the reason that has been explained, the deviations of the numerically computed affinities and their theoretical predictions were also observed to be beyond the error. We also showed that, as corollaries of the fluctuation theorem for the currents, the fluctuation-dissipation relations and Onsager reciprocal relations are satisfied. In particular, we verified in detail that the second-order nonlinear response coefficients of the currents are related to the first-order responses of the diffusivities, as predicted by theory [29, 69, 71]. The signal-amplifying effect, the typical functionality of transistors, was realized within the stochastic approach.

In Chapter 7, we investigated charge transport in three tunnel junctions that are coupled to a common quantum dot or conductive island, thus giving rise to two currents. Like the second stochastic model in Chapter 3, the state of the present system is also characterized by one random variable, representing its charge occupancy. The difference is that the transition rates for the electron tunneling are nonlinear. The evolution operator of the master equation of this system is modified to include the counting parameters. Because of the one-variable characterization of the state, the modified evolution operator can be written in a matrix form, thus enabling the numerical calculation to find the leading eigenvalue which is the cumulant generating function of the system. The symmetry of the so-obtained cumulant generating function were checked, as predicted by the fluctuation theorem. Moreover, the mean values of the currents and their diffusivities can be obtained by numerically differentiating the cumulant generating function with respect to the counting parameters. Continuing the procedure of numerical differentiations with respect to the affinities, the responses of the cumulants can be evaluated. Comparing the results, the Onsager reciprocal relations together with their generalizations were again tested. Under certain conditions, the staircase pattern of the current-voltage characteristics was obtained. This finds its origin in the Coulomb blockade effect.

In summary, we have studied in this thesis charge transport in several mesoscopic systems. In particular, the functionalities realized in the two semiconductor devices, i.e., diodes and transistors, illustrate that the stochastic approach provides a powerful computational tool for the simulation of electronic devices. Besides, these mesoscopic systems were used to address the fundamental issue of microreversibility in nonequilibrium statistical mechanics. The fluctuation theorem was shown to hold in various cases. The coarse-grained model for nonequilibrium systems in contact with several reservoirs was developed. The aim of this coarse-grained model is to give an estimation of affinities from the first and second cumulants of the probability distribution of currents. The scope of its application was clarified, and an interesting inequality was also found. Because of the relative easy access to the first two cumulants in counting statistics, it is hoped that this coarse-grained model can find more broader applications in physical, chemical, and biological systems.

Finally, an open question can be raised. It is naturally to conjecture that the dynamic nature of electric field according to Maxwell's equations would also make an impact on the transport properties. The stochastic approach for charge transport that we have used relies on the assumption

that the electric field propagates instantaneously, thus abruptly imposing interactions between charged particles, no matter how long in the distance between them. However, this is not the case in reality according to the Special Relativity. Therefore, a more complete stochastic approach incorporating the dynamic nature of electric field remains to be developed, and with this approach we may hope to obtain more realistic transport properties including all the electromagnetic effects.

Appendix A

Intrinsic Energy Change in Electrostatic Systems

In this appendix, we explicitly give the calculation of the intrinsic energy change associated with the transitions of charged particles in discretized mesoscopic systems that are studied in this thesis. This intrinsic energy change is defined as the result of total electrostatic energy change minus the work done by the external voltage source.

The Conductive Channel in Chapter 4

Using the results of Ref. [62], the discretized Poisson equation (4.19) is written in the matrix form

$$\mathbf{C} \cdot \mathbf{\Phi} = \mathbf{O}, \tag{A.1}$$

where

$$\mathbf{C} = \alpha \begin{pmatrix} 2 & -1 & & & & & \\ -1 & 2 & -1 & & & & \\ & \ddots & \ddots & \ddots & & & \\ & & -1 & 2 & -1 & & \\ & & & \ddots & \ddots & \ddots & \\ & & & & -1 & 2 & -1 \\ & & & & & -1 & 2 \end{pmatrix} \qquad \text{with} \qquad \alpha = \frac{\epsilon \Omega}{\Delta x^2}, \tag{A.2}$$

and

$$\mathbf{\Phi} = \begin{pmatrix} \Phi_1 \\ \Phi_2 \\ \vdots \\ \Phi_i \\ \vdots \\ \Phi_{L-1} \\ \Phi_L \end{pmatrix}, \qquad \mathbf{O} = e \begin{pmatrix} N_1 - N_- \\ N_2 - N_- \\ \vdots \\ N_i - N_- \\ \vdots \\ N_{L-1} - N_- \\ N_L - N_- \end{pmatrix} + \alpha \begin{pmatrix} \Phi_{\mathrm{L}} \\ 0 \\ \vdots \\ 0 \\ \vdots \\ 0 \\ \Phi_{\mathrm{R}} \end{pmatrix}. \tag{A.3}$$

$\{N_i\}_{i=1}^{L}$ are the numbers of mobile particles of positive charge $+e$ in discretized cells, and N_- is the number of fixed ions of negative charge $-e$ in each discretized cell. The electrostatic potential is given by

$$\mathbf{\Phi} = \mathbf{C}^{-1} \cdot \mathbf{O}, \tag{A.4}$$

with

$$\left(\mathbf{C}^{-1}\right)_{ij} = \begin{cases} \frac{i}{\alpha(L+1)}(L+1-j) & \text{if} \quad i \leq j, \\ \frac{j}{\alpha(L+1)}(L+1-i) & \text{if} \quad i > j. \end{cases} \tag{A.5}$$

The intrinsic energy change ΔU associated with the transitions of charged particles is calculated in terms of the change of U defined as[1]

$$U = \frac{1}{2}\mathbf{\Phi} \cdot \mathbf{C} \cdot \mathbf{\Phi} = \frac{1}{2}\mathbf{O} \cdot \mathbf{C}^{-1} \cdot \mathbf{O}. \tag{A.6}$$

When a charged particle transits from the ith to the $(i+1)$th cell, then

$$\Delta U_{i,i+1} = \frac{1}{2}\left(\mathbf{O}' \cdot \mathbf{C}^{-1} \cdot \mathbf{O}' - \mathbf{O} \cdot \mathbf{C}^{-1} \cdot \mathbf{O}\right), \tag{A.7}$$

where

$$O'_k = O_k - e\delta_{k,i} + e\delta_{k,i+1}. \tag{A.8}$$

We thus have that

$$\Delta U_{i,i+1} = +e(\Phi_{i+1} - \Phi_i) + \frac{e^2}{2}\Big[\left(\mathbf{C}^{-1}\right)_{i,i} - 2\left(\mathbf{C}^{-1}\right)_{i,i+1} + \left(\mathbf{C}^{-1}\right)_{i+1,i+1}\Big]. \tag{A.9}$$

Using Eq. (A.5), we find that

$$\Delta U_{i,i+1} = +e(\Phi_{i+1} - \Phi_i) + \frac{e^2 L \Delta x^2}{2(L+1)\epsilon\Omega}. \tag{A.10}$$

We notice that, for transitions at the boundaries, the above expression holds by taking the values of the potentials in the reservoirs, $\Phi_0 = \Phi_{\mathrm{L}}$ and $\Phi_{L+1} = \Phi_{\mathrm{R}}$.

The p-n Junction Diode in Chapter 5

The calculation of intrinsic energy change in p-n junction diodes is much the same as that in conductive channels, except that there are more species of charge carriers. The discretized Poisson equation (5.40) is written in the matrix form (A.1) with the same expressions for $\mathbf{\Phi}$ and $\mathbf{C}$ as those in Eqs. (A.2)-(A.3). Instead, $\mathbf{O}$ is expressed as

$$\mathbf{O} = e\begin{pmatrix} P_1 - N_1 + D_1 - A_1 \\ P_2 - N_2 + D_2 - A_2 \\ \vdots \\ P_i - N_i + D_i - A_i \\ \vdots \\ P_{L-1} - N_{L-1} + D_{L-1} - A_{L-1} \\ P_L - N_L + D_L - A_L \end{pmatrix} + \alpha \begin{pmatrix} \Phi_{\mathrm{L}} \\ 0 \\ \vdots \\ 0 \\ \vdots \\ 0 \\ \Phi_{\mathrm{R}} \end{pmatrix}, \tag{A.11}$$

where

- $\{P_i\}_{i=1}^{L}$ are the numbers of mobile holes of positive charge $+e$ in discretized cells;
- $\{N_i\}_{i=1}^{L}$ are the numbers of mobile electrons of negative charge $-e$ in discretized cells;

[1] U is defined such that it not only includes the electrostatic energy stored in the system, but also accounts for the work done by the external voltage source.

- $\{D_i\}_{i=1}^{L}$ are the numbers of fixed donors of positive charge $+e$ in discretized cells;
- $\{A_i\}_{i=1}^{L}$ are the numbers of fixed acceptors of negative charge $+e$ in discretized cells.

The intrinsic energy changes associated with transitions of electrons and holes between cells are given by

$$\Delta U_{i,i+1}^{(N)} = -e(\Phi_{i+1} - \Phi_i) + \frac{e^2 L \Delta x^2}{2(L+1)\epsilon\Omega}, \tag{A.12}$$

$$\Delta U_{i,i+1}^{(P)} = +e(\Phi_{i+1} - \Phi_i) + \frac{e^2 L \Delta x^2}{2(L+1)\epsilon\Omega}. \tag{A.13}$$

For transitions at the boundaries, these expressions hold by taking the values of the potentials in the reservoirs, $\Phi_0 = \Phi_{\rm L}$ and $\Phi_{L+1} = \Phi_{\rm R}$.

The Bipolar n-p-n Junction Transistor in Chapter 6

The species of charge carriers in n-p-n junction transistors are the same as those in p-n junction diodes. The discretized Poisson equation (6.18) is written in the matrix form (A.1) with the same expressions for $\mathbf{\Phi}$ as that in Eq. (A.3). Instead, C is here expressed as

$$\mathsf{C} = \alpha \begin{pmatrix} 2 & -1 & & & & & \\ -1 & 2 & -1 & & & & \\ & \ddots & \ddots & \ddots & & & \\ & & -1 & 2 & -1 & & \\ & & & \ddots & \ddots & \ddots & \\ & & & & -1 & 2 & -1 \\ & & & & & -1 & 2 \end{pmatrix} + \gamma \begin{pmatrix} 0 & & & & & & \\ & \ddots & & & & & \\ & & 0 & & & & \\ & & & 2 & & & \\ & & & & 0 & & \\ & & & & & \ddots & \\ & & & & & & 0 \end{pmatrix} \tag{A.14}$$

with

$$\alpha = \frac{\epsilon\Omega}{\Delta x^2}, \qquad \gamma = \frac{\epsilon\Omega}{\Delta y^2}, \tag{A.15}$$

and

$$\mathbf{O} = e \begin{pmatrix} P_1 - N_1 + D_1 - A_1 \\ P_2 - N_2 + D_2 - A_2 \\ \vdots \\ P_i - N_i + D_i - A_i \\ \vdots \\ P_{L-1} - N_{L-1} + D_{L-1} - A_{L-1} \\ P_L - N_L + D_L - A_L \end{pmatrix} + \alpha \begin{pmatrix} \Phi_C \\ 0 \\ \vdots \\ 0 \\ \vdots \\ 0 \\ \Phi_E \end{pmatrix} + 2\gamma \begin{pmatrix} 0 \\ \vdots \\ 0 \\ \Phi_B \\ 0 \\ \vdots \\ 0 \end{pmatrix}. \tag{A.16}$$

Here, we have assumed that only the discretized cell with index $i = m$ is in contact with the *Base*, as the case of the actual scheme. The intrinsic energy change associated with the transition of an electron of charge $-e$ from the ith to the $(i+1)$th cell is given by the change in the energy of U (A.6), reading

$$\Delta U_{i,i+1}^{(N)} = \frac{1}{2}\left(\mathbf{O}' \cdot \mathsf{C}^{-1} \cdot \mathbf{O}' - \mathbf{O} \cdot \mathsf{C}^{-1} \cdot \mathbf{O}\right), \tag{A.17}$$

where

$$O'_k = O_k + e\delta_{k,i} - e\delta_{k,i+1}. \tag{A.18}$$

We thus have that

$$\Delta U^{(N)}_{i,i+1} = -e(\Phi_{i+1} - \Phi_i) + \frac{e^2}{2}\left[\left(\mathbf{C}^{-1}\right)_{i,i} - 2\left(\mathbf{C}^{-1}\right)_{i,i+1} + \left(\mathbf{C}^{-1}\right)_{i+1,i+1} \right]. \tag{A.19}$$

A similar expression holds for hole transitions since they have the charge $+e$,

$$\Delta U^{(P)}_{i,i+1} = +e(\Phi_{i+1} - \Phi_i) + \frac{e^2}{2}\left[\left(\mathbf{C}^{-1}\right)_{i,i} - 2\left(\mathbf{C}^{-1}\right)_{i,i+1} + \left(\mathbf{C}^{-1}\right)_{i+1,i+1} \right]. \tag{A.20}$$

The inverse of the matrix $\mathbf{C}$ here is computed numerically[2]. For transitions at the boundaries, we have

$$\Delta U^{(N)}_{0,1} = -e(\Phi_1 - \Phi_C) + \frac{e^2}{2}\left(\mathbf{C}^{-1}\right)_{1,1}, \tag{A.21}$$

$$\Delta U^{(N)}_{1,0} = -e(\Phi_C - \Phi_1) + \frac{e^2}{2}\left(\mathbf{C}^{-1}\right)_{1,1}, \tag{A.22}$$

$$\Delta U^{(N)}_{L,L+1} = -e(\Phi_E - \Phi_L) + \frac{e^2}{2}\left(\mathbf{C}^{-1}\right)_{L,L}, \tag{A.23}$$

$$\Delta U^{(N)}_{L+1,L} = -e(\Phi_L - \Phi_E) + \frac{e^2}{2}\left(\mathbf{C}^{-1}\right)_{L,L}, \tag{A.24}$$

$$\Delta U^{(N)}_{B,i} = -e(\Phi_i - \Phi_B) + \frac{e^2}{2}\left(\mathbf{C}^{-1}\right)_{i,i}, \tag{A.25}$$

$$\Delta U^{(N)}_{i,B} = -e(\Phi_B - \Phi_i) + \frac{e^2}{2}\left(\mathbf{C}^{-1}\right)_{i,i}, \tag{A.26}$$

for electrons, and similar expressions for holes.

The Tunnel Junction in Chapter 7

Suppose there are N excess electrons in the central region between the three tunnel junctions (see Figure 7.1), and for convenience, $V_p = 0$. Thus, we have

$$\frac{Q_1}{C_1} + \frac{Q_0}{C_0} = V_1 - V_0, \tag{A.27}$$

$$\frac{Q_2}{C_2} + \frac{Q_0}{C_0} = V_2 - V_0, \tag{A.28}$$

$$Q_1 + Q_2 - Q_0 = Ne. \tag{A.29}$$

Here, Q_i denotes the charge stored in the ith capacitor, and the positive directions are set from the electrodes $1, 2$ to the electrode 0. Solving the above equations, we get

$$\frac{Q_0}{C_0} = \frac{V_0C_0 + V_1C_1 + V_2C_2}{C_0 + C_1 + C_2} - \frac{Ne}{C_0 + C_1 + C_2} - V_0, \tag{A.30}$$

$$\frac{Q_1}{C_1} = V_1 - \frac{V_0C_0 + V_1C_1 + V_2C_2}{C_0 + C_1 + C_2} + \frac{Ne}{C_0 + C_1 + C_2}, \tag{A.31}$$

$$\frac{Q_2}{C_2} = V_2 - \frac{V_0C_0 + V_1C_1 + V_2C_2}{C_0 + C_1 + C_2} + \frac{Ne}{C_0 + C_1 + C_2}. \tag{A.32}$$

Consequently, we obtain the voltage of the central region,

$$V_{\mathrm{M}}(N) = \frac{V_0C_0 + V_1C_1 + V_2C_2}{C_0 + C_1 + C_2} - \frac{Ne}{C_0 + C_1 + C_2}. \tag{A.33}$$

[2]The library GSL provides the function `gsl_linalg_LU_invert` for computing the inverse of a matrix from LU decomposition. Since this is a C/C++ library, it can be conveniently called in highly computationally demanding simulations.

The total electrostatic energy stored in the three junctions is given by

$$E(N) = \frac{Q_0^2}{2C_0} + \frac{Q_1^2}{2C_1} + \frac{Q_2^2}{2C_2}, \tag{A.34}$$

and therefore the change of electrostatic energy is

$$\Delta E = E(N') - E(N) = \frac{Q_0'^2 - Q_0^2}{2C_0} + \frac{Q_1'^2 - Q_1^2}{2C_1} + \frac{Q_2'^2 - Q_2^2}{2C_2}, \tag{A.35}$$

The work done by the external voltage source can be calculated as

$$W = V_0 \Delta \mathcal{Q}_0 + V_1 \Delta \mathcal{Q}_1 + V_2 \Delta \mathcal{Q}_2, \tag{A.36}$$

where $\Delta \mathcal{Q}_i$ denotes the charge transferred from the voltage source to the ith electrode. If an electron tunnels form electrode 1 to central region, for example, then

$$\Delta \mathcal{Q}_0 = -Q_0' + Q_0, \tag{A.37}$$
$$\Delta \mathcal{Q}_1 = Q_1' - Q_1 - e, \tag{A.38}$$
$$\Delta \mathcal{Q}_2 = Q_2' - Q_2. \tag{A.39}$$

The intrinsic energy change associated with the tunneling of an electron across one junction is given by

$$\Delta U = \Delta E - W. \tag{A.40}$$

In this way, we finally obtain that

$$\Delta U_i^{(\pm)} = \mp e \left[V_{\mathrm{M}}(N) - V_i \right] + E_c, \tag{A.41}$$

where

$$E_c = \frac{e^2}{2(C_0 + C_1 + C_2)}. \tag{A.42}$$

Analogy Between the Discretized Conductive Channel and Capacitors Connected in Series

The discretized conductive channel can be seen as many identical capacitors connected in series, with each cell being the middle region between two neighboring capacitors. We set the positive direction to be from the left reservoir to the left reservoir. Let $q_0, q_1, q_2, \cdots, q_L$ denote the charges stored in capacitors, then from electrodynamics we have

$$q_j = \alpha(\Phi_j - \Phi_{j+1}), \tag{A.43}$$

where $\alpha = \epsilon\Omega/\Delta x^2$ is the capacitance of each capacitor. Summing Eq. (A.43) with subscript running from $j = 0$ to $j = L$, we get

$$\frac{1}{\alpha} \sum_{j=0}^{L} q_j = \Phi_{\mathrm{L}} - \Phi_{\mathrm{R}}. \tag{A.44}$$

where the notations $\Phi_{\mathrm{L}} = \Phi_0$ and $\Phi_{\mathrm{R}} = \Phi_{L+1}$ are used for convenience. From the law of charge conservation, we have the recurrence

$$q_{j+1} - q_j = e(N_{j+1} - N_-), \tag{A.45}$$

according to which we can write down the following expressions:

$$q_0 = q_0, \tag{A.46}$$
$$q_1 = q_0 + e(N_1 - N_-), \tag{A.47}$$
$$q_2 = q_0 + e(N_1 - N_-) + e(N_2 - N_-), \tag{A.48}$$
$$\vdots$$
$$q_n = q_0 + e(N_1 - N_-) + e(N_2 - N_-) + \cdots + e(N_L - N_-). \tag{A.49}$$

Summing the above expressions and using Eq. (A.44), we obtain

$$q_0 = \frac{1}{L+1}\left[\alpha\left(\Phi_\mathrm{L} - \Phi_\mathrm{R}\right) - e\sum_{k=1}^{L}(L+1-k)(N_k - N_-)\right]. \tag{A.50}$$

When a particle of charge $+e$ transits from the ith to $(i+1)$th cell, the charges stored in the capacitors redistribute themselves, giving the following values,

$$q'_j = q_j + \frac{e}{L+1} - e\delta_{j,i}. \tag{A.51}$$

The intrinsic energy change associated with this transition is calculated as

$$\begin{aligned}\Delta U_{i,i+1} &= \Delta E - W \\ &= \frac{1}{2\alpha}\left[\sum_{j=0}^{L} q'^2_j - \sum_{j=0}^{L} q_j^2\right] - \left(\Phi_\mathrm{L}\Delta\mathcal{Q}_\mathrm{L} + \Phi_\mathrm{R}\Delta\mathcal{Q}_\mathrm{R}\right) \\ &= \frac{1}{2\alpha}\sum_{j=0}^{L}(q'_j + q_j)(q'_j - q_j) - \left[\Phi_\mathrm{L}(q'_0 - q_0) - \Phi_\mathrm{R}(q'_L - q_L)\right].\end{aligned} \tag{A.52}$$

Substituting Eqs. (A.44) and (A.51) into Eq. (A.52), we finally obtain that

$$\Delta U_{i,i+1} = +e(\Phi_{i+1} - \Phi_i) + \frac{e^2 L\Delta x^2}{2(L+1)\epsilon\Omega}, \tag{A.53}$$

which is in agreement with Eq. (A.10). For transitions at the boundaries, the above expression holds.

Appendix B

Stochastic Process of Langevin Type

The numbers of particles in the cells of discretized mesoscopic systems studied in this thesis are typically large. In this large-number limit, the Markov jump process describing the time evolution of the mesoscopic systems can be approximated by the corresponding Langevin stochastic process [86]. In this way, much faster simulation can be implemented. This appendix is meant to explicitly present the details of such approximation.

The Markov Stochastic Model in Section 3.2

In the limit where $N \gg 1$, the operators $\exp(\pm\partial_N)$ can be expanded up to second order in the partial derivatives ∂_N in Eq. (3.54). In this way, we get the Fokker-Planck equation

$$\partial_t \mathscr{P} = \sum_{i=0}^{2} \left\{ -\partial_N \left[\left(W_i^{(+)} - W_i^{(-)} \right) \mathscr{P} \right] + \partial_N^2 \left[\left(W_i^{(+)} + W_i^{(-)} \right) \mathscr{P} \right] \right\} \tag{B.1}$$

for the time evolution of the probability density $\mathscr{P}$. This shows that the variables N obeys the following stochastic differential equation of Langevin type,

$$\frac{\mathrm{d}N}{\mathrm{d}t} = \sum_{i=0}^{2} F_i, \tag{B.2}$$

expressed in terms of the fluxes

$$F_i = W_i^{(+)} - W_i^{(-)} + \sqrt{W_i^{(+)} + W_i^{(-)}}\,\xi_i(t), \tag{B.3}$$

and the Gaussian white noises $\xi_i(t)$ satisfying the properties:

$$\langle \xi_i(t) \rangle = 0, \tag{B.4}$$

$$\langle \xi_i(t)\xi_j(t') \rangle = \delta_{ij}\delta(t-t'). \tag{B.5}$$

The Conductive Channel in Chapter 4

In the limit where $N_i \gg 1$, the operators $\exp(\pm\partial_{N_i})$ can be expanded up to second order in the partial derivatives ∂_{N_i} in Eq. (4.20). In this way, we get the Fokker-Planck equation

$$\begin{aligned} \partial_t \mathscr{P} = \sum_{i=0}^{L} \Bigg\{ & -\partial_{N_i} \left[\left(W_{i-1}^{(+)} - W_{i-1}^{(-)} - W_i^{(+)} + W_i^{(-)} \right) \mathscr{P} \right] \\ & + \partial_{N_i}^2 \left[\frac{1}{2} \left(W_{i-1}^{(+)} + W_{i-1}^{(-)} + W_i^{(+)} + W_i^{(-)} \right) \mathscr{P} \right] + \partial_{N_i}\partial_{N_{i+1}} \left[-\left(W_i^{(+)} + W_i^{(-)} \right) \mathscr{P} \right] \Bigg\}. \end{aligned} \tag{B.6}$$

for the time evolution of the probability density $\mathscr{P}$. This shows that the variables N_i obeys the following stochastic differential equations of Langevin type,

$$\frac{\mathrm{d}N_i}{\mathrm{d}t} = F_{i-1} - F_i, \tag{B.7}$$

expressed in terms of the fluxes

$$F_i = W_i^{(+)} - W_i^{(-)} + \sqrt{W_i^{(+)} + W_i^{(-)}}\xi_i(t), \tag{B.8}$$

and the Gaussian white noises $\xi_i(t)$ satisfying the properties:

$$\langle \xi_i(t) \rangle = 0, \tag{B.9}$$
$$\langle \xi_i(t)\xi_j(t') \rangle = \delta_{ij}\delta(t-t'). \tag{B.10}$$

The p-n Junction Diode in Chapter 5

In the limit where $X \gg 1$, the operators $\exp(\pm\partial_X)$ can be expanded up to second order in the partial derivatives ∂_X in Eq. (5.41) ($X = N_i, P_i$). In this way, we get the Fokker-Planck equation

$$\begin{aligned}
\partial_t \mathscr{P} = \sum_{i=0}^{L} \Bigg\{ & -\partial_{N_i}\left[\left(W_{i-1}^{(+N)} - W_{i-1}^{(-N)} - W_i^{(+N)} + W_i^{(-N)}\right)\mathscr{P}\right] \\
& + \partial_{N_i}^2\left[\frac{1}{2}\left(W_{i-1}^{(+N)} + W_{i-1}^{(-N)} + W_i^{(+N)} + W_i^{(-N)}\right)\mathscr{P}\right] \\
& + \partial_{N_i}\partial_{N_{i+1}}\left[-\left(W_i^{(+N)} + W_i^{(-N)}\right)\mathscr{P}\right] + (N \rightleftharpoons P)\Bigg\} \\
& + \sum_{i=1}^{L}\Bigg\{ -(\partial_{N_i} + \partial_{P_i})\left[\left(W_i^{(+)} - W_i^{(-)}\right)\mathscr{P}\right] + (\partial_{N_i} + \partial_{P_i})^2\left[\frac{1}{2}\left(W_i^{(+)} + W_i^{(-)}\right)\mathscr{P}\right]\Bigg\}
\end{aligned} \tag{B.11}$$

for the time evolution of the probability density $\mathscr{P}$. This shows that the variables N_i and P_i obey the following stochastic differential equations of Langevin type:

$$\frac{\mathrm{d}N_i}{\mathrm{d}t} = F_{i-1}^{(N)} - F_i^{(N)} + R_i, \tag{B.12}$$
$$\frac{\mathrm{d}P_i}{\mathrm{d}t} = F_{i-1}^{(P)} - F_i^{(P)} + R_i, \tag{B.13}$$

expressed in terms of the fluxes and reaction rates:

$$F_i^{(N)} = W_i^{(+N)} - W_i^{(-N)} + \sqrt{W_i^{(+N)} + W_i^{(-N)}}\xi_i^{(N)}(t), \tag{B.14}$$
$$F_i^{(P)} = W_i^{(+P)} - W_i^{(-P)} + \sqrt{W_i^{(+P)} + W_i^{(-P)}}\xi_i^{(P)}(t), \tag{B.15}$$
$$R_i = W_i^{(+)} - W_i^{(-)} + \sqrt{W_i^{(+)} + W_i^{(-)}}\eta_i(t), \tag{B.16}$$

and the Gaussian white noises $\xi_i^{(N)}(t)$, $\xi_i^{(P)}(t)$, $\eta_i(t)$ satisfying the properties:

$$\langle \xi_i^{(N)}(t) \rangle = \langle \xi_i^{(P)}(t) \rangle = \langle \eta_i(t) \rangle = 0, \tag{B.17}$$
$$\langle \xi_i^{(N)}(t)\xi_j^{(N)}(t') \rangle = \langle \xi_i^{(P)}(t)\xi_j^{(P)}(t') \rangle = \langle \eta_i(t)\eta_j(t') \rangle = \delta_{ij}\delta(t-t'), \tag{B.18}$$
$$\langle \xi_i^{(N)}(t)\xi_j^{(P)}(t') \rangle = \langle \eta_i(t)\xi_j^{(N)}(t') \rangle = \langle \eta_i(t)\xi_j^{(P)}(t') \rangle = 0. \tag{B.19}$$

The Bipolar n-p-n Junction Transistor in Chapter 6

In the limit where $X \gg 1$, the operators $\exp(\pm\partial_X)$ can be expanded up to second order in the partial derivatives ∂_X in Eq. (6.19) ($X = N_i, P_i$). In this way, we have the following Fokker-Planck equation

$$\begin{aligned}
\partial_t \mathscr{P} = &\sum_{i=1}^{L} \Bigg\{ - \partial_{N_i} \left[\left(W_{i-1}^{(+N)} - W_{i-1}^{(-N)} - W_i^{(+N)} + W_i^{(-N)} \right) \mathscr{P} \right] \\
&+ \partial_{N_i}^2 \left[\frac{1}{2} \left(W_{i-1}^{(+N)} + W_{i-1}^{(-N)} + W_i^{(+N)} + W_i^{(-N)} \right) \mathscr{P} \right] \\
&+ \partial_{N_i} \partial_{N_{i+1}} \left[- \left(W_i^{(+N)} + W_i^{(-N)} \right) \mathscr{P} \right] + (N \rightleftharpoons P) \Bigg\} \\
&+ \sum_{i=1}^{L} \Bigg\{ - (\partial_{N_i} + \partial_{P_i}) \left[\left(W_i^{(+)} - W_i^{(-)} \right) \mathscr{P} \right] \\
&+ (\partial_{N_i} + \partial_{P_i})^2 \left[\frac{1}{2} \left(W_i^{(+)} + W_i^{(-)} \right) \mathscr{P} \right] \Bigg\} \\
&+ \sum_{iB} \Bigg\{ - \partial_{N_i} \left[\left(W_{iB}^{(+N)} - W_{iB}^{(-N)} \right) \mathscr{P} \right] \\
&+ \partial_{N_i}^2 \left[\frac{1}{2} \left(W_{iB}^{(+N)} + W_{iB}^{(-N)} \right) \mathscr{P} \right] + (N \rightleftharpoons P) \Bigg\},
\end{aligned} \tag{B.20}$$

for the time evolution of the probability density $\mathscr{P}$. This shows that the variables N_i and P_i obey stochastic differential equations of Langevin type:

$$\frac{\mathrm{d}N_i}{\mathrm{d}t} = F_{i-1}^{(N)} - F_i^{(N)} + R_i + \chi_{iB} F_{iB}^{(N)}, \tag{B.21}$$

$$\frac{\mathrm{d}P_i}{\mathrm{d}t} = F_{i-1}^{(P)} - F_i^{(P)} + R_i + \chi_{iB} F_{iB}^{(P)}, \tag{B.22}$$

with the following fluxes and reaction rates:

$$F_i^{(N)} = W_i^{(+N)} - W_i^{(-N)} + \sqrt{W_i^{(+N)} + W_i^{(-N)}}\, \xi_i^{(N)}(t), \tag{B.23}$$

$$F_i^{(P)} = W_i^{(+P)} - W_i^{(-P)} + \sqrt{W_i^{(+P)} + W_i^{(-P)}}\, \xi_i^{(P)}(t), \tag{B.24}$$

$$R_i = W_i^{(+)} - W_i^{(-)} + \sqrt{W_i^{(+)} + W_i^{(-)}}\, \eta_i(t), \tag{B.25}$$

$$F_{iB}^{(N)} = W_{iB}^{(+N)} - W_{iB}^{(-N)} + \sqrt{W_{iB}^{(+N)} + W_{iB}^{(-N)}}\, \xi_{iB}^{(N)}(t), \tag{B.26}$$

$$F_{iB}^{(P)} = W_{iB}^{(+P)} - W_{iB}^{(-P)} + \sqrt{W_{iB}^{(+P)} + W_{iB}^{(-P)}}\, \xi_{iB}^{(P)}(t), \tag{B.27}$$

and the Gaussian white noises $\xi_i^{(N)}(t)$, $\xi_i^{(P)}(t)$, $\eta_i(t)$, $\xi_{iB}^{(N)}(t)$, $\xi_{iB}^{(P)}(t)$ satisfying the properties:

$$\langle \xi_i^{(N)}(t)\rangle = \langle \xi_i^{(P)}(t)\rangle = \langle \eta_i(t)\rangle = \langle \xi_{iB}^{(N)}(t)\rangle = \langle \xi_{iB}^{(P)}(t)\rangle = 0, \tag{B.28}$$

$$\langle \xi_i^{(N)}(t)\, \xi_j^{(N)}(t')\rangle = \delta_{ij}\delta(t-t'), \tag{B.29}$$

$$\langle \xi_i^{(P)}(t)\, \xi_j^{(P)}(t')\rangle = \delta_{ij}\delta(t-t'), \tag{B.30}$$

$$\langle \eta_i(t)\, \eta_j(t')\rangle = \delta_{ij}\delta(t-t'), \tag{B.31}$$

$$\langle \xi_{iB}^{(N)}(t)\, \xi_{jB}^{(N)}(t')\rangle = \delta_{ij}\delta(t-t'), \tag{B.32}$$

$$\langle \xi_{iB}^{(P)}(t)\, \xi_{jB}^{(P)}(t')\rangle = \delta_{ij}\delta(t-t'), \tag{B.33}$$

$$\langle \xi_i^{(N)}(t)\, \xi_j^{(P)}(t')\rangle = \langle \xi_{iB}^{(N)}(t)\, \xi_{jB}^{(P)}(t')\rangle = 0, \tag{B.34}$$

$$\langle \eta_i(t)\, \xi_j^{(N,P)}(t')\rangle = \langle \eta_i(t)\, \xi_{jB}^{(N,P)}(t')\rangle = \langle \xi_i^{(N,P)}(t)\, \xi_{jB}^{(N,P)}(t')\rangle = 0. \tag{B.35}$$

Discretized Langevin Stochastic Process in Time

To simulate the Langevin stochastic process, time is discretized into equal intervals Δt and the white Gaussian noises are replaced by Gaussian random variables. The typical stochastic differential equation of Langevin type reads

$$\frac{\mathrm{d}X}{\mathrm{d}t} = F, \tag{B.36}$$

with the fluctuating flux given by

$$F = W_+ - W_- + \sqrt{W_+ + W_-}\,\xi(t). \tag{B.37}$$

Here, $\xi(t)$ is the Gaussian white noise that satisfy the properties:

$$\langle \xi(t)\rangle = 0, \tag{B.38}$$

$$\langle \xi(t)\xi(t')\rangle = \delta(t-t'). \tag{B.39}$$

By discretization in time, we get

$$X(t+\Delta t) = X(t) + F\Delta t, \tag{B.40}$$

where

$$F = W_+ - W_- + \sqrt{W_+ + W_-}\,\frac{G(t)}{\sqrt{\Delta t}}, \tag{B.41}$$

with $G(t)$ being the independent identically distributed Gaussian random variables of zero mean value and unit variance[1]. After the discretization of time into equal intervals Δt, the evolution can be simulated with a recurrence involving independent Gaussian random variables. Moreover, the currents can be expressed in the framework of Langevin stochastic process.

[1]The library GSL provides the function `gsl_ran_gaussian` for generating the Gaussian random numbers, with the mean $\mu = 0$ and the standard deviation σ as one of the arguments.

Appendix C

The Continuum Limit

The Conductive Channel in Chapter 4

In the continuum limit where $\Delta x \to 0$ and $\Delta t \to 0$, we can recover the stochastic partial differential equations (4.7) with the current density (4.8) from the Langevin stochastic equations (B.7)-(B.8), as follows. First, we note that the approximation $\psi(\Delta U) \approx \exp(-\beta\Delta U/2)$ holds if $\beta\Delta U \ll 1$. Next, using Eqs. (4.21), (4.22), and (4.23) in the limit $\Delta x \to 0$, Eq. (B.8) gives the flux

$$F_i \approx -\frac{D}{\Delta x^2}\mathrm{e}^{-\beta e\Phi_{i+1/2}}\left(\mathrm{e}^{\beta e\Phi_{i+1}}N_{i+1} - \mathrm{e}^{\beta e\Phi_i}N_i\right) + \frac{1}{\Delta x}\sqrt{D(N_i + N_{i+1})}\xi_i(t), \tag{C.1}$$

where $\Phi_{i+1/2} \approx (\Phi_i + \Phi_{i+1})/2$. Substituting this expression into Eq. (B.7), we find the continuity equation (4.7) with the current density (4.8) in the form (4.14). Because of Eqs. (B.8)-(B.10), the noise fields obey Eqs. (4.11)-(4.13). The stochastic partial differential equation is thus recovered in the continuum limit.

The p-n Junction Diode in Chapter 5

In the continuum limit where $\Delta x \to 0$ and $\Delta t \to 0$, we can recover the stochastic partial differential equations (5.13)-(5.14) with the current and rate densities (5.15)-(5.17) from the Langevin stochastic equations (B.12)-(B.16), as follows. Again, we note that the approximation $\psi(\Delta U) \approx \exp(-\beta\Delta U/2)$ holds if $\beta\Delta U \ll 1$. Next, using Eqs. (5.42), (5.43), and (5.48) in the limit $\Delta x \to 0$, Eq. (B.14) gives the flux

$$F_i^{(N)} \approx -\frac{D_n}{\Delta x^2}\mathrm{e}^{\beta e\Phi_{i+1/2}}\left(\mathrm{e}^{-\beta e\Phi_{i+1}}N_{i+1} - \mathrm{e}^{-\beta e\Phi_i}N_i\right) + \frac{1}{\Delta x}\sqrt{D_n(N_i + N_{i+1})}\xi_i^{(N)}(t), \tag{C.2}$$

where $\Phi_{i+1/2} \approx (\Phi_i + \Phi_{i+1})/2$. Besides, using Eqs. (5.46) and (5.47), the rate (B.16) becomes

$$R_i = \Omega\left(k_+ - k_-\frac{N_i}{\Omega}\frac{P_i}{\Omega}\right) + \sqrt{\Omega\left(k_+ + k_-\frac{N_i}{\Omega}\frac{P_i}{\Omega}\right)}\eta_i(t). \tag{C.3}$$

Substituting these expressions into Eq. (B.12) and dividing it by Ω, we find the electron balance equation (5.13) with the current density (5.15) in the form (5.30), together with the source (5.17). The hole balance equation (5.14) is similarly deduced from Eq. (B.13). Because of Eqs. (B.14)-(B.19), the noise fields obey Eqs. (5.20)-(5.29) since $\delta_{ij}/\Omega \to \delta^3(\mathbf{r} - \mathbf{r}')$ in the limit $\Omega \to 0$. The stochastic partial differential equations are thus recovered in the continuum limit.

Appendix D

Variable Rescaling

For numerical convenience, the values of physical quantities and parameters listed in Tables 5.1, 5.2 and 6.1 are directly used in simulation. Accordingly, the results in Chapters 5 and 6 are also given in terms of these values that are used in the simulations. In this appendix, we present a procedure for recaling the variables so that dimensionless quantities can be defined. In this way, it becomes possible to the compare these dimensionless quantities with those from experiments which should be also converted to dimensionless ones according to the same procedure.

The intrinsic carrier density $\nu = \sqrt{k_+/k_-}$ introduced in Eq. (5.4) is used to define the dimensionless densities of all charge carriers[1],

$$n_* \equiv n/\nu, \quad p_* \equiv p/\nu, \quad a_* \equiv a/\nu, \quad d_* \equiv d/\nu. \tag{D.1}$$

The intrinsic carrier lifetime is introduced,

$$\tau = \frac{1}{k_-\nu} = \frac{1}{\sqrt{k_+k_-}}, \tag{D.2}$$

so that we can define the dimensionless time

$$t_* \equiv t/\tau. \tag{D.3}$$

Considering that $D_n = D_p = D$ is supposed in simulation, the position is rescaled as

$$x_* \equiv x/l_{\text{diff}}, \qquad \text{where} \qquad l_{\text{diff}} = \sqrt{D\tau} = \sqrt{\frac{D}{\sqrt{k_+k_-}}} \tag{D.4}$$

is the intrinsic carrier diffusion length before recombination. As a consequence of these definitions, the dimensionless current densities are given by

$$j_{n*} \equiv \frac{j_n}{j_{\text{unit}}}, \quad j_{p*} \equiv \frac{j_p}{j_{\text{unit}}}, \qquad \text{with} \qquad j_{\text{unit}} = \frac{\nu l_{\text{diff}}}{\tau} = \sqrt{\sqrt{\frac{k_+}{k_-}} \cdot k_+ D}. \tag{D.5}$$

The dimensionless electric field and potential are defined by

$$\mathcal{E}_* \equiv \frac{\mathcal{E}}{\mathcal{E}_{\text{unit}}} \qquad \text{with} \qquad \mathcal{E}_{\text{unit}} = \frac{1}{l_{\text{diff}}\beta e} = \sqrt{\frac{\sqrt{k_+k_-}}{D}} \cdot \frac{1}{\beta e}, \tag{D.6}$$

[1] This ν denotes the electron and hole densities in the so-called intrinsic semiconductor where there is no impurity doped.

and

$$\Phi_* \equiv \frac{\Phi}{\Phi_{\text{unit}}} \qquad \text{with} \qquad \Phi_{\text{unit}} = \frac{1}{\beta e}. \tag{D.7}$$

Using the values listed in Table 5.1, we have

$$\nu = 1, \quad \tau = 100, \quad l_{\text{diff}} = 1, \quad j_{\text{unit}} = 0.01, \quad \mathcal{E}_{\text{unit}} = 1, \quad \Phi_{\text{unit}} = 1, \tag{D.8}$$

and the relevant numerical results in Chapters 5 and 6 can be easily converted to the dimensionless ones by dividing values in Eq. (D.8).

According to the above procedure of variable rescaling, the set of ODEs (5.32)-(5.37) takes the following dimensionless form:

$$\frac{\mathrm{d}n_*}{\mathrm{d}x_*} = -j_{n*} - n_*\mathcal{E}_*, \tag{D.9}$$

$$\frac{\mathrm{d}p_*}{\mathrm{d}x_*} = -j_{p*} + p_*\mathcal{E}_*, \tag{D.10}$$

$$\frac{\mathrm{d}j_{n*}}{\mathrm{d}x_*} = 1 - n_*p_*, \tag{D.11}$$

$$\frac{\mathrm{d}j_{p*}}{\mathrm{d}x_*} = 1 - n_*p_*, \tag{D.12}$$

$$\frac{\mathrm{d}\mathcal{E}_*}{\mathrm{d}x_*} = \alpha\left(p_* - n_* + d_* - a_*\right), \tag{D.13}$$

$$\frac{\mathrm{d}\Phi_*}{\mathrm{d}x_*} = -\mathcal{E}_*. \tag{D.14}$$

These ODEs only depend on the unique dimensionless parameter

$$\alpha \equiv \left(\frac{l_{\text{diff}}}{\lambda}\right)^2 = \epsilon^{-1}\beta e\nu D\tau, \tag{D.15}$$

where

$$\lambda \equiv \sqrt{\frac{\epsilon}{\beta e^2 \nu}} \tag{D.16}$$

is the intrinsic Debye screening length.

Appendix E

Numerical Methods

In this appendix, we briefly introduce some numerical methods that have been used in this thesis.

Newton-Raphson Method

In numerical analysis, the Newton-Raphson method is a root-finding algorithm for iteratively producing better approximations to the roots of nonlinear equations. Suppose that $\mathbf{F}(\mathbf{x})$ is an operator from the linear normed space $\mathcal{H}$ to the linear normed space $\mathcal{Y}$. These two spaces can be identical with each other, and their norms are denoted by $||\cdot||_{\mathcal{H}}$ and $||\cdot||_{\mathcal{Y}}$, respectively. If when $||\mathbf{h}||_H \to 0$ we have

$$||\mathbf{F}(\mathbf{x}+\mathbf{h}) - \mathbf{F}(\mathbf{x}) - \mathbf{P}\cdot\mathbf{h}||_{\mathcal{Y}} = O(||\mathbf{h}||_{\mathcal{H}}^2), \tag{E.1}$$

then we call $\mathbf{P}$ the derivative operator of $\mathbf{F}(\mathbf{x})$ at point $\mathbf{x}$ from $\mathcal{H}$ to $\mathcal{Y}$. We henceforth use $\mathbf{F}'(\mathbf{x})$ as the notation for the derivative operator $\mathbf{P}$. In vector form, $\mathbf{F}$, $\mathbf{x}$, $\mathbf{h}$ are written as

$$\mathbf{F} = \begin{pmatrix} F_1 \\ \vdots \\ F_m \end{pmatrix}, \qquad \mathbf{x} = \begin{pmatrix} x_1 \\ \vdots \\ x_m \end{pmatrix}, \qquad \mathbf{h} = \begin{pmatrix} h_1 \\ \vdots \\ h_m \end{pmatrix}. \tag{E.2}$$

If the function F_i is continuous and differentiable in the neighborhood of $\mathbf{x}$, then

$$F_i(x_1+h_1,\cdots,x_m+h_m) = F_i(x_1,\cdots,x_m) + \sum_{j=1}^{m} \frac{\partial F_i(x_1,\cdots,x_m)}{\partial x_j} h_j + O(||\mathbf{h}||_{\mathcal{H}}^2). \tag{E.3}$$

So the derivative operator $\mathbf{F}'(\mathbf{x})$ can be expressed in matrix form as

$$\mathbf{F}'(\mathbf{x}) = \left[\frac{\partial F_i}{\partial x_j}\right]. \tag{E.4}$$

Now, suppose that $\mathbf{X}$ is the root of equation $\mathbf{F}(\mathbf{x}) = \mathbf{0}$, $\mathbf{x}_n$ is an approximation to $\mathbf{X}$, then we have

$$||\mathbf{F}(\mathbf{X}) - \mathbf{F}(\mathbf{x}_n) - \mathbf{F}'(\mathbf{x}_n)\cdot(\mathbf{X}-\mathbf{x}^n)||_{\mathcal{Y}} = O(||\mathbf{X}-\mathbf{x}_n||_{\mathcal{H}}^2), \tag{E.5}$$

which can be approximately written as

$$\mathbf{F}(\mathbf{x}_n) + \mathbf{F}'(\mathbf{x}_n)\cdot(\mathbf{X}-\mathbf{x}_n) \approx \mathbf{F}(\mathbf{X}) \tag{E.6}$$

if $||\mathbf{X}-\mathbf{x}^n||$ is very small. Because $\mathbf{F}(\mathbf{X}) = \mathbf{0}$, we have

$$\mathbf{F}(\mathbf{x}_n) + \mathbf{F}'(\mathbf{x}_n)\cdot(\mathbf{X}-\mathbf{x}_n) \approx \mathbf{0}. \tag{E.7}$$

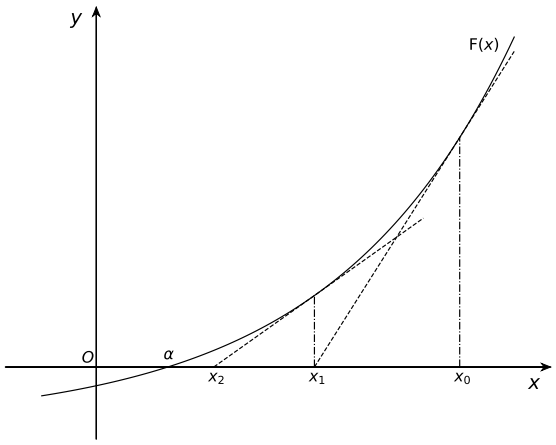

Figure E.1: Schematic diagram of the Newton-Raphson method in the one-dimensional case.

If the root of equation

$$\mathbf{F}(\mathbf{x}_n) + \mathbf{F}'(\mathbf{x}_n) \cdot (\mathbf{X} - \mathbf{x}_n) = \mathbf{0} \tag{E.8}$$

exists, then it can be used as a further approximation to $\mathbf{X}$ and calculated as

$$\mathbf{x}_{n+1} = \mathbf{x}_n - (\mathbf{F}'(\mathbf{x}_n))^{-1} \cdot \mathbf{F}(\mathbf{x}_n). \tag{E.9}$$

This iterative process begins with an initial guess $\mathbf{x}_0$ for the root of $\mathbf{F}(\mathbf{x}) = \mathbf{0}$, and successively gives better and better approximation. Figure E.1 schematically shows how the Newton-Raphson method implemented with a one-dimensional function $f(x)$. For more detailed account of the Newton-Raphson, readers are referred to Ref. [113].

Numerical Differentiation and Interpolation

In numerical analysis, differentiation describes the procedure for estimating the derivatives of a mathematical function using several data points of this function. The simplest method is to use finite difference approximations. In the following, we list some central-difference formulae approximating the derivatives with the truncation error of different orders. Given some values of a one-variable function $f(x)$ at several equispaced nodes

$$\{ih\} \qquad \text{for} \qquad i = -n, \cdots, n, \tag{E.10}$$

we have

$$f'(0) \approx \frac{f_1 - f_{-1}}{2h}, \tag{E.11}$$

$$f''(0) \approx \frac{f_1 - 2f_0 + f_{-1}}{h^2}, \tag{E.12}$$

$$f^{(3)}(0) \approx \frac{f_2 - 2f_1 + 2f_{-1} - f_{-2}}{2h^3}, \tag{E.13}$$

$$f^{(4)}(0) \approx \frac{f_2 - 4f_1 + 6f_0 - 4f_{-1} + f_{-2}}{h^4}, \tag{E.14}$$

all with the truncation error of order $O(h^2)$. Here, h denotes the equispaced interval and f_i is the short-hand notation of the function value $f(ih)$. The formulae of higher order $O(h^4)$ are given by

$$f'(0) \approx \frac{-f_2 + 8f_1 - 8f_{-1} + f_{-2}}{12h}, \tag{E.15}$$

$$f''(0) \approx \frac{-f_2 + 16f_1 - 30f_0 + 16f_{-1} - f_{-2}}{12h^2}, \tag{E.16}$$

$$f^{(3)}(0) \approx \frac{-f_3 + 8f_2 - 13f_1 + 13f_{-1} - 8f_{-2} + f_{-3}}{8h^3}, \tag{E.17}$$

$$f^{(4)}(0) \approx \frac{-f_3 + 12f_2 - 39f_1 + 56f_0 - 39f_{-1} + 12f_{-2} - f_{-3}}{6h^4}. \tag{E.18}$$

These formulae can be checked with Taylor series. For mixed partial derivatives of $f(x, y)$, the function values $f_{i,j}$ [short-hand notation of $f(ih_1, jh_2)$] at a grid of equispaced nodes

$$\{(ih_1, jh_2)\} \qquad \text{for} \qquad i = -n, \cdots n \qquad \text{and} \qquad j = -m, \cdots, m, \tag{E.19}$$

are used. Here, h_1 and h_2 are equispaced intervals in the x-axis and y-axis, respectively. Some relevant formulae are

$$\frac{\partial^2 f}{\partial x \partial y}(0,0) = \frac{f_{1,1} - f_{1,-1} - f_{-1,1} + f_{-1,-1}}{4h_1 h_2} + O(h_1^2 h_2^2), \tag{E.20}$$

$$\frac{\partial^3 f}{\partial x^2 \partial y}(0,0) = \frac{f_{1,1} - 2f_{0,1} + f_{-1,1} - f_{1,-1} + 2f_{0,-1} - f_{-1,-1}}{2h_1^2 h_2} + O(h_1^2 h_2^2), \tag{E.21}$$

$$\frac{\partial^4 f}{\partial x^2 \partial y^2}(0,0) = \frac{f_{1,1} - 2f_{0,1} + f_{-1,1} - 2f_{1,0} + 4f_{0,0} - 2f_{-1,0} + f_{1,-1} - 2f_{0,-1} + f_{-1,-1}}{h_1^2 h_2^2} + O(h_1^2 h_2^2), \tag{E.22}$$

which can be deduced by integrating the formulae for one-variable functions.

In numerical analysis, interpolation describes the procedure used to construct a function which goes through a given set of data points. According to the Weierstrass approximation theorem [114], for every continuous function $f(x)$ defined on an interval $[a, b]$, there exists a set of polynomial functions $P_n(x)$ for $n = 0, 1, 2, \cdots$, each of degree n, that approximates $f(x)$ with uniform convergence over $[a, b]$ as n tends to infinity, that is

$$\lim_{n\to\infty} \left(\max_{a \le x \le b} |f(x) - P_n(x)| \right) = 0. \tag{E.23}$$

One the other hand, the polynomial $P_n(x)$ of degree n interpolating the $n + 1$ points

$$\{x_i, f(x_i)\} \qquad \text{for} \qquad i = 0, \cdots, n, \tag{E.24}$$

is unique. Three standard interpolation methods are available, i.e., those of Vandermonde, Newton, Lagrange [115, 116]. In the following, we only present the Lagrange interpolation which is the most clever construction of the interpolating polynomial directly leading to an analytical formula. We henceforth use $L_n(x)$ as the notation of $P_n(x)$, indicating that the polynomial is obtained with the Lagrange method. The Lagrange polynomial is constructed as follows,

$$L_n(x) = \sum_{i=0}^{n} \left[\prod_{j=0, j\neq i}^{n} \left(\frac{x - x_j}{x_i - x_j} \right) \right] f(x_i), \tag{E.25}$$

with the residual given by

$$R_n(x) = f(x) - L_n(x) = \frac{f^{(n+1)}(\xi)}{(n+1)!} \omega_{n+1}(x), \tag{E.26}$$

where

$$\omega_{n+1} = \prod_{j=0}^{n}(x - x_j). \tag{E.27}$$

For the two-variable function $f(x, y)$, the Lagrange polynomial

$$L(x, y) = \sum_{i,j}\left[\prod_{m\neq i, n\neq j}\left(\frac{x - x_m}{x_i - x_m}\right)\left(\frac{y - y_n}{y_j - y_n}\right)\right] f(x_i, y_j) \tag{E.28}$$

is constructed using the points distributed on a regular grid. Interestingly, some formulae of numerical differentiation can be obtained by differentiating Lagrange polynomials interpolating the several given points. One thing to be cautious is the Runge's phenomenon which is the problem of oscillations at the edges of an interval that occurs when using polynomial interpolation with too high degree over a set of equispaced interpolation points. For more detailed account of interpolation, readers are referred to Refs. [115, 116].

Padé Approximation

In mathematics, Padé approximants form a particular type of rational fraction approximation to the value of the function. They often gives a better approximation of the function than truncating its Taylor series and may still work where the Taylor series does not converge. For these reasons Padé approximants are extensively used in computer calculations. A function $f(x)$ is represented by a formal power series,

$$f(x) = c_0 + c_1 x + c_2 x^2 + \cdots = \sum_{l=0}^{\infty} c_l x^l, \tag{E.29}$$

where $c_0 \neq 0$ by convention. The Padé approximation to $f(x)$ is the quotient

$$R_{m,n}(x) = \frac{P_m(x)}{Q_n(x)} = \frac{a_0 + a_1 x + a_2 x^2 + \cdots + a_m x^m}{b_0 + b_1 x + b_2 x^2 + \cdots + b_n x^n}, \tag{E.30}$$

where $P_m(x)$ and $Q_n(x)$ are polynomials of degrees m and n, respectively. The denominator is usually normalized by setting $b_0 = 1$. So, $f(x) = R_{m,n}(x)$ gives

$$\left(c_0 + c_1 x + c_2 x^2 + \cdots\right)\left(1 + b_1 x + b_2 x^2 + \cdots + b_n x^n\right) = a_0 + a_1 x + a_2 x^2 + \cdots + a_m x^m, \tag{E.31}$$

the $m + 1$ independent numerator coefficients and n denominator coefficients making $m + n + 1$ unknown coefficients. Equating the coefficients of x^{m+1}, x^{m+2}, $\cdots$, x^{m+n} in Eq. (E.31), we get

$$b_n c_{m-n+1} + b_{n-1} c_{m-n+2} + \cdots + c_{m+1} = 0, \tag{E.32}$$
$$b_n c_{m-n+2} + b_{n-1} c_{m-n+3} + \cdots + c_{m+2} = 0, \tag{E.33}$$
$$\vdots$$
$$b_n c_m + b_{n-1} c_{m+1} + \cdots + c_{m+n} = 0, \tag{E.34}$$

which becomes a set of n linear equations for the n unknown denominator coefficients. By solving the system of linear equation we find b_i. The numerator coefficients a_0, a_1, $\cdots$, a_m immediately

Table E.1: A portion of the Padé table for exponential function e^x.

$\frac{1}{1}$	$\frac{1}{1-x}$	$\frac{1}{1-x+\frac{1}{2}x^2}$	$\frac{1}{1-x+\frac{1}{2}x^2-\frac{1}{6}x^3}$
$\frac{1+x}{1}$	$\frac{1+\frac{1}{2}x}{1-\frac{1}{2}x}$	$\frac{1+\frac{1}{3}x}{1-\frac{2}{3}x+\frac{1}{6}x^2}$	$\frac{1+\frac{1}{4}x}{1-\frac{3}{4}x+\frac{1}{4}x^2-\frac{1}{24}x^3}$
$\frac{1+x+\frac{1}{2}x^2}{1}$	$\frac{1+\frac{2}{3}x+\frac{1}{6}x^2}{1-\frac{1}{3}x}$	$\frac{1+\frac{1}{2}x+\frac{1}{12}x^2}{1-\frac{1}{2}x+\frac{1}{12}x^2}$	$\frac{1+\frac{2}{5}x+\frac{1}{20}x^2}{1-\frac{3}{5}x+\frac{3}{20}x^2-\frac{1}{60}x^3}$
$\frac{1+x+\frac{1}{2}x^2+\frac{1}{6}x^3}{1}$	$\frac{1+\frac{3}{4}x+\frac{1}{4}x^2+\frac{1}{24}x^3}{1-\frac{1}{4}x}$	$\frac{1+\frac{3}{5}x+\frac{3}{20}x^2+\frac{1}{60}x^3}{1-\frac{2}{5}x+\frac{1}{20}x^2}$	$\frac{1-\frac{1}{2}x+\frac{1}{10}x^2+\frac{1}{120}x^3}{1-\frac{1}{2}x+\frac{1}{10}x^2-\frac{1}{120}x^3}$

follow from Eq. (E.31) by equating the coefficients of 1, x, x^2, $\cdots$, x_m:

$$a_0 = c_0, \tag{E.35}$$
$$a_1 = c_1 + b_1 c_0, \tag{E.36}$$
$$a_2 = c_2 + b_1 c_1 + b_2 c_0, \tag{E.37}$$
$$\vdots$$
$$a_m = c_m + \sum_{i=1}^{m} b_i c_{m-i}. \tag{E.38}$$

After obtaining all the coefficients in the polynomials $P_m(x)$ and $Q_n(x)$, the Padé approximant $R_{m,n}(x)$ is calculated. It is common practice to display the Padé approximants $R_{m,n}$ in a table which is therefore called Padé table. Table E.1 is a portion of Padé table for the exponential function e^x. For detailed account of Padé approximation, readers are referred to Refs. [117, 118, 119][1].

Error Analysis

The formula for derivatives approximated by numerical differences can be written in the following general form,

$$\frac{\partial^{m+n} f}{\partial x^m \partial y^n} = \sum_{i,j} k_{i,j} f(x_i, y_j) + O(h_1^r h_2^s). \tag{E.39}$$

Apart from the truncation error itself, another source of error is the numerical evaluation of the function at different points. Suppose that the variances of the numerical values of the function are denoted as $\sigma^2 [f(x_i, y_j)]$, then the root-mean-square errors on the derivatives (E.39) can be evaluated as

$$\mathrm{RMSE}\left(\frac{\partial^{m+n} f}{\partial x^m \partial y^n}\right) \equiv \sqrt{\sigma^2 \left[\frac{\partial^{m+n} f}{\partial x^m \partial y^n}\right]} \approx \sqrt{\sum_{i,j} k_{i,j}^2 \sigma^2 [f(x_i, y_j)]} \tag{E.40}$$

up to a correction of $O(h_1^r h_2^s)$ coming from truncation error.

Given a random sample $\{Z_1, \cdots, Z_n\}$ of size n from a Gaussian distribution of mean value μ and variance σ^2, the sample average is defined as $\langle Z \rangle = (1/n) \sum_{i=1}^{n} Z_i$, having the expected value

[1] The Python package Scipy provides the function `linalg.expm` for computing the matrix exponential using Padé approximation.

μ. The sample average $\langle Z \rangle$ has the root-mean-square error

$$\mathrm{RMSE}\left(\langle Z \rangle\right) = \sqrt{\mathbb{E}\left[\left(\frac{1}{n}\sum_{i=1}^{n} Z_i - \mu\right)^2\right]} = \sqrt{\frac{\sigma^2}{n}}. \tag{E.41}$$

The unbiased sample variance $S^2_{n-1} = \sum_{i=1}^{n}(Z - \langle Z \rangle)^2/(n-1)$ has the expected value σ^2 and the root-mean-square error on it is equal to

$$\mathrm{RMSE}\left(S^2_{n-1}\right) = \sqrt{\mathbb{E}\left[\left(\frac{1}{n-1}\sum_{i=1}^{n}\left(Z - \langle Z \rangle\right)^2 - \sigma^2\right)^2\right]} = \sqrt{\frac{2}{n-1}\sigma^4}. \tag{E.42}$$

If we define the mean current $J \equiv \langle Z \rangle / t$ and the diffusivity $D \equiv S^2_{n-1}/(2t)$, then the root-mean-square errors on them can be estimated as

$$\mathrm{RMSE}\left(J\right) = \sqrt{\frac{\sigma^2}{nt^2}} \approx \sqrt{\frac{2D}{nt}}, \tag{E.43}$$

$$\mathrm{RMSE}\left(D\right) = \sqrt{\frac{2\sigma^4}{4t^2(n-1)}} \approx \sqrt{\frac{2D^2}{n-1}}. \tag{E.44}$$

The procedure used to estimate the error on numerical computation of the affinities $A_1 = \ln(W_{10}/W_{01})$ and $A_2 = \ln(W_{20}/W_{02})$ in the Section 3.2 is as follows. From Eqs. (3.111)-(3.118), the expressions of the numerical affinities are expanded with respect to the values of the mean currents and their diffusivities up to linear terms such as

$$\Delta A_1 \approx a\Delta J_1 + b\Delta J_2 + c\Delta D_{11} + d\Delta D_{22} + e\Delta D_{12}, \tag{E.45}$$

in terms of some coefficients a, b, c, d, and e, which are related to the transition rates in Eqs.(3.111)-(3.116). Accordingly, the root-mean-square error is estimated as

$$\mathrm{RMSE}\left(A_1\right) \approx \sqrt{a^2\sigma^2(J_1) + b^2\sigma^2(J_2) + c^2\sigma^2(D_{11}) + d^2\sigma^2(D_{22}) + e^2\sigma^2(D_{12})}, \tag{E.46}$$

where $\sigma^2(J_i)$ and $\sigma^2(D_{ij})$ are the variances which apparently can be obtained as the square of Eqs. (E.43)-(E.44). A similar expression holds for the error on A_2.

Appendix F

Computer Programming

> *Computer programming is an art, because it applies accumulated knowledge to the world, because it requires skill and ingenuity, and especially because it produces objects of beauty. A programmer who subconsciously views himself as an artist will enjoy what he does and will do it better.*
>
> — Donald E. Knuth

Computer programming plays an increasing important role in scientific research. Actually, it has become one of the pillars in scientific research, to be complementary with theory and experiment. A scientist might build a model to describe a physical system according to the underlying laws, then use a computer to calculate the results and display them. This has become a widely adopted paradigm in scientific community. So, computer programming is an essential part of training for a student to become a scientist. A set of easy-to-adopt and effective practices for computer programming are described in Ref. [120]. In order to give readers a glimpse at the numerical work behind presented results, the present appendix is devoted to some general aspects of computer programming in this thesis studies. In this appendix, we will have some general remarks about object-oriented programming, briefly introduce some useful softwares and libraries, and show some C++ codes used for numerical simulations.

Object-Oriented Programming with C++ and Python

Object-oriented programming (OOP) is a programming paradigm focusing on objects, which are entities associated with attributes (also known as member data) and methods (also known as member functions). The most basic concept in OOP is the class, which is a compound data type constructed from the elementary data type, such as integers and floating-point numbers. The corresponding methods are also offered in class definition. The defined class then serves as a blueprint of the thing of interest that can either be concrete or abstract. An instantiation of the defined class is called an object. The advantages of OOP include but are not limited to

- structured way of programming (intuitive and very quick to develop for a prototype);
- easy to adapt and maintain;
- easy to package up code into libraries for use by others.

There are many general-purpose programming languages with the object-oriented feature, such as C++ [121, 122, 123, 124] and Python. C++ is at low-level and compiled, with the capability of performing stunning feats of computation. It is often used in simulations, especially those that are computationally expensive. On the contrary, Python is at high-level and interpreted, allowing developers to write programs with fewer lines than some other programming languages. The most

notable advantage of Python is that there are a lot of well-documented libraries available for data analysis, visualization, and so on. It should be mentioned here that there are API (Application Programming Interfaces) for bridging C++ and Python together. This is what is called hybrid programming, and in doing so we can have strengths from both sides.

Some Useful Softwares and Libraries

There is no point to reinvent the wheel, as the saying goes. Using a variety of available softwares and libraries can greatly improve the efficiency of scientific research. Here, we list some softwares and libraries with brief introduction. They are

- Linux – It represents a family of open source Unix-like operating systems widely used in scientific computing. The common distributions are Ubuntu, CentOS, Debian, and so on.
- Vim – It is a highly configurable text editor for efficiently creating and changing any kind of text.
- GNU Make – It is a utility that requires a file, `Makefile`, which defines a set of tasks to be executed. It is used to facilitate compiling a program from source code. Ref. [125] gives more detailed account.
- GSL (GNU Scientific Library) – It is a numerical library for C/C++ programmers. It a free software under the GNU General Public License.
- g++ – It is an open-source C++ compiler included in GCC (GNU Compiler Collection).
- OpenMP (Open Multi-Processing) – It is an application programming interface (API) that supports multi-platform shared memory multiprocessing programming in C/C++ and Fortran.
- OpenMPI – It is an open-source message passing interface (MPI). It is often used in parallel computation in computer clusters.
- CUDA (Compute Unified Device Architecture) – It is a parallel computing platform and application programming interface (API) that allows software developers to use CUDA-enabled graphics processing unit (GPU) for general purpose processing.
- Matplotlib – It is a Python 2D plotting package which produces publication quality figures in a variety of formats.
- Numpy – It is a fundamental package for scientific computing with Python. It offers many routines for processing the operations between arrays.
- Scipy – It is a Python-based ecosystem of open-source softwares for mathematics, science, and engineering.

C++ Code for Simulating the Diode System

Here, we show the code for simulating the diode system. It is written in the following files:

- `Class_vector.cpp`, `Class_vector.h`,
- `Class_matrix.cpp`, `Class_matrix.h`,
- `Class_diode.cpp`, `Class_diode.h`,
- `Function_diode_evolving.cpp`,

- `Function_random_number_generating.cpp`,
- `Main.cpp`,
- `Makefile`,

which are compiled and linked with the tool **Make** according to instructions written in `Makefile`. Object-oriented programming is implemented such that we define a diode class named `Cdiode`. An instantiation of `Cdiode` is a diode object which is a state specifying the discretized distribution of electrons, holes, and potentials. The time evolution of the diode system is driven by a function which takes a diode object at time t and the time step $\mathrm{d}t$ as the arguments and return another diode object at time $t + \mathrm{d}t$. The brief description of functionalities of the code in each file can be found in the captions of the code appended below.

Listing F.1: `Class_vector.cpp`. The definition of the vector class `Cvector`. This class is used as a supporting data type in the definition of the diode class `Cdiode`.

```
#include <iostream>
#include "Class_matrix.h"
using std::cin;
using std::cout;
using std::endl;
class Cvector
{
	public:
		int m_dimensions;
		double *m_vector;

		Cvector(void);
		Cvector(double num, int dim);
		Cvector(const Cvector &vector);
		~Cvector(void);
		Cvector &operator=(const Cvector &vector);
		Cvector operator+(const Cvector &vector) const;
		Cvector operator-(const Cvector &vector) const;
		Cvector operator*(double multiplier) const;
		double &operator()(int);

	private:
		friend Cvector operator*(double multiplier, Cvector vector);
};

Cvector::Cvector()
{
	m_dimensions=0;
	m_vector=nullptr;
}

Cvector::Cvector(double num, int dim)
{
	m_dimensions=dim;
	m_vector=new double[m_dimensions];
	for(int i{0}; i<m_dimensions; i++) *(m_vector+i)=num;
}

Cvector::Cvector(const Cvector &vector)
{
	m_dimensions=vector.m_dimensions;
	m_vector=new double[m_dimensions];
	for(int i{0}; i<m_dimensions; i++) *(m_vector+i)=*(vector.m_vector+i);
}

Cvector::~Cvector()
{
	delete [] m_vector;
	m_vector=nullptr;
	m_dimensions=0;
}

Cvector &Cvector::operator=(const Cvector &vector)
```

```
{
        if(this==&vector) return *this;
        delete [] m_vector;
        m_vector=nullptr;
        m_dimensions=vector.m_dimensions;
        m_vector=new double[m_dimensions];
        for(int i{0}; i<m_dimensions; i++) *(m_vector+i)=*(vector.m_vector+i);
        return *this;
}

Cvector Cvector::operator+(const Cvector &vector) const
{
        Cvector vec(0.0, m_dimensions);
        for(int i{0}; i<m_dimensions; i++) *(vec.m_vector+i)=*(m_vector+i)+*(vector.m_vector+i);
        return vec;
}

Cvector Cvector::operator-(const Cvector &vector) const
{
        Cvector vec(0.0, m_dimensions);
        for(int i{0}; i<m_dimensions; i++) *(vec.m_vector+i)=*(m_vector+i)-*(vector.m_vector+i);
        return vec;
}

Cvector Cvector::operator*(double multiplier) const
{
        Cvector vec(0.0, m_dimensions);
        for(int i{0}; i<m_dimensions; i++) *(vec.m_vector+i)=*(m_vector+i)*multiplier;
        return vec;
}

double &Cvector::operator()(int index)
{
        return *(m_vector+index);
}

Cvector operator*(double multiplier, Cvector vector)
{
        return vector*multiplier;
}
```

Listing F.2: `Class_vector.h`. The declaration of `Cvector`.

```
#ifndef class_vector_h
#define class_vector_h
class Cmatrix;
class Cvector
{
        public:
                int m_dimensions;
                double *m_vector;

                Cvector(void);
                Cvector(double, int);
                Cvector(const Cvector &);
                ~Cvector(void);
                Cvector &operator=(const Cvector &);
                Cvector operator+(const Cvector &) const;
                Cvector operator-(const Cvector &) const;
                Cvector operator*(double) const;
                double &operator()(int);

        private:
                friend Cvector operator*(double, Cvector);
};
#endif
```

Listing F.3: `Class_matrix.cpp`. The definition of the matrix class `Cmatrix`. This class is used as a supporting data type in the definition of the diode class `Cdiode`.

```
#include <iostream>
```

```
#include "Class_vector.h"
using std::cin;
using std::cout;
using std::endl;
class Cmatrix
{
	public:
		int m_dimensions;
		double **m_matrix;

		Cmatrix(void);
		Cmatrix(double num, int dim);
		Cmatrix(const Cmatrix &matrix);
		~Cmatrix(void);
		Cmatrix &operator=(const Cmatrix &matrix);
		Cvector operator*(const Cvector &vector) const;
		double &operator()(int row, int column);
};

Cmatrix::Cmatrix()
{
	m_dimensions=0;
	m_matrix=nullptr;
}

Cmatrix::Cmatrix(double num, int dim)
{
	m_dimensions=dim;
	m_matrix=new double*[m_dimensions];
	for(int i{0}; i<m_dimensions; i++) *(m_matrix+i)=new double[m_dimensions];
	for(int i{0}; i<m_dimensions; i++)
	{
		for(int j{0}; j<m_dimensions; j++)
		{
			if(i==j) *(*(m_matrix+i)+j)=num;
			else *(*(m_matrix+i)+j)=0.0;
		}
	}
}

Cmatrix::Cmatrix(const Cmatrix &matrix)
{
	m_dimensions=matrix.m_dimensions;
	m_matrix=new double*[m_dimensions];
	for(int i{0}; i<m_dimensions; i++) *(m_matrix+i)=new double[m_dimensions];
	for(int i{0}; i<m_dimensions; i++)
	{
		for(int j{0}; j<m_dimensions; j++) *(*(m_matrix+i)+j)=*(*(matrix.m_matrix+i)+j);
	}
}

Cmatrix::~Cmatrix()
{
	for(int i{0}; i<m_dimensions; i++)
	{
		delete [] *(m_matrix+i);
		*(m_matrix+i)=nullptr;
	}
	m_dimensions=0;
	delete [] m_matrix;
	m_matrix=nullptr;
}

Cmatrix &Cmatrix::operator=(const Cmatrix &matrix)
{
	if(this==&matrix) return *this;
	for(int i{0}; i<m_dimensions; i++)
	{
		delete [] *(m_matrix+i);
		*(m_matrix+i)=nullptr;
	}
	delete [] m_matrix;
```

```
74          m_matrix=nullptr;
75          m_dimensions=matrix.m_dimensions;
76          m_matrix=new double*[m_dimensions];
77          for(int i{0}; i<m_dimensions; i++)
78          {
79                  *(m_matrix+i)=new double[m_dimensions];
80                  for(int j{0}; j<m_dimensions; j++) *(*(m_matrix+i)+j)=*(*(matrix.m_matrix+i)+j);
81          }
82          return *this;
83  }
84
85  Cvector Cmatrix::operator*(const Cvector &vector) const
86  {
87          Cvector vec(0.0, m_dimensions);
88          for(int i{0}; i<m_dimensions; i++)
89          {
90                  for(int j{0}; j<vector.m_dimensions; j++) *(vec.m_vector+i)=*(vec.m_vector+i)+*(*(
                        ↪ m_matrix+i)+j)*(vector.m_vector+j);
91          }
92          return vec;
93  }
94
95  double &Cmatrix::operator()(int row, int column)
96  {
97          return *(*(m_matrix+row)+column);
98  }
```

Listing F.4: `Class_matrix.h`. The declaration of `Cmatrix`.

```
1   #ifndef class_matrix_h
2   #define class_matrix_h
3   class Cvector;
4   class Cmatrix
5   {
6           public:
7                   int m_dimensions;
8                   double **m_matrix;
9
10                  Cmatrix(void);
11                  Cmatrix(double, int);
12                  Cmatrix(const Cmatrix &);
13                  ~Cmatrix(void);
14                  Cmatrix &operator=(const Cmatrix &);
15                  Cvector operator*(const Cvector &) const;
16                  double &operator()(int, int);
17  };
18  #endif
```

Listing F.5: `Class_diode.cpp`. The definition of the diode class `Cdiode`.

```
1   #include <iostream>
2   #include <cmath>
3   #include "Class_vector.h"
4   #include "Class_matrix.h"
5   using std::cin;
6   using std::cout;
7   using std::endl;
8   class Cdiode
9   {
10          public:
11                  static int m_L[2];
12                  static double m_epsilon;
13                  static double m_alpha;
14                  static double m_beta;
15                  static double m_e;
16                  static double m_dL;
17                  static double m_D_electron;
18                  static double m_D_hole;
19                  static double m_k_generation;
20                  static double m_k_recombination;
21                  static double m_volume;
```

```
22              static double m_section;
23              static double m_electron_L;
24              static double m_electron_R;
25              static double m_hole_L;
26              static double m_hole_R;
27              static double m_potential_L;
28              static double m_potential_R;
29              static Cvector m_acceptor;
30              static Cvector m_donor;
31              static Cvector m_electron_initial_state;
32              static Cvector m_hole_initial_state;
33              static Cmatrix m_c_inverse;
34              static bool initializing(double e_L, double h_L, double p_L, double e_R, double h_R,
                    ↪ double p_R);
35
36              Cvector m_electron;
37              Cvector m_hole;
38              Cvector m_charge;
39              Cvector m_potential;
40
41              Cdiode(void);
42              bool coordinating(void);
43              Cdiode &operator=(const Cdiode &state);
44 };
45
46 int Cdiode::m_L[2]={20, 20};
47 double Cdiode::m_epsilon=0.01;
48 double Cdiode::m_alpha=0.0;
49 double Cdiode::m_beta=1.0;
50 double Cdiode::m_e=1.0;
51 double Cdiode::m_dL=0.1;
52 double Cdiode::m_D_electron=0.01;
53 double Cdiode::m_D_hole=0.01;
54 double Cdiode::m_k_generation=0.01;
55 double Cdiode::m_k_recombination=0.01;
56 double Cdiode::m_electron_L=0.0;
57 double Cdiode::m_electron_R=0.0;
58 double Cdiode::m_hole_L=0.0;
59 double Cdiode::m_hole_R=0.0;
60 double Cdiode::m_potential_L=0.0;
61 double Cdiode::m_potential_R=0.0;
62 double Cdiode::m_volume=0.0;
63 double Cdiode::m_section=0.0;
64 Cvector Cdiode::m_acceptor(0.0, 0);
65 Cvector Cdiode::m_donor(0.0, 0);
66 Cvector Cdiode::m_electron_initial_state(0.0, 0);
67 Cvector Cdiode::m_hole_initial_state(0.0, 0);
68 Cmatrix Cdiode::m_c_inverse(0.0, 0);
69
70 bool Cdiode::initializing(double e_L, double h_L, double p_L, double e_R, double h_R, double p_R)
71 {
72        int L=m_L[0]+m_L[1];
73        m_electron_L=e_L;
74        m_electron_R=e_R;
75        m_hole_L=h_L;
76        m_hole_R=h_R;
77        m_potential_L=p_L;
78        m_potential_R=p_R;
79        m_acceptor=Cvector(0.0, L);
80        m_donor=Cvector(0.0, L);
81        m_electron_initial_state=Cvector(0.0, L);
82        m_hole_initial_state=Cvector(0.0, L);
83        m_c_inverse=Cmatrix(0.0, L);
84        for(int i=0; i<m_L[0]; i++)
85        {
86               m_electron_initial_state(i)=400;
87               m_hole_initial_state(i)=1600;
88               m_acceptor(i)=m_hole_initial_state(i)-m_electron_initial_state(i);
89               m_donor(i)=0;
90        }
91        for(int i=m_L[0]; i<L; i++)
92        {
```

```
93                m_electron_initial_state(i)=1600;
94                m_hole_initial_state(i)=400;
95                m_acceptor(i)=0;
96                m_donor(i)=m_electron_initial_state(i)-m_hole_initial_state(i);
97        }
98        m_volume=std::sqrt(m_k_recombination*m_electron_initial_state(0)*m_hole_initial_state(0)/
              ↪ m_k_generation);
99        m_section=m_volume/m_dL;
100       m_alpha=m_epsilon*m_volume/(m_dL*m_dL);
101       for(int i{0}; i<L; i++)
102       {
103               for(int j{0}; j<L; j++)
104               {
105                       if(i<=j)
106                               m_c_inverse(i, j)=1.0*((i+1)*(L-j))/(m_alpha*(L+1));
107
108                       else
109                               m_c_inverse(i, j)=1.0*((j+1)*(L-i))/(m_alpha*(L+1));
110               }
111       }
112       return true;
113 }
114
115 Cdiode::Cdiode()
116 {
117       int L=m_L[0]+m_L[1];
118       m_electron=Cvector(0.0, L);
119       m_hole=Cvector(0.0, L);
120       m_charge=Cvector(0.0, L);
121       m_potential=Cvector(0.0, L);
122       m_electron=m_electron_initial_state;
123       m_hole=m_hole_initial_state;
124       coordinating();
125 }
126
127 Cdiode &Cdiode::operator=(const Cdiode &state)
128 {
129       m_electron=state.m_electron;
130       m_hole=state.m_hole;
131       m_charge=state.m_charge;
132       m_potential=state.m_potential;
133       return *(this);
134 }
135
136 bool Cdiode::coordinating()
137 {
138       int L=m_L[0]+m_L[1];
139       m_charge=m_e*(m_donor-m_acceptor-m_electron+m_hole);
140       Cvector O=m_charge;
141       O(0)=O(0)+m_alpha*m_potential_L;
142       O(L-1)=O(L-1)+m_alpha*m_potential_R;
143       m_potential=m_c_inverse*O;
144       return true;
145 }
```

Listing F.6: `Class_diode.h`. The declaration of `Cdiode`.

```
1  #ifndef class_diode_h
2  #define class_diode_h
3  class Cvector;
4  class Cvector;
5  class Cdiode
6  {
7         public:
8                 static int m_L[2];
9                 static double m_epsilon;
10                static double m_alpha;
11                static double m_beta;
12                static double m_e;
13                static double m_dL;
14                static double m_D_electron;
15                static double m_D_hole;
```

```
16                static double m_k_generation;
17                static double m_k_recombination;
18                static double m_volume;
19                static double m_section;
20                static double m_electron_L;
21                static double m_electron_R;
22                static double m_hole_L;
23                static double m_hole_R;
24                static double m_potential_L;
25                static double m_potential_R;
26                static Cvector m_acceptor;
27                static Cvector m_donor;
28                static Cvector m_electron_initial_state;
29                static Cvector m_hole_initial_state;
30                static Cmatrix m_c_inverse;
31                static bool initializing(double, double, double, double, double, double);
32
33                Cvector m_electron;
34                Cvector m_hole;
35                Cvector m_charge;
36                Cvector m_potential;
37
38                Cdiode(void);
39                bool coordinating(void);
40                Cdiode &operator=(const Cdiode &);
41 };
42 #endif
```

Listing F.7: `Function_diode_evolving.cpp`. The function that drives the time evolution of the diode system. The algorithm is based on the stochastic process of Langevin type.

```
1  #include <iostream>
2  #include <tuple>
3  #include <cmath>
4  #include <vector>
5  #include "Class_vector.h"
6  #include "Class_matrix.h"
7  #include "Class_diode.h"
8  std::vector<double> random_number_generating(int);
9  using std::cin;
10 using std::cout;
11 using std::endl;
12 std::tuple<Cdiode, Cvector, Cvector, double> diode_evolving(Cdiode &state, double dt)
13 {
14         int L=Cdiode::m_L[0]+Cdiode::m_L[1];
15         double alpha=Cdiode::m_alpha;
16         double beta=Cdiode::m_beta;
17         double e=Cdiode::m_e;
18         double epsilon=Cdiode::m_epsilon;
19         double dL=Cdiode::m_dL;
20         double D_electron=Cdiode::m_D_electron;
21         double D_hole=Cdiode::m_D_hole;
22         double kg=Cdiode::m_k_generation;
23         double kr=Cdiode::m_k_recombination;
24         double volume=Cdiode::m_volume;
25         double potential_L=Cdiode::m_potential_L;
26         double potential_R=Cdiode::m_potential_R;
27         double electron_L=Cdiode::m_electron_L;
28         double electron_R=Cdiode::m_electron_R;
29         double hole_L=Cdiode::m_hole_L;
30         double hole_R=Cdiode::m_hole_R;
31         Cvector F_n(0.0, L+1), F_p(0.0, L+1);
32         double current{0.0};
33         double k_electron, k_hole;
34         double CDU, DUp, DUm, fp, fm;
35         double Wg, Wr;
36         double R[L];
37         double Wp_electron[L+1], Wm_electron[L+1], Wp_hole[L+1], Wm_hole[L+1];
38
39         k_electron=D_electron/(dL*dL);
40         k_hole=D_hole/(dL*dL);
41
```

```
42          CDU=0.5*e*e*L/(alpha*(L+1));
43
44          DUp=e*(state.m_potential(0)-potential_L)+CDU;
45          fp=beta*DUp/(exp(beta*DUp)-1.0);
46          DUm=e*(0-state.m_potential(0)+potential_L)+CDU;
47          fm=beta*DUm/(exp(beta*DUm)-1.0);
48          Wp_electron[0]=fm*k_electron*electron_L;
49          Wm_electron[0]=fp*k_electron*state.m_electron(0);
50          Wp_hole[0]=fp*k_hole*hole_L;
51          Wm_hole[0]=fm*k_hole*state.m_hole(0);
52
53          for(int i{1}; i<L; i++)
54          {
55                  DUp=e*(state.m_potential(i)-state.m_potential(i-1))+CDU;
56                  fp=beta*DUp/(exp(beta*DUp)-1.0);
57                  DUm=e*(0-state.m_potential(i)+state.m_potential(i-1))+CDU;
58                  fm=beta*DUm/(exp(beta*DUm)-1.0);
59                  Wp_electron[i]=fm*k_electron*state.m_electron(i-1);
60                  Wm_electron[i]=fp*k_electron*state.m_electron(i);
61                  Wp_hole[i]=fp*k_hole*state.m_hole(i-1);
62                  Wm_hole[i]=fm*k_hole*state.m_hole(i);
63          }
64
65          DUp=e*(potential_R-state.m_potential(L-1))+CDU;
66          fp=beta*DUp/(exp(beta*DUp)-1.0);
67          DUm=e*(0-potential_R+state.m_potential(L-1))+CDU;
68          fm=beta*DUm/(exp(beta*DUm)-1.0);
69          Wp_electron[L]=fm*k_electron*state.m_electron(L-1);
70          Wm_electron[L]=fp*k_electron*electron_R;
71          Wp_hole[L]=fp*k_hole*state.m_hole(L-1);
72          Wm_hole[L]=fm*k_hole*hole_R;
73
74          std::vector<double> gaussian{random_number_generating(3*L+2)};
75          int j{0};
76          double S;
77          S=(Wp_electron[0]+Wm_electron[0])/dt;
78          S=sqrt(S)*gaussian[j++];
79          F_n(0)=Wp_electron[0]-Wm_electron[0]+S;
80          S=(Wp_hole[0]+Wm_hole[0])/dt;
81          S=sqrt(S)*gaussian[j++];
82          F_p(0)=Wp_hole[0]-Wm_hole[0]+S;
83          for(int i{1}; i<L; i++)
84          {
85                  S=(Wp_electron[i]+Wm_electron[i])/dt;
86                  S=sqrt(S)*gaussian[j++];
87                  F_n(i)=Wp_electron[i]-Wm_electron[i]+S;
88                  S=(Wp_hole[i]+Wm_hole[i])/dt;
89                  S=sqrt(S)*gaussian[j++];
90                  F_p(i)=Wp_hole[i]-Wm_hole[i]+S;
91          }
92          S=(Wp_electron[L]+Wm_electron[L])/dt;
93          S=sqrt(S)*gaussian[j++];
94          F_n(L)=Wp_electron[L]-Wm_electron[L]+S;
95          S=(Wp_hole[L]+Wm_hole[L])/dt;
96          S=sqrt(S)*gaussian[j++];
97          F_p(L)=Wp_hole[L]-Wm_hole[L]+S;
98
99          for(int i{0}; i<L; i++)
100         {
101                 Wg=kg*volume;
102                 Wr=kr*state.m_electron(i)*state.m_hole(i)/volume;
103                 S=(Wg+Wr)/dt;
104                 S=sqrt(S)*gaussian[j++];
105                 R[i]=Wg-Wr+S;
106         }
107
108         Cdiode next_state;
109
110         for(int i{0}; i<L; i++)
111         {
112                 next_state.m_electron(i)=state.m_electron(i)+dt*(F_n(i)-F_n(i+1)+R[i]);
113                 if(next_state.m_electron(i)<0) cout<<"alarm"<<endl;
```

```
114                 next_state.m_hole(i)=state.m_hole(i)+dt*(F_p(i)-F_p(i+1)+R[i]);
115                 if(next_state.m_hole(i)<0) cout<<"alarm"<<endl;
116         }
117         next_state.coordinating();
118         for(int i{0}; i<L+1; i++)
119         {
120                 current+=e*(F_p(i)-F_n(i))/(L+1); // total current including the contribution of
                        ↪ displacement current
121         }
122         return std::make_tuple(next_state, F_n, F_p, current);
123 }
```

Listing F.8: `Function_random_number_generating.cpp`. The function that generates independent identically distributed Gaussian random numbers of zero mean value and unit variance.

```
1  #include <iostream>
2  #include <tuple>
3  #include <vector>
4  #include <gsl/gsl_rng.h>
5  #include <gsl/gsl_randist.h>
6  using std::cin;
7  using std::cout;
8  using std::endl;
9  static gsl_rng* generator=nullptr;
10
11 bool random_initializing()
12 {
13         generator=gsl_rng_alloc(gsl_rng_default);
14         gsl_rng_set(generator, 0); // seeded with 0
15         return true;
16 }
17
18 std::vector<double> random_number_generating(int num)
19 {
20         gsl_rng_env_setup(); // setup the environment for random number generation
21         double sigma{1.0};
22         gsl_rng* r=generator;
23         std::vector<double> gaussian(num, 0.0);
24         for(auto &gau:gaussian) gau=gsl_ran_gaussian(r, sigma); //generating gaussian distribution
               ↪ numbers with mu=0 and sigma
25         return std::move(gaussian);
26 }
27
28 bool random_finalizing()
29 {
30         gsl_rng_free(generator);
31         delete [] generator;
32         generator=nullptr;
33         return true;
34 }
```

Listing F.9: `Main.cpp`. The main function in which the counting statistics of the signed cumulated charge transfers is performed.

```
1  #include <iostream>
2  #include <fstream>
3  #include <cmath>
4  #include <iomanip>
5  #include <tuple>
6  #include "Class_vector.h"
7  #include "Class_matrix.h"
8  #include "Class_diode.h"
9  std::tuple<Cdiode, Cvector, Cvector, double> diode_evolving(Cdiode &, double);
10 bool random_initializing(void);
11 bool random_finalizing(void);
12 using std::cin;
13 using std::cout;
14 using std::endl;
15 int main(int argc, char *argv[])
16 {
17         random_initializing();
```

```
18
19          int L=Cdiode::m_L[0]+Cdiode::m_L[1];
20          double e=Cdiode::m_e;
21          double beta=Cdiode::m_beta;
22          double dt=0.05;
23
24          int e_L{400}, h_L{1600};
25          int e_R{1600}, h_R{400};
26          double V{1.0};
27          double p_L=V-std::log(h_L/h_R)/(beta*e);
28          double p_R{0.0};
29
30          Cdiode::initializing(e_L, h_L, p_L, e_R, h_R, p_R);
31
32          Cvector F_n(0.0, L+1), F_p(0.0, L+1);
33          double current;
34
35          Cdiode state;
36
37          for(int i{0}; i<50000; i++) std::tie(state, std::ignore, std::ignore, std::ignore)=
                ↪ diode_evolving(state, dt);
38
39          std::ofstream fout("Statistics.out");
40          fout.setf(std::ios_base::showpoint);
41          fout.setf(std::ios::right);
42
43          int runs{5000};
44          double Delta_t=10.0;
45          int times=static_cast<int>(Delta_t/dt);
46          for(int i{0}; i<runs; i++)
47          {
48                  double charge_1{0.0}, charge_2{0.0};
49                  for(int j{0}; j<times; j++)
50                  {
51                          std::tie(state, F_n, F_p, current)=diode_evolving(state, dt);
52                          charge_1+=(F_p(L/2)-F_n(L/2))*dt;
53                          charge_2+=current*dt/e;
54                  }
55                  fout<<std::setw(15)<<std::setprecision(8)<<charge_1<<" ";
56                  fout<<std::setw(15)<<std::setprecision(8)<<charge_2<<'\n';
57                  if((100*i)%runs==0) cout<<100.0*i/runs<<endl;
58          }
59
60          fout.close();
61
62          random_finalizing();
63          return 0;
64  }
```

Listing F.10: `Makefile`. The file to be read by the compiling-and-linking utility **Make**.

```
1  objects=Main.o Class_vector.o Class_matrix.o Class_diode.o Function_diode_evolving.o
       ↪ Function_random_number_generating.o
2  Main: $(objects)
3          g++ -std=c++11 -o Main $(objects) -lgsl -lgslcblas
4  Main.o: Main.cpp Class_vector.h Class_matrix.h Class_diode.h
5          g++ -std=c++11 -c Main.cpp
6  Class_vector.o: Class_vector.cpp Class_matrix.h
7          g++ -std=c++11 -c Class_vector.cpp
8  Class_matrix.o: Class_matrix.cpp Class_vector.h
9          g++ -std=c++11 -c Class_matrix.cpp
10 Class_diode.o: Class_diode.cpp Class_vector.h Class_matrix.h
11         g++ -std=c++11 -c Class_diode.cpp
12 Function_diode_evolving.o: Function_diode_evolving.cpp Class_vector.h Class_matrix.h Class_diode.h
13         g++ -std=c++11 -c Function_diode_evolving.cpp
14 Function_random_number_generating.o: Function_random_number_generating.cpp
15         g++ -std=c++11 -c Function_random_number_generating.cpp
16 clean:
17         rm -rf $(objects)
```

Bibliography

[1] Wassim M. Haddad. “Thermodynamics: The Unique Universe Science”. In: *Entropy* 19, 621 (2017).

[2] Wayne M. Saslow. “A History of Thermodynamics: The Missing Manual”. In: *Entropy* 22, 77 (2020).

[3] A. I. Khinchin. *Mathematical Foundations of Statistical Mechanics*. Dover, 1949.

[4] Ta-You Wu. “Boltzmann’s H Theorem and the Loschmidt and the Zermelo Paradoxes”. In: *International Journal of Theoretical Physics* 14 (1975), pp. 289–294.

[5] Josiah Willard Gibbs. *Elementary Principles in Statistical Mechanics*. New York: Charles Scribner’s Sons, 1902.

[6] Richard P. Feynman. *Statistical Mechanics: A Set of Lectures*. Frontiers in Physics. CRC Press, 1998.

[7] Albert Einstein. “Über die von der molekularkinetischen Theorie der Wärme geforderte Bewegung von in ruhenden Flüssigkeiten suspendierten Teilchen”. In: *Annalen der Physik* 17 (1905), pp. 549–560.

[8] A. Einstein. *Investigations on the Theory of the Brownian Movement*. New York: Dover, 1956.

[9] William Sutherland. “LXXV. A Dynamical Theory of Diffusion for Non-Electrolytes and the Molecular Mass of Albumin”. In: *Philosophical Magazine* 9 (1905), pp. 781–785.

[10] M. von Smoluchowski. “Zur kinetischen Theorie der Brownschen Molekularbewegung und der Suspensionen”. In: *Annalen der Physik* 326 (1906), pp. 756–780.

[11] G. E. Uhlenbeck and L. S. Ornstein. “On the Theory of the Brownian Motion”. In: *Physical Review* 36 (1930), pp. 823–841.

[12] Ming Chen Wang and G. E. Uhlenbeck. “On the Theory of the Brownian Motion II”. In: *Reviews of Modern Physics* 17 (1945), pp. 323–342.

[13] J. B. Johnson. “Thermal Agitation of Electricity in Conductors”. In: *Nature* 119 (1927), pp. 50–51.

[14] J. B. Johnson. “Thermal Agitation of Electricity in Conductors”. In: *Physical Review* 32 (1928), pp. 97–109.

[15] H. Nyquist. “Thermal Agitation of Electric Charge in Conductors”. In: *Physical Review* 32 (1928), pp. 110–113.

[16] Lars Onsager. “Reciprocal Relations in Irreversible Processes. I.” In: *Physical Review* 37 (1931), pp. 405–426.

[17] Lars Onsager. “Reciprocal Relations in Irreversible Processes. II.” In: *Physical Review* 38 (1931), pp. 2265–2279.

[18] H. B. G. Casimir. “On Onsager’s Principle of Microscopic Reversibility”. In: *Reviews of Modern Physics* 17 (1945), pp. 343–350.

[19] Melville S. Green. “Markoff Random Processes and the Statistical Mechanics of Time-Dependent Phenomena”. In: *The Journal of Chemical Physics* 20 (1952), pp. 1281–1295.

[20] Melville S. Green. “Markoff Random Processes and the Statistical Mechanics of Time-Dependent Phenomena. II. Irreversible Processes in Fluids”. In: *The Journal of Chemical Physics* 22 (1954), pp. 398–413.

[21] Ryogo Kubo. “Statistical-Mechanical Theory of Irreversible Processes. I. General Theory and Simple Applications to Magnetic and Conduction Problems”. In: *Journal of the Physical Society of Japan* 12 (1957), pp. 570–586.

[22] Ryogo Kubo, Mario Yokota, and Sadao Nakajima. “Statistical-Mechanical Theory of Irreversible Processes. II. Response to Thermal Disturbance”. In: *Journal of the Physical Society of Japan* 12 (1957), pp. 1203–1211.

[23] R. Kubo. “The Fluctuation-Dissipation Theorem”. In: *Reports on Progress in Physics* 29 (1966), pp. 255–284.

[24] Denis J. Evans, E. G. D. Cohen, and G. P. Morriss. “Probability of Second Law Violations in Shearing Steady States”. In: *Physical Review Letters* 71 (1993), pp. 2401–2404.

[25] G. Gallavotti and E. G. D. Cohen. “Dynamical Ensembles in Nonequilibrium Statistical Mechanics”. In: *Physical Review Letters* 74 (1995), pp. 2694–2697.

[26] G. Gallavotti and E. G. D. Cohen. “Dynamical Ensembles in Stationary States”. In: *Journal of Statistical Physics* 80 (1995), pp. 931–970.

[27] Kurchan J. “Fluctuation Theorem for Stochastic Dynamics”. In: *Journal of Physics A: Mathematical and General* 31 (1998), pp. 3719–3729.

[28] Joel L. Lebowitz and Herbert Spohn. “A Gallavotti-Cohen-Type Symmetry in the Large Deviation Functional for Stochastic Dynamics”. In: *Journal of Statistical Physics* 95 (1999), pp. 333–365.

[29] David Andrieux and Pierre Gaspard. “Fluctuation Theorem and Onsager Reciprocity Relations”. In: *The Journal of Chemical Physics* 121 (2004), pp. 6167–6174.

[30] David Andrieux and Pierre Gaspard. “Fluctuation Theorem for Transport in Mesoscopic Systems”. In: *Journal of Statistical Mechanics: Theory and Experiment*, P01011 (2006).

[31] David Andrieux and Pierre Gaspard. “Fluctuation Theorem for Currents and Schnakenberg Network Theory”. In: *Journal of Statistical Physics* 127 (2007), pp. 107–131.

[32] D. Andrieux, P. Gaspard, T. Monnai, et al. “The Fluctuation Theorem for Currents in Open Quantum Systems”. In: *New Journal of Physics* 11, 043014 (2009).

[33] G. M. Wang, E. M. Sevick, Emil Mittag, et al. “Experimental Demonstration of Violations of the Second Law of Thermodynamics for Small Systems and Short Time Scales”. In: *Physical Review Letters* 89, 050601 (2002).

[34] Effrosyni Seitaridou, Mandar M. Inamdar, Rob Phillips, et al. “Measuring Flux Distributions for Diffusion in the Small-Numbers Limit”. In: *The Journal of Physical Chemistry B* 111 (2007), pp. 2288–2292.

[35] Y. Utsumi, D. S. Golubev, M. Marthaler, et al. “Bidirectional Single-Electron Counting and the Fluctuation Theorem”. In: *Physical Review B* 81, 125331 (2010).

[36] Shuji Nakamura, Yoshiaki Yamauchi, Masayuki Hashisaka, et al. “Nonequilibrium Fluctuation Relations in a Quantum Coherent Conductor”. In: *Physical Review Letters* 104, 080602 (2010).

[37] Shuji Nakamura, Yoshiaki Yamauchi, Masayuki Hashisaka, et al. “Fluctuation Theorem and Microreversibility in a Quantum Coherent Conductor”. In: *Physical Review B* 83, 155431 (2011).

[38] B. Küng, C. Rössler, M. Beck, et al. “Irreversibility on the Level of Single-Electron Tunneling”. In: *Physical Review X* 2, 011001 (2012).

[39] B. Küng, C. Rössler, M. Beck, et al. “Test of the Fluctuation Theorem for Single-Electron Transport”. In: *Journal of Applied Physics* 113, 136507 (2013).

[40] C. Jarzynski. “Nonequilibrium Equality for Free Energy Differences”. In: *Physical Review Letters* 78 (1997), pp. 2690–2693.

[41] C. Jarzynski. “Equilibrium Free-Energy Differences from Nonequilibrium Measurements: A Master-Equation Approach”. In: *Physical Review E* 56 (1997), pp. 5018–5035.

[42] Christopher Jarzynski. “Nonequilibrium Work Theorem for A System Strongly Coupled to A Thermal Environment”. In: *Journal of Statistical Mechanics: Theory and Experiment*, P09005 (2004).

[43] C. Jarzynski. “Nonequilibrium Work Relations: Foundations and Applications”. In: *The European Physical Journal B: Condensed Matter and Complex Systems* 64 (2008), pp. 331–340.

[44] Christopher Jarzynski. “Rare Events and the Convergence of Exponentially Averaged Work Values”. In: *Physical Review E* 73, 046105 (2006).

[45] Christopher Jarzynski. “Equalities and Inequilities: Irreversibility and the Second Law of Thermodynamics at the Nanoscale”. In: *Annual Review of Condensed Matter Physics* 2 (2011), pp. 329–351.

[46] L. D. Landau and E. M. Lifshitz. *Mechanics*. Third Edition. Translated from the Russian by J. B. Sykes and J. S. Bell. Butterworth-Heinemann, 1976.

[47] Gavin E. Crooks. “Entropy Production Fluctuation Theorem and the Nonequilibrium Work Relation for Free Energy Differences”. In: *Physical Review E* 60 (1999), pp. 2721–2726.

[48] G. N. Bochkov and Yu. E. Kuzovlev. “General Theory of Thermal Fluctuations in Nonlinear Systems”. In: *Soviet Journal of Experimental and Theoretical Physics* 45 (1977), pp. 125–130.

[49] G. N. Bochkov and Yu. E. Kuzovlev. “Fluctuation-Dissipation Relations for Nonequilibrium Processes in Open Systems”. In: *Soviet Journal of Experimental and Theoretical Physics* 49 (1979), pp. 543–551.

[50] G. N. Bochkov and Yu. E. Kuzovlev. “Nonlinear Fluctuation-Dissipation Relations and Stochastic Models in Nonequilibrium Thermodynamics. I. Generalized Fluctuation-Dissipation Theorem”. In: *Physica A: Statistical Mechanics and its Applications* 106 (1981), pp. 443–479.

[51] G. N. Bochkov and Yu. E. Kuzovlev. “Nonlinear Fluctuation-Dissipation Relations and Stochastic Models in Nonequilibrium Thermodynamics. II. Kinetic Potential and Variational Principles for Nonlinear Irreversible Processes”. In: *Physica A: Statistical Mechanics and its Applications* 106 (1981), pp. 480–520.

[52] Gerhard Hummer and Attila Szabo. “Free Energy Profile from Single-Molecule Pulling Experiments”. In: *Proceedings of the National Academy of Sciences of the United States of America* 107 (2010), pp. 21441–21446.

[53] Jan Liphardt, Sophie Dumont, Steven B. Smith, et al. “Equilibrium Information from Nonequilibrium Measurements in an Experimental Test of Jarzynski’s Equality”. In: *Science* 296 (2002), pp. 1832–1836.

[54] D. Collin, F. Ritort, C. Jarzynski, et al. “Verification of the Crooks Fluctuation Theorem and Recovery of RNA Folding Free Energies”. In: *Nature* (2005), pp. 231–234.

[55] Daan Frenkel and Berend Smit. *Understanding Molecular Simulation: From Algorithms to Applications*. Second Edition. Academic Press, 2002.

[56] Denis J. Evans and Debra J. Searles. “The Fluctuation Theorem”. In: *Advances in Physics* 51 (2002), pp. 1529–1585.

[57] Massimiliano Esposito, Upendra Harbola, and Shaul Mukamel. “Nonequilibrium Fluctuations, Fluctuation Theorems, and Counting Statistics in Quantum Systems”. In: *Reviews of Modern Physics* 81 (2009), pp. 1665–1702.

[58] Michele Campisi, Peter Hänggi, and Peter Talkner. "Colloquium: Quantum Fluctuation Relations: Foundations and Applications". In: *Reviews of Modern Physics* 83 (2011), pp. 771–791.

[59] Udo Seifert. "Stochastic Thermodynamics, Fluctuation Theorems and Molecular Machines". In: *Reports on Progress in Physics* 75, 126001 (2012).

[60] R. Klages, W. Just, and C. Jarzynski, eds. *Nonequilibrium Statistical Physics of Small Systems: Fluctuation Relations and Beyond*. Weinheim: Wiley-VCH, 2013.

[61] Pierre Gaspard. "Multivariate Fluctuation Relations for Currents". In: *New Journal of Physics* 15, 115014 (2013).

[62] David Andrieux and Pierre Gaspard. "Stochastic Approach and Fluctuation Theorem for Ion Transport". In: *Journal of Statistical Mechanics: Theory and Experiment*, P02057 (2009).

[63] T. De Donder and P. Van Rysselberghe. *Thermodynamic Theory of Affinity*. Menlo Park CA: Stanford University Press, 1936.

[64] D. Lacoste and K. Mallick. "Fluctuation Theorem for the Flashing Ratchet Model of Molecular Motors". In: *Physical Review E* 80, 021923 (2009).

[65] I. Prigogine. *Introduction to Thermodynamics of Irreversible Processes*. New York: Wiley, 1967.

[66] S. R. de Groot and P. Mazur. *Nonequilibrium Thermodynamics*. Dover, 1984.

[67] H. B. Callen. *Thermodynamics and An Introduction to Thermostatistics*. Second Edition. New York: Wiley, 1985.

[68] R. L. Stratonovich. *Nonlinear Nonequilibrium Thermodynamics I*. Berlin: Springer-Verlag, 1992.

[69] David Andrieux and Pierre Gaspard. "A Fluctuation Theorem for Currents and Non-Linear Response Coefficients". In: *Journal of Statistical Mechanics: Theory and Experiment*, P02006 (2007).

[70] Pablo I. Hurtado, Carlos Pérez-Espigares, Jesús J. del Pozo, et al. "Symmetries in Fluctuations Far From Equilibrium". In: *Proceedings of the National Academy of Sciences of the United States of America* 108 (2011), pp. 7704–7709.

[71] M. Barbier and P. Gaspard. "Microreversibility, Nonequilibrium Current Fluctuations, and Response Theory". In: *Journal of Physics A: Mathematical and Theoretical* 51, 355001 (2018).

[72] P. Billingsley. *Probability and Measure*. Third Edition. New York: Wiley, 1995.

[73] Terrell L. Hill. "Studies in Irreversible Thermodynamics III. Models for Steady State and Active Transport Across Membranes". In: *Journal of Theoretical Biology* 10 (1966), pp. 399–441.

[74] Terrell L. Hill. "Studies in Irreversible Thermodynamics IV. Diagrammatic Representation of Steady State Fluxes for Unimolecular Systems". In: *Journal of Theoretical Biology* 10 (1966), pp. 442–459.

[75] T. L. Hill. *Thermodynamics for Chemists and Biologists*. Addison-Wesley, 1968.

[76] G. F. Oster and C. A. Desoer. "Tellegen's Theorem and Thermodynamic Inequalities". In: *Journal of Theoretical Biology* 32 (1971), pp. 219–241.

[77] George Oster, Alan Perelson, and Aharon Katchalsky. "Network Thermodynamics". In: *Nature* 234 (1971), pp. 393–399.

[78] J. Schnakenberg. "Network Theory of Microscopic and Macroscopic Behavior of Master Equation Systems". In: *Reviews of Modern Physics* 48 (1976), pp. 571–585.

[79] D.-Q. Jiang, M. Qian, and M.-P. Qian. *Mathematical Theory of Nonequilibrium Steady States: On the Frontier of Probability and Dynamical Systems*. Springer, 2004.

[80] Daniel T. Gillespie. “A General Method for Numerically Simulating the Stochastic Time Evolution of Coupled Chemical Reactions”. In: *Journal of Computational Physics* 22 (1976), pp. 403–434.

[81] Donald E. Knuth. *The Art of Computer Programming, Volume 2: Seminumerical Algorithms*. Third Edition. Boston: Addison-Wesley, 1997.

[82] Milton Abramowitz and Irene A. Stegun, eds. *Handbook of Mathematical Functions with Foromulas, Graphs, and Mathematical Tables*. National Bureau of Standards, 1972.

[83] C. W. Gardiner. *Handbook of Stochastic Methods*. Third Edition. Berlin: Springer, 2004.

[84] John David Jackson. *Classical Electrodynamics*. Third Edition. Wiley, 1999.

[85] 郭硕鸿. 电动力学. 第三版. "Shuohong Guo. Electrodynamics. Third Edition. Beijing:Higher Education Press, 2008.". 北京: 高等教育出版社, 2008.

[86] Pierre Gaspard. “Brownian Motion, Dynamical Randomness and Irreversibility”. In: *New Journal of Physics* 7, 77 (2005).

[87] Pierre Gaspard and Raymond Kapral. “Finite-Time Fluctuation Theorem for Diffusion-Influenced Surface Reactions”. In: *Journal of Statistical Mechanics: Theory and Experiment* 8, 083206 (2018).

[88] W. Shockley. “The Theory of *p-n* Junctions in Semiconductors and *p-n* Junction Transistors”. In: *Bell System Technical Journal* 28 (1949), pp. 435–489.

[89] W. Shockley. *Electrons and Holes in Semiconductors*. Princeton, New Jersey: D. Van Nostrand, 1950.

[90] 刘恩科, 朱秉升, and 罗晋生. 半导体物理学. 第七版. "Enke Liu, Bingsheng Zhu, jinsheng Luo. Semiconductor Physics. Seventh Edition. Publishing House of Electronics Industry, 2008.". 北京: 电子工业出版社, 2008.

[91] N. W. Ashcroft and N. D. Mermin. *Solid State Physics*. Philadelphia: Saunders College, 1976.

[92] S. M. Sze and Kwok K. Ng. *Physics of Semiconductor Devices*. Third Edition. Hobboken: Wiley, 2007.

[93] Kevin F. Brennan. *Introduction to Semiconductor Devices: For Computing and Telecommunications Applications*. Cambridge University Press, 2005.

[94] Jean-Pierre Colinge and Cynthia A. Colinge. *Physics of Semiconductor Devices*. New York: Kluwer Academic Publisher, 2005.

[95] Donald A. Neamen. *Semiconductor Physics and Devices: Basic Principles*. Third Edition. McGraw-Hill, 2003.

[96] 华成英 and 童诗白, eds. 模拟电子技术基础. 第四版. "Chengying Hua, Shibai Tong. Basics of Analog Circuit Technology. Fourth Edition. Beijing:Higher Education Press, 2006.". 北京: 高等教育出版社, 2006.

[97] R. van Zon, S. Ciliberto, and E. G. D. Cohen. “Power and Heat Fluctuation Theorems for Electric Circuits”. In: *Physical Review Letters* 92, 130601 (2004).

[98] N. Garnier and S. Ciliberto. “Nonequilibrium Fluctuations in a Resistor”. In: *Physical Review E* 71, 060101 (2005).

[99] S. Joubaud, N. B. Garnier, and S. Ciliberto. “Fluctuations of the total entropy production in stochastic systems”. In: *Europhysics Letters* 82, 30007 (2008).

[100] H. Hurwitz. “Voltage Fluctuations in a Diode”. In: *Physical Review* 172 (1968), pp. 207–211.

[101] Jiuliang Liu and Jizhou He. “Diode System Rectifying Thermal Fluctuations”. In: *Physical Review E* 82, 022101 (2010).

[102] Ya. M. Blanter and M. Büttiker. “Shot Noise in Mesoscopic Conductors”. In: *Physics Reports* 336 (2000), pp. 1–166.

[103] W. Shockley. “Currents to Conductors Induced by a Moving Point Charge”. In: *Journal of Applied Physics* 9 (1938), pp. 635–636.

[104] S. Ramo. “Currents Induced by Electron Motion”. In: *Proceedings of the IRE* 27 (1939), pp. 584–585.

[105] W. Shockley, M. Sparks, and G. K. Teal. “*p-n* Junction Transistors”. In: *Physical Review* 83 (1951), pp. 151–162.

[106] J. J. Ebers and J. L. Moll. “Large-Signal Behavior of Junction Transistors”. In: *Proceedings of the IRE* 42 (1954), pp. 1761–1772.

[107] Adel S. Sedra and Kenneth Carless Smith, eds. *Microelectronic Circuits*. Sixth Edition. Oxford: Oxford University Press, 2010.

[108] Pierre Gaspard, Patrick Grosfils, Mu-Jie Huang, et al. “Finite-Time Fluctuation Theorem for Diffusion-Influenced Surface Reactions on Spherical and Janus Catalytic Particles”. In: *Journal of Statistical Mechanics: Theory and Experiment* 12, 123206 (2018).

[109] M. Amman, R. Wilkins, E. Ben-Jacob, et al. “Analytic Solution for the Current-Voltage Characteristic of Two Mesoscopic Tunnel Junctions Coupled in Series”. In: *Physical Review B* (1991), pp. 1146–1149.

[110] D. V. Averin and K. K. Likharev. “Coulomb Blockade of Single-Electron Tunneling, and Coherent Oscillations in Small Tunnel Junctions”. In: *Journal of Low Temperature Physics* 62 (1986), pp. 345–373.

[111] M. A. Kastner. “The Single-Electron Transistor”. In: *Reviews of Modern Physics* 64 (1992), pp. 849–858.

[112] Gregory Bulnes Cuetara, Massimiliano Esposito, and Pierre Gaspard. “Fluctuation Theorems for Capacitively Coupled Electronic Currents”. In: *Physical Review B* 84, 165114 (2011).

[113] N. S. 巴赫瓦洛夫, N. P. 热依德科夫, and G. M. 柯别里科夫. *数值方法*. 第 5 版. Translated by 陈阳舟 from "N. S. Bakhvalov, N. P. Zhidkov, G. M. Kobelkov, Numerical Methods, 5th edition, 2007" in the Russian and proofreaded by 蔡大用 and 王小群. 北京: 高等教育出版社, 2014.

[114] Marshall H. Stone. “The Generalized Weierstrass Approximation Theorem”. In: *Mathematics Magazine* 21 (1948), pp. 237–254.

[115] Mariano Gasca and Thomas Sauer. “Polynomial Interpolation in Several Variables”. In: *Advances in Computational Mathematics* 12 (2000), pp. 377–410.

[116] J. F. Steffensen. *Interpolation*. Second Edition. Dover, 2006.

[117] Jr. George A. Baker. *Essentials of Padé Approximants*. Academic Press, 1975.

[118] Jr. George A. Baker and Peter Graves-Morris. *Padé Approximants. Part I: Basic Theory*. Addison-Wesley Publishing, 1981.

[119] Jr. George A. Baker and Peter Graves-Morris. *Padé Approximants. Part II: Extensions and Applications*. Addison-Wesley Publishing, 1981.

[120] Greg Wilson, D. A. Aruliah, C. Titus Brown, et al. “Best Practices for Scientific Computing”. In: *PLOS Biology* 12, e1001745 (2014).

[121] 范磊. *从新手到高手: C++ 全方位学习*. "Lei Fan. From Novice to Expert: C++ All-Round Learning. Beijing:Science Press, 2009". 北京: 科学出版社, 2009.

[122] Stanley B. Lippman, Josée Lajoie, and Barbara Moo. *C++ Primer*. Fifth Edition. Addison-Wesley Professional, 2012.

[123] Ivor Horton. *Ivor Horton's Beginning Visual C++ 2012*. Sixth Edition. Wrox Beginning Guides. Indianapolis: John Wiley & Sons, 2012.

[124] Stephen Prata. *C++ Primer Plus*. Sixth Edition. Addison-Wesley Professional, 2011.

[125] John Graham-Cumming. *The GNU Make Book*. San Francisco: No Starch Press, 2015.